Developing nanostructured electrodes for renewable energy applications

by

Sabari Rajendran

B.Tech., CSIR - Central Electrochemical Research Institute, 2017

AN ABSTRACT OF A DISSERTATION

submitted in partial fulfillment of the requirements for the degree

DOCTOR OF PHILOSOPHY

Department of Chemistry
College of Arts and Sciences

KANSAS STATE UNIVERSITY
Manhattan, Kansas

2024

Abstract

The energy transition from fossil fuels to renewable energy sources is the approach globally adopted to address the climate change driven by emission of greenhouse gases. Owing to the intermittent nature of solar and wind energies, the development of energy storage technologies such as sustainable rechargeable batteries of high energy density beyond the current lithium-ion batteries is critical to accelerate this energy transition to achieve net-zero carbon emissions. Lithium metal batteries such as lithium-sulfur and lithium-air offer high theoretical energy densities of 2567 Wh/kg and 3505 Wh/kg, respectively. For battery energy storage applications, safer aqueous zinc-ion batteries (AZIBs) are another attractive option. The commercialization of next generation batteries is hindered by challenges such as poor cycle life, poor charge efficiency associated with the respective anode and cathode materials. This dissertation comprises of studies aimed towards improving our understanding on the working of various anode and cathode materials directed towards the development of high-performance next-generation batteries.

Implementing three-dimensional (3-D) hosts is one of the effective approaches to mitigate dendrite formation in lithium metal anodes (LMAs). However, the formation and evolution of electrodeposited lithium (e-Li) and solid electrolyte interphase (SEI) on 3-D LMA hosts remain understudied. To address this, mechanistic studies conducted using a model 3-D nanostructured host based on vertically aligned carbon nanofibers (VACNFs) grown on Cu foil (VACNF/Cu) are discussed in Chapter 2. Chemical and morphological analysis uncovers the different types of SEIs forming in lithiated VACNF/Cu. Upon plating, Li electrodeposits dominantly as dense, infiltrative, columnar micro-grains that help to enhance the electrochemical performance. The VACNFs that are not engulfed by infiltrative-Li are coaxially coated with nanoscale Li. The SEI accumulation

during each cycle causes loss of electrolyte leading to cell failure. Further studies to elucidate the effect of plating and stripping kinetics on the morphology of e-Li and on the cycling performance of 3-D LMAs are discussed in Chapter 3. Microscopic analysis and electrochemical tests with decoupled Li plating/stripping rates reveal that a moderate current density (~ 1.0 mA/cm^2) is necessary for obtaining dense, columnar e-Li morphology, governed by classical nucleation and growth theory, which exhibits the highest performance. Low current density (≤ 0.10 mA/cm^2) results in sparsely distributed noodle-like Li with inferior stripping efficiency but could be converted into dense flat islands by applying a high pressure in the electrode/separator stacks.

In Chapter 4, the development of binder-free air cathodes toward Li-air batteries based on transition metal (Ni) and noble metal alloy (PtRu) deposited VACNF arrays grown on carbon substrates (VACNF-Ni and VACNF-PtRu respectively) is discussed. The VACNF-Ni and VACNF-PtRu air cathodes deliver enhanced discharge capacity by forming thin film-like Li_2O_2. The coverage of VACNFs' surface with catalyst nanoparticles offers improved cycling stability by preventing degradation of carbon at oxidizing potentials. Chapter 5 discusses the development of nanostructured hybrids consisting of V_2O_5 nanoribbons and reduced graphene oxide as AZIB cathodes. The hybrids are synthesized using a facile coprecipitation method utilizing divalent cations (Zn^{2+} and Mn^{2+}). The pre-intercalation of Zn^{2+} ions facilitates faster Zn^{2+} diffusion into the V_2O_5 structure thereby enhances the specific capacity of the hybrid material, while the inclusion of Mn^{2+} during coprecipitation benefits to improve the cycling stability of the cathode by providing stable pillars between V_2O_5 layers due to the stronger interaction between the Mn^{n+} ions and the V_2O_5 framework. Further studies on 3-D LMAs are discussed in Chapter 6. In conclusion, the scientific knowledge gained could aid in advancing high-performance energy storage technologies thereby supporting the shift towards renewable energy sources.

Developing nanostructured electrodes for renewable energy applications

by

Sabari Rajendran

B.Tech., CSIR - Central Electrochemical Research Institute, 2017

A DISSERTATION

submitted in partial fulfillment of the requirements for the degree

DOCTOR OF PHILOSOPHY

Department of Chemistry
College of Arts and Sciences

KANSAS STATE UNIVERSITY
Manhattan, Kansas

2024

Approved by:

Major Professor
Dr. Jun Li

Copyright

Abstract

The energy transition from fossil fuels to renewable energy sources is the approach globally adopted to address the climate change driven by emission of greenhouse gases. Owing to the intermittent nature of solar and wind energies, the development of energy storage technologies such as sustainable rechargeable batteries of high energy density beyond the current lithium-ion batteries is critical to accelerate this energy transition to achieve net-zero carbon emissions. Lithium metal batteries such as lithium-sulfur and lithium-air offer high theoretical energy densities of 2567 Wh/kg and 3505 Wh/kg, respectively. For battery energy storage applications, safer aqueous zinc-ion batteries (AZIBs) are another attractive option. The commercialization of next generation batteries is hindered by challenges such as poor cycle life, poor charge efficiency associated with the respective anode and cathode materials. This dissertation comprises of studies aimed towards improving our understanding on the working of various anode and cathode materials directed towards the development of high-performance next-generation batteries.

Implementing three-dimensional (3-D) hosts is one of the effective approaches to mitigate dendrite formation in lithium metal anodes (LMAs). However, the formation and evolution of electrodeposited lithium (e-Li) and solid electrolyte interphase (SEI) on 3-D LMA hosts remain understudied. To address this, mechanistic studies conducted using a model 3-D nanostructured host based on vertically aligned carbon nanofibers (VACNFs) grown on Cu foil (VACNF/Cu) are discussed in Chapter 2. Chemical and morphological analysis uncovers the different types of SEIs forming in lithiated VACNF/Cu. Upon plating, Li electrodeposits dominantly as dense, infiltrative, columnar micro-grains that help to enhance the electrochemical performance. The VACNFs that are not engulfed by infiltrative-Li are coaxially coated with nanoscale Li. The SEI accumulation

during each cycle causes loss of electrolyte leading to cell failure. Further studies to elucidate the effect of plating and stripping kinetics on the morphology of e-Li and on the cycling performance of 3-D LMAs are discussed in Chapter 3. Microscopic analysis and electrochemical tests with decoupled Li plating/stripping rates reveal that a moderate current density (~ 1.0 mA/cm^2) is necessary for obtaining dense, columnar e-Li morphology, governed by classical nucleation and growth theory, which exhibits the highest performance. Low current density (≤ 0.10 mA/cm^2) results in sparsely distributed noodle-like Li with inferior stripping efficiency but could be converted into dense flat islands by applying a high pressure in the electrode/separator stacks.

In Chapter 4, the development of binder-free air cathodes toward Li-air batteries based on transition metal (Ni) and noble metal alloy (PtRu) deposited VACNF arrays grown on carbon substrates (VACNF-Ni and VACNF-PtRu respectively) is discussed. The VACNF-Ni and VACNF-PtRu air cathodes deliver enhanced discharge capacity by forming thin film-like Li_2O_2. The coverage of VACNFs' surface with catalyst nanoparticles offers improved cycling stability by preventing degradation of carbon at oxidizing potentials. Chapter 5 discusses the development of nanostructured hybrids consisting of V_2O_5 nanoribbons and reduced graphene oxide as AZIB cathodes. The hybrids are synthesized using a facile coprecipitation method utilizing divalent cations (Zn^{2+} and Mn^{2+}). The pre-intercalation of Zn^{2+} ions facilitates faster Zn^{2+} diffusion into the V_2O_5 structure thereby enhances the specific capacity of the hybrid material, while the inclusion of Mn^{2+} during coprecipitation benefits to improve the cycling stability of the cathode by providing stable pillars between V_2O_5 layers due to the stronger interaction between the Mn^{n+} ions and the V_2O_5 framework. Further studies on 3-D LMAs are discussed in Chapter 6. In conclusion, the scientific knowledge gained could aid in advancing high-performance energy storage technologies thereby supporting the shift towards renewable energy sources.

Table of Contents

List of Figures

List of Abbreviations

3-D	Three-dimensional
AZIB	Aqueous zinc-ion battery
BE	Binding energy
CC	Carbon cloth
CE	Coulombic efficiency
CNF	Carbon nanofiber
CNT	Carbon nanotube
CP	Carbon paper
CSIR	Council of Scientific and Industrial Research
CTE	Counter electrode
CV	Cyclic voltammetry
CVD	Chemical vapor deposition
DME	1,2-dimethylethane
DMF	Dimethylformamide
DoD	Depth-of-discharge
DOL	1,3-dioxolane
EDS	Energy dispersive spectroscopy
e-Li	Electrodeposited lithium
EV	Electric vehicle
FESEM	Field emission scanning electron microscope
FIB	Focused ion beam

GDE	Gas diffusion electrode
GITT	Galvanostatic intermittent titration technique
GO	Graphene oxide
HER	Hydrogen evolution reaction
ICE	Internal combustion engine
IPA	Isopropyl alcohol
KU	The University of Kansas
LAB	Lead-acid battery
LDH	Layered double hydroxide
LIB	Li-ion battery
LITFSI	Lithium bis(trifluoromethanesulfonyl)imide
LMA	Lithium metal anode
LMB	Lithium metal battery
LOB	Lithium oxygen battery
MWCNT	Multi-walled carbon nanotubes
NRs	Nanoribbons
OCV	Open circuit voltage
OER	Oxygen evolution reaction
ORR	Oxygen reduction reaction
PAN	Polyacrylonitrile
PECVD	Plasma enhanced chemical vapor deposition
PTFE	Polytetrafluoroethylene
PVDF	Polyvinylidene fluoride

RE	Reference electrode
rGO	Reduced graphene oxide
SEI	Solid electrolyte interphase
SEM	Scanning electron microscope
SERS	Surface enhanced Raman scattering
SHE	Standard hydrogen electrode
SOC	State-of-charge
STEM	Scanning transmission electron microscopy
TEM	Transmission electron microscope
TGA	Thermogravimetric analysis
THF	Tetrahydrofuran
VACNF	Vertically aligned carbon nanofibers
WE	Working electrode
XPS	X-ray photoelectron spectroscopy
XRD	X-ray diffraction

Acknowledgements

First and foremost, I sincerely thank Prof. Jun Li for being a great mentor throughout my Ph.D. journey. None of this would have been possible without his intellectual guidance and moral support. I am grateful to have him as a teacher who dedicated an immense amount of invaluable time to my education over these years. I thank him for the unwavering support and patience, especially during my failures. I am also grateful for the trust he has in me, providing me with numerous opportunities for learning science and developing myself as a better thinker.

I wish to express my gratitude to my supervisory committee members Dr. Takashi Ito, Dr. Tendai Gadzikwa, and Dr. Suprem Das for their insightful suggestions that helped me to gain newer perspectives and for their support during all phases of my doctoral study. I would like to extend my gratitude to Dr. Xianglin Li and Syed Shoaib Hassan Zaidi at The University of Kansas, Dr. Placidus Amama and Dr. Duy Hua at Kansas State University (KSU), as well as Marc Andelman at Mespilus for fruitful collaborations on various projects.

I am thankful to Dr. Dan Boyle at KSU and Dr. Balamurugan Balasubramanian at University of Nebraska, Lincoln for teaching and helping me with the transmission electron microscopy imaging and the X-ray photoelectron spectroscopy measurements, respectively. My gratitude to our current and past department heads Dr. Christer Aakeröy and Dr. Daniel Higgins for their support. I would like to thank Michael Hinton and Dr. Boris Averkiev for their guidance in teaching undergraduate labs. I also thank Dr. Tingting Liu and Dr. Sadish Karunaweera for training and helping me to keep the lab spaces a safe place for everyone. I express my sincere gratitude to Tobe Eggers, Bart Bath, Ron Jackson, Jim Hodgson, and Kimberly Ross who helped me in numerous ways during these five years.

My heartfelt gratitude to our lab group – Dr. Ayyappan Elangovan, Dr. Yang Song, Gage Wright, Dr. Kamalambika Muthukumar, Dr. Archana Sekar for their teachings and assistance. I would like to extend my gratitude to Zawad Hossain, Bingun Habarakadage and Zahirul Saddam for their support. I wish to express my gratitude towards various entities within KSU such as Graduate School, College of Arts and Sciences, K-State libraries, Graduate Student Council (GSC), Phi Lambda Upsilon (PLU) and Department of Chemistry. Their provision of resources has been instrumental in my journey through graduate study. I am deeply thankful to the Department of Chemistry and Johnson Cancer Research Center for their financial support in terms of assistantship and fellowships. My gratitude extends to PLU, College of Arts and Sciences and GSC for awarding travel grants that enabled me to present my research in various national conferences. I am grateful for the encouraging support and recognition from the members of various award selection committees in the Department of Chemistry. I am grateful for the funding supported by the National Science Foundation (CBET-2054754, DMR-1707585) and the National Aeronautics and Space Administration (Kansas NASA EPSCoR Program - 80NSSC23M0100).

My sincere thanks to my mentors and colleagues during my first job at Exide Industries Limited – K. Janakiram, Sagar Sengupta, Mani Baskar, Ravi Gopi, K. C. Hemanth Kumar, N. Anand, G. Basha, K. Vignesh, Baskar Sharma, Esther Sowbba who were resourceful and instrumental in facilitating in my transition to an industrial work environment. I would like to express my deepest gratitude to my mentors and teachers during my undergraduate years at CSIR-Central Electrochemical Research Institute (CECRI) – Dr. S. Ravichandran, Dr. D. Jeyakumar, Dr. Subbiah Alwarappan, Dr. V. Ganesh, V. Nandakumar, Dr. L. John Berchmans, Dr. P. Murugan, Dr. Sheela Berchmans, Dr. Sundar Mayavan, Dr. B. Subramanian, Dr. A.K. Nanda Kumar, Dr. A. Manokaran, Dr. G. Sreedhar, Dr. Vijayamohanan K Pillai, Dr. Ramesh Mohan, Dr.

N. Karikalan, Dr. Vignesh Sundaresan, Dr. Chockkalingam. They introduced the field of electrochemistry and inspired me to pursue a scientific career in it. I would like to thank my school principal Dr. N. Banumathy for her selfless support and encouragement. I would like to extend my thankfulness to my school teachers for their support.

I would like to thank my best friend Archana for her love, care and support throughout these years. I express my gratitude to my friends – S.R. Vignesh, N. Sangeetha, S. Praveen, Manhattan Family, and others who helped me navigate through challenging times with ease. Special thanks to the cutest little friends – Shasini, Pupi, Aami, and Vettri for the blissful days.

My heartfelt gratitude goes to my sister R. Nivedha for her unwavering love and support. I am also deeply thankful to my well-wishers, Arappalli, A. Ravichandran, A. Arunkumar, Ramachandran, for their constant encouragement. Lastly, I owe an immeasurable debt of gratitude to my parents, M. Rajendran and R. Sumathi, for their unconditional love, care, trust, encouragement, and countless sacrifices.

Dedication

To my parents and my uncle Arunkumar,

whose only wish is for my happiness.

Preface

The dissertation comprises of the following chapters.

Chapter 1: This chapter provides the motivation of this dissertation, covering the fundamental concepts and existing challenges in Li metal batteries (LMBs) and aqueous Zn-ion batteries (AZIBs). It discusses various strategies and potential solutions to address the challenges associated with realizing Li metal anodes (LMAs), air cathodes, and AZIB cathodes. The chapter also introduces the nanostructured electrode materials used throughout this dissertation to address the challenges.

Chapter 2: This presents a paper published in *Carbon* (2023). The chapter reports on the fabrication and characterization of a three-dimensional (3-D) array of vertically aligned carbon nanofibers (VACNF), which is proposed as a potential carbon host for LMAs. The lithiophilic nature of VACNF is demonstrated using various characterization tools. The morphology of the electrodeposited Li (e-Li) and the composition of the solid electrolyte interphase (SEI) on the VACNF electrodes are unraveled. The VACNF array exhibits superior stability and reversibility for Li plating/stripping compared to planar copper electrodes, attributed to its high surface area and lithiophilic properties. The chapter delves into the morphology of electrodeposited lithium and explores the observed mode of failure.

Chapter 3: This features a paper published in *Chemical Engineering Journal* (2024). This chapter examines the effect of Li plating/stripping current densities on the performance of the 3-D LMA based on VACNFs. It uncovers the dependance of e-Li morphology on various plating current densities, which is instrumental in tuning the performance of VACNF. A moderate current

density of 1.0 mA/cm^2 exhibits the highest cycling performance owing to formation of a denser, columnar Li microstructure.

Chapter 4: This chapter elucidates the use of either Ni or PtRu deposited on 3D VACNFs as potential cathodes for Li-oxygen batteries (LOBs). The chapter reveals that VACNF-Ni exhibits superior specific and areal discharge capacities. Meanwhile, VACNF-PtRu demonstrates a superior stability, attributed to the suppression of Li_2CO_3 formation during discharge. The chapter also explores the impact of various carbon substrates, such as carbon cloth and carbon paper. This work, which resulted in a co-authored paper published in *Nano Research Energy* (2023), was conducted in collaboration with Dr. Xianglin Li' group at The University of Kansas (KU). The electrochemical characterization and post-testing characterization of the electrodes was carried out by Syed Shoaib Hassan Zaidi at KU.

Chapter 5: This chapter introduces a hybrid nanostructure based on divalent metal cations (Zn^{2+} and Mn^{2+}) pre-intercalated V_2O_5 nanoribbons/reduced graphene oxide (M-V_2O_5 NRs/rGO) towards application as cathodes for AZIBs. The chapter reveals that the prepared Zn-V_2O_5 NRs/rGO hybrid exhibits a high reversible specific capacity. Meanwhile, the (Mn+Zn)-V_2O_5 NRs/rGO demonstrates promising stability, although with a lower specific capacity, revealing the pillar-effect of Mn^{n+} ions. The ion storage mechanism and Zn^{2+} diffusion kinetics are also discussed. This work culminated in a co-authored paper that was published in *ACS Sustainable Chemistry & Engineering* (2023).

Chapter 6: This chapter outlines the perspective future studies stemming from the dissertation. It first describes the extension of the work in Chapters 2 & 3, focusing on the development of a lithiophilic coating on VACNF for use as a LMA host. This involves sputter-

coating metallic Au nanoparticles on VACNF and investigating its performance in relation to e-Li morphology and cycling stability. The chapter then discusses the preliminary work on the development of low-tortuous electrospun carbon nanofibers as a host for LMA.

Chapter 7: The major conclusions drawn from the four major research chapters of this dissertation and future prospective research directions are presented.

Chapter 1 - Introduction

1.1 Motivation

Billions of years ago, nature cracked the code for harnessing energy which enabled the existence of life itself. The ability of human beings to harness, store, and transport various forms of energy, facilitated by science, has been the driving force for the advancements in our life. One of the consequences of our ferocious appetite for energy is anthropogenic global warming which threatens our own existence. For the period of 2011-2020, the average surface temperature has increased by 1.09 °C compared to pre-industrial levels (1850-1900).[1] This acceleration of global warming (shown in Figure 1.1a), driven by the emission of greenhouse gases (CO_2, methane, N_2O, etc.), has led to climate change, marked by extreme weather conditions, ocean acidification, and a rise in sea levels. These changes adversely affect life on earth.[2, 3] As a global effort to limit greenhouse gas emissions, in 2015, 196 countries adopted the Paris Agreement to limit the increase in the global average temperature below 2 °C, preferably 1.5 °C above pre-industrial levels.[4] Energy use for electricity, heat generation and transportation sectors is the major contributor of CO_2 emission accounting for 73.2% in 2020.[5] To achieve the environmental goals, the world is transitioning from the use of fossil fuels to cleaner, renewable energy resources such as solar, wind, hydro, etc. to produce electricity. In 2022, renewable energy accounted for 19% of the total energy production while it is projected that renewables would surpass coal to become the largest source of electricity by 2028 (Figure 1.1b).[6] To limit greenhouse gas emissions by transportation, internal combustion engine (ICE) vehicles are being replaced by electric vehicles (EVs) with major automakers promising to phase out production of ICE and a complete transition to EVs. These efforts realized an exponential growth in EV sales with over 26 million vehicles on the road in 2022 (Figure 1.1c).[7] The exponential growth of electricity generation from renewable sources of

intermittent nature such as solar and wind, along with the electrification of automotive sector, drives the increased demand for energy storage technologies. Rechargeable battery is one of the proven technologies that has been successfully applied for energy storage applications.

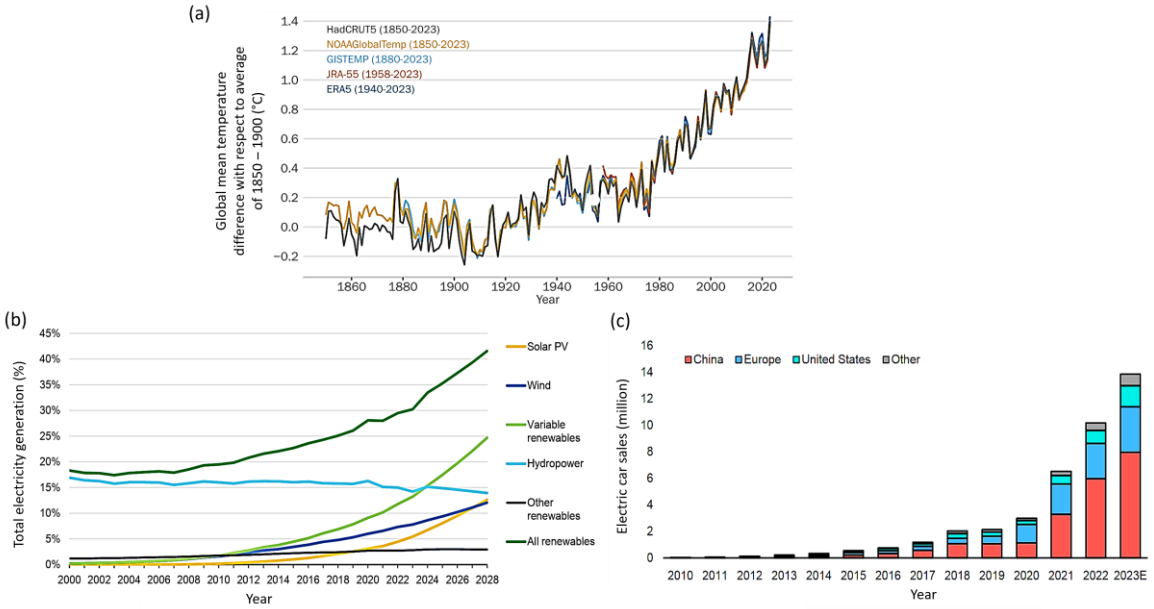

Figure 1.1. (a) Increase in global mean temperature compared to pre-industrial levels (1850 – 1900). Reprinted from *Provisional State of the Global Climate 2023*, World Meteorological Organization, https://wmo.int/publication-series/provisional-state-of-global-climate-2023, under CC license. (b) Electricity generation by renewable technologies. Reprinted from IEA (2024), *Renewables 2023*, IEA, Paris https://www.iea.org/reports/renewables-2023, License: CC BY 4.0. (c) Electric car sales globally. Reprinted from IEA (2023), Global EV Outlook 2023, IEA, Paris https://www.iea.org/reports/global-ev-outlook-2023, License: CC BY 4.0.

1.2 Batteries - Fundamentals

Batteries are electrochemical energy storage devices that store electrical energy in the form of chemical energy. Based on their rechargeability, they are classified into primary and secondary batteries. Primary batteries are non-rechargeable while secondary batteries are rechargeable. A typical electrochemical cell or a battery consists of three essential components – a cathode, an anode and an electrolyte. A cathode consists of an active material that has a lower electrochemical

potential, defined as partial molar Gibbs free energy (μ_C) in J/mol.[8] Whereas, an anode has a higher electrochemical potential (μ_A). The electrolyte acts as an ionic conductor facilitating the transport of ions from one electrode to another. The difference between the electrochemical potentials is measured as the open circuit voltage (OCV) of the cell (Figure 1.2a).[9] When connected to an external load, the anode oxidizes and releases electrons that flow through the external circuit. The cathode accepts the electrons from the anode and gets reduced. As a result of this, the Fermi level of the anode decreases while that of the cathode increases resulting in lowering of the free energy (or potential) difference. This process is known as discharge. The electrochemical cell delivers energy until the cathode and/or the anode cannot be further reduced/oxidized, respectively. The amount of charge that can be stored in the cathode/anode, normalized to their mass is defined as the specific capacity of the electrode. The cell capacity is limited by either the cathode or the anode depending upon the cell design. The product of the cell capacity and the nominal voltage during the discharge defines the gravimetric energy density of the cell. To recharge the cell, an external power source is used to drive the reactions in the opposite direction, i.e., oxidation and reduction reactions at the cathode and anode, respectively. The charge and discharge processes in a typical lithium-ion battery is shown in Figure 1.2b.

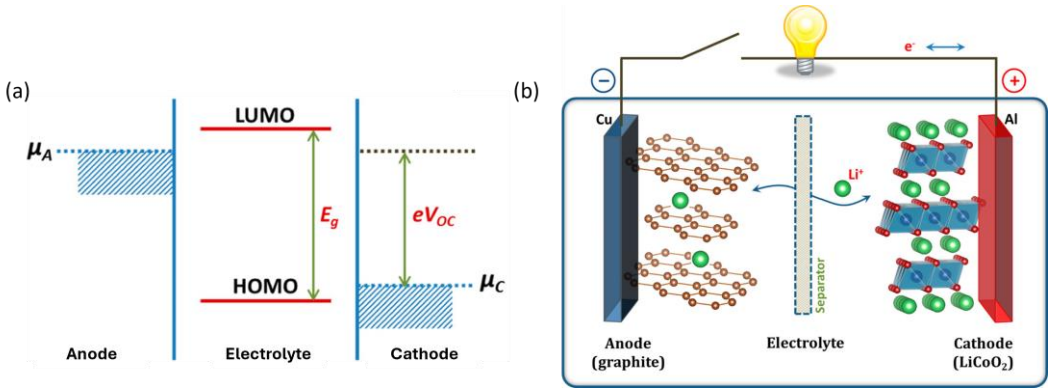

Figure 1.2. (a) Relative energies of electrodes and electrolyte in an electrochemical cell. (b) Schematic of a rechargeable Li-ion cell. Reprinted (adapted) from *J. Am. Chem. Soc.* 2013, 135, 4, 1167–1176. Copyright 2013 American Chemical Society.

1.3 History of Batteries

The history of batteries dates to the early 1800s. The first battery, invented by Alessandro Volta in 1800, was a pile of zinc anode and silver cathode disks separated by a cloth soaked in aqueous sodium chloride electrolyte.[10-12] The invention was soon followed by discoveries of different battery chemistries and new cell designs towards the development of commercial energy storage devices. In 1859, a rechargeable lead-acid battery (LAB) with lead metal electrodes in aqueous sulfuric acid electrolyte was introduced by Gaston Plantè. The actual anode and cathode active materials of a LAB are lead and lead oxide, respectively. LABs offer an energy density of 35 – 40 Wh/kg and are widely used in uninterrupted power supply, grid storage and automotive (ignition and lighting) applications. Despite its low energy density, LAB technology holds 70% of the total energy storage market due to its low cost.[13, 14] In 1866, Leclanché cell was developed. It consists of a zinc rod anode and a manganese oxide cathode with aqueous ammonium chloride solution as the electrolyte. Leclanché cells paved the way to the development of commercial primary zinc-carbon and alkaline batteries which are currently in use. A rechargeable nickel cadmium battery where the electrolyte does not participate in reactions was discovered by Waldmar Junger in 1901. Ni-Cd batteries have an energy density of 40 – 60 Wh/kg.[15, 16] The development of Ni-Cd batteries led to development of other rechargeable nickel-based batteries such as Nickel metal hydride, Ni-Zn, Ni-Fe batteries.[17] They are currently used in a small proportion of portable electronics. In 1932, Heise and Schumacher developed the primary zinc-air battery with alkaline electrolyte. Primary cells are currently used in hearing aids and the development of rechargeable cells is still under research. Improving the energy density and enhancing the performance of batteries has always been an urgent necessity during any period of time to address the ever-increasing energy demand and with the requirements of technological

innovations. Considering the desired characteristics such as lowest redox potential (-3.04 V vs standard hydrogen electrode (SHE)) and highest theoretical specific capacity (3,860 mAh/g), lithium metal is an obvious choice as the anode material. This led to the exploration for lithium metal-based batteries as early as the late 1960s.[12, 18] The first rechargeable lithium metal battery (LMB) was demonstrated by Stanley Whittingham in 1976 with a lithium metal anode (LMA), a titanium disulfide cathode and an organic electrolyte containing lithium salt.[19] However, the commercialization of rechargeable LMAs is hampered by the risk of fire hazard during charging due to the occurrence of internal short-circuit by dendrites. It is to be noted that to improve the battery energy density, in addition to the use of high-capacity cathodes and anodes, a right chemistry that outputs a high voltage is essential. In addition to the dendrite risk and a low cell voltage of <2.5V due to the higher energy level of the sulfides limited the energy density.[20] Using $LiCoO_2$, a layered oxide cathode developed by John Goodenough in 1979 and carbonaceous anode (petroleum coke), Akira Yoshino invented the first commercially viable lithium-ion battery (LIB) in 1983.[21, 22] Since then, LIBs have found a plethora of applications such as EVs, portable electronics, battery energy storage systems, etc. The Nobel Prize in Chemistry in 2019 is a standing proof to the benefits of LIBs to humankind.[23] Nevertheless, to satisfy the increasing energy demands of the future, the search for better battery chemistries is still on.

1.4 Introduction to Explored Battery Chemistries

1.4.1 Lithium Metal Anode

1.4.1.1 Working and Challenges

In the quest to develop lighter, powerful batteries for the future, research on developing reversible LMAs has been revived since LIBs are reaching their theoretical limits. LMAs when combined with typical cathodes of LIBs, can improve the energy density to ~440 Wh/kg. Whereas when coupled with high-capacity cathode materials such as oxygen, sulfur, the energy density of the battery systems increases to 3505 Wh/kg and 2567 Wh/kg, respectively.[24] During discharge/charge, the electrochemical redox reactions that take place in a LMA are a seemingly simple one electron transfer as shown below:

Discharge: $Li^{(0)} \rightarrow Li^{+} + 1e^{-}$ (Li electrodepostion/plating) ..... (1.1)

Charge: $Li^{+} + 1e^{-} \rightarrow Li^{(0)}$ (Li stripping) ..... (1.2)

The solid lithium metal oxidizes into lithium ions that diffuse into the electrolyte solution during discharge/stripping leaving behind the current collector. During charge, electrodeposition/plating of Li occurs on the current collector creating a new solid phase. These phase changes involve an infinite amount of volume change which makes the system a spatially dynamic one.[25] This is in complete contrast to that of graphite anode of LIBs where the volume expansion is only 2.4%.[26] The expansion and contraction during cycling generally results in electrode degradation. Lithium metal, being a strong reductant, readily reacts with the electrolyte that comes into contact with it. This results in the formation of a chemically formed solid electrolyte interphase (SEI).[27] The composition of the SEI depends upon the electrolyte composition. The as manufactured lithium foil itself will contain a native SEI composed of oxides

and nitrides.[28] In addition to the formation of SEI via chemical reactions, with the lowering of electrode potential during the charging process, SEI forms electrochemically.[29] The so formed SEI is highly heterogeneous in nature. It has been found that the SEI consists of inorganic Li compounds such as Li_2O, Li_xNO_y, Li_2CO_3, etc. embedded in an organic amorphous polymeric matrix.[30-32] Each of these compounds have different Li^+ ion conductive and mechanical properties.[33, 34] A heterogeneous SEI leads to varied ion conductive pathways causing different rates of electrodeposition at different locations. The infinite volume change involved with Li plating/stripping results in cracks in SEI which act as hotspots for preferred lithium reduction leading to heterogeneous plating.[35]

During Li plating, the Li^+ ions depleted at the SEI/electrolyte interface must be restored by the diffusion of Li^+ from the bulk electrolyte. When plating lithium continuously, when the surface concentration of lithium drops to zero, there is a ramification of electric field which accelerates the lithium deposition rate locally leading to growth of dendritic structures.[36-39] The Li dendrites can pierce through the separator and reach the cathode resulting in internal short-circuits. This is a fire hazard as the heat generated due to passage of short-circuit current can ignite the inflammable organic electrolyte.[40] Hence, Li dendrites are considered as a safety risk that must be addressed for successful commercial application. In addition, the Li dendrites consume electrolyte and active Li as their freshly formed surface with increased area reacts with the electrolyte forming fresh SEI. Consumption of active Li reduces the useful capacity of the cell while electrolyte consumption can lead to increased heterogeneities. Similar to the Li plating, Li stripping is quite heterogeneous as well. Locally, Li stripping occurs at different rates at different locations. When the stripping occurs at the points of connection between the electrodeposited Li and the current collector, the active Li gets electrically disconnected leading to capacity loss.[41-43] These metallic Li which cannot

participate in further cycling is known as inactive/dead Li. These aforementioned challenges such as dendrite formation, unstable SEI, heterogeneous plating, dead lithium formation collectively result in poor performance of LMAs, as shown in Figure 1.3.[24]

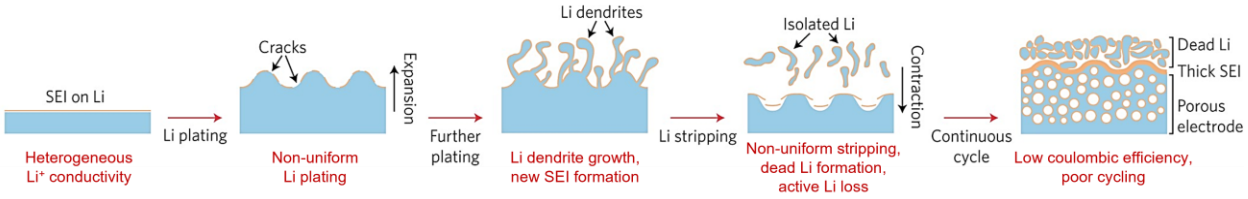

Figure 1.3. Schematic showing the challenges associated with LMAs. Reprinted (adapted) with permission from *Nature Nanotech* 12, 194–206 (2017). Copyright 2017 Springer Nature Limited.

1.4.1.2 Strategies to Enhance the Performance

From the challenges discussed, it can be realized that an ideal LMA should be a dense structure with a stable SEI that exhibits homogeneous Li plating/stripping. To develop stable LMAs, scientific researchers are tackling the issues via different avenues including electrolyte modification, application of artificial SEIs, application of external pressure, use of host frameworks, and use of solid electrolyte.[44] This section serves to provide a brief introduction to these strategies. In the case of liquid electrolyte systems, changes in electrolyte composition were found to cause a stark difference in the performance of LMAs. At the beginning, carbonate-based electrolytes that are currently being used for lithium-ion batteries were adopted for studying LMAs. However, it was found that use of ether-based electrolytes improved the cycling stability of LMAs. With the inclusion of additives such as $LiNO_3$, polysulfides, etc., the cycling performance got further improved.[45] Advancements in electrolyte development such as the development of high salt concentration and localized high concentration electrolytes enable cycling of LMAs with CE greater than 99%.[46-48] Further studies uncovered that the constituents of

the electrolyte have a pronounced effect on SEI composition and electrodeposited Li morphology, which in turn influences the reversibility of LMAs.[49] Though electrolyte modification achieved desired electrodeposited Li morphologies and more stable SEIs, it does not prevent continuous electrolyte consumption completely. With the exhaustion of additives, their beneficial effects disappear.[50] In addition, electrochemically formed SEIs dissolute leading to capacity loss.[51, 52] To prevent continuous formation of SEIs, artificial SEI layers of desirable properties were applied to LMAs.[53-55] With the absence of any mechanism to prevent the volume change during cycling, it is not possible to avoid SEI cracking. Three-dimensional (3-D) conductive structures are studied extensively as hosts for LMAs to alleviate the thickness fluctuations. In general, 3-D conductive hosts should have a high surface area, enough mechanical strength and be lithiophilic in nature.[56-58] The rationale behind the use of 3-D hosts is to extend the Sand's time, the characteristic time it takes for the initiation of growth of dendrites, by lowering the local current density. The use of solid electrolyte instead of liquid electrolyte eliminates the safety issues associated with dendrite formation. However, other challenges such as inferior ionic conductivity, poor electrode-electrolyte interface which hinder their incorporation.[59] Among these various approaches to improve LMA's performance, our research focus was on the application of 3-D conductive hosts.

1.4.2 Air Cathodes

As mentioned earlier, lithium-oxygen (or) lithium-air batteries (LOB) are nearly ten times energy dense than the current lithium-ion batteries. The first rechargeable LOB was reported by Abraham et al. in 1996.[60] It uses lithium metal as the anode and oxygen as the cathode material as shown in Figure 1.4. Ideally, oxygen is obtained from the atmospheric air. Since one of the active

materials is acquired from the surroundings and is not included in the cell, the energy density of the battery is quite high. In the cathode side, the overall reactions that take place are given.[61, 62]

Discharge: $2Li^+ + O_2 + 2e^- \rightarrow Li_2O_2$ (Oxygen reduction reaction (ORR)) ..... (1.3)

Charge: $Li_2O_2 \rightarrow 2Li^+ + O_2 + 2e^-$ (Oxygen evolution reaction (OER)) ..... (1.4)

The standard redox potential for the reactions is 2.96 V vs Li^+/Li or -0.08 V vs SHE. The ORR is a multi-step reaction which involves the electrochemical formation of lithium superoxide (LiO_2) as an intermediate. The intermediate either via chemical or electrochemical means gets converted into lithium peroxide as the product. The formation of Li_2O_2 from LiO_2 occurs via two different mechanisms – surface mechanism and solution mediated mechanism.[63-65] In the surface mechanism, the Li_2O_2 is electrochemically converted to LiO_2 on the surface of the electrode. This results in the formation of film-like Li_2O_2. If the solvation of LiO_2 is low, the discharge step proceeds with the surface mechanism. Strong interaction between the LiO_2 and the electrode's surface also facilitates film-like Li_2O_2.[66] In the solution mediated mechanism, LiO_2 dissolution occurs to form superoxide anion and Li^+ which then undergoes the following disproportionation reaction to form toroid shaped Li_2O_2. The use of solvents with high donor number such as dimethyl sulfoxide, presence of water molecules favors solution mediated mechanism.[67, 68] The formation of thin film-like discharge products is preferrable due to their ease of rechargeability owing to their lower resistance than thicker toroid-like structures.[69]

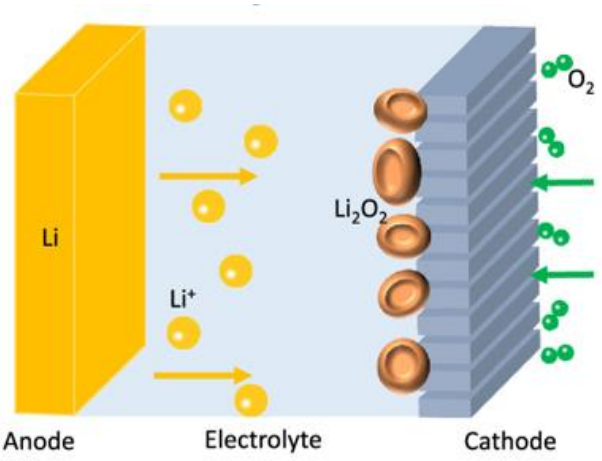

Figure 1.4. Schematic representation of a LOB. Reprinted (adapted) from *Acc. Chem. Res*. 2021, 54, 3, 632–641. Copyright 2021 American Chemical Society.

From equations 1.3 and 1.4, it can be realized that conductive material, electrolyte, and gas diffusion pathways are necessary for the transport of electrons, lithium ions, and oxygen gas, respectively. To achieve that, typically gas diffusion electrodes (GDEs) that are made up of carbon-based gas diffusion layers with macroporous structure coated with a layer of microporous amorphous carbon are being used as the cathode substrate.[70] From here on, the terms GDEs and air cathodes will be used interchangeably. These GDEs are commonly used in fuel cells.[71] The electrochemical reaction takes place at the interface involving three different phases – oxygen in gas phase, GDE in solid phase, and electrolyte in liquid phase. The air cathode is similar to a fuel cell cathode operating with oxygen as the fuel. Ideally, as long as there is availability of oxygen, the cell should operate continuously. However, this does not take place. The discharge process of the cathode ceases when one of the reactants cannot reach the interfacial reaction sites. Mostly, it occurs by the blockage of gas diffusion pathways due to the buildup of solid Li_2O_2 product.[72] Hence, the cathode capacity is limited by the ability of the GDEs to continue its function. Since

Li_2O_2 is a poor conductor, during deep discharge, the buildup of a thick Li_2O_2 layer blocks the electron transfer passivating the electrode and diminishing the rechargeability of the electrode.[73]

In addition, the ORR and OER reactions themselves are sluggish in nature requiring large overpotentials (η) to occur with significant kinetics. Large overpotentials during charge and discharge processes decrease the energy density as well as the energy efficiency of the cell. To improve the ORR/OER kinetics, researchers have adopted redox mediators and solid-state catalysts. The redox mediators 2,5-di-tert-butyl-1,4-benzoquinone (DBBQ), benzo[1,2-b:4,5-b′]dithiophene-4,8-dione (BDTD), vitamin K2 catalyze ORR while (2,2,6,6-tetramethylpiperidin-1yl)oxyl (TEMPO), tetrathiafulvalene (TTF), and lithium iodide (LiI) catalyze OER.[74] Solid-state catalysts include metals such as Au, Pt, Au, Co, Ru, multimetallics such as RuIrCeNi and metal oxides such as NiO, MnO, RuO_2.[75] Another critical challenge in the air cathode is the formation of passivating byproducts such as Li_2CO_3, LiOH.[76, 77] During charging, the superoxide anion reacting with the carbon, binder and/or electrolyte is an undesired side reaction leading to Li_2CO_3 deposition. The lithium carbonate deposits increase the charging overpotential impeding the rechargeability of the cathode. The high potentials applied during charging also oxidizes the carbon substrate to form Li_2CO_3. It has been reported that carbon oxidation occurs at potentials > 3.5 V vs Li^+/Li in organic electrolytes.[78, 79] Apart from reducing the overpotentials for OER and ORR, the catalysts help to promote the decomposition of Li_2CO_3 as well. These issues in air cathodes limit their reversible cycling capacity, charge efficiency and cycle life.

Air cathodes of suitable materials and architecture are necessary for the development of LOB. To minimize the loss of energy density, it is necessary for the air cathodes to be lightweight in nature. For that reason, carbon-based electrodes are well-suited for air cathodes. Carbon materials are conductive as well. To enhance the reversible discharge capacity, the surface area of

air cathodes should be very high to provide abundant active reaction sites.[80] However, it has been reported that apart from high surface area, pore size and pore structure of the air cathodes is also important to facilitate oxygen and Li^+ transport.[80-82] The chemical nature of the air cathode affects the morphology of deposited Li_2O_2. Amorphous film-like Li_2O_2 which can be decomposed at lower overpotentials form on the surface of multi-walled carbon nanotubes (MWCNTs) functionalized with oxygen due to the high surface binding affinity.[68] For carbon-based air cathodes, carbon corrosion is an issue that needs to be addressed. It is well known that graphitic carbon structures offer relatively high corrosion resistance compared to amorphous ones.[83] Commercial carbon based GDEs use binders such as polyvinylidene fluoride (PVDF) and polytetrafluoroethylene (PTFE) which are also prone to decomposition in the oxidizing environment during charging.[84, 85] From these, it can be drawn that ideal air cathodes should be lightweight, conductive, corrosion resistant while possessing high surface area and appropriate pore architecture. The use of catalysts would help to improve energy efficiency and cycling performance.

1.4.3 Aqueous Zinc-Ion Batteries

A potential battery chemistry that can complement LIBs in applications such as battery energy storage systems is rechargeable aqueous zinc-ion batteries (AZIBs) owing to their safety, low-cost, and sustainability.[86] AZIBs use zinc metal anode and aqueous electrolyte. The use of aqueous electrolyte offers the safety feature since they are non-flammable. Its ionic conductivity (~ 1 S/cm) is also higher than that of organic electrolyte by a factor of ~ 100. On the other hand, zinc metal has beneficial properties such as compatibility with aqueous electrolytes, low cost (ca. 2.8 USD/kg), high recyclability, low redox potential (-0.762 V vs SHE) and high theoretical

capacity (820 mAh/g).[87-90] Though zinc metal based batteries with alkaline electrolyte (Zn-air, Zn-Ni, Zn-MnO_2) have been in the market, they are not attractive for large scale energy storage systems either due to their low energy density (140 Wh/kg for Zn-Ni) or due to lack of rechargeable behavior (Zn-air, Zn-MnO_2). It is the demonstration of cathode materials working reversibly in mildly acidic electrolytes that renewed the interest for rechargeable AZIBs development.[91] Since then, a variety of cathode materials based on oxides of vanadium and manganese, Prussian blue analogues, layered chalcogenides, and polyanions have been developed as shown in Figure 1.5.[87, 92] The reactions that occur in a AZIB anode involve the plating and stripping of zinc metal during charge and discharge, respectively. The zinc storage mechanism in the cathode differs based on the type of cathode material being used. In MnO_2 based cathodes, conversion type reaction occurs while in V-based and other cathodes, Zn^{2+} intercalation/deintercalation or Zn^{2+}/H^{+} co-insertion/extraction occurs.[93]

However, commercialization of AZIBs requires the challenges associated with the cathode as well as the anode to be addressed. On the anode side, development of zinc metal suffers from issues such as dendrite growth, surface passivation, and hydrogen evolution reaction (HER).[94, 95] On the other hand, there are issues such as cathode dissolution, formation of byproducts, structural disintegration that lead to fast capacity fading in cathodes.[96] Zn^{2+} ions, even though their ionic radius (0.76 Å) similar to that of Li^{+}, due to its higher oxidation state, form strong solvation sheaths ($Zn[H_2O]_6)^{2+}$ with a radius of 5.5 Å and interact strongly with the electronegative atoms of the cathode material imparting structural distortion. Also, it slows down the diffusion of Zn^{2+} ions requiring high overpotentials for insertion and extraction processes.[92, 93, 97] Cathode dissolution is a prominent issue in Mn-based cathodes in mildly acidic electrolyte that results in loss of active material when they dissolute permanently or precipitate out as irreversible products. Dissolution

of V-based cathodes due to co-insertion of Zn^{2+} and H_2O molecules have also been reported.[98, 99] The formation of hydrogen bonds between H_2O and lattice O^{2-} weakens the V-O bonds inducing dissolution. In cathodes where H^+ intercalation is involved, due to lowering of local pH, flake-like layered double hydroxide (LDH) forms on the surface. Though LDH is reversible, its poor contact with the electrode is expressed as a concern as permanent loss of active Zn^{2+} can occur when they get electrically disconnected.[100] Due to these issues, AZIB cathodes exhibit poor cycle life. In addition, most of the cathode materials are of semi-conductive nature requiring a good electrical network with conductive additives. The electrochemical performance of different classes of cathodes can be generalized as follows: manganese oxides display high capacity and high operating voltage, but cycle life and rate capability are poor; Prussian blue analogues yield a high discharge voltage, but the capacity is poor; V-based oxide materials exhibit moderate capacity and a decent cycle life.[101] The relatively better performance of vanadium-based cathodes is attributed to the different valence states of vanadium (V^{3+}, V^{4+}, V^{5+}) and large interlayer spacing promoting Zn^{2+} diffusion kinetics. The tunability of oxidation states of vanadium to accommodate Zn^{2+} ions make V-based materials as good cathodes for AZIBs.[102]

To improve the Zn^{2+} diffusion kinetics and the stability of the cathode, pre-intercalation with cations such as Zn^{2+}, Mg^{2+}, Ni^{2+}, Mn^{2+}, Li^+, Na^+, K^+, NH^{4+} or neutral molecules such as H_2O, PEDOT, etc. is a strategy that has been successfully utilized.[103-107] Both the pre-intercalated ions and molecules widen the interlayer spacing aiding easier intercalation and deintercalation of Zn^{2+} ions. The pre-intercalated cations interact strongly with the O^{2-} of the oxide cathodes by means of electrostatic attraction or covalent linkages thereby stabilizing the cathode structure from disintegration during cycling. Pre-intercalating with neutral molecules helps to reduce the electrostatic interaction between the inserted Zn^{2+} ions and the lattice atoms of the cathode. The

structure of the cathode material also impacts the Zn^{2+} diffusion kinetics.[108, 109] Nanomaterials which facilitate shorter diffusion pathlengths for Zn^{2+} ions enable faster diffusion. Owing to their high surface area and nanoscale dimensions, they also provide access to more active sites for Zn^{2+} storage. To improve the electron transport from the active sites to the current collector, composite materials by combining the cathode materials with materials with high electronic conductivity, mechanical and electrochemical stability. Since carbon nanomaterials of various morphologies such as nanotubes, nanofibers, graphene sheets possess all these desired properties, they are commonly employed. In addition to improving electronic properties, they also help to prevent restacking of two-dimensional cathode nanomaterials.

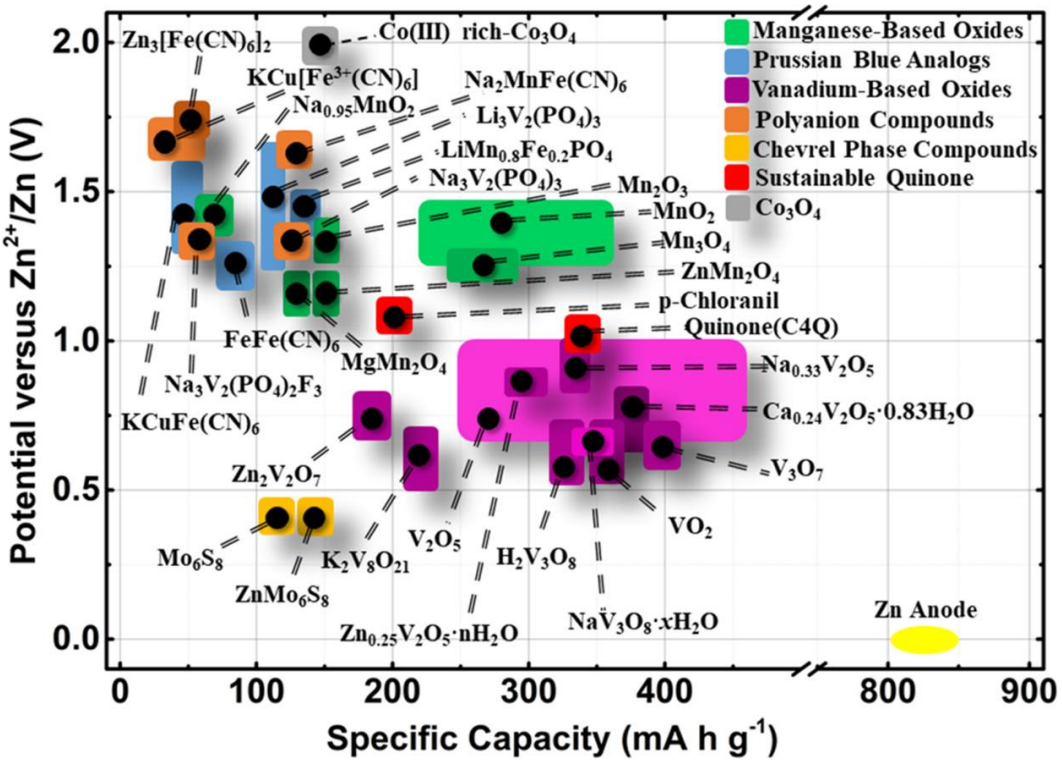

Figure 1.5. Comparison of different AZIB cathode materials. Reprinted (adapted) with permission from *ACS Energy Lett.* 2018, 3, 10, 2480–2501. Copyright 2018 American Chemical Society.

1.5 Electrode Materials of Study

1.5.1 Vertically Aligned Carbon Nanofibers

Vertically aligned carbon nanofibers (VACNFs) are a class of carbon nanofibers with a unique internal architecture (Figure 1.6a) consisting of a series of conical graphitic cups with α ranging from 5° to 30° stacked upon one another throughout the length of the fiber.[110] This structure differs from typical single-walled or MWCNTs which consist of long sheets of graphene rolled into concentric cylindrical tubes with α = 0. As the name suggests, VACNFs are grown as an array of fibers with vertical alignment on a substrate. VACNFs are self-supported as shown in Figure 1.6b unlike the MWCNTs grown using thermal chemical vapor deposition (CVD) which stand upright due to crowding effect.[111] In carbon nanotubes (CNTs), the basal carbon atoms form its surface except at the ends of the tubes. Whereas in VACNFs, the edges of the graphitic cups are exposed. The edges contain carbon atoms with broken, dangling bonds which render the surface electrochemically active and facilitate functionalization with desired moieties.[112, 113] Despite being called carbon nanofibers they differ from solid fibers since they are hollow inside.[114, 115] The growth of VACNFs was first demonstrated by Chen et al., on Ni (100) wafers using plasma enhanced (PE) hot filament CVD.[116] Ren et al., demonstrated that VACNFs can be grown on glass at temperatures below 666 °C.[117] Gaseous precursors such as methane and acetylene are used as carbon sources to grow VACNFs. In addition to the carbon precursor, a reductant such as hydrogen, ammonia are used as a diluent and plasma source. The growth requires a catalyst which decomposes the precursor radicals generated in the plasma. To prevent the diffusion of catalyst into the substrate, a barrier layer is applied. Typically, Ni, Co, Fe and Mo nanoparticles are used as catalysts. Among them, it was found that Ni exhibits higher growth rate probably due to faster diffusion and segregation of carbon in Ni and yields well-aligned VACNFs as well.[118] Among

various barrier materials, Cr was found to exhibit the highest growth activity.[119] The growth process initiates by the formation of carbon by decomposition of precursors on the catalyst surface which then dissolves and diffuses into the catalyst nanoparticle.[120, 121] On reaching supersaturation, the carbon precipitates out as graphitic layers. The amorphous carbon that covers the catalyst surface is etched away by atomic hydrogen and radicals produced in the ammonia plasma. This process keeps the catalyst nanoparticle active and the continuous carbon deposition results in growth of nanofibers. Depending upon the interaction between the nanoparticle and the substrate as well as the growth kinetics, VACNFs grow by either tip-growth or base-growth mode.[122] In the base-growth mode, the nanoparticle remains attached to the substrate and the VACNF grows in length above the catalyst nanoparticle. In case of tip-growth mode, the catalyst particle gets detached from the surface and remains on top as the VACNF grows as shown in Figure 1.6c. Cui et al. observed that during the beginning of tip growth, carbon gets deposited as planar graphitic sheets. After a while, deposition occurs as conical graphitic cups along with the faceting of catalyst nanoparticle into inverted teardrop or pear shape. The growth process occurs within the plasma sheath under the influence of an electric field normal to the substrate surface. The electrostatic interaction helps align the fiber growth parallel to the electric field. Merkulov proposed a negative feedback mechanism operating to balance the compressive and tensile stresses to equalize the growth rate in all directions to be the vertical alignment mechanism.[123] The growth ceases when the catalyst is poisoned by the deposition of amorphous carbon.

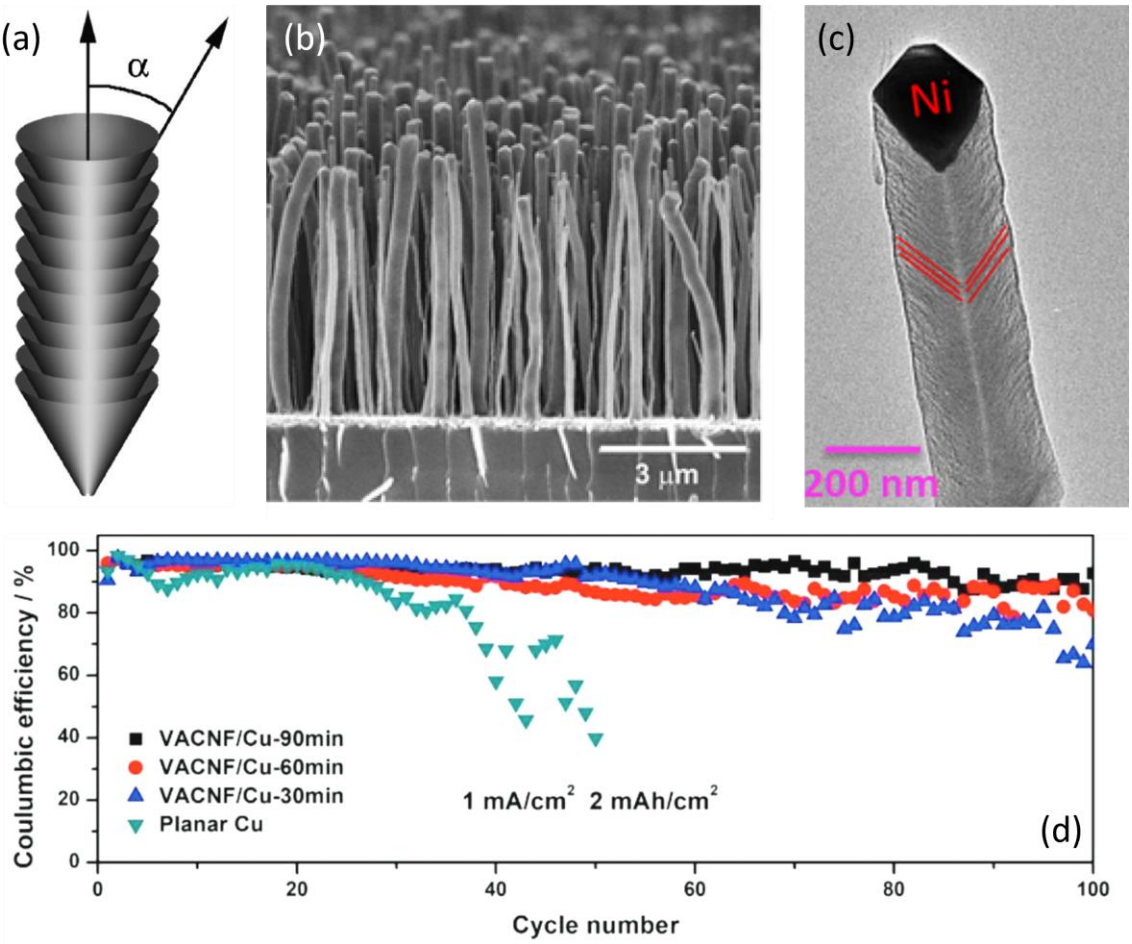

Figure 1.6. (a) A conically stacked graphitic cups model of VACNF. Reprinted from *J. Appl. Phys.* 97, 041301 (2005), with the permission of AIP Publishing. (b) Cross-sectional view of VACNF showing their vertical alignment. Reprinted (adapted) from *ACS Appl. Mater. Interfaces* 2014, 6, 9, 6865–6871. Copyright 2014 American Chemical Society. (c) TEM image of a single VACNF showing its internal structure. Reprinted with permission from *J. Electrochem. Soc.*, 2020 167 066523. Copyright 2020 IOP Publishing. (d) Cycling performance of VACNF/Cu when used as a 3-D conductive LMA host. Reprinted with permission from *Adv. Funct. Mater.* 2020, 30, 1906444. Copyright 2019 John Wiley and Sons.

Depending on the PECVD operating parameters, catalyst thickness, growth time, etc., the density, diameter and height of VACNFs can be tuned.[121] The VACNFs grown using PECVD are inherently doped with nitrogen. Also, the exposure of dangling bonds on the graphitic edges to air results in formation of oxygen-containing functional groups on the VACNFs' surface. These

desired properties of VACNFs such as vertically aligned pore structure, high conductivity, electrochemical activity make them suitable for a wide range of applications such as biosensors, batteries, and fuel-cells.[113, 124-127] Chen et al. have shown that VACNFs grown on Cu foil is a suitable 3-D host material for LMAs.[128] The 3-D VACNFs stabilized the cycling of lithium metal anode as shown in Figure 1.6d. A stable operation of a full cell consisting of a sulfur@pyrolyzed polyacrylonitrile cathode and a Li anode loaded into VACNF/Cu electrode host for over 600 cycles has also been demonstrated.

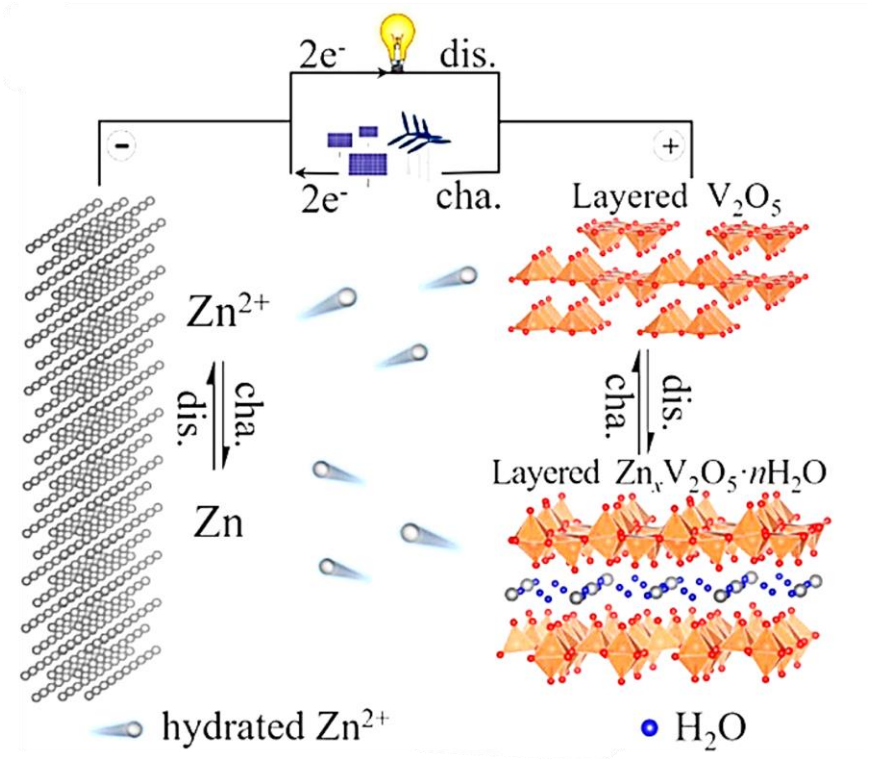

Figure 1.7. Schematic of an aqueous ZIB with a V_2O_5 cathode. Reprinted (adapted) with permission from *ACS Energy Lett.* 2018, 3, 6, 1366–1372. Copyright 2018 American Chemical Society.

1.5.2 Vanadium Pentoxide Nanoribbons/Reduced Graphene Oxide Nanohybrid

Vanadium can exist in different oxidation states from +2 to +5 and forms different oxides such as VO, V_2O_3, VO_2, V_2O_5. Synthesis of vanadium oxides with V atoms in mixed oxidation states such as V_4O_9, V_3O_7, V_6O_{13} has also been reported.[129] Among these the most stable V_2O_5 have been developed for applications such as batteries, supercapacitors, water electrolysis, sensors, etc.[125, 130, 131] Owing to their layered structure with large interlayer spacing (4.37 Å) which is tunable, V_2O_5 was is a promising cathode material for AZIBs as depicted in Figure 1.7.[132] Among various polymorphs of V_2O_5, orthorhombic α-V_2O_5 is the thermodynamically stable phase. Each V_2O_5 unit stores two Zn^{2+} ions leading to a theoretical capacity of 294 mAh/g.[133-135] The adjacent layers of V_2O_5 are bound by weak van der Waals forces. Compared to bulk powder, nanomaterials offer high specific surface area and short diffusion pathlengths that are beneficial for energy storage applications.[91] Researchers have synthesized V_2O_5 nanomaterials in various morphologies such as nanorods, nanoribbons (NRs), nanotubes, nanobelts, nanofibers and nanoflowers. Hydrothermal method is the most common route of synthesis. The duration for the hydrothermal method typically lasts between 3 to 48 hours. Liquid phase exfoliation assisted by microwaves is a faster method to produce V_2O_5 NRs via top-down approach from bulk V_2O_5 powder within one hour.[131] V_2O_5 NRs are few atomic layer thick one-dimensional nanomaterials with widths less than 50 nm and lengths spanning several microns. Other synthesis techniques include atomic layer deposition, chemical vapor deposition, etc. The nanoscale dimensions are beneficial for intercalation of ions by improving the utilization of V_2O_5 units for ion storage and ion diffusion kinetics.[136-138] Since, the conductivity of V_2O_5 is low (~10^{-5} S/cm), use of highly conductive materials such as graphene, CNTs, reduced graphene oxide (rGO) to form hybrid structures for efficient electron transfer. With the formation of layer-by-layer hybrids, these conductive materials

can also enhance the structural stability of V_2O_5 and help to minimize the loss of active surface area due to restacking of layered nanomaterials. Considering that V_2O_5 NRs being a layered 1-D material, two-dimensional graphene is structurally compatible to form layer-by-layer hybrid structures. For successful formation of layer-by-layer hybrids, the components should possess suitable surface charges and form stable suspensions in the chosen solvent system. V_2O_5 NRs form stable suspensions in water. However, graphene or rGO cannot be used since it aggregates in aqueous solution. Hence, graphene oxide (GO) which is dispersible in aqueous solution due to the surface oxygen groups and exhibit graphene like properties when reduced, is typically used to form layer-by-layer hybrids.[139] Depending on the choice of charge neutralization agents to initiate the hybrid formation, the properties and interlayer spacing can be tuned easily. Based on these design principles, divalent transition metal cation mediated co-precipitation synthesis method was developed to form M-V_2O_5 NR/rGO hybrids and their electrochemical performance as ZIB cathodes was studied.

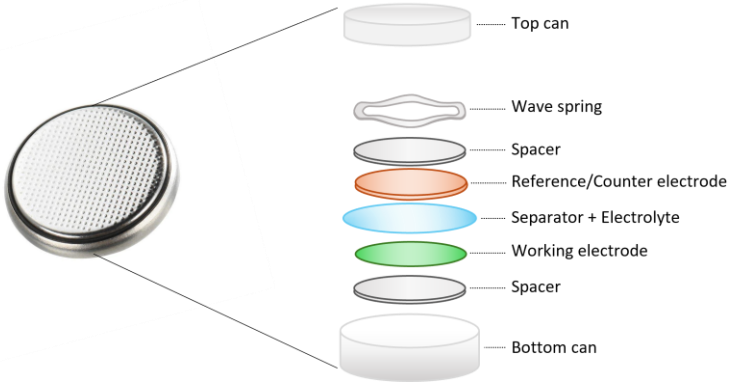

Figure 1.8. Schematic of a half-cell assembly in a coin-cell.

1.6 Electrochemical Characterization of Batteries

1.6.1 Half-Cell Studies

In order to study a particular electrode alone, a typical electrochemical setup involves a three-electrode arrangement consisting of a working electrode (WE), a reference electrode (RE) and a counter electrode (CTE). The potential of the WE, the electrode of study, will be monitored/polarized with respect to that of a non-polarizable RE. The CTE where the counter reactions that occur to maintain electroneutrality will be designed such that it does not limit the reaction rate. The use of a three-electrode setup allows to obtain unambiguous detection of the WE's response without the influence of the CTE. However, it is very challenging to construct a three-electrode cell to characterize battery materials reliably and the obtained performance cannot be extended to practical cells.[140] The availability of metals such as Li, Na, Zn which exhibit fast kinetics and very small overpotentials made it possible to conduct half-cell studies for battery electrodes in practically relevant, highly reproducible coin cells.[141, 142] These metal electrodes with capacities exceeding that of the WE by several times serve as both RE and CTE. With a proper design and choice of operating parameters, the influence from the metal electrodes can be minimized.[143] The type of metal electrode is chosen based on the system under study. For studying hosts for LMAs and air cathodes, a thick Li foil is used. While for zinc-ion cathodes, a Zn foil is used as the RE and CTE. A typical half-cell assembly in a coin cell setup is shown in Figure 1.8. In general, once characterized, full cells will be assembled in coin cells or pouch cells with suitable anode and cathode materials with limited excess capacity and limited electrolyte to evaluate the performance under practically useful energy densities.

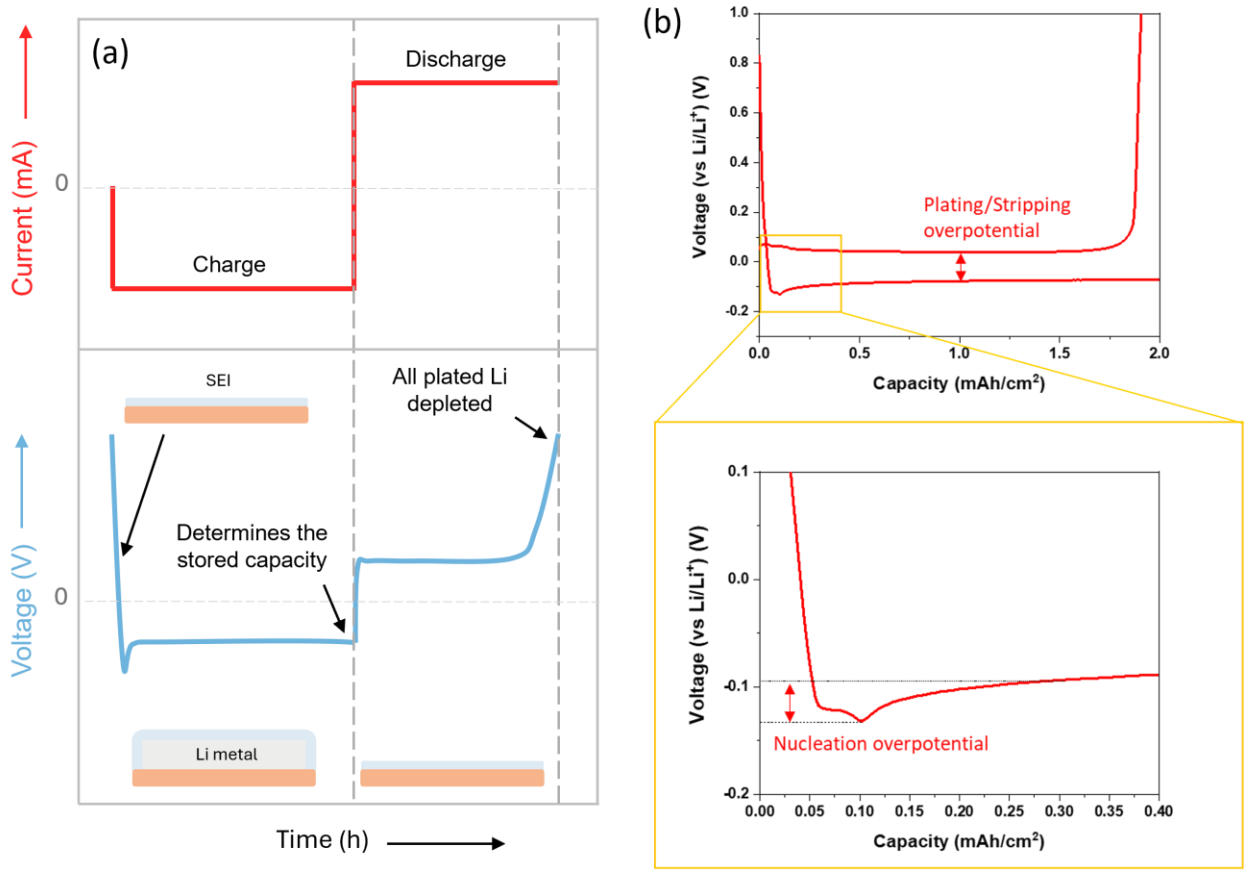

Figure 1.9. (a) Galvanostatic charge/discharge protocol for coulombic efficiency determination. (b) Determination of Li nucleation and Li plating/stripping overpotentials.

1.6.2 Electrochemical Characterization of LMAs

1.6.2.1 Coulombic Efficiency Cycling

Coulombic efficiency (CE) is an important parameter for understanding the reversibility of lithium metal anodes. To determine the CE, a half-cell comprising the host as the WE and a thick lithium foil as the RE and the CTE is used. The CE is calculated as the percentage of Li capacity that can be stripped off completely from the Li plated in the preceding step.[144, 145] As shown in Figure 1.9a, the plating and stripping steps are conducted in constant current or galvanostatic mode at a predetermined current density. For the plating step, the Li capacity can be varied by changing

the duration of electrodeposition. The duration of Li stripping step is limited by a cut-off voltage, typically, 1.0 V. These steps are repeated in cycles to analyze the life of the electrode. The voltage profiles that emerge as a result of applied galvanostatic charge/discharge procedure provide more information. During charging, the potential of WE polarize in the negative direction and reactions start to occur to deliver the set current. At potentials above 0 V vs Li^+/Li, reduction of electrolyte, metal oxides and lithium intercalation occurs. When these reactions could not be driven at the specified rates, Li electrodeposition starts to occur at negative potentials. Lithium electrodeposition involves the instantaneous nucleation of Li atoms and the subsequent growth of nucleated Li. The nucleation process poses a higher energy barrier as it involves adsorption of Li^+ atoms on the host surface and hence a larger overpotential. However, the growth step occurs at a slightly lower overpotential as the adsorption of Li^+ atoms on existing Li nuclei is favored. This results in a dip in the potential which signifies onset of Li nucleation as shown in Figure 1.9b. The potential dip rises to a less negative potential and forms a stable plateau indicating the beginning of the growth process. The additional overpotential for Li nucleation is calculated from the difference between the lowest point in the potential dip and the plateau region. The Li nucleation overpotential is indicative of the lithiophilic nature of the host/current collector. The overpotentials for Li growth and stripping are typically calculated together as Li plating/stripping overpotential from the magnitude of the potential difference between the plateaus in charge and discharge curves. The long-term stability of the electrode is assessed by cycling as shown in Figure 1.10a. The electrode will be declared as being failed when the CE starts to decay.

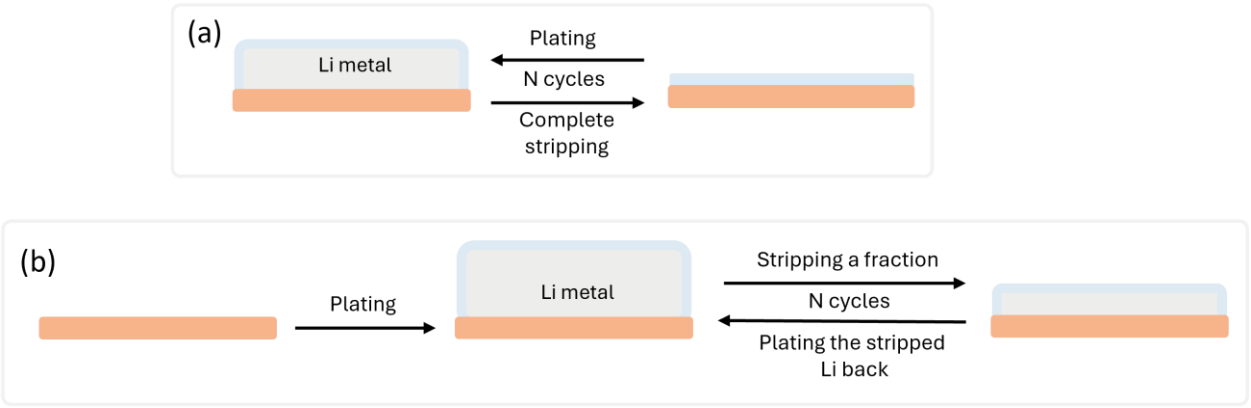

Figure 1.10. (a) Coulombic efficiency cycling and (b) Symmetric cell cycling procedure for lithium metal anodes.

1.6.2.2 Symmetric Cell Cycling

In the coulombic efficiency cycling protocol, all of the plated Li is stripped in the subsequent step. This helps to evaluate the performance under 100 % depth-of-discharge (DoD) conditions. To evaluate the stability of the anode under different DoD, a symmetrical cell assembly comprising of similar electrodes of same capacity. Galvanostatic testing under different DoDs is conducted by regulating the cycling capacity. Symmetric cells are constructed by assembling a pair of LMAs in charged state. This is straightforward for LMAs prepared using melt infusion method. However, for current collectors/hosts which utilize electrodeposition method, construction of true symmetric cells involves an additional step of electrodeposition of Li into the host in a half-cell to prepare Li loaded electrodes. The electrochemically loaded Li electrodes need to be harvested to assemble a true symmetric cell. The disassembly and handling steps might contribute to errors in capacity estimation. A more convenient way in practice to assess such hosts without involving multiple assemblies is to form pseudo-symmetric cells by plating a defined amount of Li in the half-cell setup and then apply the symmetric cycling protocol (shown in Figure 1.10b) to plate/strip a fraction of active Li.

1.6.3 Electrochemical Characterization of Cathodes

1.6.3.1 Galvanostatic Charge/Discharge Cycling

The maximum specific capacity that can be extracted from an air cathode is determined using a deep discharge test. It involves the application of a galvanostatic discharge process until the working electrode's potential decreases to a cut-off value, typically 1.5 V (vs Li^+/Li). This capacity corresponds to the 100% DoD. By charging the air cathode back by applying a constant current until the potential reaches an upper limit of 4.5 V, the CE/rechargeability of the electrode can be evaluated. Higher discharge capacity and coulombic efficiency are desired. Similar to testing of LMAs, the long term cyclability of air cathodes is assessed by cycling them at different DoDs using galvanostatic charge/discharge steps. In the case of AZIB cathodes, similar galvanostatic charge/discharge protocols with appropriate upper and lower voltage cut-offs, the specific capacity and long-term stability can be evaluated. By testing at different charge/discharge rates, the rate performance of the cathode can be determined. The resulting voltage curves are characteristic of the cathodes under study. From the potential steps, the overpotentials for the specific electrochemical reaction steps can be assessed as shown in Figure 1.11a.

1.6.3.2 Cyclic Voltammetry

Cyclic voltammetry (CV) is a versatile and powerful technique to understand the electrochemical oxidation and reduction of molecular species by sweeping the working electrode potential between two set potentials at certain scan rate in the form of triangular wave form. This results in a current response with oxidation (charge) and reduction (discharge) peaks as shown in Figure 1.11b. These peaks correspond to the plateaus in the voltage curves of GCD tests observed in Figure 1.11a. The peak separation is indicative of the reversibility of the reactions. The

charge/discharge overpotentials can be determined from the shift in peak positions with respect to the theoretical potentials for the redox reactions. The peak area can be used to obtain the electrode's capacity. By collecting cyclic voltammograms at different scan rates, the reversibility of the cathode material under different rates can be evaluated. Typically for battery materials, with increase in rate, the overpotentials increase, i.e., peak separation increases.

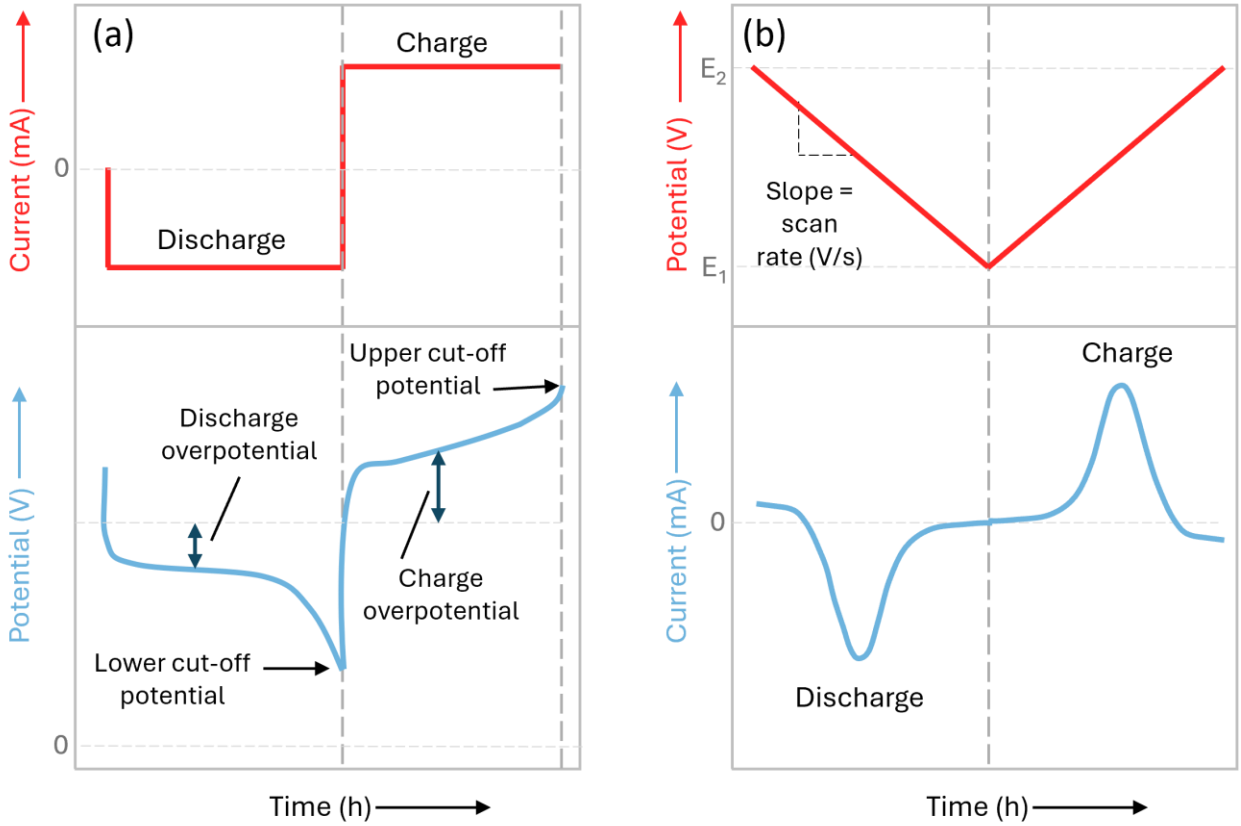

Figure 1.11. Testing protocols and their corresponding output for (a) galvanostatic charge/discharge and (b) CV.

1.6.3.3 Galvanostatic Intermittent Titration Technique

Galvanostatic intermittent titration technique (GITT) is used to determine the diffusion coefficients of ions in intercalation type electrodes. In a GITT experiment, typically a series of

constant current pulses is applied to a battery followed by relaxation periods, during which the equilibrium potential for the given state of charge (SoC) is reached as shown in Figure 1.11a. The pulses are applied until the cut-off voltage is reached. A typical GITT curve for an AZIB cathode is shown in Figure 1.11b. The width and amplitude of the current pulse and the duration of relaxation is chosen in such a way that the electrode operates close to equilibrium or steady-state conditions. For AZIB cathodes, the diffusion coefficients of Zn^{2+} in V_2O_5 structure can be calculated using the following equation,

$$D_{Zn^{2+}} = \frac{4}{\pi\tau}\left(\frac{n_m V_m}{A}\right)^2 \left(\frac{\Delta E_s}{\Delta E_t}\right)^2 \quad \text{..... (1.5)}$$

where D_{Zn}^{2+} is the Zn^{2+} diffusion coefficient in cm^2/s, τ is the pulse duration in s, n_m is the number of moles of active material in mol, V_m is the molar volume of the active material in cm^3 /mol, A is the geometric area of the electrode, ΔE_S is the change in the steady state voltage in V, ΔE_t is the voltage change due to the current pulse in V.

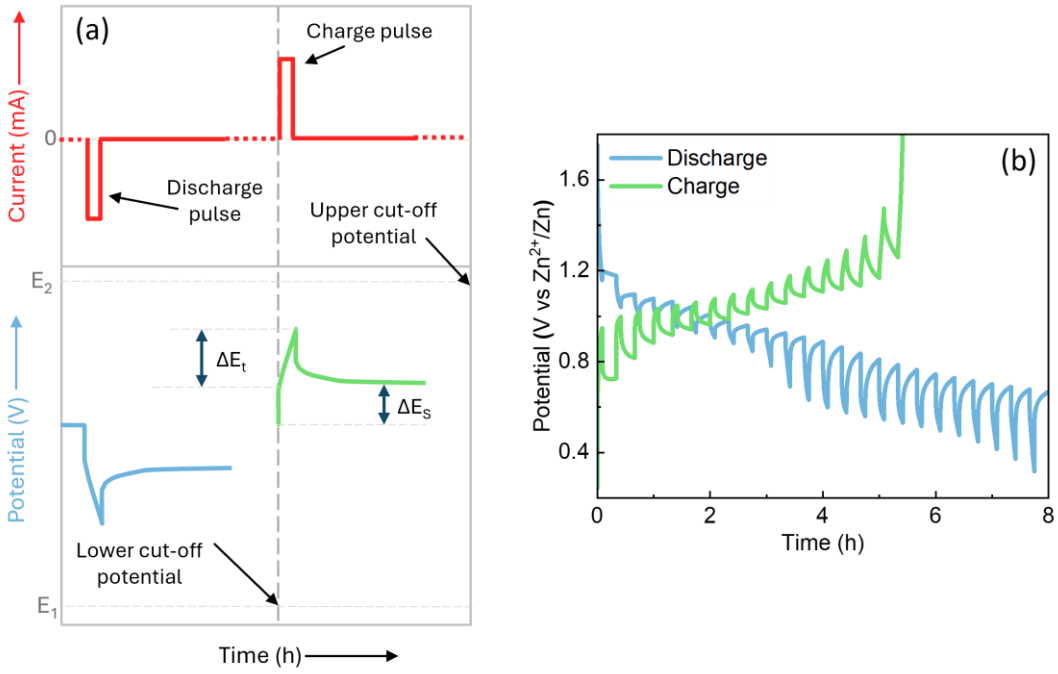

Figure 1.12. (a) GITT pulse and voltage profile. (b) Typical GITT charge/discharge voltage profiles for a AZIB cathode.

Chapter 2 - Mechanistic Understanding of Li Metal Anode Processes in a Model 3D Conductive Host Based on Vertically Aligned Carbon Nanofibers

Reprinted (adapted) from *Carbon*, 212 (2023), 118174.

2.1 Introduction

The ever-increasing global energy demand drives the need for the development of new battery technologies with higher energy density than the commercially available LIBs. Some of the promising candidates as the next generation batteries include lithium-sulfur and LOBs as they offer theoretical energy densities of 2567 Wh/kg and 3505 Wh/kg, respectively.[146] Both battery chemistries use lithium as the anode material. LMA is considered as the "holy grail" among various anode materials due to its highest theoretical capacity (3860 mAh/g) and its lowest redox potential (-3.04 V vs SHE).[24, 147] Though the LMA possesses these desired theoretical properties, the heterogeneous nature of lithium plating and stripping results in problems such as unstable SEI, formation of lithium dendrites and electrically isolated dead Li.[24, 148-150] Also being a hostless anode, lithium plating involves a virtually infinite volume expansion. All these result in poor CE, loss of active Li, and poor cycling life, which hinder the commercialization of LMAs. Solving these issues associated with LMAs is essential in developing next generation batteries.

The formation of lithium dendrites is a serious concern as they pose a risk of creating an internal short-circuit by penetrating through the separator and reaching the cathode.[151] Besides inducing a sudden failure, the short-circuit easily causes fire due to the use of flammable

electrolytes. Approaches commonly explored to prevent dendrites include use of 3-D conductive hosts as current collectors, addition of electrolyte additives, and application of artificial SEIs and solid-state electrolytes.[152-156] Among these, 3-D conductive hosts suppress the formation of dendrites by extending the time for depleting Li+ on the anode surface during Li plating, owing to the reduction in the local current density. It is also claimed that 3D hosts homogenize the electric field to facilitate uniform plating.[128, 152] In addition to these, the lower local current density is beneficial for more uniform stripping that prevents formation of dead lithium.[157] The rigidity and porosity of 3D hosts offer preserved room to accommodate the continuous Li plating/stripping during cycling without causing electrode volume changes.

Common 3-D conductive host materials include copper, carbon, metal alloys, etc.[158] Carbon based 3-D hosts are favorable due to their high tunability in size, structure and chemical properties.[159] However, common carbon materials are inherently lithiophobic and hence require heteroatom doping or surface coatings with lithiophilic materials (such as ZnO, Ag, etc.) to serve as an effective host for LMA.[160, 161] Though the host surface can be rendered lithiophilic, common 3D carbon hosts such as carbon cloth, carbon paper, etc., possess high tortuosity which decreases Li+ diffusivity impairing the complete utilization of available pore volume.[162-164] Also, it is important to have a low tortuous structure to avoid uneven filling of pore volume.[165] On these aspects, several studies have successfully developed lithiophilic 3-D carbon materials as hosts for high performance LMAs.[163, 166, 167] Lin et. al. designed a composite material to store Li metal between the rGO layers.[168] The layered Li-rGO composite exhibited a smooth surface without formation of dendrites for 100 cycles, but the structure of the SEI on the internal surface of rGO layers during lithiation/delithiation processes was unknown. Similarly, in the study by Fang et. al., Ag nanoparticle–embedded nitrogen-doped carbon macroporous fibers were used as the host

material to achieve more than 500 cycles with the CE higher than 98% at 1 mA/cm^2. The improvement in performance was attributed to the lithiophilic nitrogen doped carbon sites and functional Ag nanoparticles, which acted as nucleation sites for Li plating, while the macroporous framework mitigated the volume variation during cycling.[163] From the scanning electron microscopy (SEM) and transmission electron microscopy (TEM) images, it can be observed that Li growth occurred within the hollow spaces as well as on the outer surface of the fibers. It is noteworthy that, at high capacities, globules formed on the surface. Though the 3-D hosts help to achieve stable cycling of LMAs by preventing dendrite formation, it is not clear whether other issues, such as continuous formation of SEI and dead Li, still limit the performance. Huan Li et. al., employed in-situ Raman to understand the lithium nucleation behavior in low surface area defective graphene electrodes. They found that, with the use of high surface area electrode, the cell failed by electrolyte consumption.[169] However, they did not provide a good mechanistical understanding of the structure and nature of the innate SEI on the 3-D material. It needs to be emphasized that, in addition to Li plating and stripping, Li intercalation and deintercalation processes could also occur in carbon based 3-D hosts.[128, 170] The unanswered fundamental scientific questions include where the SEI forms and its nature, what happens to the SEI at increased Li plating capacity, and what happens to the carbon host during the Li intercalation and plating, etc. These are crucial for designing better 3-D host architectures for LMA.

In a previous study, we demonstrated that VACNF arrays, with a unique internal microstructure consisting of conically stacked graphitic cups, can serve as a low-tortuosity brush-like conductive 3-D carbon host for high-performance LMAs.[128] In this study, we have chosen VACNFs grown on Cu substrate (VACNF/Cu) as the 3-D host to understand the critical processes involved in LMA. The following characteristics of VACNF arrays make it an ideal model to

answer the aforementioned fundamental questions. VACNFs are graphitic carbon inherently doped with nitrogen atoms and functionalized with oxygenated groups at the sidewalls, rendering them more lithiophilic compared to other 3-D carbon hosts.[128] While other carbonaceous 3-D hosts require additional methods to be employed to either dope with heteroatoms or to coat with lithiophilic materials. The high aspect ratio of VACNFs provides a large surface area while their vertical alignment and open pore structure (~80% porosity) offer short and low tortuous pathways for fast and uniform Li^+ ions diffusion throughout the whole electrode.[127, 171, 172] To compare with, 3D hosts based on carbon cloth (CC) and carbon paper (CP) consist of micron sized or nano sized carbon fibers stacked horizontally with a wide range of pore sizes from few microns to tens of microns in diameter.[162, 163] Most of the 3-D hosts are quite thick with poorly defined pore structure and high tortuosity resulting in non-uniform filling of Li thereby impeding the complete utilization of pore volume.[173] The high surface area of these hosts is an outcome of their large thicknesses. Also, they would decrease the specific capacity of 3-D LMAs. In contrast, VACNF/Cu is designed such that the entire pore volume would be utilized for the capacity being tested. The VACNFs can be easily scraped off from the copper substrate and transferred to TEM grids, making it possible to evaluate the details of SEI and Li plating on individual VACNFs. This was difficult with common carbon host structures. In brief, the stark contrast between VACNFs and other 3-D hosts lies in its well-defined, aligned pore structure with inherent lithiophilic nature which makes it a less complicated 3-D host structure to study as model system.

In this chapter, we employ various characterization techniques such as in-situ Raman microscopy, X-ray photoelectron spectroscopy (XPS) depth profiling, cryo-TEM, field-emission SEM (FESEM) to gain deeper understanding on the structure, composition and dynamics of SEI, Li intercalation/deintercalation, and Li plating/stripping in VACNF arrays. These studies are

correlated with the enhanced electrochemical performance using VACNF arrays as a 3-D LMA host. Interestingly, both SEI and electrodeposited Li (e-Li) are highly heterogeneous over a wide length scale. Two types of SEIs, on top of the VACNF array and around individual VACNFs, are formed during intercalation process, which are further reduced into more compact SEIs during Li plating. The morphology of e-Li is composed of micron-scale columnar Li grains infiltrated into VACNF arrays and nanoscale coaxial Li sheath wrapped around individual VACNFs in the interstitial area between the columnar Li grains. They behave differently during Li stripping. The 3-D structured host reduces the irreversible SEI formation and electrolyte consumption compared to planar Cu electrode but cannot eliminate them. These critical factors provide useful insights to develop future solutions to further enhance the performance of LMAs.

2.2 Materials and Methods

2.2.4 Chemicals and Materials

Electrolyte solution containing 1.0 M lithium bis(trifluoromethanesulfonyl)imide (LiTFSI) in 1,3-dioxolane (DOL) and 1,2-dimethoxyethane (DME) (1:1, v/v) with 1 wt % $LiNO_3$ additive was purchased from Dodochem Limited (Suzhou, China). Copper foils (99.999 %) were purchased from Fisher Scientific (Hampton, NH) and GoodFellow Corporation (Pittsburgh, PA). Li foil, CR2032 coin cell casings, spacers, and wave springs were purchased from MTI Corporation (Richmond, CA). The separators Celgard 2400 and glass fiber discs were purchased from Celgard (Charlotte, NC) and El-Cell GmbH (Hamburg, Germany), respectively.

2.2.5 VACNF/Cu Electrode Preparation

An 84 µm thick copper foil was used as the substrate for the growth of VACNFs. A 300 nm thick Cr barrier layer and a 30 nm thick Ni catalyst layer were sputter coated using a high-vacuum Perkin Elmer 4400 series magnetron sputtering system at UHV Sputtering Inc. (Morgan Hill, CA). VACNFs were grown using a DC biased PECVD unit (Black Magic, Aixtron, CA) following the same procedure reported in previous studies.[127, 128, 173] In brief, the substrate was heated to 500 °C at a rate of 250 °C/min with ammonia gas at a flow rate of 250 sccm, at a pressure of 3.9 Torr. Under these conditions, a DC plasma at 40 W was applied for 60 s to dewet and break the Ni film into randomly distributed Ni nanoparticles. Then, the temperature was increased to 750 °C at a rate of 0 °C/min while 70 sccm acetylene gas was introduced as the carbon precursor along with the ammonia gas to give a steady-state pressure of 4.8 Torr. The process was continued for 90 min to grow 15 µm long VACNFs on Cu.

2.2.6 Materials Characterization

The morphology of the electrodes was studied using Topcon/ISI/ABT DS 130F FESEM (Akashi Beam Technology Corporation, Tokyo, Japan) and Helios NanoLab 660 (FEI, OR) with a focused ion beam (FIB) milling functionality. To image intercalated and/or electroplated lithium on VACNF/Cu hosts, the electrodes were harvested from half-cells by disassembling in an Ar-filled glovebox. The harvested electrodes were washed by immersing in DME several times. After drying in the antechamber of glovebox under vacuum, FESEM samples were prepared back in the glovebox. The prepared samples were then stored in a tightly sealed container filled with ultrapure Ar. The samples were exposed to ambient air for a few seconds during transferring from the sealed container to the sample stage. Before FIB milling, a 2 µm thick Pt layer was deposited to protect

the underneath structure from ion beam damage. An ECC-Opto-Std optical cell (El-Cell GmbH, Hamburg, Germany) was used for in-situ Raman experiments. A glass fiber separator (El-Cell GmbH, Hamburg, Germany) of 0.65 mm thickness and 10 mm diameter was used. The VACNF/Cu and Li foil electrodes of 3.0 mm wide and 15.0 mm long were placed side by side on top of the glass fiber separator. The optical cell was filled with 1.0 M LiTFSI in DOL and DME (1:1, v/v) with 1 wt% $LiNO_3$ electrolyte. A constant current of 10 μA was applied for Li intercalation/deintercalation cycles while the cell voltage was varied between 0.0 – 1.0 V (vs Li^+/Li). For lithium plating, 10 μA was employed for a duration of 13 hours. Lithium stripping was carried out at the same current till the voltage reached 1.0 V (vs Li^+/Li). Raman spectra were acquired using a DXR Raman microscope (Thermo Fisher Scientific, Madison, WI) with a 532 nm laser at a power of 10 mW, using a 10× objective lens with a slit width of 25 μm at different electrode potentials while cycling. A total of 16 exposures for a duration of 10 s per exposure was used. XPS depth profiling was carried out using a PHI 5000 Versa XPS system (Chanhassen, MN) with a monochromatized Al Kα source (1486.7 eV) with a 400 μm spot size. Samples were prepared according to the sample preparation procedure followed for FESEM imaging. Shirley background was used for XPS analysis. The C 1s peak at 284.60 eV was used as the standard to calibrate all XPS spectra. The morphology of individual VACNFs was imaged using a Philips CM 100 TEM at a 100 kV acceleration voltage in low dose mode at -175 °C using a Gatan cryo-holder. The VACNFs were transferred to TEM grids by scraping them from the electrode inside a glovebox. The TEM grids were stored in Ar filled storage holders and plunged in liquid nitrogen without exposing to air. This was followed by transfer of the TEM grid to the cryo-holder using a cryo-station. The cryo-shield was used to prevent the sample from exposure to air during the transfer from cryo-station to TEM.

2.2.7 Electrochemical Characterization

VACNF/Cu or planar Cu foil electrodes of 15 mm in diameter were used as the working electrode to assemble half-cells using CR2032 casings. A 25 μm thick Celgard 2400 and a 0.65 mm thick Li foil were used as the separator and counter electrode, respectively. A 0.3 mm thick stainless steel wave spring and two pieces of 0.2 mm thick stainless-steel spacers were used to provide consistent pressure and good contact between the components. The Li foils were polished using 200 and 400 grit sandpapers before assembling. 250 μL of 1.0 M LiTFSI in DOL/DME (1:1, v/v) solvent with 1 wt% $LiNO_3$ additive was used as the electrolyte in the flooded condition. The half-cells were assembled in an argon-filled glovebox (Mbraun MB10 Compact, Stratham, NH) with oxygen and water levels below 0.5 ppm. The assembled half-cells were tested using a battery testing system (Neware, Shenzhen, China) at room temperature. Five cycles of Li intercalation/deintercalation at 50 μA were done between 0.0 V and 1.0 V (vs Li^+/Li) before Li plating. Li plating and stripping processes were conducted by applying a constant current density of 1.0 mA/cm^2 to obtain desired capacities. For the CE test, a capacity of 2.0 mAh/cm^2 was employed. The upper cut-off voltage for Li stripping was 1.0 V vs Li^+/Li. The CE was calculated as the ratio of Li stripping capacity to Li plating capacity, expressed in units of percentage. The symmetric cycling measurement was done with coin cells with a working electrode (VACNF/Cu or planar Cu) vs. a Li disk counter electrode at 1.0 mA/cm^2 with a cycling capacity of 1.0 mAh/cm^2. Prior to symmetric cycling, the working electrodes were cycled at 1.0 mA/cm^2 for 2.0 mAh/cm^2 capacity for three times followed by plating 2.0 mAh/cm^2 of Li.

2.3 Results and Discussion

2.3.1 Materials and Electrochemical Characterization of VACNF/Cu Electrode

Firstly, the structure and chemical composition of pristine VACNF/Cu, the chosen model LMA host for this study, was carefully characterized. The FESEM images of the VACNF grown on Cu substrate for 90 min are shown in Figures 2.1a to 2.1c, A.1a, and A.1b. As seen at a 30° perspective view, the VACNFs form an array with rather uniform vertical alignment. A scratch was purposely made on the VACNF array in Figure 2.1a so that their length can be viewed at the cross-section. From the top view images (Figures 2.1c and A.1b), the VACNFs are highly aligned perpendicular to the surface of the Cu substrate. Per the calculation shown on Figure A.1c, the porosity was found to be ~78.6%. The average length and diameter of the VACNFs were determined to be ~14 μm and ~154 nm, respectively. A histogram of the fiber diameter is shown in Figure A.2, which is defined by the diameter of the Ni catalyst particle at the tip of each VACNF. TEM and HRTEM images of VACNF (Figures 2.1d and A.3) illustrate the conically stacked graphitic cups with an abundance of graphitic edges on the surface of sidewalls. Since the VACNFs grew by the tip growth mode, the inverse tear drop shaped Ni catalyst retained at the tip of the VACNF and was covered by a few layers of carbon. This was validated by the XPS data (Figure A.4) which confirmed the presence of Ni within a depth of 2 – 10 nm from the surface. The XPS results (Figure A.5) also revealed that the VACNFs were doped with 2.9% and 7.3% of nitrogen and oxygen, respectively. The N 1s peak can be deconvoluted into four peaks with the binding energies (BEs) at 396.3, 398.4, 400.5, and 402.5 eV, corresponding to pyridinic N, pyrrolic N, graphitic N, and pyridinic N oxide, respectively. The O 1s peak was deconvoluted into four components with BEs at 531.2, 532.2, 533.4, and 535.1 eV corresponding to C-O, C=O in carboxylic group (-COOH), -OH group and adsorbed water, respectively. To understand the

location of dopants, the top surface of pristine VACNF array was etched using Ar^+ at a rate of 0.08 nm/s for 60 s. This translates to removal of ~4.8 nm thick materials, which is equivalent to ~14 layers of graphitic planes. As shown in Figure A.5, after etching, the O at% decreased by 69% to a total of 0.9%. Meanwhile, N at% slightly decreased to 7.0%. However, the composition of the N doping changed as follows. The amount of pyridinic N oxide decreased significantly by about 53% while the amount of pyridinic N and pyrrolic N increased by 54% and 25%, respectively. The significant decrease in oxygen and pyridinic N oxide directs that oxygenated functional groups are present only on the exposed edges of VACNFs. After etching off the surface, the pyridinic N and pyrrolic N groups located within the few layers from the surface would also get removed but those located deeper will get exposed. Also, during the etching, graphitic nitrogen situated close to the surface may get converted to pyridinic/pyrrolic N. Due to the absence of oxygen during the etching process, pyridinic N oxides are not formed. This proves that nitrogen dopants are present throughout the structure of VACNFs while oxygen functional groups are present only at the graphitic edges.

Half-cells were constructed with VACNF/Cu and planar Cu electrodes as working electrodes to evaluate their performance as LMA hosts. The CE was assessed at 1.0 mA/cm^2 with a cycling capacity of 2.0 mAh/cm^2, based on our previous work that filling the entire pore volume of VACNF/Cu with Li would yield a plating capacity of 2.0 mAh/cm^2. As shown in Fig. 1e, the CE for VACNF/Cu was only around 87.8% in the first cycle, owing to the formation of initial SEI and the intercalation of Li^+ ions into the graphitic structure of VACNFs. From the second cycle, the CE was stabilized at ~98% and retained at this level for about 130 cycles. In the case of planar Cu, the cell was only stable for about 44 cycles with a lower average CE of 95.4%. The higher CE and longer cycle life of VACNF/Cu over planar Cu make the advantages of using 3-D hosts for

LMA quite evident, which are supported recent studies.[174, 175] The capacity associated with Li intercalation into VACNFs and SEI formation were significantly reduced in cycle #2-5, as shown in the Li plating voltage curves in Figures 2.1f and A.6. In the first cycle, a capacity of about 0.05 – 0.07 mAh/cm^2 was consumed in the potential range of 0.2 – 0.0 V (vs Li^+/Li). This can be attributed to lithium intercalation into VACNFs, translating to a specific capacity of 84 – 117 mAh/g_{VACNF} which is only 22 – 31% of theoretical capacity of graphite. Hence, only a small portion of graphitic carbon in VACNFs (likely only at the exterior surface) is intercalated with Li^+ at 1.0 mA/cm^2 current density (the typical rate where Li plating is done in later discussion). Even at a lower current of 0.028 mA/cm^2, the lithiation capacity was ~150 mAh/g_{VACNF} (~40% of the theoretical capacity of graphite) as shown in Figure A.7. This small Li intercalation is helpful to make VACNFs lithiophilic before Li plating starts while maintaining their structural integrity. After stable cycling for ~130 cycles, the CE of VACNF/Cu started to decline continuously to a minimal value of 66% in the 182nd cycle. Beyond this point, the CE increased from 66% to 78% (in the 200th cycle) and then became very unstable. The planar Cu foil electrode showed a similar behavior but with a much shorter life. The behavior of increasing CE towards the end of cycle life could be due to reattachment of physically isolated lithium particles that resulted in increased stripping capacity.[176, 177] Whether the use of VACNFs which can act as 3-D conductive wires improves the chances of reattachment of dead Li is an interesting topic of future studies.

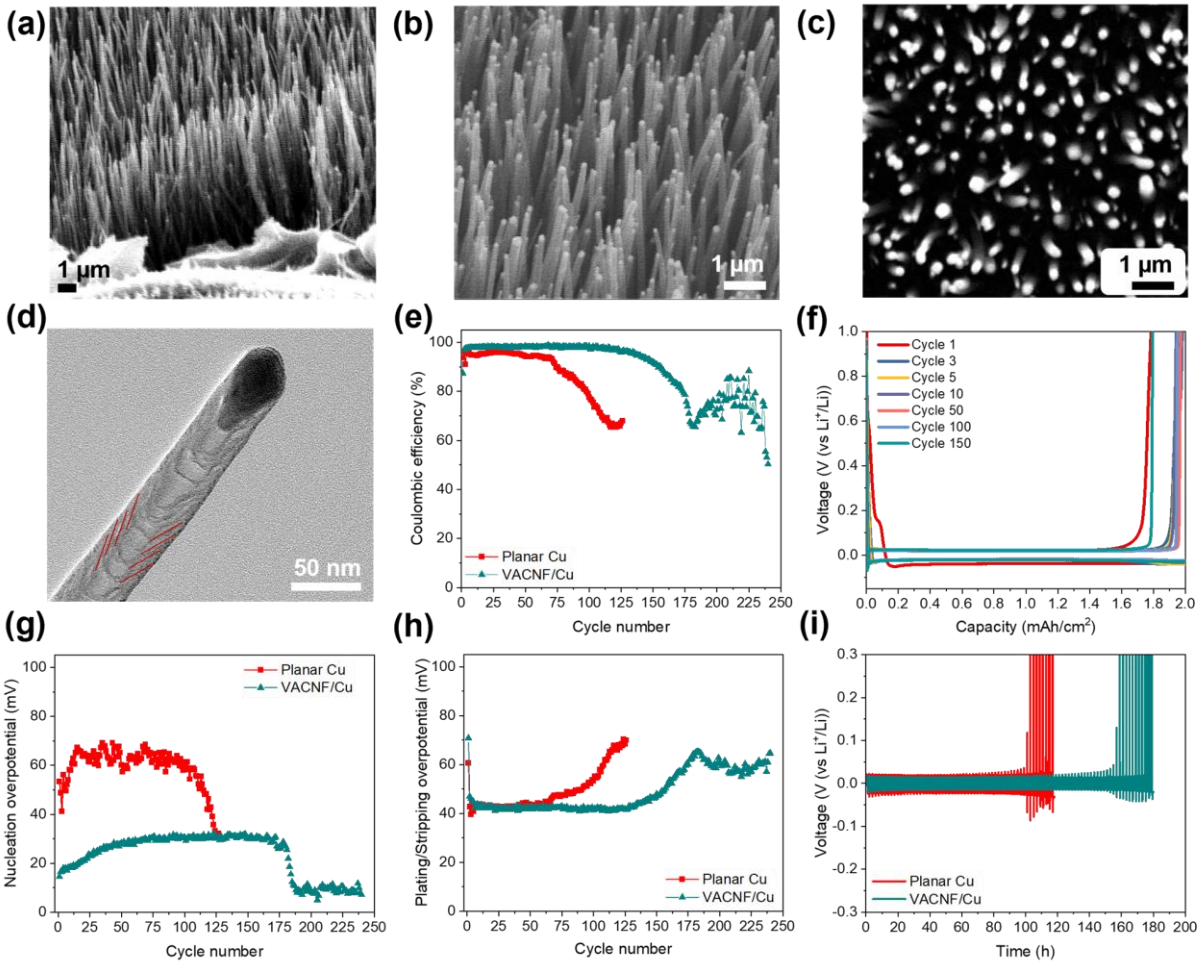

Figure 2.1. FESEM images of VACNF grown on Cu substrate at (a), (b) a 30° perspective view, and (c) a 0° top view. (d) TEM image of a VACNF. (e) CE during Li plating/stripping cycling with 2.0 mAh/cm^2 capacity at 1.0 mA/cm^2 for VACNF/Cu and planar Cu electrodes, respectively. (f) Voltage curves for Li plating/stripping on a VACNF/Cu electrode at different cycles. Evolution of (g) Li nucleation overpotential and (h) Li plating/stripping overpotential over cycles shown in (e). (i) Symmetric cycling performance of VACNF/Cu and planar Cu electrodes, respectively, plated with 2.0 mAh/cm^2 Li at a cycling capacity of 1.0 mAh/cm^2 and a current density of 1.0 mA/cm^2. Reprinted (adapted) from *Carbon*, 212 (2023), 118174. Copyright 2023 Elsevier Ltd.

The Li plating/stripping overpotential (η_{ps}) and the Li nucleation overpotential (η_{nuc}) were calculated as depicted in Fig. S8. In the stable cycles, VACNF/Cu and planar Cu had similar η_{ps} of ~40 mV (Figure 2.1h), but showed distinct behavior in η_{nuc} (Figure 2.1g). In the first cycle, VACNF/Cu exhibited a lower η_{nuc} of 14.5 mV compared to that of planar Cu (53.4 mV). The lower

nucleation overpotential for VACNF/Cu is due to the high surface area of VACNFs and the lithiophilic nature owing to graphitic edges, N and O doping, and Li intercalation. These factors collectively decreased the energy barrier for the Li nucleation process. In following cycles, the η_{nuc} of VACNF/Cu gradually increased and got stabilized at 30.1 mV (Figure 2.1g). When the CE started to decline, the η_{nuc} quickly dropped to 8.1 mV, a value lower than the initial η_{nuc}. This trend was observed for planar Cu as well but in much earlier cycles. This could be an indicator for the growth of uncontrolled high-surface-area Li structures and/or activation of unstripped lithium sites of previous cycles in the dynamic environment inside the coin cell, which facilitate Li nucleation. As shown in Figure 2.1h, during this same period, the η_{ps} increased to ~65 mV for both electrodes, indicating accumulation of SEI/dead Li due to increased consumption of electrolyte during the end of cycle life.[176] This would lead to zones where electrolyte is deprived, making the electrode surface more heterogeneous and leaving behind a large amount of dead Li and SEI as indicated by the low CE. While it is well known that 3-D conductive host, such as VACNF arrays, can improve the reversibility of Li plating/stripping (Table A.1), it is important to understand the failure mechanism to gain insights into strategies for further improvement, which is the foci of this study.

Symmetric cell cycling was also performed to understand the stability of SEI and reversibility of Li plating/stripping. The cycling capacity was kept at 1.0 mAh/cm^2, i.e., 50% degree of discharge (DoD), at a rate of 1.0 mA/cm^2 using VACNF/Cu and Cu electrodes plated with 2.0 mAh/cm^2 vs a Li foil counter electrode. As shown in Figure 2.1i, VACNF/Cu electrode exhibited a longer cycling life (156 h) when compared with planar Cu (100 h). This improvement in performance could be attributed to higher reversibility of Li plating/stripping and a more stable SEI formation in VACNF/Cu electrode. For both electrodes, the cells failed by an increase in the electrode potential due to unavailability of sufficient active Li to deliver the defined stripping

capacity. Consistent with the previous report, VACNF/Cu is indeed a superior LMA host compared to planar Cu.[128] With the testing conditions employed in this study, no internal short circuits due to dendritic growth were observed. However, the electrochemical data indicates continuous consumption of electrolyte and active Li, consistent with recent literature.[169, 178, 179] Further characterization was carried out to shed light on the processes that occurred on VACNFs during the Li intercalation/deintercalation and Li plating/stripping.

2.3.2 Morphological Analysis of Electrodeposited Li Using FESEM

To understand the morphology of electrodeposited Li (e-Li) on VACNF/Cu, FESEM images were taken after plating different capacities of Li at 1.0 mA/cm^2, as shown in Figures 2.2a to 2.2f. After depositing a low capacity of about 0.75 mAh/cm^2 of Li, micron-scale particles of Li of an average size of 2.7 μm were observed (as the darker spots in Figure 2.2a). The density of micron-scale Li particles was calculated to be about 5.6 x 10^6 particles/cm^2. Figures 2.2b to 2.2f revealed that the VACNF/Cu plated with the full capacity of 2 mAh/cm^2 Li displayed two different morphologies – (i) micron-scale, pillar-like, columnar Li infiltrating the open spaces among the VACNFs (referred to as infiltrative e-Li), (ii) nanoscale Li that coaxially deposited on the surface of individual VACNFs (referred to as nanoscale e-Li) in the area between the micron-scale columnar grains. The columnar structure of infiltrative e-Li without pores are generally reported to be favorable for Li metal anodes as it reduces the active surface area, thereby decreasing the consumption of active Li and electrolyte due to irreversible SEI formation.[42, 180] FIB-FESEM image (Figure 2.2f) further showed that the infiltrative Li was non-porous in nature, and it completely filled the pore volume among the VACNFs. The enhancement in reversibility/CE of Li plating/stripping on VACNF/Cu electrode could be attributed to this columnar Li morphology.

VACNFs acted as conductive wires to maximize the electrical connection with the plated Li and reduced formation of dead Li. The growth of columnar Li in the unique low-tortuous open pore structure of VACNF arrays demonstrates the effectiveness of 3-D structure on improving the e-Li morphology. Besides the micron-scale columnar infiltrative e-Li, nanoscale e-Li were observed on the VACNFs that were not engulfed by the infiltrative e-Li. The histogram analysis of the diameters of VACNFs after Li plating with different capacities and after Li stripping were analyzed as shown in Figure A.10. It revealed that the average fiber diameter increased from ~154 nm to ~163 nm after plating 0.75 mAh/cm^2. It further increased to about ~226 nm after an additional plating of 1.25 mAh/cm^2 Li. The increase in fiber diameter can be attributed to the coaxial sheath of nanoscale e-Li and the SEI. The sheath thicknesses was about 4.5 nm and 36 nm for Li capacity of 0.75 and 2.0 mAh/cm^2, respectively.

After completely stripping Li from the fully plated VACNF/Cu (with 2.0 mAh/cm^2 capacity), the infiltrative e-Li was clearly removed, leaving behind only the soft SEI skins floating in the VACNF host (Figures 2.2g to 2.2i). Contrary to the uniform SEI thin films on planar electrode surface, the SEI skins left off from infiltrative e-Li were of wrinkled 3-D nature, wrapping around the bundle of VACNFs as shown in Figure A.11. This also offers additional evidence for the engulfing nature of infiltrative e-Li. It is quite surprising that most of the studies on 3-D conductive hosts were not able to observe such stripped SEI skins even though their CE is less than 98%.[163] One of the possibilities is that most 3-D conductive hosts were made of powder materials which had complicated tortuous composite structure. The SEI can be disrupted during the electrode preparation for SEM or TEM imaging. The open vertical architecture of VACNF array serves as a unique model to observe the plated Li and stripped SEI skins without disrupting the electrode structure.

As for the coaxially plated nanoscale e-Li, the sidewall of the VACNFs became smoother after completing Li stripping and their average diameter was reduced to 161 nm. The coaxial SEI sheath left behind by nanoscale e-Li is very thin and cannot be observed using FESEM. However, from the similar average diameter between the VACNFs after plating of 0.75 mAh/cm^2 Li and those after complete Li stripping, it can be concluded that, at the low plating capacity of 0.75 mAh/cm^2, only a small fraction of Li was plated as nanoscale e-Li sheath. With further plating, more Li was deposited as the nanoscale e-Li in the interstitial area of infiltrative e-Li particles. The high surface area of nanoscale e-Li would theoretically consume a greater amount of electrolyte if the SEI were to continuously form over cycles. However, considering the improved cycling performance of VACNF/Cu than planar Cu foil and the significant decrease in SEI capacity from second cycle on (i.e., the charging capacity at potentials higher than 0 V in Figure A.6), the SEI on the nanoscale e-Li likely remains as a stable elastic sheath during Li plating and stripping cycles.

In contrast to the e-Li morphology on VACNF arrays, the e-Li on planar Cu exhibited a very different morphology consisting of stacked spherical particles (as shown in Figures A.12a and A.12b) consistent with literature.[181, 182] The average size of the spherical particles was 2.1 μm after plating 0.75 mAh/cm^2 of Li. The presence of whisker-like/dendritic Li was also observed (pointed by yellow arrows in Figure A.12c). After stripping Li, abundant SEI skins shed from Li particles were left on the surface of planar Cu (Figures A.12d and A.12e). Also, dead dendritic Li were present as indicated in Figure A.12f. Without having any structural support as in VACNF/Cu, there is a greater amount of dead Li as well as dendritic Li.[41] This microscopic observation correlates well with the lower CE and shorter cycle life of planar Cu electrodes.

2.3.3 In-Situ Raman Spectroscopic Analysis

Since Raman spectroscopy is a proven characterization tool for studying carbon-based structures, we applied it for in-situ study of the changes in VACNFs during Li intercalation/deintercalation and Li plating/stripping processes. The experiments were performed using a commercially available optical cell from El-cell with a sapphire window for the laser probe. A side-by-side configuration (Figure 2.3a) was found to be the optimal set up with minimal background signal from electrolyte while proper electrochemical control can be applied (as discussed below Figure A.14 in Appendix A). It is to be noted that a potential gradient exists across the electrode surface in this configuration. To minimize this effect, a low current of 10 μA was used to allow sufficient time for the Li^+ ion diffusion. Normal charge-discharge curves could be obtained, and the measurements were made at designated points in Figure 2.3b without disrupting the processes. The Raman spectrum of the pristine VACNF in Figure A.13 showed the characteristic Raman bands at ~1350 cm^{-1} and ~1550 cm^{-1} corresponding to D and G bands of graphitic carbon, respectively. The D band is associated with the vibrational modes of carbon atoms in defect sites and edges of the graphitic planes while the G band is attributed to the vibrations of sp^2 hybridized carbon atoms in the graphitic planes. Their intensity ratio (I_D/I_G) is an indicator of the defect density in graphitic carbon materials. For pristine VACNFs, the I_D/I_G ratio was 0.92. The high I_D in VACNFs is due to the abundance of graphitic edges and the defect sites doped with nitrogen and oxygen functional groups.

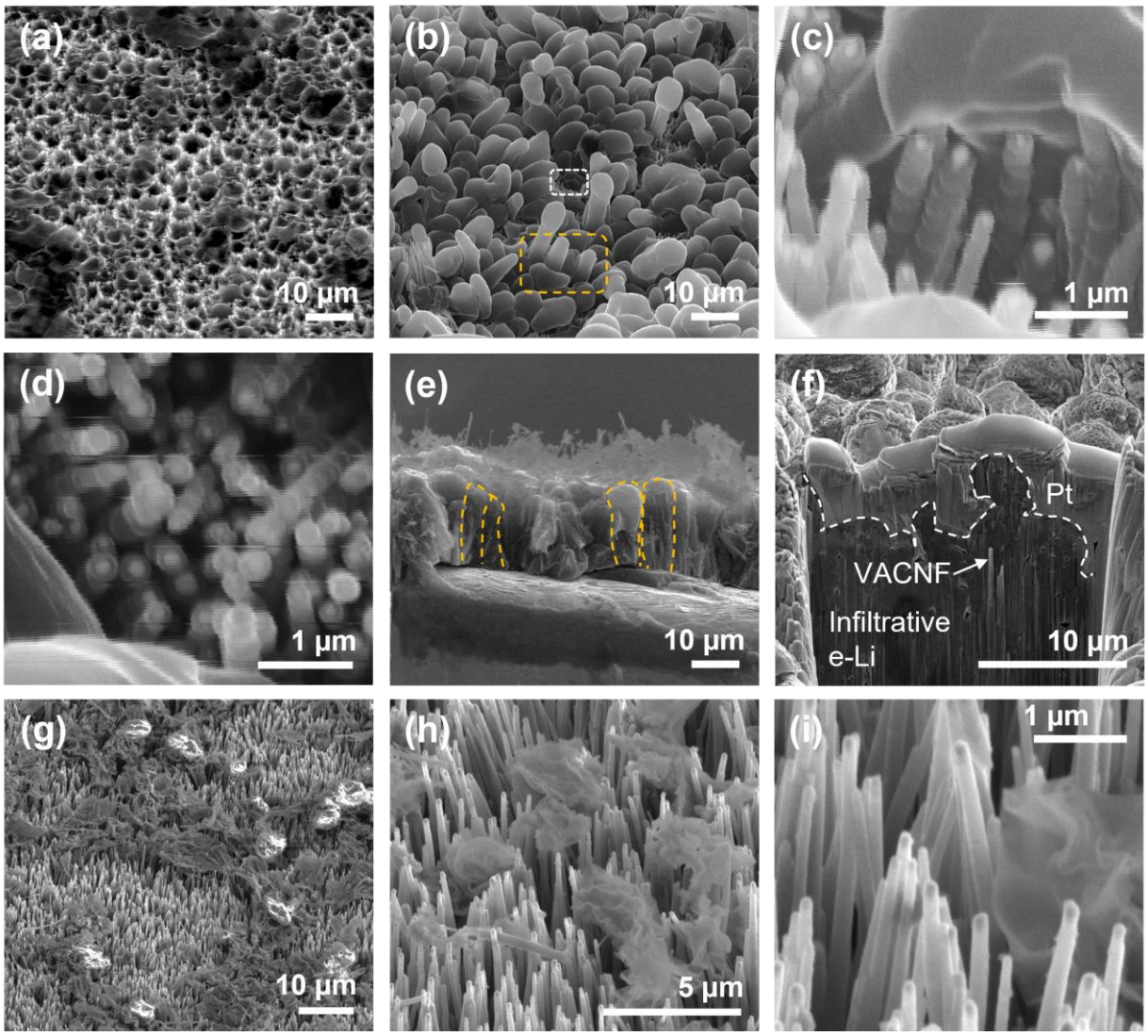

Figure 2.2. FESEM images at 30° perspective view of VACNF/Cu electrodes after Li plating at 1.0 mA/cm2 to the capacity of (a) 0.75 mAh/cm^2 and (b) 2.0 mAh/cm^2. (c) The FESEM images at 30° perspective view and (d) top view of the region highlighted using white dashed rectangle in panel b. (e) Cross-sectional and (f) FIB-milled cross-sectional FESEM images of VACNF/Cu plated with 2.0 mAh/cm^2 Li. A protective layer of 2 µm thick Pt layer was deposited on the top surface to protect the structure underneath from Ga+ ion beam damage as shown in Figure A.9. (g) – (i) FESEM images at 30° perspective view of Li-plated VACNF/Cu electrodes after completely stripping the 2.0 mAh/cm^2 plated Li at a rate of 1.0 mA/cm^2. Reprinted (adapted) from *Carbon*, 212 (2023), 118174. Copyright 2023 Elsevier Ltd.

First, the VACNF/Cu electrode was lithiated/delithiated by cycling between 1.0 V and 0.0 V vs Li^+/Li in which range no Li plating occurred. Figure 2.3c shows the changes in the

characteristic D and G bands of VACNFs during Li intercalation and deintercalation. Additional data are reported in Figure A.15. For the laser focal size of 2 μm, it collects signals from about 30 – 60 VACNFs and the electrolyte filled within the open spaces among VACNFs. Hence, the Raman spectra included the bands corresponding to the VACNFs as well as a set of sharp bands from the electrolyte (Figure A.16). Like others, we were unsuccessful in detecting the components of SEI such as Li_2O, Li_2CO_3, etc.[183] Even though these materials are Raman active, the signal is too weak due to their nanoscale nature. Hence our foci are the D and G bands which clearly decreased and finally disappeared upon Li intercalation. Interestingly, during Li deintercalation, they reappeared without significant change in the band shapes. This is an indication for reversible Li intercalation and deintercalation without structural damage. This reversible phenomena of Li intercalation/deintercalation were repeated for several cycles. The complete disappearance of D and G bands confirms that Li intercalation compounds formed in VACNFs which caused strong light absorption and reduced the depth from which the Raman scattering may occur.[184] The disappearance of G band can be also attributed to the Pauli blocking of interband optical transition preventing resonant Raman process.[185] The formation of lithium intercalation compounds on the surface of VACNFs before lithium plating is beneficial as it further improves the lithiophilicity and electronic conductivity.[186]

However, the changes in D & G bands versus the degree of lithiation were quite different from that of pure graphite particles. In case of pure graphite, the G band changes before the D band, which shifts initially, broadens, splits into two and finally disappears during lithiation.[184] For other defective carbon materials, D bands disappear first and reappear later attributed to preference of Li^+ toward defect sites.[169] For VACNFs, the D band disappeared later and reappeared earlier than the G band. As from the earlier estimation, the lithiation capacity of VACNFs is rather

low (30% - 40%). It was also observed that the color of lithiated VACNF remained black/grey (Figure A.17a) while fully lithiated graphite (LiC_6) is golden yellow.[187] Both in-situ Raman study (Figures 2.3 and A.15) and FESEM characterization (Figures A.17b and A.17c) demonstrated that VACNFs undergo reversible lithiation and delithiation, likely involving only a thin layer at the sidewall surface of VACNFs, which does not damage their inherent structure. Since the defect sites located deeper within the VACNFs might not be available compared to sp^2 carbons on the outer portions, the Li intercalation caused the G band to disappear earlier than the D band. This corroborates with the early revelation by XPS that N atoms are rather uniformly doped inside VACNFs while oxygenated functional groups only present at the exposed edges at the exterior sidewall surface. Other techniques such as operando XRD, in-situ cryo-TEM, and DFT studies might be able to provide more insights into the lithium intercalation mechanism.

Next, the lower voltage limit at 0 V was removed to allow Li plating/stripping cycling at 10 μA current while Raman spectra were collected (Figures 2.3d and A.18). As the cell voltage decreased to 0 V, similar changes in the D and G bands to those during Li intercalation/deintercalation cycles were observed. When the cell voltage was reduced to negative values, a new band appeared at ~1850 cm^{-1}. This band can be attributed to lithium acetylide/carbide (Li_2C_2) which formed through reactions of Li with pre-existing SEI or electrolyte.[183] It is reported that Li_2C_2 is a component of SEI.[188] The origin of this band is due to the surface enhanced Raman scattering (SERS) effect of nanoscale e-Li on individual VACNFs.[183] With further Li plating, the intensity of Li_2C_2 peak increased indicating the growth of nanoscale e-Li. The FESEM images (Figures 2.2c and 2.2d) clearly show that their size remains in the nanoscale range even after plating 2.0 mAh/cm^2. When the plated lithium was stripped off, the Li_2C_2 band vanished completely along with the reappearance of D and G bands of VACNFs. The vanishing of Li_2C_2

band can be attributed to complete dissolution of nanoscale e-Li after stripping (and loss of the SERS effect) rather than disappearance of Li_2C_2 since Li_2C_2 is part of the irreversible SEI. Thus, Li_2C_2 band serves as a good indicator of the formation of nanoscale e-Li. To the best of our knowledge, this is the first in-situ Raman observation of reversible formation and stripping of nanoscale Li on 3-D hosts using lithium acetylide/carbide as an indicator. It would be interesting to study further whether this can be used to reveal the presence of dead Li and Li dendrites in nanoscale regime using micro-Raman imaging.

2.3.4 Chemical and Structural Analysis of SEI.

2.3.4.1 XPS Depth Profiling

XPS depth profiling based on Ar^+ ion etching for different time periods was employed to understand the chemical composition of the SEI formed on Li-intercalated VACNFs (Figures 2.4 and A.19). Interestingly, after Li intercalation, Ni 2p signals were absent. For pristine VACNFs, as stated earlier, the ability to observe Ni 2p peaks makes it a good internal reference for the position of VACNF tips while performing depth analysis. This confirms the presence of a SEI layer on top of the VACNF array (see Figure 2.4a) with a thickness greater than the sampling depth of XPS. Deconvolution of the C 1s peak showed the existence of five different C atoms. The deconvoluted peaks at 282.7, 284.6, 286.5, 288.6, and 290.0 eV can be assigned to carbide (-C=C-), alkyl or aliphatic groups (C-C/C-H), alkoxy groups (C-OR), carboxyl groups (R-COO) and carbonates (CO_3^{2-}), respectively, with the alkyl or aliphatic groups (C-C/C-H) being the dominant one. The F 1s peak was deconvoluted into two peaks at 688.5 and 684.9 eV corresponding to -CF_x and LiF, respectively. The decomposition of the salt LiTFSI resulted in the formation of these compounds and the content of polymeric -CF_x was much higher than LiF. The O 1s peak yielded

four components corresponding to Li_2O, C=O, Li_2CO_3 and $ROCO_2Li$ (or) N-O at 528.2, 530.7, 531.8, and 533.5 eV, respectively.[189, 190] Since $LiNO_3$ was used as the additive, Li_3N and -NC/-NH groups were also found in the SEI (Figure A.19a). Deconvolution of S 2p peaks revealed the presence of SO_3^{2-} and sulfone groups on the surface and the presence of lithium sulfides in the deeper layers (Figure A.19b).[191, 192]

From these deconvoluted high-resolution spectra of C 1s, F 1s, and O 1s peaks, it can be understood that a greater fraction of the topmost layer of the SEI consist of organic compounds such as RCOOLi, Li-O-R, Li-O-R-O-Li, $-CF_X$, etc., which are formed by the reductive decomposition of solvents and salt. In depth profiling by XPS, a decrease in the organic species accompanied by an increase in the inorganic compounds such as LiF, Li_2O was observed in deeper regions after 60 s of Ar^+ ion etching. The Li_2CO_3 content, however, remained similar at different depths, indicating its homogeneous distribution throughout the SEI. From these observations, it can be concluded that the SEI consists of mainly an organic matrix whose inner layer is enriched with LiF and Li_2O while Li_2CO_3 homogeneously distributed throughout the matrix. This is consistent with the recent findings in literature where inorganic lithium compounds are found to be embedded in an amorphous polymeric organic matrix.[32] With continuing the Ar^+ etching for 240 s, XPS signals from Ni 2p were detected as shown in Fig. A.20. This is an indication that the SEI lying on top of the VACNF arrays are mostly etched off. From this, the thickness of this top SEI layer was calculated to be 19.2 nm based on the Ta_2O_3 calibration standard. Since the composition of SEI is of heterogeneous nature, the actual thickness might be larger due to the higher sputtering yield for soft organic SEI.

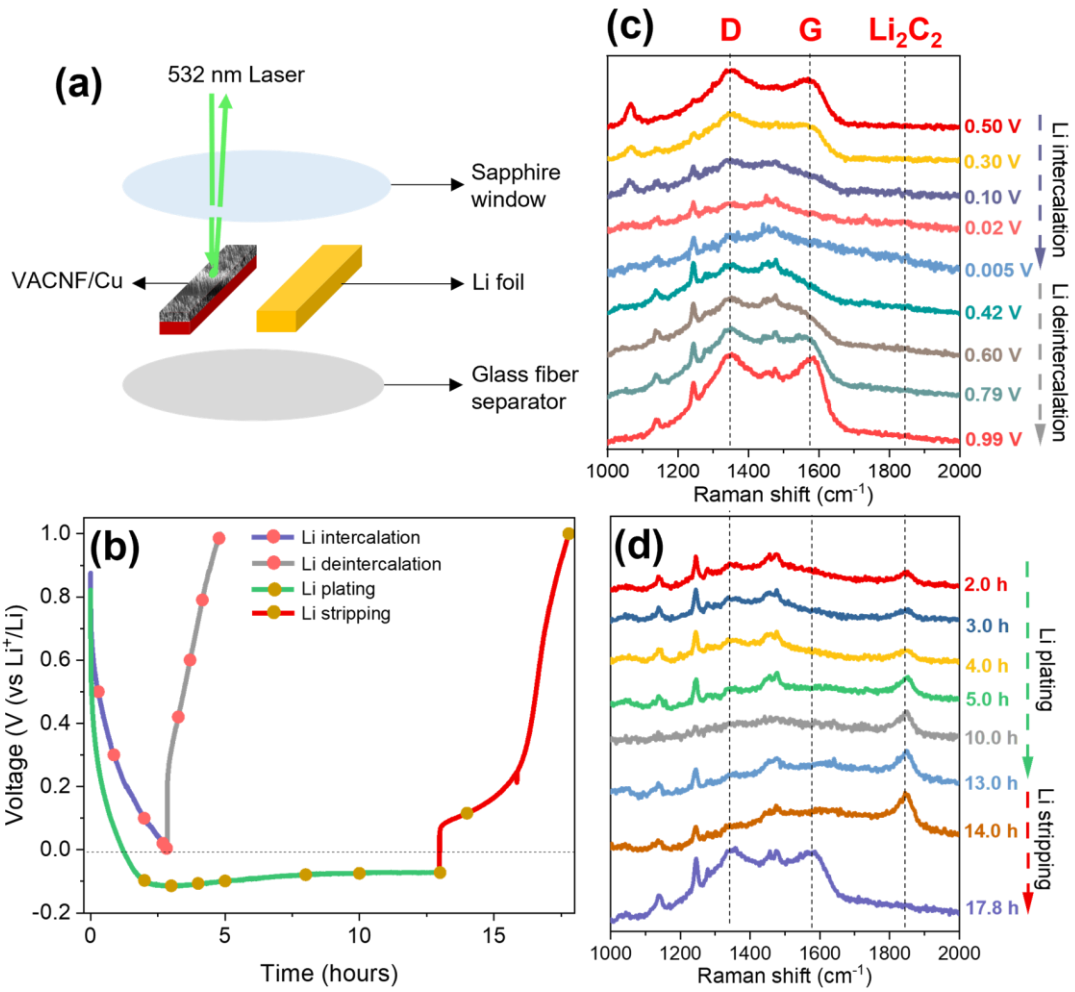

Figure 2.3. (a) Electrode configuration used for in-situ Raman measurements. (b) Voltage curves during Li intercalation/deintercalation and Li plating/stripping at 10 μA for VACNF/Cu electrode during in-situ Raman measurements. In-situ Raman spectra of VACNF/Cu electrode (c) taken around the voltages highlighted as solid pink circles in panel b during Li intercalation/deintercalation and (d) taken around the designated time highlighted as solid yellow circles during Li plating/stripping processes. The Raman spectra were collected during the cycling without interrupting the cycling. Reprinted (adapted) from *Carbon*, 212 (2023), 118174. Copyright 2023 Elsevier Ltd.

If the SEI only exists above the VACNF array, the signals from the SEI components should fade away versus the sputtering time. However, we observed a SEI with a composition resembling that of the inner layer of the SEI located on top of the VACNF array even after etching for 360s. This observation indicates the existence of a SEI on the sidewall of VACNFs as well. The SEIs on top and side of lithiated VACNFs are designated as top SEI and side SEI, respectively. The organic

component of SEI is attributed to incomplete reduction of solvents and salt while their complete reduction leads to inorganic compounds.[189] Taking this into account, the formation of top SEI and side SEI might occur in different stages based on the extent of electrolyte reduction. In the first stage, most of the electrolyte might have been reduced completely which takes place around the sidewall surfaces of VACNFs. This becomes the solid-state barrier for the Li^+ ions intercalating into the VACNFs. Simultaneously, another SEI layer might form on top of the VACNF array. In the second stage, the electrolyte reduction is likely incomplete and occurs mostly on top of the VACNF array. With the help of depth profiling by XPS, we were able to reveal the formation of two different SEIs during the Li intercalation into VACNFs.

For Li plated VACNF/Cu, the high-resolution XPS spectra of Ni 2p, C 1s, F 1s, and O 1s of VACNFs after plating with 2.0 mAh/cm^2 of Li are shown in Figure A.21. The SEI formed on Li plated VACNFs, designated as e-Li SEI, was found to have a mosaic structure similar to that of side SEI of Li-intercalated VACNFs prior to Li plating. Considering the existence of two different types of e-Li as illustrated in Figure 2.2, the composition revealed by XPS can be assigned to the top surface of the SEIs of micron-scale columnar Li grains as well as an outer sheath around the coaxial nanoscale Li. The 3-D nature of e-Li SEI as shown in Figures 2.2g – 2.2i indicates that, during Li plating, the preformed top and side SEIs are likely transformed into similar compositions which are rich in inorganic compounds. The outer region consisted of a higher content of inorganic compounds such as Li_2C_2, LiF, Li_2O and Li_2CO_3 compared to that of the preformed top SEI. With the increased depth, these contents increased further. The higher content of inorganic compounds could be attributed to the higher degree of reduction due to its direct contact with e-Li. The heterogeneous 3-D structure of the e-Li made it difficult to quantify the thickness of e-Li SEI.

Nevertheless, our current study provides the first observation on this, which could provide useful guidance for future studies.

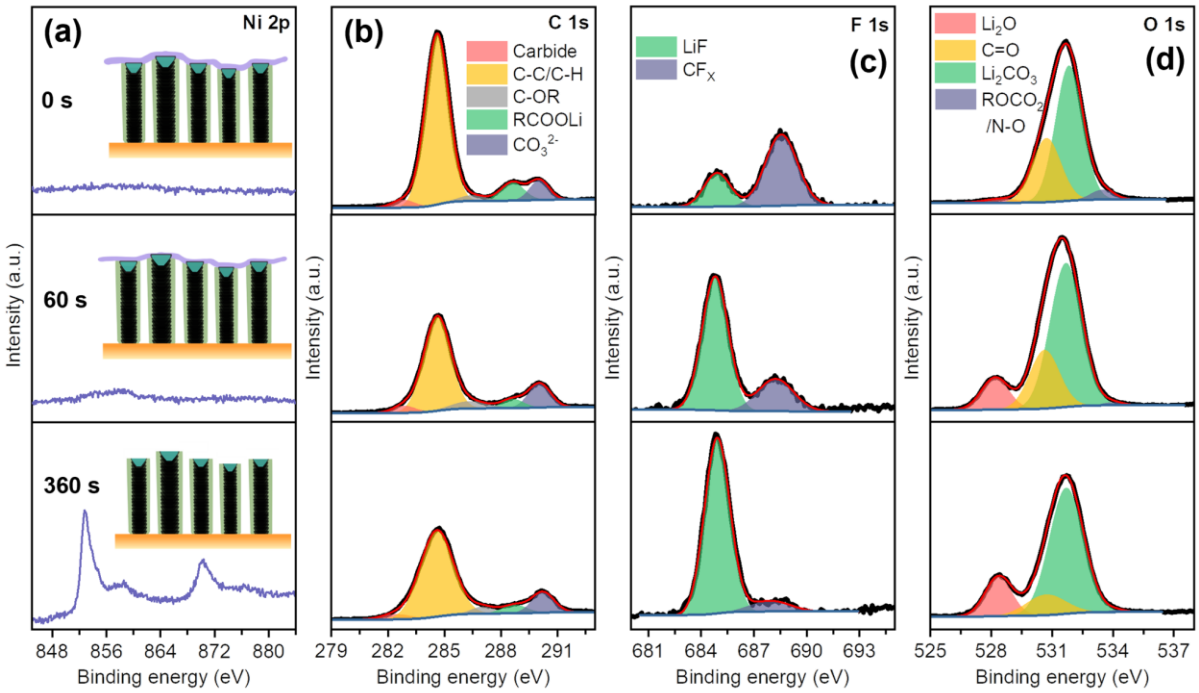

Figure 2.4. XPS depth profiling of Li intercalated VACNF/Cu electrode. High-resolution spectra of (a) Ni 2p, (b) C 1s, (c) F 1s, (d) O 1s. Ar^+ ion etching rate is 0.08 nm/s calibrated using Ta_2O_3. Inset in Fig. 4a shows graphical images to illustrate the depth at which XPS signals were collected. Reprinted (adapted) from *Carbon*, 212 (2023), 118174. Copyright 2023 Elsevier Ltd.

2.3.4.2 Cryo-TEM Imaging of VACNFs After Lithiation and Lithium Plating

A cryo-TEM image of a pristine VACNF processed in the same manner as other samples is shown in Figure 2.5a revealing that the structure of VACNF is unaffected by the employed sample preparation method (including scraping, washing with the solvent and depositing on TEM grids). It could be observed that the diameter of a pristine VACNF was approximately equal to the widest part of the Ni nanoparticle. Upon lithiation, a co-axial film was observed only at the sidewall of the VACNF, which can be assigned as the side SEI (Figure 2.5b). Surprisingly, the top

SEI which was unveiled by XPS cannot be found on top of the Ni nanoparticle in the cryo-TEM image. This suggests that the top SEI is likely a continuous self-sustained film which is loosely attached to tips of the VACNF array. It may have been easily lifted off when the VACNFs were scraped off the Cu substrate during sample preparation. The FESEM images of pristine VACNF/Cu (Figures A.22a – A.22c) and lithiated VACNF/Cu (Figures A.22e – A.22g) prepared by the same method further revealed the presence of nanoscale side SEI film around individual VACNFs. The pristine VACNF array collapsed into 1 – 2 μm wide pyramid shaped bundles as a result of the elastocapillary aggregation caused by the capillary forces during drying of DME solvent following electrode washing. This phenomenon was well documented in our previous work.[193-195] Importantly, our previous work demonstrated that a thin coaxial polymeric coating (down to ~20 nm in thickness) on each VACNFs was sufficient to prevent such elastocapillary aggregation.[193-195] Indeed, the lithiated VACNFs in Figures A.22e – A.22g were able to retain the vertical array structure without collapsing into microbundles. This further validates the presence of the coaxial side SEI sheath.

Figures 2.5c and A.23 reveal the nature of nanoscale e-Li that forms uniformly on the individual VACNFs resulting in the coaxial Li deposition around the entire VACNF surface. The thickness of the nanoscale e-Li and its corresponding SEI were in the range of 10 – 21 nm and 30 – 60 nm after plating with 0.75 mAh/cm^2 and 2.0 mAh/cm^2, respectively. It is to be noted that these VACNFs observed under TEM are mostly from the interstitial regions between the infiltrative-Li grains since the VACNFs in later ones are embedded inside Li grains and are not easy to be broken free. Most of the growth of nanoscale e-Li seems to occur in the later part of plating step and some nanoscale e-Li still exists even after plating a capacity of 2.0 mAh/cm^2, which are consistent with the FESEM results in Figures 2.2b and 2.2c. In contrast to the Li-

intercalated sample, the tip of Li-plated VACNFs was covered by Li metal and e-Li SEI. The coaxial Li deposition is favored for suppressing dendrite growth, which may be enhanced by further improving lithiophilicity in our future studies.[186] The SAED pattern in Figure A.24 shows the amorphous nature of nanoscale e-Li on VACNFs. It was reported that, at low current densities, Li was normally electrodeposited as amorphous "glassy" Li, which was favored for stable and reversible Li plating/stripping.[196] The high surface area provided by the VACNFs resulting in a local low current density can be attributed to the formation of this amorphous Li. During subsequent stripping of the e-Li, the thickness of the coaxial film around the VACNFs was reduced as shown in Figure 2.5d. Since the formation of SEI is irreversible, the coaxial film on Li-stripped VACNFs can be assigned to the SEI of nanoscale e-Li. Figure A.25 shows that the coaxial SEI after Li stripping bulged into a small bubble due to the heating effect of electron beam, which further confirms its coaxial and elastic nature. The difference in the appearance between side SEI and the SEI on the surface nanoscale e-Li confirms the transformation of preformed SEIs at intercalation stage into chemically distinct e-Li SEI (richer with inorganic components) as shown in Figure A.21.

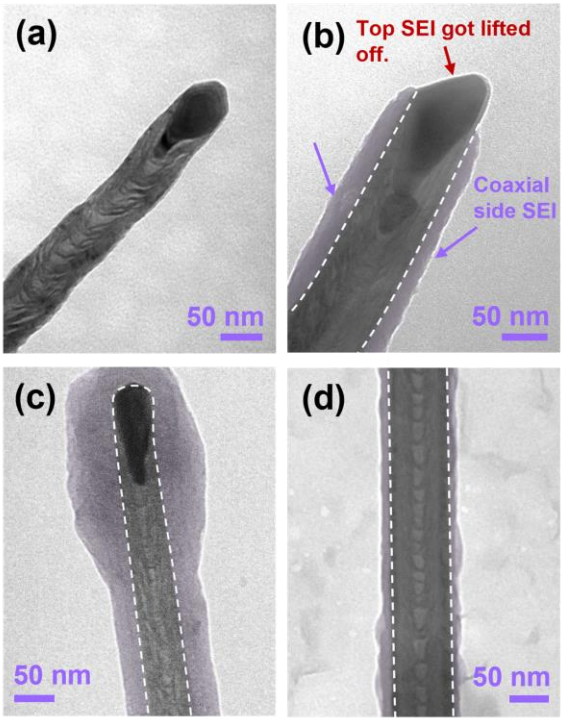

Figure 2.5. Cryo-TEM images of VACNFs scraped off from the electrodes (a) in the pristine condition, (b) after Li intercalation, (c) after plating with 2.0 mAh/cm^2 of Li at 1.0 mA/cm^2, and (d) after completely stripping of plated Li at 1.0 mA/cm^2. Reprinted (adapted) from *Carbon*, 212 (2023), 118174. Copyright 2023 Elsevier Ltd.

The insights gained so far are schematically illustrated in Figure 2.6. XPS and cryo-TEM measurements revealed the existence of two different types of SEIs during the Li intercalation stage, including (i) top SEI and (ii) side SEI. The top SEI is rich in organic moieties due to incomplete decomposition of electrolyte while the side SEI is rich in inorganic lithium compounds. The top SEI blankets the VACNFs array while the side SEI forms a coaxial sheath uniformly wrapping the individual VACNFs. Spectroscopic data from in-situ Raman and electrochemical data showed that the outer layer of VACNFs were lithiated, making it lithiophilic that favored the lithium nucleation in the following Li electrodeposition. The lithiation and delithiation processes occur reversibly without damaging the structural integrity. During Li plating, e-Li grows into two

different morphologies, (i) infiltrative e-Li and (ii) nanoscale e-Li, along with the formation of a new SEI on the e-Li surface that is rich with inorganic lithium compounds. Infiltrative e-Li exhibits a dense, non-porous, micron-scale columnar structure infiltrating the pore volume between VACNFs. A small amount of e-Li exists in the interstitial area between the infiltrative e-Li grains, as nanoscale Li deposits coaxially around the individual VACNFs. During Li stripping, the infiltrative e-Li leaves behind irreversible SEI skins loosely attached to the VACNF arrays. The SEI of nanoscale e-Li is also rich with inorganic compounds but behaves as an elastic sheath coaxially wrapped around individual VACNFs.

2.3.5 FESEM Imaging of VACNF/Cu After Li Plating/Stripping Cycling

The morphology of VACNF/Cu electrodes after Li plating/stripping cycling was studied using FESEM. Due to the irreversible and dynamic nature, a large amount of infiltrative e-Li's SEI skins formed in previous stripping cycles started to accumulate on top of the VACNF arrays (Figure A.26). As shown in Figures A.27a to A.27c, at the end of 50 cycles, the e-Li's SEI completely covered the top surface of VACNF/Cu electrode. The accumulated SEI skins are likely dominated by the top SEI and e-Li SEI that broke off from the electrode during Li stripping. The irreversible shedding of SEI skins not only consumes electrolyte, but also affects the accessibility of graphitic edges of VACNFs for Li nucleation in the subsequent cycles and increases the tortuosity of the electrode.[197] This is well reflected in the electrochemical performance where an increase in the Li plating/stripping overpotential was observed towards the end of the cycle life. In comparison, even thicker layers of dead Li mixed with SEI skins were observed in cycled planar Cu electrodes (Figures A.27d to A.27f). Continuous consumption of lithium nitrate additive and its exhaustion leading to changes in morphology of lithium were also observed.[45, 50] These led to

the highly nonuniform optical image in Figure A.27d. From this, it can be concluded that accumulation of dead Li and SEI and electrolyte consumption were the primary reasons for the failure of planar Cu electrodes. These are reduced but not eliminated in 3-D nanostructured electrodes such as VACNF arrays. Further studies to quantify SEI and dead Li, and understand their evolution are necessary to develop mitigation solutions. Nevertheless, a common observation of both cycled VACNF/Cu and planar Cu electrodes is the high degree of heterogeneity in multiscale. Development of 3-D host structures that can facilitate formation of stable SEIs is critical for commercialization of Li metal anodes.

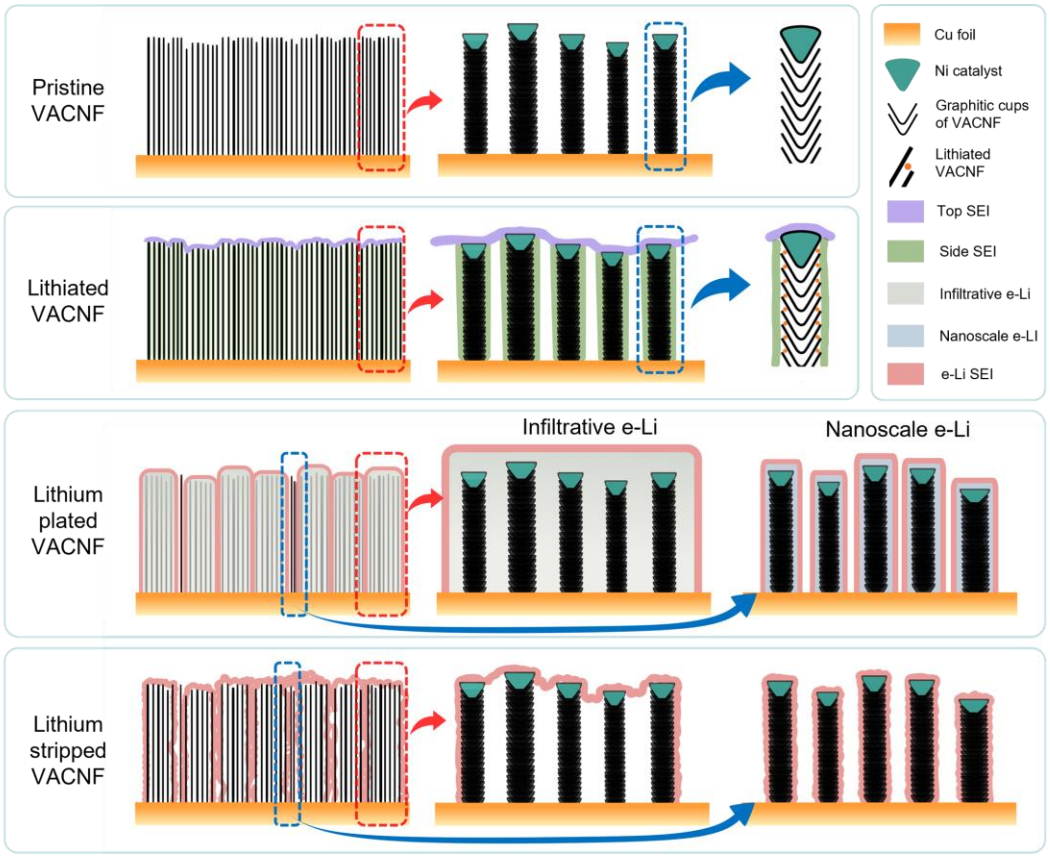

Figure 2.6. Schematic to illustrate the structure of SEI formed during Li intercalation, Li plating/stripping and the morphology of electrodeposited Li on VACNF/Cu electrode. Reprinted (adapted) from *Carbon*, 212 (2023), 118174. Copyright 2023 Elsevier Ltd.

2.4 Conclusion

VACNF array electrodes are employed as a model 3-D conductive host to understand the critical issues toward future LMAs. The fundamental issues, such as the structure of SEI and the morphological evolution of Li deposition, during the lithium plating/stripping processes were studied with various spectroscopic and microscopic techniques. At electrode potentials positive to Li^+/Li, lithium intercalation and deintercalation occur at the VACNF sidewall in a reversible manner without disrupting its structure. The lithiation makes the VACNFs more lithiophilic which favors subsequent lithium plating. During electrodeposition onto the VACNF/Cu electrode, lithium grows into two different morphologies - the micron-scale columnar infiltrative Li and the nanoscale coaxial Li sheath. Reversible lithiation/delithiation and Li plating/stripping were observed in situ based on the D and G bands of graphitic carbon and the Raman band of lithium acetylide, respectively. The high performance of VACNF/Cu as a LMA host is attributed to the combination of the low surface area of solid infiltrative Li grains and the stable SEI on the surface of nanoscale Li. Depth profiling XPS revealed the formation of two types of SEIs at the Li intercalation stage, i.e., a continuous organic rich SEI film loosely attached to the top surface of the VACNF array and an inorganic rich coaxial SEI sheath around individual VACNFs. During Li plating, they were both transformed into an inorganic phase rich SEI directly on the surface of the electrodeposited lithium. After stripping Li, loose SEI skins from the infiltrative Li grains were left loosely on the VACNF array and started to accumulate during cycling while the coaxial SEI on the nanoscale Li remained as a stable elastic sheath. The loose SEI skins were the main factor for electrolyte consumption and increased heterogeneity, eventually leading to cell failure. Though 3-D hosts enhance the performance of LMAs proving to be a promising route for suppressing dendrite formation, other challenges, such as continuous electrolyte consumption, need to be

overcome. Further developments in terms of host structure design, surface modification and electrolyte additive optimization are needed to improve the uniformity of lithium nucleation and to achieve stable, robust SEIs during cycling are essential to realize viable 3-D LMAs. These results provide useful insights to guide in the future design and development of 3-D host structures for long-life LMAs. For 3-D hosts similar to VACNF/Cu, application of preformed artificial SEIs or in-situ formed SEIs with high Li^+ conductivity and mechanical/chemical stability during cycling need to be further studied to develop better solutions. Other approaches such as enhanced lithiophilicity by surface treatment might also be adopted for similar low tortuous 3-D hosts towards high performance LMAs.

Chapter 3 - Deciphering the Effect of Nucleation/Growth Kinetics on the Morphology of Li Plating/Stripping on Vertically Aligned Carbon Nanofibers - a Low-Tortuosity 3-D Nanostructured Carbon Host

Reprinted (adapted) from *Chemical Engineering Journal*, 484 (2024), 149515.

3.1 Introduction

High energy density batteries are essential for achieving the decarbonization goals in the transition to clean energies and for meeting future energy demands.[198] Lithium metal is considered as the holy grail of anode materials for next-generation high energy density batteries owing to its highest theoretical charge storage capacity (3860 mAh/g) and the lowest redox potential (-3.04 V vs. SHE). LMA when paired up with high Ni-NMC cathodes (>200 mAh/g) or high-capacity cathodes such as sulfur or oxygen, enables the potential development of batteries with energy densities greater than 500 Wh/kg, significantly surpassing the 350 Wh/kg limit of today's LIBs.[199, 200] Among all possible configurations of rechargeable LMBs, the anode-free LMBs offer the highest possible theoretical energy density as it does not involve excess lithium, which also lowers the manufacturing cost and improves the safety in operation.[201-204] Since electrodeposition (or plating) of lithium on the current collector is the key process during the charging step, it is critical to develop a deeper understanding on the lithium nucleation and growth on the current collector. The properties of electrodeposited lithium and the LMA performance are found to strongly depend

on the nature of current collector, electrolyte, operating conditions, and plating/stripping parameters.[45, 205-209]

Among the influential parameters, the applied current density *j* has been found to be a key variable since it regulates the rate of reduction of Li^+ ions to Li metal. Several studies on planar copper current collectors have demonstrated that the microscopic morphology strongly depends on the plating current density *j*.[210-214] In general, the Li nuclei density N_n increases with the magnitude of *j* following the classical nucleation and growth theory.[210-214] The plated Li tends to form sparsely distributed large irregular Li nuclei when it is deposited at low *j* but to form densely populated and more uniform Li particles of smaller sizes at high *j*. On the other hand, macroscopic electrochemical studies have indicated that the electrodeposited Li is more reversible and stable at low *j*, possibly due to the lower concentration gradient and more homogeneous electric field distribution.[149, 215, 216] The formation of dendritic Li structures is accelerated when the Li^+ ion concentration depletes at the anode surface. The average time that it takes for the dendrites to start growing is represented by the Sand's time t_{Sand}[36] which increases as the *j* is reduced. The microscopic and macroscopic studies seem to point the opposite directions in how to reduce Li dendrite growth by regulating the plating current density *j*. Since dendrite growth during charging or lithium electrodeposition is one of the critical issues limiting the development of LMAs,[24, 38, 217] it is important to unravel the hidden connections between the seemingly controversial macroscopic and microscopic observations and develop new mitigating strategies.

Several approaches, such as modification of the current collector, electrolyte and operating parameters, have been successfully developed to mitigate dendrite growth and enhance the CE and cycle life.[218] The use of high-surface-area 3-D hosts was found to be effective in delaying the dendrite formation, which was attributed to the reduced local current density *j* and the

homogenized electric field compared to those on the planar electrodes.[128, 219-221] The lower *j* apparently increased the Sand's time t_{Sand} and delayed the onset of dendrite formation. However, this will make the microscopic morphology of the plated Li more heterogeneous, as predicted by the nucleation and growth theory validated on the planar electrodes. It is expected that the 3-D hosts will induce lower nucleation density (i.e., lower surface coverage) and larger grain sizes due to the lower local current density. But the microscopic morphology of Li plating onto the 3-D hosts and how it changes vs. the plating current density *j* have not been well studied so far. This is challenging since most studies on 3-D host materials employed random porous structures, making it difficult to reveal the microscopic structure of the Li infiltrated into the hosts. In fact, even on planar electrodes, two different morphologies of Li have been reported under the similar conditions of electrodeposition, i.e., at $j \leq 0.1$ mA/cm^2 in the standard ether electrolyte (1.0 M LiTFSI in DOL and DME (v/v 1:1) with 1 wt% $LiNO_3$ additive).[182, 210, 222] Pei et al.[210] and Huang et al.[222] observed island-like Li growth while Park et al.[182] observed fibrous Li growth on planar copper electrodes. The island-like Li growth with a low surface area and low porosity is a desired morphology as it can be stripped more efficiently leaving less dead lithium and SEI. In contrast, fibrous Li is more prone to form dead Li due to the higher probability for breaking off the Li fibers during the non-homogeneous stripping.[42, 205] In addition, the higher aspect ratio and larger exposed surface area of fibrous Li would increase the electrolyte consumption due to the repeated SEI formation. It is critical to looking into these issues in 3-D hosts in order to develop reliable LMAs.

In this study, we aim to systematically explore the impact of the Li electrodeposition rate on the morphology of resulting Li deposits on a brush-like 3-D host based on VACNFs grown on Cu foils. VACNFs are N-doped graphitic carbon fibers grown by PECVD.[223] They have a unique internal structure consisting of conically stacked graphitic cups along the axis (commonly referred

to as bamboo-like MWCNTs. The side-wall surface of VACNFs is composed of electrochemically active graphitic edges which are spontaneously oxygenated in the air. In our previous studies, we have demonstrated that the VACNF/Cu can serve as an effective 3-D carbon host to enhance the stability and reversibility of LMAs.[128, 224] Given its desirable properties such as the high porosity (~80%), vertically aligned pore structure and the lithiophilic surface, VACNF/Cu electrode serves as a model 3-D host for this study. Its well-defined vertical structure allows the observation of the microscopic morphology of infiltrated Li at different stages of Li plating and stripping.

We first demonstrate that a higher pressure between the electrode/separator stack inside the coin-cells tends to induce densely packed Li morphology, as reported in literature.[204, 205, 225-227] The non-uniform internal pressure distribution and varied pressure among different coin cells may be the cause for discrepancies among literature. By consistently controlling the coin cell with a minimal pressure, we were able to investigate the intrinsic effect of the plating current density on the microscopic morphology of Li metal plated on both planar Cu and 3-D VACNF/Cu electrodes. The 3-D VACNF/Cu electrode clearly showed superior stability and improved reversibility in continuous plating/stripping cycling tests. Our results unraveled the drastic change in Li morphology vs. the plating current density on both electrodes, following the classical nucleation and growth theory. Though lowering the local plating current density with the VACNF/Cu electrode exhibited enhanced stability in cycling tests, the formation of large irregular Li grains with the long noodle-like morphology poses a concern for dendrite growth and safety in practical LMBs that require much longer cycling lives. To our surprise, electrochemical characterization showed that the stripping current density also affected the electrode performance. By decoupling the plating and stripping current density at different values, the performance can be optimized by balancing the macroscopic electrochemical observation and microscopic morphology during Li

plating/stripping. This study provides new insights for further development of host structures and charge/discharge protocols for achieving the best LMA performance.

3.2 Materials and Methods

3.2.1 Chemicals and Materials

Electrolyte (1.0 M LiTFSI in DOL/DME (1:1, v/v) with 1 wt% LiNO3 additive) was purchased from Dodochem Limited (Suzhou, China). Copper foils (99.999 %) were purchased from Fisher Scientific (Hampton, NH) and GoodFellow Corporation (Pittsburgh, PA). Li foil, CR2032 coin cell casings, spacers, and wave springs were purchased from MTI Corporation (Richmond, CA). Celgard 2400 separator was purchased from Celgard (Charlotte, NC).

3.2.2 Preparation of VACNF/Cu Electrode

An 84 µm thick copper foil was used as the substrate for the growth of VACNFs. A 300 nm thick Cr barrier layer and a 30 nm thick Ni catalyst layer were sputter coated using a high-vacuum Perkin Elmer 4400 series magnetron sputtering system at UHV Sputtering Inc. (Morgan Hill, CA). VACNFs were grown using a DC-biased PECVD unit (Black Magic, Aixtron, CA) following the same procedure reported in previous studies [127, 128, 172, 228, 229]. In brief, the substrate was heated to 500 °C at a rate of 200 °C/min with ammonia gas at a flow rate of 250 sccm, at a pressure of 3.9 Torr. Under these conditions, a DC plasma at 510 V and 40 W was applied for 60 s to dewet and break the Ni film into randomly distributed Ni nanoparticles. Then, the temperature was increased to 750 °C at a rate of 250 °C/min while 70 sccm acetylene gas was introduced as the carbon precursor along with ammonia, the etching/reducing gas to give a steady-state pressure of 4.8 Torr. The process was continued for 90 minutes to grow 15 µm long VACNFs on Cu. For

some experiments, we used VACNFs of 15 μm length, grown for 120 minutes on 100 μm thick copper foil, with a 100 nm thick Cr barrier layer and a 24 nm thick Ni catalyst layer.

3.2.3 Materials Characterization

The morphology of the electrodes was studied using Topcon/ISI/ABT DS 130F FESEM (Akashi Beam Technology Corporation, Tokyo, Japan) and Helios NanoLab 660 (FEI, OR) with a FIB milling functionality. To image the electrodes after lithium plating/stripping, they were harvested from coin-cells by disassembling in an Ar-filled glovebox. The harvested electrodes were washed by immersing in DME several times. After drying in the antechamber of glovebox under vacuum, the FESEM samples were prepared back inside the glovebox. The prepared samples were then stored in a tightly sealed container filled with ultrapure Ar. The samples were only exposed to the ambient air for a few seconds during the transfer from the sealed container to the sample stage of the FESEM. Before FIB milling, a 2 μm thick Pt layer was deposited to protect the underneath structure from ion beam damage. The morphology of individual VACNFs was imaged using a Philips CM 100 TEM at a 100 kV acceleration voltage in the low dose mode at -175 °C using a Gatan cryo-holder. The VACNFs were transferred to TEM grids by scraping them from the electrode inside a glovebox. The TEM grids were stored in Ar-filled storage holders and plunged in liquid nitrogen without exposure to the air. This was followed by transferring the TEM grid to the cryo-holder using a cryo-station. The cryo-shield was used to prevent the sample from exposure to the air during the transfer from cryo-station to TEM.

3.2.4 Electrochemical Characterization

VACNF/Cu or planar Cu foil electrodes of 15 mm in diameter were used as the working electrode to assemble half-cells using CR2032 casings. A 25 μm thick Celgard 2400 and a 0.60 mm thick Li foil were used as the separator and counter electrode, respectively. A 0.3 mm thick stainless steel wave spring (1.4 mm height) and two pieces of 0.2 mm thick stainless-steel disk spacers were used as mechanical supports to provide consistent pressure and good contact between the components. Cell assembly was done using an MTI hydraulic crimping machine by applying ~750 psi pressure. The Li foils were polished using 200 and 400 grit sandpapers before assembling. 250 μL of 1.0 M LiTFSI in DOL/DME (1:1, v/v) solvent with 1 wt% $LiNO_3$ additive was used as the electrolyte. The half-cells were assembled in an argon-filled glovebox (Mbraun MB10 Compact, Stratham, NH) with oxygen and water levels below 0.5 ppm. To visualize the internal pressure inside coin cells, Fujifilm Prescale films (4LW, 3LW, 2LW, and LW) covering a range of pressures from 7.2 to 1400 psi were used in dry dummy cells with different compression % (see details in Fig. S2 and the following text descriptions in SI). The assembled half-cells were tested using a battery testing system (Neware, Shenzhen, China) at room temperature. Five cycles of Li intercalation/deintercalation at 50 μA were applied between 0.0 V and 1.0 V (vs. Li^+/Li) before Li plating to activate the electrode. For the plating/stripping cycling tests, a capacity of 2.0 mAh/cm^2 was employed. The upper cut-off voltage for Li stripping was 1.0 V vs Li^+/Li. The CE was determined by the ratio of the capacity of Li stripped to the capacity of Li plated, and it is expressed in percentage.

3.3 Results and Discussion

3.3.1 Preliminary Characterization

Figure 3.1a illustrates the opposite trends of Sand's time (t_{Sand}) and nucleation rate (ν_n) vs. the plating current density j. Sand's time is defined as the time that it takes for the Li^+ ion concentration to deplete at the anode surface leading to the onset of ramified electric field and growth of dendrites. The relationship between t_{Sand} and the current density j is outlined in Equation 3.1:[230]

$$t_{Sand} = \pi D_e \left(\frac{z_c C_0 F}{2 j t_a}\right)^2 \quad \text{..... (3.1)}$$

where D_e is the effective diffusion coefficient, z_C is the charge of cation (+1 for Li^+ ion), C_0 is the Li^+ concentration in the bulk electrolyte, and t_a is the anion transference number. Sand's time is inversely proportional to j^2. Thus, with the use of high-surface-area 3-D current collectors, the decrease in local current density helps to extend the Sand's time compared to planar electrodes and hence delay the onset of dendrite growth. However, the decrease in j also reduces the nucleation overpotential η_n, the driving force for Li nucleation and growth, leading to decrease in the nucleation rate ν_n following Equation 3.2:[231]

$$\nu_n \propto \exp\left(\frac{-1}{log^2 j}\right) \quad \text{..... (3.2)}$$

Associated with this, the nucleation density N_n also drastically decreases as j is reduced.[210]

Based on literature, it is commonly accepted that the electrodeposition of lithium at low current densities leads to growth of large inhomogeneous islands without dendrite formation. While most studies in literature focused on the homogeneity of the electric field which is superior at low current densities, the impact of the nucleation rate ν_n and nucleation density N_n are often overlooked.[215] The nucleation process is critical for lithium electrodeposition since it occurs

rapidly within the short time at the beginning of electrodeposition and the further growth mainly occurs at the nucleated sites rather than forming fresh nuclei on the uncovered surface.[232] Given that 3-D current collectors inherently offer a lower local current density, it is expected that the nucleation density N_n will be further reduced, which will significantly affect the morphology of Li plating.

VACNF/Cu consists of a well-defined brush-like structure as shown in Figure 3.1b. The TEM image (Figure B.1) of a representative VACNF shows the unique conically stacked graphitic cup structure under an inverse tear-drop-shaped Ni nanoparticle catalyst at the tip. This unique structure provides abundant electrochemically active graphitic edges exposed on the sidewall surface. The structure and characteristics of VACNF/Cu electrode was thoroughly studied and documented in our previous reports.[127, 128, 224, 228, 229] The average diameter of the VACNFs used in this study was ~154 nm and the length was controlled as ~ 14 µm. Based on their high aspect ratio and density (~ 1 x 10^9 fibers/cm^2), it was estimated that the VACNF array provides ~70 times higher surface area than a planar current collector. The individual VACNFs were perpendicular to the copper substrate and were well separated from each other by about 100 – 300 nm, resulting in a low-tortuosity structure with a high porosity of ~ 79%. The VACNFs were found to be inherently doped with 7.3 at% of N across the whole CNF and 2.9 at% of O functionalized at the sidewall surface, which improved their lithiophilicity.[128, 224] These properties are desired to enhance the performance as a conductive 3-D host for LMAs as demonstrated in our previous studies.[128, 224]

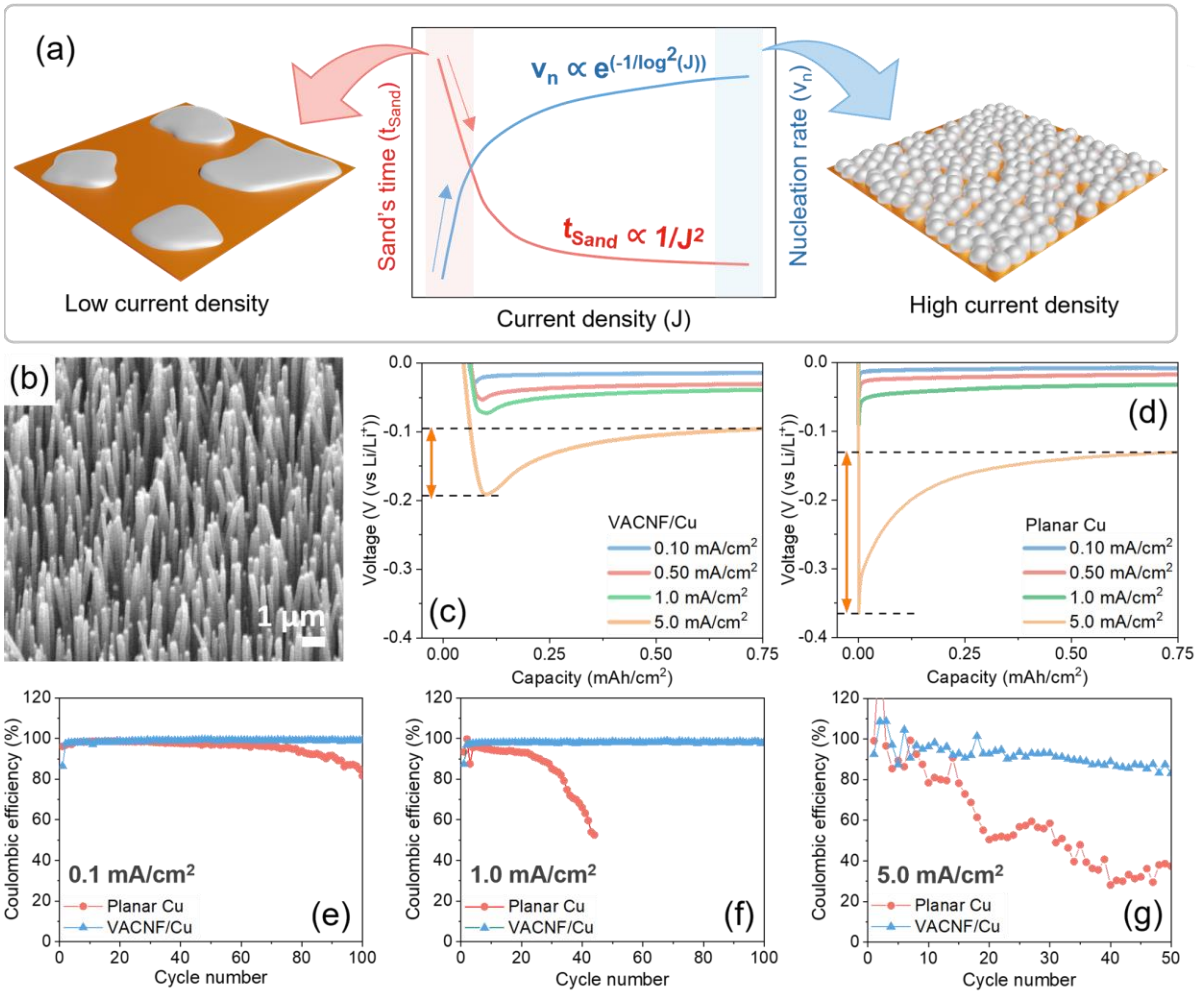

Figure 3.1. (a) Schematic illustration of the opposite trends of Sand's time t_{Sand} and nucleation rate v_n vs. the Li plating current density j. (b) A 30° perspective view FESEM image of the pristine VACNF/Cu electrode. Li plating voltage curves at different current densities for (c) VACNF/Cu and (d) planar Cu electrodes. The coulombic efficiency during plating/stripping cycling of VACNF/Cu and planar Cu electrodes with a Li plating capacity of 2.0 mAh/cm^2 at the symmetric plating/stripping current density of (e) 0.1 mA/cm^2, (f) 1.0 mA/cm^2, and (g) 5.0 mA/cm^2. Reprinted (adapted) from *Chemical Engineering Journal,* 484 (2024), 149515. Copyright 2024 Elsevier Ltd.

Figures 3.1c and 3.1d show the typical galvanostatic voltage curves of the first Li plating step for VACNF/Cu and planar Cu electrodes, respectively, at different current densities. For the planar Cu, a sharp voltage dip was observed during the electrodeposition, indicating the fast nucleation of Li without any intercalation/alloying. In the case of VACNF/Cu, the voltage dip was

delayed to appear at the capacities of ~ 0.080 to 0.10 mAh/cm^2 due to partial Li intercalation into the graphitic structure of VACNFs, as reported in our previous studies.[128, 224] With the increase in plating capacity, the voltage increased and formed a plateau with lower overpotentials, indicating reaching the steady-state Li growth limited by mass transport of Li^+ ions from the bulk solution. From these curves, lithium nucleation overpotentials (η_n) were calculated as the potential difference between the lowest voltage dip and the following plateau. The η_n was found to increase with the current density, consistent with Butler-Volmer kinetics. For VACNF/Cu, the η_n was observed to be 13.6, 23.0, 33.8 and 95.2 mV for the current density of 0.10, 0.50, 1.0 and 5.0 mA/cm^2, respectively. Conversely, for planar Cu, the η_n was found to be 33.6, 44.3, 58.6 and 234.3 mV for the same respective current densities. It is evident that the magnitude of η_n was significantly smaller in 3-D VACNF/Cu than that of planar Cu electrode at all the tested current densities. This can be attributed to the lithiophilic nature and the high surface area of VACNF/Cu electrodes.[224]

For further characterization, conventional symmetric plating/stripping cycling tests[144, 145] were performed on VACNF/Cu and planar Cu electrodes at varied current densities (Figures 3.1e – 3.1g) with the plating and stripping current set at the same values. At the low current density with j = 0.10 mA/cm^2, the cycling performance was relatively stable and lasted longer for both VACNF/Cu and planar Cu electrodes. VACNF/Cu exhibited a stable CE averaging around 98.8% for 100 cycles, which is equivalent to 4000 hours of cycling time. For the planar Cu, the CE declined to 81.5% after 100 cycles. Under a higher cycling rate with j = 1.0 mA/cm^2, the average CE slightly dropped to around 98.0% for VACNF/Cu and the electrode was able to maintain a stable performance for 100 cycles. In comparison, the planar Cu failed quite early, with the CE dropped to 74.8% after 35 cycles. With further increase in the current density to j = 5.0 mA/cm^2, the performance of the planar Cu further degraded rapidly from the beginning of the cycling. The

VACNF/Cu exhibited a better performance in comparison to the planar Cu, but its CE decreased from ~ 100% to ~ 83% after 50 cycles along with much larger variations in each cycle. The observed declining trend in CE and stability vs. the plating/stripping rate is consistent with other reports[233-235] and the prediction by the Sand's equation (Equation 3.1). From these results, it is concluded that the 3-D VACNF/Cu performs better than planar Cu at all cycling rates, which can be attributed to its 3-D conductive structure with superior lithiophilic nature to reduce Li dendrite formation. Here we focus on further study of the microscopic morphology of Li plating, which underlies the observed macroscopic performance enhancement in CE and cycle life.[128, 224]

3.3.2 Effect of Plating/Stripping Kinetics on Li Morphology

3.3.2.1 Effect on Li Morphology by the Internal Pressure on the Electrode Surface

Our goal is to carry out morphological analysis to understand how the current density affects the structure of Li plating and its correlation on the cell performance. However, it is known that the morphology of electrodeposited Li strongly depends on the pressure inside the cells.[205, 236] The discrepancies in morphology in literature are largely attributed to the uncontrolled pressure or nonuniform distribution of the pressure inside the cell.[237, 238] Figure B.2 illustrates the internal configuration of the coin-cells used in this study. As revealed by the optical image of a pressure-sensitive film (Prescale film by Fujifilm) used in a dry dummy coin-cell, the pressure distribution inside the cell is highly nonuniform (Figure 3.2a). A higher pressure was applied around the periphery than that at the center of the electrode disk. The morphological analysis of the electrode across its diameter was applied after plating 0.20 mAh/cm^2 of Li on the planar Cu disk at 0.10 mA/cm^2. The SEM images revealed that the plated Li had distinct morphologies at different locations. At the center of the electrode, the Li showed whisker or fibrous shapes (Figures 3.2b

and 3.2c) similar to the observation by Park et al.[182] But at the spot close to the periphery, larger flat irregular Li islands were observed (Figures 3.2d and 3.2e), consistent with the report by Pei et al.[210] To further validate the pressure effect, studies were conducted by constructing coin-cells with increased internal pressure. Optical images of pressure-sensitive films with different internal pressures are shown in Figure B.3. With increase in compression% (as described in Appendix B), the magnitude of internal pressure increases in both center and periphery but maintaining the non-uniform pressure distributions in coin-cells. The morphologies of Li plated at 0.10 mA/cm^2 up to 0.75 mAh/cm^2 capacity were examined at four different spots from the center to the edge of the planar Cu disk electrode. Figures B.4b – B.4i were from a coin-cell with 16% higher compression (see description in Appendix B) which show a clear lateral expansion in the boundary of flat Li islands when moving from center to the edge. Interestingly, the compressed islands show darker contrast in SEM images, reflecting the dense and more conductive Li metal grains while the uncompressed Li structures at the center show brighter features in SEM images. With further increase to 38% higher compression, flat Li islands could be observed at all spots from the center to the edge of the electrode along with the presence of some fibrous Li at the island boundaries (Figures B.4j – B.4q). The fraction of compressed flat Li islands increases when moving from the center to the edge. Clearly, the higher pressure causes formation of flat Li islands while the lower pressure leads to the intrinsic fibrous Li morphology. Such transformation from porous Li structures into dense compact structures under high pressures has also been observed in different electrolytes.[226, 236] Our study confirmed the elastic deformation of Li deposits by pressure in the ether electrolyte that is commonly used for Li-S batteries. To exclude the pressure effect and examine the intrinsic morphology of Li plating, the following studies are carried out using the

coin-cell configuration shown in Figure B.2 and focused on the spots at the center of the electrode which has the minimal internal pressure.

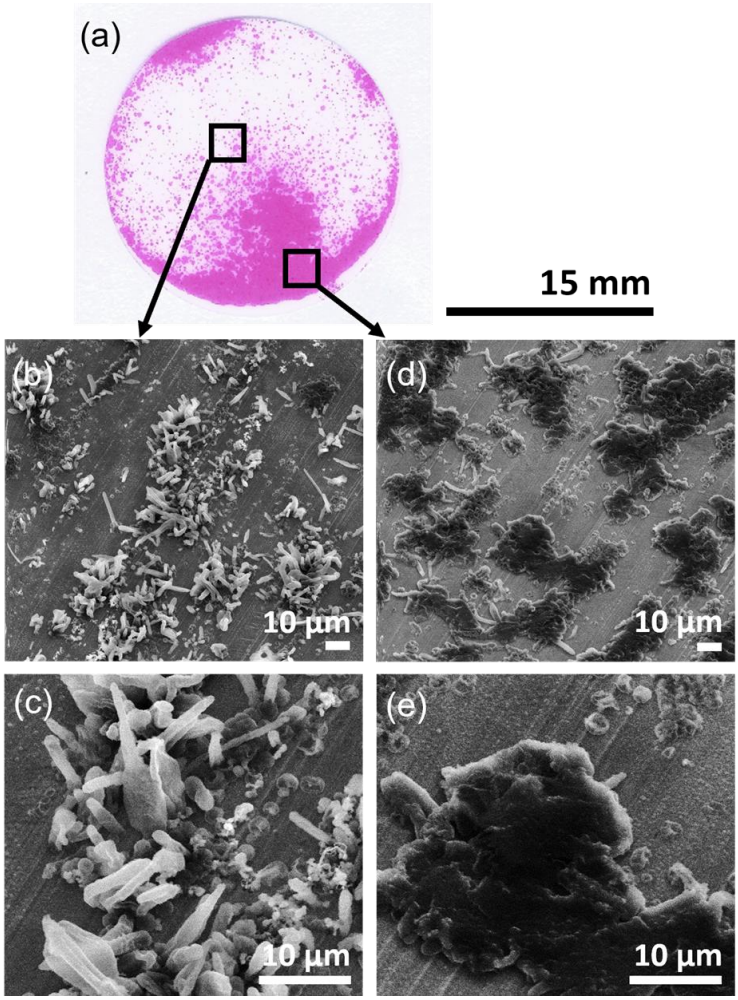

Figure 3.2. (a) Optical image of a developed Prescale film showing the pressure distribution inside the coin cell configuration shown in Figure B.2. The 30° perspective view FESEM images of a planar Cu electrode plated with 0.20 mAh/cm^2 Li at 0.10 mA/cm^2 which are imaged at (b) & (c) center and (d) & (e) periphery of the electrode. Reprinted (adapted) from *Chemical Engineering Journal*, 484 (2024), 149515. Copyright 2024 Elsevier Ltd.

3.3.2.2 Effect on the Morphology by Li Plating/Stripping Kinetics on Planar Cu

Figure 3.3 shows the FESEM images of Li electrodeposited on planar Cu electrodes under different current densities (0.10, 1.0 and 5.0 mA/cm^2) up to varied plating capacities (0.20, 0.75 and 2.0 mAh/cm^2). As shown in Figures 3.3a – 3.3c, at the low current density of 0.10 mA/cm^2, the plated Li mainly presents as long fiber-like structures (about 1.5 mm in diameter and 3 to 20 mm in length) mixed with a small number of Li spheres of 1.7 mm in size (as highlighted by the blue arrows). Figures B.5a & B.5b further show that the initial Li plating at the low capacity formed sparse nonuniformly distributed fibrous particles with Li nucleation clustered in some spots while a large portion of bare Cu surface is uncovered. As the plating capacity was increased, the diameter and length of fiber-like Li continued to increase while the size of Li spheres only increased slightly (Figure B.6). The inhomogeneous growth rate on the different Li nuclei is probably due to the inhomogeneous electric field at different Li structures. Close to the periphery of the electrode, instead of fiber-like Li, larger smooth island-like Li deposits were present due to higher pressure at the electrode surface (Figure B.7). Closer observation of these Li islands revealed that they consisted of individual Li fibers that merged into the large flat islands (Figure B.7). Some long fibers can be seen at the boundaries of the Li islands. Similar grain boundaries were observed by Pei et al. as well.[210] After completely stripping the 0.75 mAh/cm^2 of Li plated at 0.10 mA/cm^2 and 1.0 mA/cm^2, respectively, clusters of dead Li and SEI skins were observed (Figure B.8). Their scarce distribution is consistent with the low nucleation density at 0.10 mA/cm^2 plating current density.

When the plating current density was increased to 1.0 mA/cm^2, the density of Li particles significantly increased, leaving a much smaller bare Cu surface area. The electrodeposited Li was dominated by spherical morphology (~ 1.6 mm in diameter) with a smaller proportion of fiber-like

Li (Figure 3.3d – 3.3f). Figure B.9 shows that the spherical Li particles stack to form multiple layers. When the capacity was increased to 2.0 mAh/cm^2, further growth led Li particles to merge and form larger Li microcolumns (~2.7 mm in diameter) (Figure B.3f). Upon completely stripping at the same current density (1.0 mA/cm^2), dense dead Li/SEI structures with the irregular shapes of 0.6 to 3.7 mm in size were left on the Cu surface (Figure B.10), consistent with the dense Li nucleation sites when it was plated at 1.0 mA/cm^2.

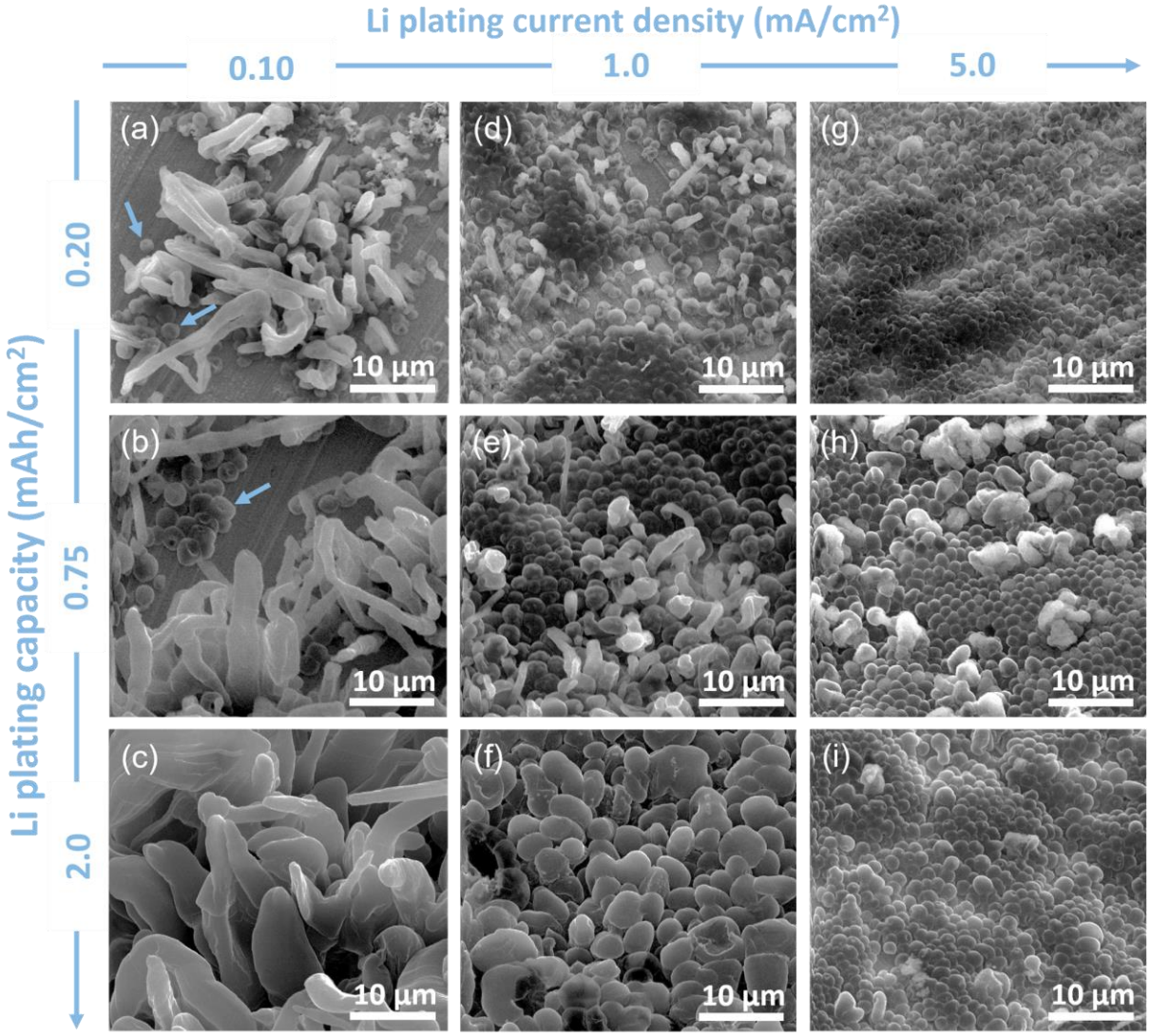

Figure 3.3. The 30° perspective view FESEM images of electrodeposited Li on planar Cu electrodes at different current densities up to various plating capacities. Reprinted (adapted) from *Chemical Engineering Journal,* 484 (2024), 149515. Copyright 2024 Elsevier Ltd.

A similar morphology of stacked spherical particles was observed when the current density was further increased to 5.0 mA/cm^2. But the particle size was reduced to ~ 1.0 mm in diameter while the Cu surface was fully covered (Figures 3.3g – 3.3j). When they were stripped completely at 5.0 mA/cm^2, a large amount of dead Li was observed as densely stacked spherical particles (Figures B.11a – B.11c). At areas where they got stripped more effectively, crumbled SEI remnants with circular outlines were found. However, when the stripping current density was reduced to 1.0 mA/cm^2, most spherical dead Li particles were removed (Figures B.11d – B.11f). Clearly, not only the plating current density but also the stripping current density is critical for the LMA performance. The application of a high stripping current density of 5.0 mA/cm^2 resulted in highly unstable cycling performance. It can thus be concluded that the inefficient stripping could be the cause for poor plating/stripping cycling performance of planar Cu at the high current density of 5.0 mA/cm^2 (Figure 3.1g) compared to those at the lower current densities (Figures 3.1e and 3.1f). Similar findings were observed by other researchers as well.[42] However, contrary to common assumptions, among the tested conditions, the homogeneity in Li nucleation and growth is poor at the low current density of 0.10 mA/cm2.[210, 216, 239, 240] Despite the heterogeneous growth, the use of low current density for the stripping step during CE cycling helps to achieve a relatively more stable performance, partially mitigated the impact of the electrodeposited lithium morphology. This illustrates that more attention should be given to microscopic nucleation kinetics in addition to the macroscopic battery tests.

3.3.2.3 Effect on the Morphology by Li Plating/Stripping Kinetics on 3-D VACNF/Cu

Figure 3.4 shows the FESEM images of Li electrodeposited at different current densities on the 3-D VACNF/Cu electrodes. When electrodeposition was done at 0.10 mA/cm^2, sparsely

distributed vertical Li microcolumns (or micropillars) of ~ 5.5 μm in diameter and height up to ~35 μm were observed even at a very low plating capacity of 0.20 mAh/cm^2 (Figures 3.4a, B.12a). An approximately equal number of darker recessed micro-spots were also observed in Figure B.12a, corresponding to the dense Li micro-grains infiltrated in the VACNF arrays. In the space between the bright protruding Li microcolumns and darker dense infiltrated micro-grains, the VACNF array is dominated by brush-like structure (Figure B.12b) similar to the pristine VACNF arrays (Figure 3.1b). As described in our previous study,[224] the fact that the VACNF array can maintain the vertical structure without collapsing into micro-bundles indicates that each VACNF is coaxially coated with nanoscale lithium or SEI sheaths which enhances its mechanical strength against the applied pressure in the coin-cell and the capillary forces exerted by the liquid electrolyte and the solvent during cell assembly/disassembly and rinsing processes. A detailed discussion on the coaxial Li/SEI coating is presented in a later section with TEM studies.

With further plating to 0.75 mAh/cm^2, the protruding microcolumns quickly grew in length, eventually folded along kinks into noodle-like structures on top of the VACNF array (Figures 3.4b, B.13a and B.13b). Further growth was witnessed as the plating capacity was increased to 2.0 mAh/cm^2. The diameter of the Li fiber also increased to ~ 8.0 μm during this process but at a rate much slower than the increase in the length. On the periphery, due to higher internal pressure, dense Li islands were observed (Figures B.13c and B.13d). As shown in Figure B.14, when completely stripped at 0.10 mA/cm^2, collapsed thin SEI skins from the surface of the noodle-like Li structure were left behind.

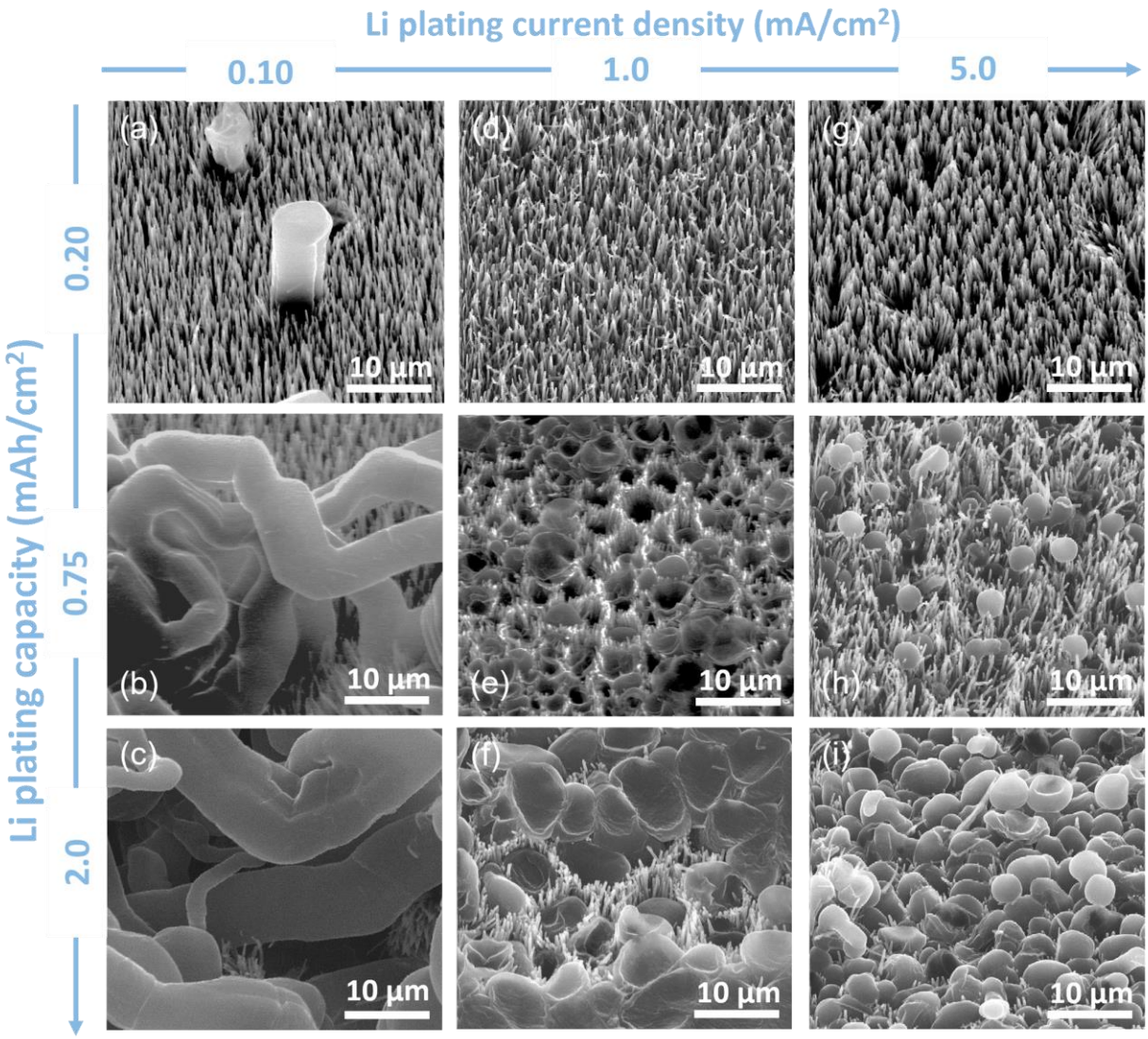

Figure 3.4. The 30º perspective view FESEM images of electrodeposited Li on VACNF/Cu at different current densities up to various plating capacities. Reprinted (adapted) from *Chemical Engineering Journal,* 484 (2024), 149515. Copyright 2024 Elsevier Ltd.

When the plating current density was increased to 1.0 mA/cm^2, the growth of tall Li microcolumns was significantly suppressed (Figure 3.4d). The plated Li at the low capacity (0.20 mAh/cm^2) was dominated by coaxial Li sheath around each VACNFs (Figures 3.4d and B.12c). At the plating capacities was increased to 0.75 mAh/cm^2, smaller (~ 3.0 - 4.9 μm in diameter) and shorter Li microcolumns were formed inside the VACNF array (Figure 3.4e). At the even higher

plating capacity of 2.0 mAh/cm^2, the diameter of the Li microcolumns further increased and merged into larger solid columns of ~ 4.8 - 10 μm in diameter which encapsulated the VACNFs inside (Figure 3.4f). The morphology change is consistent with the prediction by the classical theory of heterogeneous nucleation and growth, i.e., a higher nucleation rate ν_n and a higher nucleation density N_n would be obtained at the higher plating current density (following the blue curve in Figure 3.1b). It is to be noted that the height of Li microcolumns plated at j = 1.0 mA/cm^2 did not exceed ~20 μm. From the FIB-SEM image (Figure B.15), it can be observed that the columnar Li infiltrates the spaces among VACNFs to form dense solid structures without observable pores. Figure B.16 shows that no SEI skins were left on top of VACNF arrays after stripping the plated 0.75 mAh/cm^2 Li. Instead, coaxial SEI sheaths were observed around the VACNFs that were buried within the Li microcolumns. Similar results were also observed at the plating current density of 0.50 mA/cm^2 (Figure B.17).

When the current density was increased further to 5.0 mA/cm^2, small number of infiltrated Li micro-columns inside the VACNF array (Figure 3.4g) and coaxial Li sheath (Figure B.12d) around individual VACNFs were observed at the low plating capacity of 0.20 mAh/cm^2. As more Li is plated, in addition to the columnar Li infiltrated into the VACNF array, spherical Li particles of 2.4 to 3.2 μm in diameter were observed above the VACNF array and attached to the VACNF tips as shown in Figures 3.4h – 3.4i and B.18. This could signify the onset of more pronounced electric fields near the VACNF tips at high current densities,[241] which might lead to rapid spherical Li deposition on top instead of infiltration into VACNF arrays. In the phase field modeling study by Xu et al., it was found that focused electric fields at the tips of pillar-like host structures at current densities ≥ 5 mA/cm^2 lead to electrodeposition of lithium to occur at their tips.[242] Similar electric field simulation studies in future could provide more insights into this phenomenon on

VACNF arrays. The application of artificial SEIs along the length of VACNFs with a thickness gradient that decreases from the tip to the base could be an interesting strategy to explore in order to minimize the formation of spherical Li particles on VACNF tips. When stripped, the spherical Li particles left behind crumbled SEI skins with circular borders (Figure B.19) similar to those observed on the planar Cu electrode. This implies that the spherical Li particles are electrically connected to the tip of VACNFs. In contrast to that on the planar Cu, patches of unstripped dead Li were not observed in VACNF/Cu even after stripping at 5.0 mA/cm^2. This suggests an improved stripping efficiency of plated Li on VACNFs, probably due to the better electrical connectivity in the 3-D carbon host.

From Figure 3.4, it can also be observed that some VACNFs were not engulfed by the infiltrated columnar Li in the samples. After plating with 0.75 mAh/cm^2 Li, these VACNFs were scraped off and analyzed using cryo-TEM (Figure B.20). It was found that, at all the tested current densities, there exists a co-axial sheath of electrodeposited Li on individual VACNFs. The thickness of the Li sheath ranges between ~20 and ~110 nm. After stripping, wrinkled SEI skins of 10 – 20 nm in thickness wrapping around the VACNFs can be observed (Figure B.21). The formation of such homogeneous coaxial Li sheath illustrates the lithiophilic nature of the graphitic edges of N- and O-doped VACNFs. The coaxial Li sheath formed quickly at the initial plating period up to about 0.20 mAh/cm^2 plating capacity at all plating current densities as shown in Figures 3.4a, 3.4d, 3.4g, and B.12b – B.12d. However, the infiltrative columnar Li grew preferentially in the following plating period and thereby attributed to the dominant plated capacity.

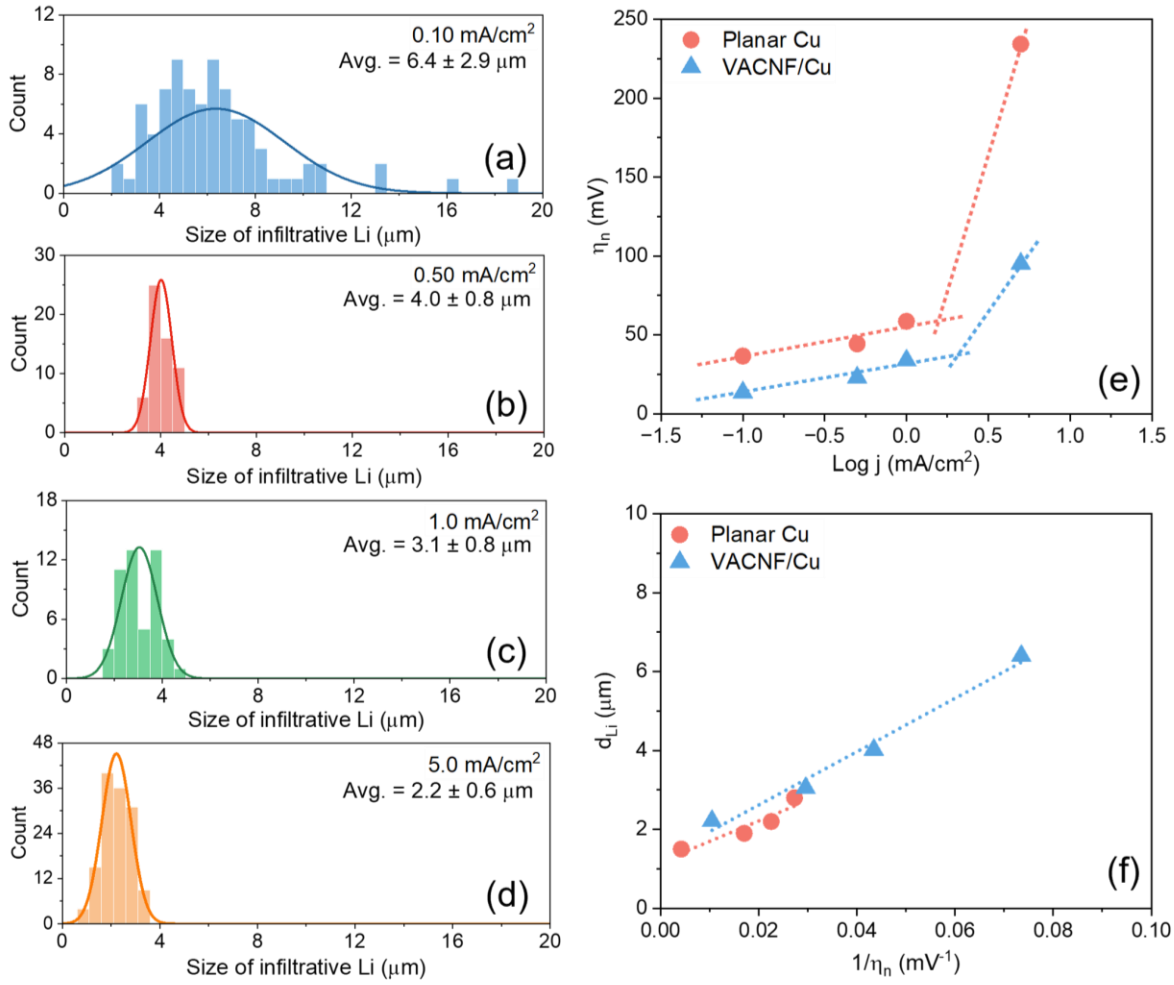

Figure 3.5. Histogram of the size distribution of infiltrative Li grains electrodeposited to a capacity of 0.75 mAh/cm^2 on VACNF/Cu at current densities of (a) 0.10 mA/cm^2, (b) 0.50 mA/cm^2, (c) 1.0 mA/cm^2, and (d) 5.0 mA/cm^2. (e) Relationship between current density (j) and Li nucleation overpotential (η_n) for planar Cu and VACNF/Cu electrodes. (f) Correlation between the size of electrodeposited Li (d_{Li}) and the inverse of Li nucleation overpotential ($1/\eta_n$) on planar Cu and VACNF/Cu electrodes. Reprinted (adapted) from *Chemical Engineering Journal*, 484 (2024), 149515. Copyright 2024 Elsevier Ltd.

3.3.2.4 Analysis of the Li Grain Size Distributions

The size distribution of electrodeposited Li grains vs. the current density on VACNF/Cu and the planar Cu is depicted in Figures 3.5a – 3.5d and B.22, respectively. Only samples with a plating capacity of 0.75 mAh/cm^2 were selected for the particle size analysis since the grains were

well separated. At the plating current density j = 0.10 mA/cm^2, the average size of electrodeposited Li on VACNF/Cu was 6.4 µm. With increase in current densities to 0.50, 1.0, and 5.0 mA/cm^2, the average grain size was reduced to 4.0, 3.1, and 2.2 µm, respectively. In the case of planar Cu, the relationship between Li grain size and the current density j followed a similar trend with the average sizes of 2.8, 2.2, 1.9, and 1.5 µm at j = 0.10, 0.50, 1.0, 5.0 mA/cm^2, respectively. The Li grain size on the VACNF/Cu host is significantly larger than that of planar Cu at all the tested current densities. This can be attributed to the lower local current density following the Sand's equation (Equation 3.1). The larger grain size, columnar morphology and improved electrical connectivity enabled by the VACNF/Cu host are beneficial in reducing undesired side reactions and boosting Li plating/stripping reversibility. This explains the enhanced stability in electrochemical cycling tests (Figures 3.1e – 3.1g). It needs to be highlighted that the distribution at 0.10 mA/cm^2, with a relative standard deviation (RSD) of ~ 44%, is much broader compared to that at higher current densities. This conveys a heightened heterogeneity at low current densities lead by sparse nucleation.

For heterogeneous nucleation, the critical nuclei size (r_{crit}) is inversely proportional to the nucleation overpotential η_n as given by Equation 3.3:[210]

$$r_{crit} = \frac{2\Upsilon V_m}{F|\eta_n|} \quad \text{(3.3)}$$

where Υ is the surface energy of Li-electrolyte interface, V_m is the molar volume of Li, and F is the Faraday's constant. The relationship between the current density j and the nucleation overpotential η_n is given by the Tafel equation, a special case of Butler-Volmer equation at low and moderate current densities:

$$\eta_n = A + B(\log j) \quad \text{(3.4)}$$

where A and B are constants. A linear relationship between η_n and log j for j = 0.10 to 1.0 mA/cm^2 is indeed shown in Figure 3.5e. At j = 5.0 mA/cm^2, deviation in the linear relationship was observed due to the change from kinetic-limited regime to mass-transfer limited regime. Clearly, the deviation observed on the planar Cu electrode is much larger than that on VACNF/Cu. Equations 3.3 and 3.4 predict that r_{crit} is inversely proportional to the log j. Figures 3.5f and B.23 show the same trend, with the Li grain size (d_{Li}) at 0.75 mAh/cm^2 plating capacity inversely proportional to log j and η_n. This reveals that uniform Li nuclei can be obtained at proper plating current density. It is worth noting that the average Li grain size on VACNF/Cu deposited at 1.0 mA/cm^2 is larger than those deposited on Cu at a much lower current density of 0.10 mA/cm^2. This further validates the lower η_n offered by the 3-D VACNF/Cu electrode, which improves the Li plating/stripping reversibility.

3.3.3 Optimal Morphology for High Performance

Based on the earlier discussion, the morphologies of electrodeposited Li on VACNF/Cu and planar Cu electrodes under the tested conditions are summarized in Figure 3.6a. The overall process is highly heterogeneous and can be affected by both the structure of current collectors and the electrochemical deposition conditions, but it is consistent with the classical nucleation and growth theory. On planar Cu, at the low current density, the initial Li nucleation density is very low, but Li rapidly grows at these nucleation sites into large irregular grains consisting of clustered long fibers. With the increase in the current density, the nucleation density is increased, accompanied by the decrease in the nucleus size to form uniformly distributed spherical particles (of a few microns in size) with presence of a small number of fiber-like structures. On the other hand, on the 3-D VACNF/Cu electrode, lithium is initially deposited as thin coaxial sheaths around

each VACNFs at all plating current densities. When the plating capacity is larger than 0.10 mAh/cm^2 at a low current density (≤ 0.10 mA/cm^2), sparse columnar Li forms, which quickly grows into long fibers folded and laid over the VACNF array as more Li is plated. At the moderate plating current density (~ 1.0 mA/cm^2), Li quickly forms columnar structure (a few microns in diameter) that infiltrate into the space among VACNFs. The microcolumns grow laterally and merge into larger grains that are mostly retained inside the VACNF array. When a high current density (5.0 mA/cm^2) is applied, the density of columnar Li increases accompanied by a reduction in their diameter. In addition to the columnar Li, a significant amount of Li is deposited on the tip of VACNFs as spherical particles (with a unform diameter of a few microns).

In literature, the fiber- or noodle-like Li plated at low *j* is considered undesirable as it leads to porous deposition and inefficient stripping.[42] Contrary to this, such Li morphology exhibits higher CE and better stability during plating/stripping cycling (as shown in Figure 3.1e). On the other hand, even though more unform Li particles infiltrated into VACNF arrays can be achieved at the high current density of 5.0 mA/cm^2, it exhibits poor cycling stability (as shown in Figure 3.1g). The microscopic morphology and the macroscopic cycling tests seem to point the opposite directions for optimizing the performance. However, it is to be noted that the earlier cycling tests employed a symmetric protocol, i.e., having the identical current densities for Li plating and stripping processes. The stripping process at the low current density may not be an issue but stripping at a high current density is known to produce a larger amount of dead Li.[42] Therefore, it is necessary to decouple the plating and stripping conditions to assess the stability of different Li morphologies. For this purpose, CE cycling tests were conducted on planar Cu and VACNF/Cu electrodes plated with 2.0 mAh/cm^2 Li using different plating current densities but stripped at a fixed moderate current density of 1.0 mA/cm^2.

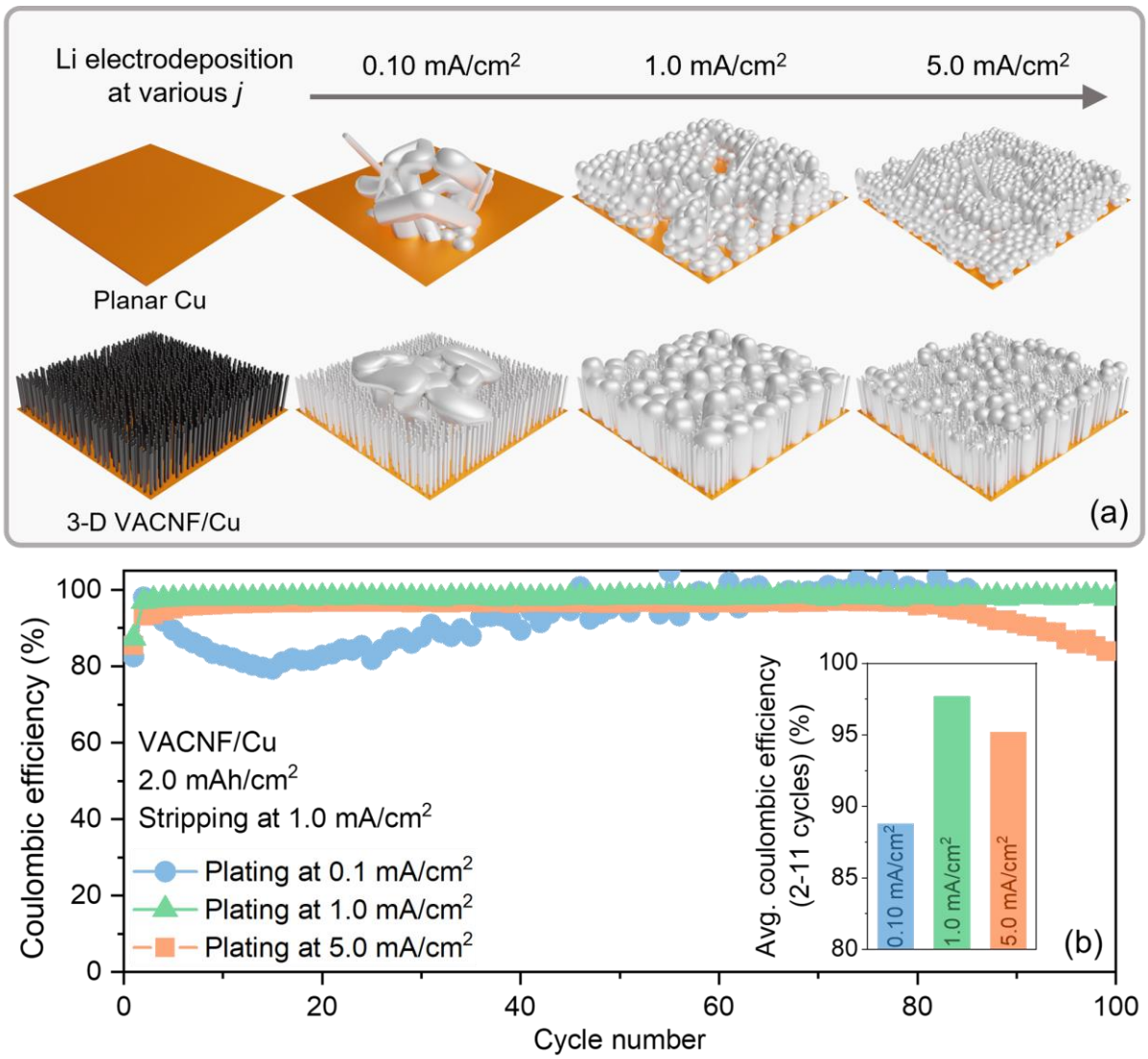

Figure 3.6. (a) A schematic illustration of the effect of the plating current density on the morphology of Li deposits on planar Cu and VACNF/Cu electrodes. (b) The coulombic efficiency during plating/stripping cycling of 2.0 mAh/cm^2 Li plated on VACNF/Cu electrodes at different current densities but stripped at the fixed current density of 1.0 mA/cm^2. Inset shows the average coulombic efficiency for cycles 2-11 at different plating current densities. Reprinted (adapted) from *Chemical Engineering Journal*, 484 (2024), 149515. Copyright 2024 Elsevier Ltd.

As shown in Figure 3.6b, the cycling was stable for the VACNF/Cu electrodes plated at 1.0 and 5.0 mA/cm^2 which were associated with micro-columnar Li morphologies. The average CEs (from cycles 2-11) were around 97.8% and 95.2% for 1.0 and 5.0 mA/cm^2, respectively. The

VACNF/Cu electrode at 0.10 mA/cm^2 plating current density exhibited the worst performance, with the CE starting to decline from the beginning of cycling and drop below 80% in the 15th cycle. After that, the CE started to increase and reached ~ 100% after 40 cycles but with a large variation, possibly owing to the reconnection of accumulated dead Li.[224] The average CE (cycles 2-11) is only 88.1%. This shows that the large noodle-like Li morphology may not exhibit a high cycling performance if the stripping current density is raised to a moderate level. In comparison, the cycling stability was inferior on planar Cu electrodes at all conditions (Figure B.24a) in similar decoupled plating/stripping studies. The planar Cu was unable to support the moderate stripping rate at 1.0 mA/cm^2 and was even worse at the stripping current density of 5.0 mA/cm^2 (Figure B.24b). Overall, as illustrated in Figures B.25 and B.26, the micro-columnar Li morphology infiltrated in the VACNFs achieved at the moderate current density (j = 1.0 mA/cm^2) exhibited the highest performance with an average CE of ~98% (cycles 2-11). The Li spheres deposited on VACNF tips by the high current density (j = 5.0 mA/cm^2) gave a slightly lower CE (~95%). The noodle-like Li morphologies plated at the low current density (j = 0.10 mA/cm^2) present the lowest CE (~88%). This unveils that a lower plating current density is not always better for LMA operations, which is against the general presumption based on the Sand's equation (Equation 3.1). This provides an insight that factors other than lowering the local current density underlie the enhanced reversibility of Li plating/stripping on 3-D conductive anodes. To improve the nucleation density under low current densities and to induce dense Li structures, highly lithiophilic coatings could be applied to host surfaces.

3.4 Conclusion

In summary, we have illustrated the correlation of the microscopic morphologies of electrodeposited lithium metal with the macroscopic performance in lithium plating/stripping cycling tests. The VACNF arrays were used as a model 3-D conductive carbon host with a well-defined vertically aligned low-tortuosity structure to compare with the planar Cu current collector. The 3-D VACNF host indeed provided much higher stability and reversibility for Li plating/stripping. The pressure on the electrode surface inside the coin-cells was found to significantly affect the morphology of Li plating, leading to discrepancies in literature. By excluding this factor, the intrinsic Li morphologies were studied at different plating current densities. It was found that Li plating on both VACNF array and planar Cu electrodes follows the classical nucleation and growth theory, with the nucleation density, nucleation rate, critical nucleation size and Li morphology regulated by the nucleation overpotential which was proportional to the logarithm of the plating current density. At the low plating current density ($\leq$ 0.10 mA/cm^2), it tended to form sparse irregular grains of fibrous Li. At the moderate plating current density (~ 1.0 mA/cm^2), it formed uniform smaller micro-columnar Li deposits. When a high plating current density (~ 5.0 mA/cm^2) was used, some Li spheres started to form at the VACNF tips. In contrary to the Sand's equation which illustrates that a lower plating current density is always beneficial in suppressing Li dendrite formation, the morphology of Li deposits was more uniform at the moderate to high plating current densities, pointing to the opposite direction in optimizing lithium plating/stripping. We found that these seemingly contradictory trends were largely due to the neglected factor that stripping processes worked better at the lower current density. In conventional cycling tests, the stripping and plating current densities were set at the same values and thus lower plating/stripping current densities seemed to exhibit better

cycling stability. By decoupling these two variables and fixing the stripping current density at ~1.0 mA/cm^2, we unraveled that the Li metal deposit with more uniform microscopic morphology at the moderate plating current density (~1.0 mA/cm^2) exhibited the highest performance. This provides new insights in optimizing the performance of LMAs based on 3-D conductive hosts. To extend the range of current densities that can induce favorable Li morphology, use of lithiophilic or artificial SEIs of gradient nature on 3-D hosts could be one of the promising strategies that need to be studied. Application of stable, artificial SEIs would also prevent continuous formation and accumulation of dead SEI resulting in further enhancement in coulombic efficiency and cycle life.

Chapter 4 - Binder-Free Electrodes Based on Ni- and PtRu- coated Vertically Aligned Carbon Nanofibers as Cathodes for Lithium Oxygen Batteries

Hassan Zaidi SS, Rajendran S, Sekar A, et al. Binder-free Li-O_2 battery cathodes using Ni- and PtRu-coated vertically aligned carbon nanofibers as electrocatalysts for enhanced stability. *Nano Research Energy*, 2023, 2: e9120055. https://doi.org/10.26599/NRE.2023.9120055.

This study was conducted in collaboration with Dr. Xianglin Li' group at KU. I prepared and characterized VACNF-based electrodes. While the electrochemical characterization and post-testing characterization of the electrodes was conducted by Syed Shoaib Hassan Zaidi at KU.

4.1 Introduction

In addition to the development of LMAs, suitable high-capacity cathodes such as sulfur, oxygen (air) are essential to develop next generation batteries such as Li-S and Li-air. But the cathode development also has its own challenges such as poor ORR/OER kinetics, electrode passivation, electrode degradation, poor cycling. To address these issues, in this chapter, the investigation of VACNFs grown directly on different carbon supports such as CC, CP using PECVD as cathodes for LOBs is reported. The study of electrodes sputter-coated to form Ni and PtRu nanoparticles anchored VACNFs to improve the ORR/OER kinetics and the results are also reported. The as-prepared electrodes are free-standing in nature without the use of any binders unlike the conventional Vulcan XC-72R electrodes. The impact of carbon substrates of different

structures on the performance is elucidated. The binder-free VACNF electrodes were characterized using FESEM, HRTEM, and XPS. From the electrochemical tests, it was found that VACNF-Ni electrode exhibited the highest specific capacity of 14.92 Ah/g while the superior cycling performance was exhibited by VACNF-PtRu.

4.2 Materials and Methods

4.2.1 Preparation of Vulcan XC-72R Electrode

Vulcan XC 72R and PTFE binder in a 70:30 weight ratio was dispersed in a solution containing isopropyl alcohol (IPA) and water (70/30 v/v) by ultrasonication for 3-4 hours to prepare the electrode slurry. The slurry was blade coated on GDL substrates 1071 HCB plain CC and Sigracet 29AA CP. The electrodes were then dried at room temperature for 24 hours and heat treated for 30 minutes for 350°C.

4.2.2 Preparation of VACNF-Based Electrodes

8 μm long VACNF arrays were grown directly on CP and CC substrates using PECVD (Aixtron Black Magic) for a growth period of 60 minutes. A Ni catalyst film of 22 nm thickness was sputter-deposited on the carbon substrates using Gatan ion beam coater. A thermal dewetting step at 500 °C in the presence of ammonia plasma was applied to break down the Ni film into randomly distributed Ni nanoparticles. During the growth step, acetylene was introduced as the carbon precursor at 63 sccm along with the ammonia flow at 250 sccm. The mass loading of VACNFs on the CC and CP substrates were 0.29 ± 0.02 and 0.14 ± 0.02 mg/cm^2 respectively. Upon completion of growth, the VACNF electrodes were transferred to the sample stage of the sputter unit to deposit Ni or PtRu (1:1 atomic%) to prepare VACNF-Ni or VACNF-PtRu

electrodes. A nominal thickness of 20 nm of either Ni or PtRu catalysts were sputter-deposited on VACNF at a rate of 0.5 Å/s using Ar^+ ion beams of 8.0 or 7.2 keV, respectively. This mass loadings of Ni and PtRu in VACNF-Ni and VACNF-PtRu electrodes were 17.8 μg/cm^2 and 34.2 μg/cm^2, respectively.

4.2.3 Materials Characterization

Imaging of pristine electrodes were done using Topcon/ISI/ABT DS 130F FESEM (Akashi Beam Technology Corporation, Tokyo, Japan). TEM and scanning TEM (STEM)/energy dispersive spectroscopy (EDS) mapping were done at 200 kV using a Tecnai Osiris S/TEM (FEI, Hillsboro, OR). XPS was done using PHI 5000 Versa (Chanhassen, MN) with a monochromatized Al Kα source (1486.7 eV). Shirley background was used for background subtraction. The binding energy (BE) of all XPS data was calibrated vs. the standard sp^2 C1s peak at 284.60 eV.

4.2.4 Electrochemical Characterization

A custom titanium battery frame was used to assemble the cell containing a cathode (Vulcan XC, bare VACNF, VACNF-Ni, and VACNF-PtRu) of 9.5 mm diameter and a Li chip of 0.25 mm thickness and 0.5 inch diameter. A Whatman glass fiber separator (GF/C, 1822-021) of 1.58 cm diameter soaked with 90 μL of electrolyte containing 1.0 M LiTFSI in dimethyl sulfoxide was used. The cell was assembled in an Ar filled glovebox (Mikrouna) with O_2 and H_2O contents below 0.1 ppm. After cell assembly, the cell was purged with pure oxygen (99.99%) on the cathode side for a minimum of 1 hour at open-circuit conditions to remove the argon. CV tests were conducted using a Biologic SP-150 potentiostat at a scan rate of 0.10 mV/s. Galvanostatic charge/discharge tests were performed at room temperature on a 4-channel Arbin MSTAT4 battery

tester at 0.10 mA/cm^2. The cut-off voltages for charge and discharge were kept as 4.5 V and 2.0 V, respectively. For the cycling stability tests, a fixed areal capacity of 0.50 mAh/cm^2 was used.

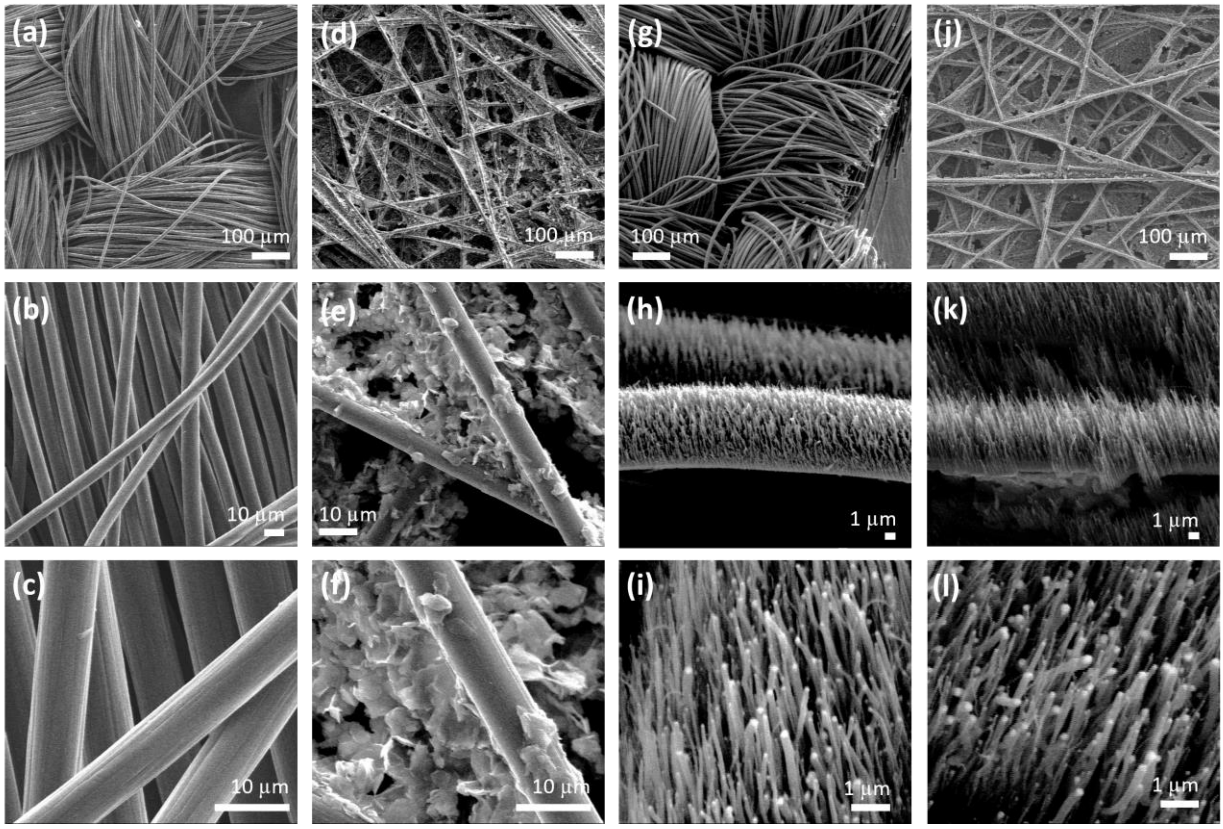

Figure 4.1. FESEM images of (a) – (c) bare CC, (d) – (f) bare CP, VACNF grown on (g) – (i) CC and (j) – (l) CP. Figures 4.1a – 4.1f are top-view images while 4.1g – 4.1l are 30º perspective images. Reprinted (adapted) under CC BY 4.0 license.

4.3 Results and Discussion

4.3.1 Materials Characterization of Pristine VACNF Electrodes

Figures 4.1a – 4.1f show the FESEM images of bare CC and CP, that were used as the substrates for VACNF growth. The CC is composed of interwoven carbon fibers of 7.6 µm diameter while the CP is made up of randomly stacked carbon fibers (6.7 µm diameter) coated with amorphous carbon. CP has a porosity of 88% and an IP gas permeability of 8 – 9 x 10^{-12} m^2

with a mean pore diameter of 48 – 51 µm. CC offers a larger mean pore diameter of 130 µm as well as a lower tortuosity of 1.33 compared to that of CP (>2). A lower tortuosity could facilitate faster Li^+ ion diffusion and better oxygen permeability. From the FESEM images of VACNF in Figures 4.1g – 4.1i, it can be observed that VACNFs were grown vertically on top surface of the individual carbon fibers of CC. The average height of the VACNFs were about 8 µm. The average diameter of the fibers was ~ 90 nm. Lack of Ni catalyst and/or limited supply of carbon precursors during growth might have contributed to the growth of shorter VACNFs on the edges of the CC's fibers. In the case of CP, VACNFs were found to be grown on the top surface of both carbon fibers as well as the amorphous carbon films present in between the fibers (Figures 4.1j – 4.1l). The Ni catalyst at the VACNFs' tips showed up as bright spots in the high magnification images. Due to the high surface area provided by the 3-D structure of VACNFs, the deposition of 20 nm (nominal thickness) of Ni by sputtering resulted in a coaxial coating of the VACNF's surface with 2-5 nm Ni nanoparticles (Figures 4.2a and 4.2b). The lattice fringes of Ni coated on the surface of an individual VACNF can be seen in Figure 4.2c. The elemental analysis of VACNF-Ni was done using STEM-EDS mapping analysis which confirmed that Ni is deposited uniformly throughout the surface of VACNFs (Figures 4.2d – 4.2g). It also revealed that VACNFs are doped with nitrogen and oxygen. Another source of oxygen could be surface oxides on Ni nanoparticles after being exposed to air. Similar results of uniform deposition were observed for VACNF-PtRu.

XPS analyses were done for VACNF, VACNF-Ni, and VACNF-PtRu samples to determine the surface elemental composition (Figures 4.3a – 4.3d). The bare VACNF was found to be doped with 6.38 at% of N and 2.67 at% of O. The presence of peaks corresponding to Ni, Pt, and Ru confirm the presence of these elements in the respective samples. From the survey spectrum, it can also be observed that the C 1s peak intensity diminished significantly for VACNF-

Ni and VACNF-PtRu samples due to the coverage of carbon surface by the Ni and PtRu nanoparticles. The C 1s peak was deconvoluted into five peaks with BEs of 284.7 eV, 285.9 eV, 287.8 eV, 291.3 eV, and 293.4 eV corresponding to sp^2, sp^3, C-O/C-N, C=O, and O-C=O respectively. The high-resolution spectra of Ni 2p in VACNF-Ni electrode was deconvoluted into three pairs of Ni $2p_{3/2}$ and Ni $2p_{1/2}$ doublets. The doublet pair with BEs 852.9 eV/870.8 eV corresponds to metallic Ni (Ni(0)) while the 855.8 eV/874.0 eV doublet pair corresponds to Ni(II) state. The remaining doublet peak are Ni 2p satellite peaks. Metallic Ni was found to contribute 77.41% of the total Ni content in VACNF-Ni electrode. The remaining 22.59% were from Ni(II) states, possibly NiO and $Ni(OH)_2$ species due to exposure to air atmosphere. For VACNF-PtRu electrode, the Pt 4f and Ru 3p high resolution spectra were analyzed. The Pt 4f peak was deconvoluted into three pairs of Pt $4f_{7/2}$ and Pt $4f_{5/2}$ doublet peaks with BEs at 71.5/74.8 eVs, 72.5/76.1 eVs, and 73.8/78.2 eVs. The corresponding Pt(0), Pt(II), and Pt(IV) states constitute 55.12%, 22.69%, and 22.18%, respectively. The deconvolution of Ru 4f peak into two pairs of $3p_{1/2}$ and $3p_{3/2}$ peaks revealed that 57.18% of Ru exist as Ru(0) while the remaining exist as Ru(IV).

4.3.2 Electrochemical Characterization:

Deep discharge tests were performed at a constant current of 0.10 mA/cm^2 to evaluate the maximum discharge capacity that can be delivered by the different cathodes of study. When deep discharged, Vulcan XC/CC exhibited a capacity of ~1.9 mAh/cm^2, about 2.2 times higher than that of Vulcan XC/CP (~ 0.85 mAh/cm^2) (Figure 4.4a). The higher discharge capacity for Vulcan carbon coated on CC when compared to the one coated on CP could be attributed to the larger mean pore diameter and the lower tortuosity of CC. These characteristics of CC help to reduce the diffusion pathlength of Li ions. Also, larger pore sizes allow for growth of discharge product by

continued access for oxygen for a longer duration without clogging the pores. A similar result of higher capacity was obtained for CC than that of CP when the Vulcan carbon coating was changed to Ni coated VACNF array (Figure 4.4b). This further reinstates the better transport properties of CC in comparison with CP. Additionally, VACNF-Ni/CC and VACNF-Ni/CP exhibited higher discharge capacities compared to that of their Vulcan carbon counterparts due to its aligned open-pore structure of VACNF offering low tortuosity.

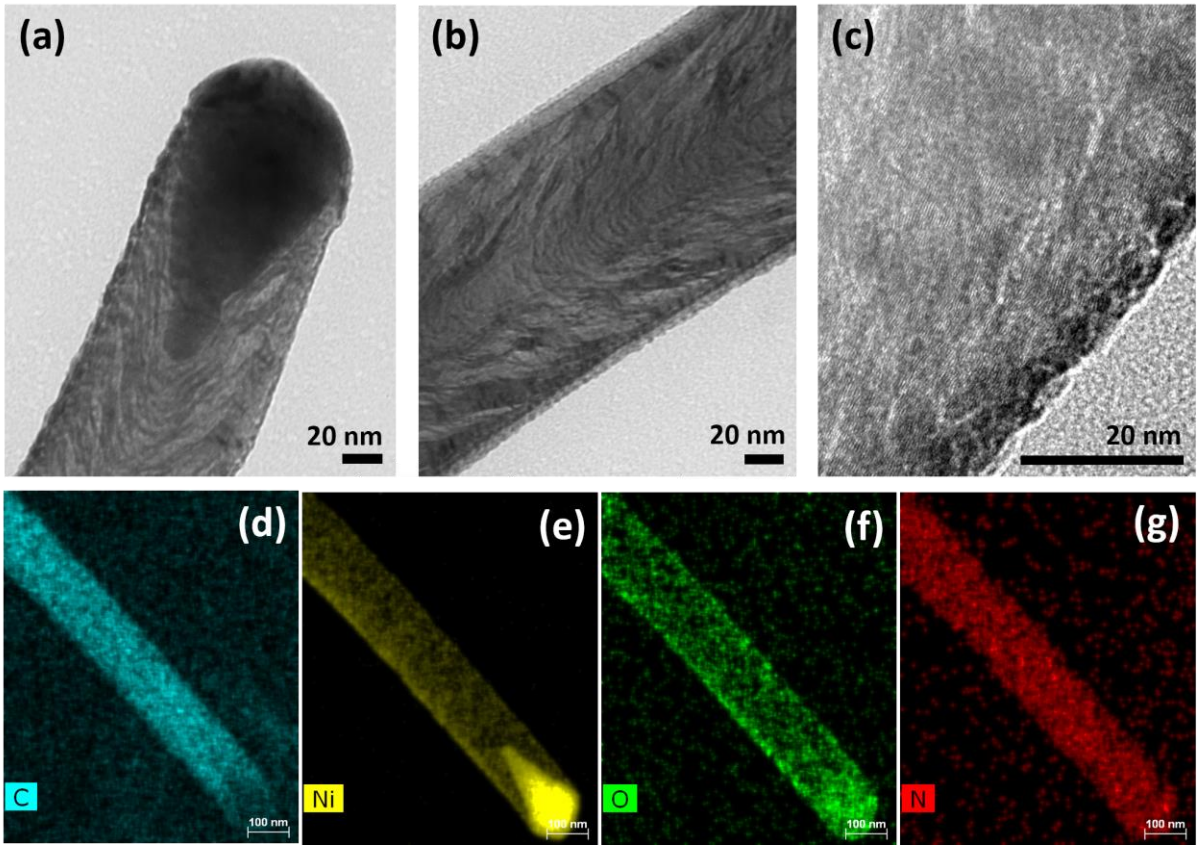

Figure 4.2. TEM images of VACNF-Ni (a) near the tip and (b) along the length of individual VACNF. (c) HRTEM image of the sidewall of VACNF-Ni. (d) – (g) STEM-EDS mapping images of a VACNF deposited with Ni. Reprinted (adapted) under CC BY 4.0 license.

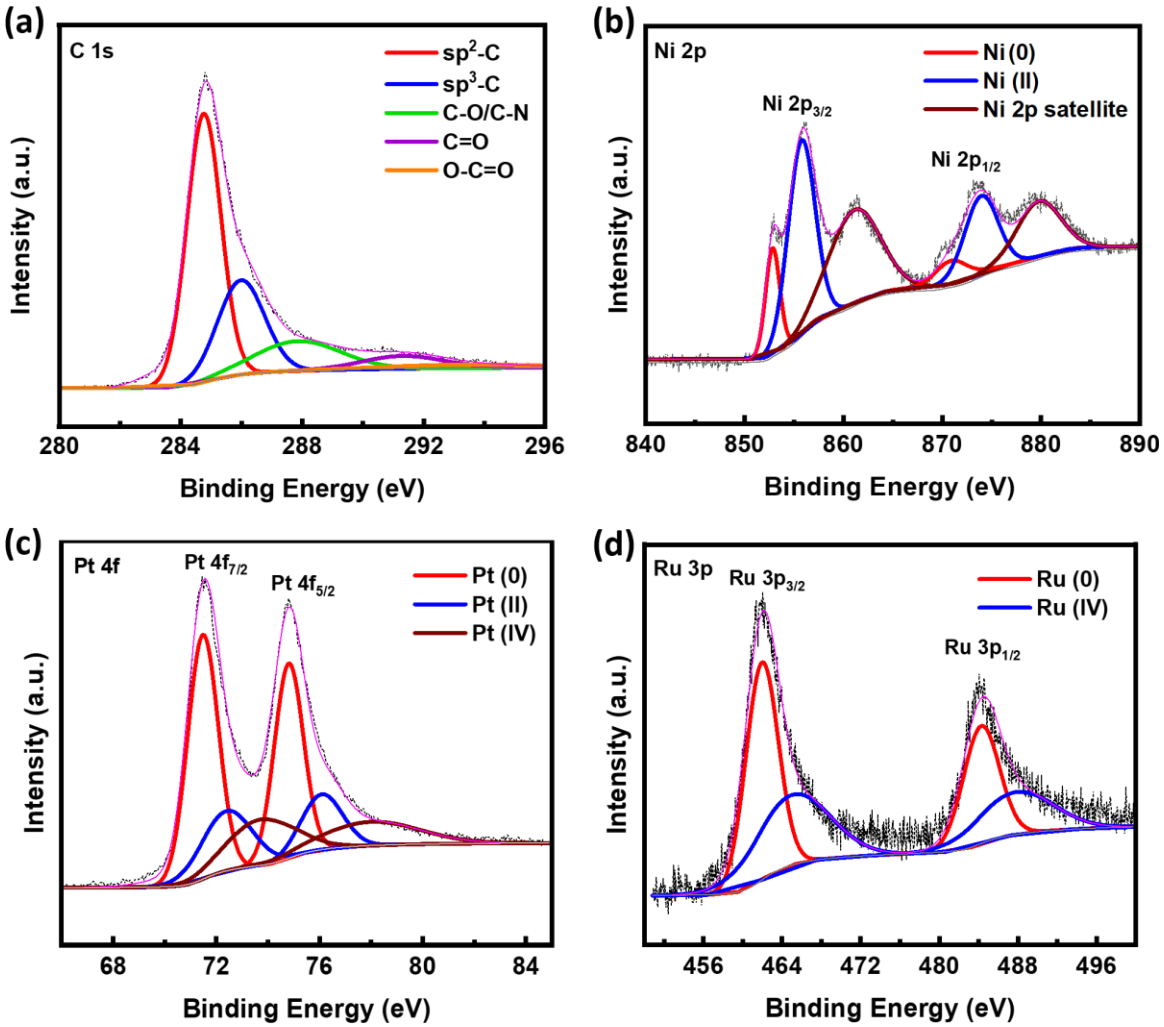

Figure 4.3. High-resolution XPS spectra of (a) C 1s of bare VACNF, (b) Ni 2p of VACNF-Ni, (c) Pt 4f and (d) Ru 3p of VACNF-PtRu electrodes. Reprinted (adapted) under CC BY 4.0 license.

4.3.3 Electrochemical Characterization:

Deep discharge tests were performed at a constant current of 0.10 mA/cm^2 to evaluate the maximum discharge capacity that can be delivered by the different cathodes of study. When deep discharged, Vulcan XC/CC exhibited a capacity of ~ 1.9 mAh/cm^2, about 2.2 times higher than that of Vulcan XC/CP (~ 0.85 mAh/cm^2) (Figure 4.4a). The higher discharge capacity for Vulcan carbon coated on CC when compared to the one coated on CP could be attributed to the larger

mean pore diameter and the lower tortuosity of CC. These characteristics of CC help to reduce the diffusion pathlength of Li ions. Also, larger pore sizes allow for growth of discharge product by continued access for oxygen for a longer duration without clogging the pores. A similar result of higher capacity was obtained for CC than that of CP when the Vulcan carbon coating was changed to Ni coated VACNF array (Figure 4.4b). This further reinstates the better transport properties of CC in comparison with CP. Additionally, VACNF-Ni/CC and VACNF-Ni/CP exhibited higher discharge capacities compared to that of their Vulcan carbon counterparts due to its aligned open-pore structure of VACNF offering low tortuosity.

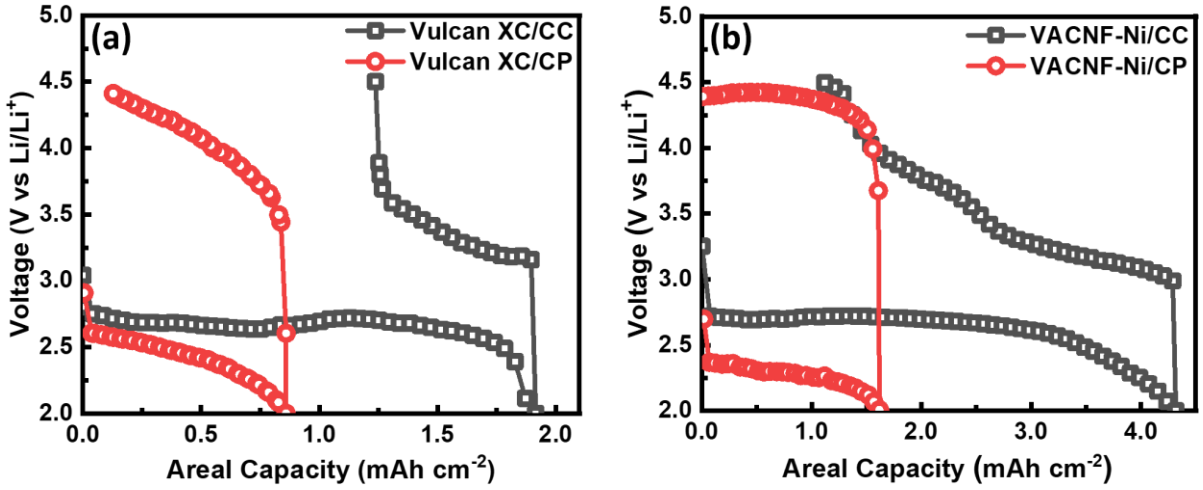

Figure 4.4. Galvanostatic charge/discharge voltage curves during deep discharge tests at 0.10 mA/cm^2 for (a) Vulcan XC and (b) VACNF-Ni electrodes prepared on CC and CP to illustrate the effect of substrates on performance. Reprinted (adapted) under CC BY 4.0 license.

Due to the superior properties of CC, further characterization was carried out with cathodes on CC substrate. Figures 4.5a and 4.5b show the comparison of deep discharge performance of tested cathode materials in terms of areal capacity and specific capacity, respectively. Among various cathodes, maximum discharge capacity was obtained for VACNF-Ni cathode (4.32

mAh/cm^2 or 14.92 Ah/g). The second highest capacity of 2.62 mAh/cm^2 or 9.07 Ah/g was delivered by the VACNF-PtRu electrode. Bare VACNF and Vulcan XC electrodes yielded specific capacities of 5.55 Ah/g and 3.83 Ah/g, respectively. The improvement in discharge capacity reflects the ability of catalyst nanoparticles to reduce oxygen and deposit lithium oxide continuously without mass and/or electronic transport limitations. The higher specific capacity by bare VACNF because of better utilization of electrode surface illustrates the advantage of utilizing superior electrode architecture for air cathodes. The aligned 3-D pore structure with ~ 78% porosity helps to accommodate the solid Li_2O_2 without passivating the electrode. However, when their areal capacities were compared, bare VACNF yielded a slightly lower capacity of 1.60 mAh/cm^2 than Vulcan-XC (1.91 mAh/cm^2). The lower areal capacity of VACNF is due to its relatively lower carbon loading, a limitation that can be overcome by increasing the active surface by growing taller VACNFs. During the charging process, the efficient oxidation of Li_2O_2 and evolution of oxygen depends on the kinetics of the catalyst used. The rechargeability after deep discharge, measured in terms of coulombic efficiency, is highest at ~ 100% for VACNF-PtRu electrode (Figure 4.5c). VACNF-Ni and VACNF electrodes showed CEs of 74.3% and 73.2%, respectively. Vulcan XC performed the least with a low CE of 35.5%. Despite the improvement in deep discharge capacity of VACNF by about ~ 2.7 times with deposition of Ni, the CE did not improve significantly. However, with the PtRu catalyst the CE reached 100% with an improvement in discharge capacity by ~ 1.6 times. Figure 4.5d shows the cycling performance of different electrodes with a cycling capacity of 0.50 mAh/cm^2. With cycling under a limited discharge/charge capacity of 0.50 mAh/cm^2, Vulcan XC electrode failed prematurely in 3 cycles. Bare VACNF operated longer for up to 8 cycles. The moderate enhancement could be partially attributed to the more stable nature of graphitic VACNFs. The VACNF-PtRu and VACNF-Ni electrodes exhibited

stable cycling for 27 cycles and 13 cycles, respectively. The coverage of the carbon surface with catalyst nanoparticles in addition to improving the ORR/OER kinetics, helps protect the carbon surface from reactive intermediate superoxide ion. This prevents formation of irreversible Li_2CO_3 leading to longer cycle life.

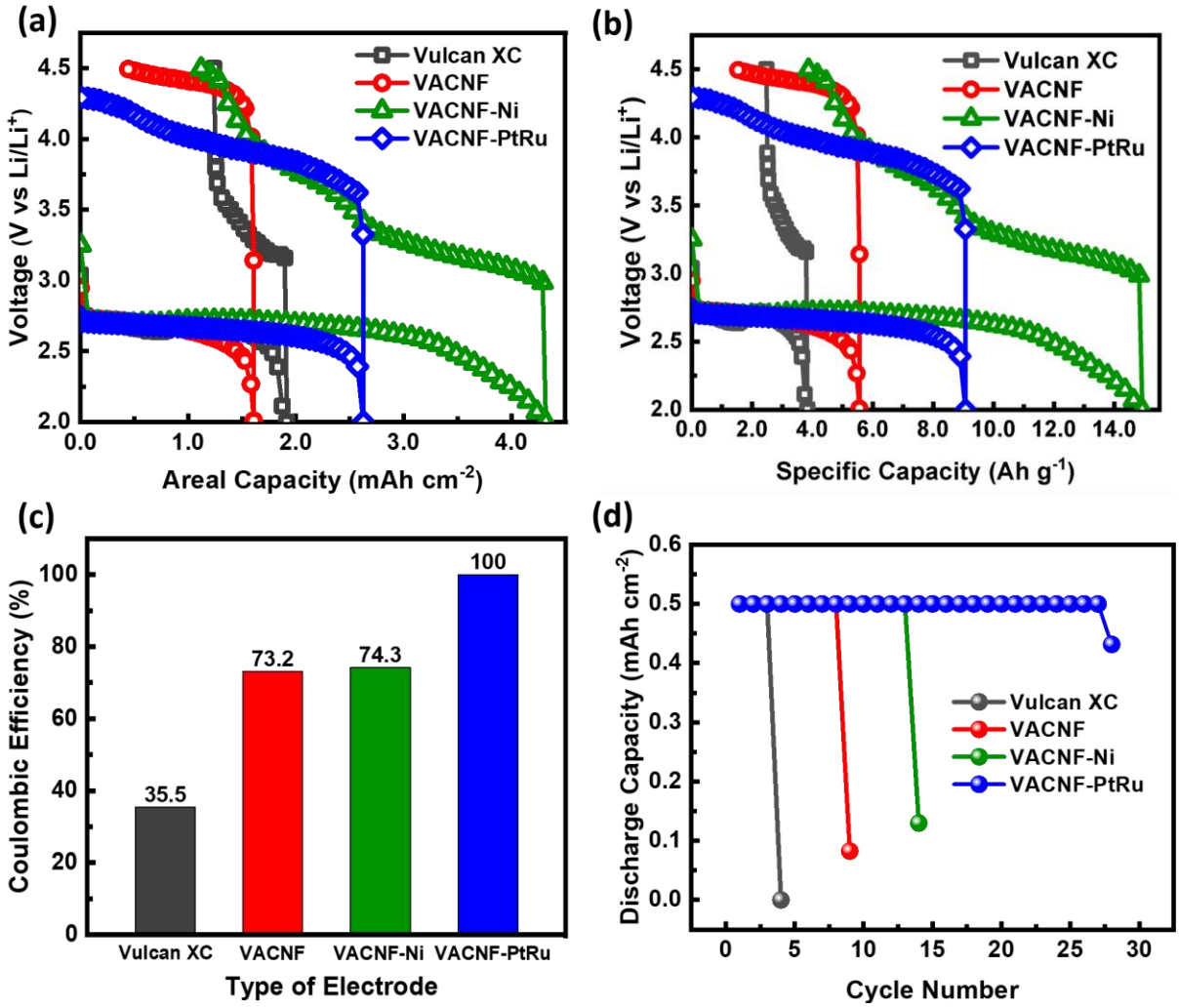

Figure 4.5. Galvanostatic charge/discharge voltage curves corresponding to deep discharge tests of different electrodes expressed in terms of (a) areal capacity and (b) specific capacity. (c) Comparison of CE among different cathodes on CC substrate. (d) Cycling performance of the various cathode materials for a cycling capacity of 0.50 mAh/cm^2. Reprinted (adapted) under CC BY 4.0 license.

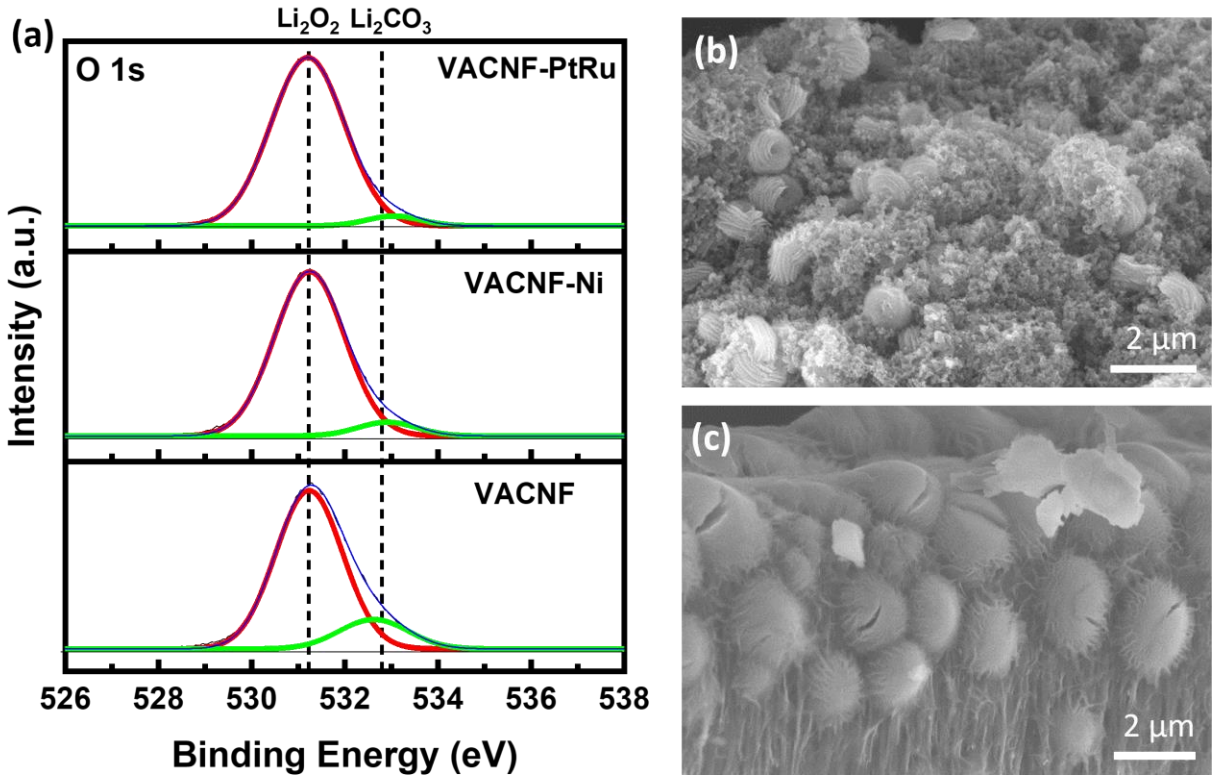

Figure 4.6. (a) High resolution O 1s XPS spectra for VACNF, VACNF-Ni, and VACNF-PtRu electrodes. FESEM images of (b) Vulcan XC and (c) VACNF-Ni electrodes after discharging completely at 0.10 mA/cm^2. Reprinted (adapted) under CC BY 4.0 license.

4.3.4 Chemical and Morphological Analysis of Discharged Product

The chemical composition of the discharged product was analyzed using XPS as shown in Figure 4.6a. From the O 1s spectra, it can be found that majority of the discharged product is Li_2O_2. In VACNF electrode, a significant amount of Li_2CO_3 indicates the presence of undesired side reaction between carbon and reactive intermediate species. With the application of Ni and PtRu nanoparticles, a significant decrease in the Li_2CO_3 content was witnessed illustrating their protective role in mitigating carbon surface reactions. Figures 4.6b and 4.6c show the morphology of discharged product at the end of deep discharge on Vulcan XC and VACNF-Ni electrodes, respectively. Li_2O_2 gets deposited as large crystalline, layered toroidal structures in Vulcan-XC

electrode. In the case of VACNF electrodes, Li_2O_2 formed as spherical and film-like structures throughout the length of VACNFs. Thin film-like structures are beneficial as they offer improved rechargeability owing to their relatively lower resistance. These observations explain the longer cycling performance exhibited by VACNF electrodes. The difference in the discharged product morphology between Vulcan XC and VACNF electrodes can be attributed to the difference in their binding affinity towards oxygen. Weaker oxygen binding promotes formation of Li_2O_2 in electrolyte solution through disproportion reaction resulting in larger toroidal structures. Whereas stronger binding due to graphitic carbon and catalyst nanoparticles favors electrochemical reduction on the electrode surfaces resulting in film like deposits.

4.4 Conclusion

VACNFs were successfully grown on carbon paper and carbon cloth. The bare VACNFs demonstrated a higher specific capacity in comparison to the commercial Vulcan XC electrode. This is attributed to their low-tortuous 3-D structure and the abundance of active sites. The existence of a maximum limit to fiber length is one of the factors limiting the areal capacity of the air cathodes based on VACNFs. When coated with Ni or PtRu nanoparticles, the specific capacity as well as the areal capacity of the VACNF electrodes were enhanced significantly due to the faster ORR/OER kinetics and the prevention of Li_2CO_3 formation. Among the different electrodes, the VACNF-Ni cathode exhibited the highest specific capacity of 14.92 Ah/g at 0.10 mA/cm^2. The VACNF-PtRu, on the other hand, exhibited the highest cycling stability (27 cycles) with 100% CE. This study offers valuable insights that could aid in the design of nanostructured electrodes for use as air cathodes.

Chapter 5 - Divalent Transition Metal Cation Mediated V_2O_5 Nanoribbon-Reduced Graphene Oxide Hybrids as Cathodes for Aqueous Zinc Ion Batteries

In this chapter, synthesis, materials characterization, and part of electrochemical characterization for the divalent transition metal cation mediated hybrids was done by Kamalambika Muthukumar. The parts that I worked on include synthesis and electrochemical characterization including long-term cycle test, GITT and ex-situ characterization post discharge/charge for the cathode materials. I also did the synthesis and characterization of Na-V_2O_5 NRs/rGO hybrid.

5.1 Introduction

The use of safer aqueous electrolyte, reasonable volumetric energy density makes AZIBs a promising battery that can complement other high energy density chemistries for large scale energy storage systems. Towards that direction, the development of hybrid nanomaterials based on vanadium pentoxide NRs as potential cathodes for AZIBs is discussed in this chapter. Using a facile coprecipitation technique mediated by divalent cations, V_2O_5 NRs on rGO nanosheets pre-intercalated with divalent cations are successfully synthesized. The synthesized nanostructured M-V_2O_5 NRs/rGO hybrids are characterized in detail to understand its structure and chemical composition. The performance of the hybrids as AZIB cathodes are evaluated and the roles of intercalation-participating and non-participating cations in the performance of the hybrid cathode

is elucidated. The use of Zn^{2+} for pre-intercalation (Zn-V_2O_5 NRs/rGO) enhances the specific capacity of the V_2O_5 NRs dramatically to 395 mAh/g at 0.50 A/g. But the Zn-V_2O_5 NRs/rGO cathode exhibits poor stability in long term cycle test at 4.0 A/g. With the replacement of a fraction of pre-intercalated Zn^{2+} with Mn^{2+}, the stability improves significantly retaining about 77% at the end of 2000 cycles. Further, the Zn^{2+} diffusivity and the energy storage mechanism of the hybrid cathodes are presented.

5.2 Materials and Methods

5.2.1 Chemicals and Materials

Vanadium pentoxide (99.6% purity) and manganese acetate tetrahydrate were purchased from ACROS Organics (Pittsburg, PA, USA). Zinc acetate (99.9% purity) and zinc sulfate monohydrate were purchased from Sigma Aldrich (St. Louis, MO, USA). Single layer GO powder and Tetrahydrofuran (THF) (99.9% purity) were purchased from ACS material LLC (Pasadena, CA) and Fisher Scientific (Hampton, NH, USA), respectively. All the chemicals were used as it is without further treatment. Coin cell casings and other components were purchased from MTI corporation (Richmond, CA, USA).

5.2.2 Synthesis of M-V_2O_5 NR/rGO Hybrids

To prepare the hybrid nanomaterial, V_2O_5 NRs were first synthesized from commercial bulk V_2O_5 powder using microwave-assisted exfoliation method. Bulk V_2O_5 powder was first soaked in deionized water for ~ 4 hours to facilitate the intercalation of water molecules between V_2O_5 layers. After soaking, the water was decanted and the V_2O_5 powder was then transferred into a 10 mL microwave glass vial containing 7.0 mL of THF. The mixture was then transferred to the

Discover SP microwave reactor and was radiated with microwaves. The temperature was ramped to 150 °C in 9 min and was then held constant for 1 hour. The reactor operated with a maximum power of 300 W. Once the reaction is completed, THF is removed completely by washing with deionized water (~ 2 times) using centrifugation. The washed mixture is redispersed in 7.0 mL of deionized water using ultrasonication for 30 minutes. The exfoliated V_2O_5 NRs was separated from the bulk V_2O_5 as a bright yellow supernatant using centrifugation. GO nanoflakes were added to ~ 10 mL of homogenous V_2O_5 NRs suspension and was subjected to ultrasonication for 20 minutes to obtain a stable, deep yellow colored homogeneous binary suspension with 20 wt% GO and 80 wt% V_2O_5. Then, freshly prepared aqueous solution of 0.10 M zinc acetate or 0.10 M (Mn+Zn) acetate containing 0.0357M Manganese acetate and 0.0643M Zinc acetate or 0.050 M sodium acetate was added in drops to the V_2O_5/GO suspension. Due to the electrostatic interaction between the negatively charged GO and V_2O_5 and the positively charged metal ions, a gel-like precipitate forms and settles at the bottom. A clear supernatant solution indicates complete formation of V_2O_5 NR/GO hybrids sandwiched by metal ions denoted as M-V_2O_5 NR/GO. The M-V_2O_5 NR/GO gel was collected, washed with DI water and then dried overnight on a hotplate at 70 $^{\circ}$C to remove water. The black colored solid obtained at the end of drying was then annealed at 300 $^{\circ}$C in N_2 atmosphere for 2 hours to convert GO into rGO resulting in M-V_2O_5 NR/rGO hybrids.

5.2.3 Materials Characterization

Raman spectroscopy was done using DXR^{TM} Raman microscope (Thermo Fisher Scientific, Madison, WI)) with a 532 nm laser at 10 mW, under a 10X objective lens with a slit width of 50 µm. X-ray diffraction (XRD) was carried out using D8 Advance diffractometer (Bruker Corporation, Karlsruhe, Germany) with a Cu Kα radiation of wavelength 0.15418 nm.

The surface chemical analysis was done using a PHI 5000 Versa XPS (Chanhassen, MN) with a monochromatized Al Kα source (1486.7 eV). The TEM images were obtained using Philips CM 100 equipped with a tungsten source and operated under 100 kV acceleration voltage. The FESEM images were obtained using a Topcon/ISI/ABT DS 130F FESEM microscope (Akashi Beam Technology Corporation, Tokyo, Japan). Thermogravimetric analysis (TGA) was done using TGA Q50 system (TA instruments - Waters LLC, New Castle, DE) in air atmosphere at a ramp rate of 10 $^{\circ}$C/min. Zetapotential values were determined using ZetaPALS Zeta Potential analyzer (Brookhaven Instruments Corporation, NY, USA).

5.2.4 Electrochemical Characterization

The working electrode was prepared by brush coating the slurry containing active material (M-V_2O_5 NR/rGO), Super P and PVDF in a weight ratio of 8:1:1 with appropriate amount of NMP. A Ti disk of 100 µm thickness and 15 mm diameter was used as the current collector for the working electrode. Coated electrodes were dried at 110°C overnight under vacuum. A Zn disk was used as the counter and reference electrode. A glass fiber separator soaked with 200 µL of 2.0 M aqueous zinc sulfate electrolyte solution was placed in between the working and counter electrodes. The galvanostatic tests were carried out using a Neware battery tester (Shenzhen, China). The GITT measurements were carried out at a current density of 0.050 A/g. The duration of each discharge/charge pulse was 300 s followed by a 900 s relaxation period. The discharge and charge cut-off voltages were set at 0.20 V and 1.80 V vs Zn^{2+}/Zn. The specific capacity was based on the mass of M-V_2O_5.

5.3 Results and Discussion

5.3.1 Synthesis Strategy for M-V_2O_5 NR/rGO Hybrid

Schematic of the synthesis design and optical images of the products obtained at each step of the synthesis are shown in Figures 5.1 and C.1, respectively. Based on literature findings that one-dimensional V_2O_5 nanostructures such as nanorods, nanoribbons, nanowires offer superior performance as zinc ion battery cathodes in terms of capacity and stability than their bulk counterparts, V_2O_5 NR was chosen for this work. The method for utilizing microwave reactor to synthesis V_2O_5 NR from bulk V_2O_5 powder was developed and reported by our group in a previous manuscript.[131] To improve the electrical and mechanical properties further, rGO was chosen as the support material to form the hybrid. To form a hybrid successfully, it is necessary for the chosen materials to be able to form stable, homogeneous suspensions in a common solvent. Since, rGO is hydrophobic in nature, to disperse well in aqueous V_2O_5 NR suspension, GO was chosen to prepare M-V_2O_5 NR/GO hybrid which can then thermally reduced later to form the desired M-V_2O_5 NR/rGO. The thermal annealing step also serves to decompose the acetate introduced during the co-precipitation step. From zetapotential analysis, it was found that both V_2O_5 NRs and GO possess negative surface charges. Because of the electrostatic repulsion, when mixed together, they form stable suspensions in water. To induce formation of hybrids, divalent positive ions – either Zn^{2+} alone or together with Mn^{2+} were added. Zn^{2+} ions were chosen as they might participate actively during charge/discharge when applied as zinc ion battery cathodes facilitating easier intercalation/deintercalation. Mn^{2+} ions were expected to provide structural support without being electrochemically involved. Monovalent positive ions such as Na^{+} were found to be ineffective in forming V_2O_5 NR/GO hybrids as evidenced by the presence of dark brown colored suspension even after adding enough ions to neutralize the V_2O_5 NR and GO. In case of divalent ions, a clear

supernatant was left behind after co-precipitation indicating successful formation of M-V_2O_5 NR/GO hybrids. During thermal annealing, in addition to conversion of GO to rGO, the metal precursors convert to metal oxides which provide ion conduction pathways while expanding the V_2O_5 layers.

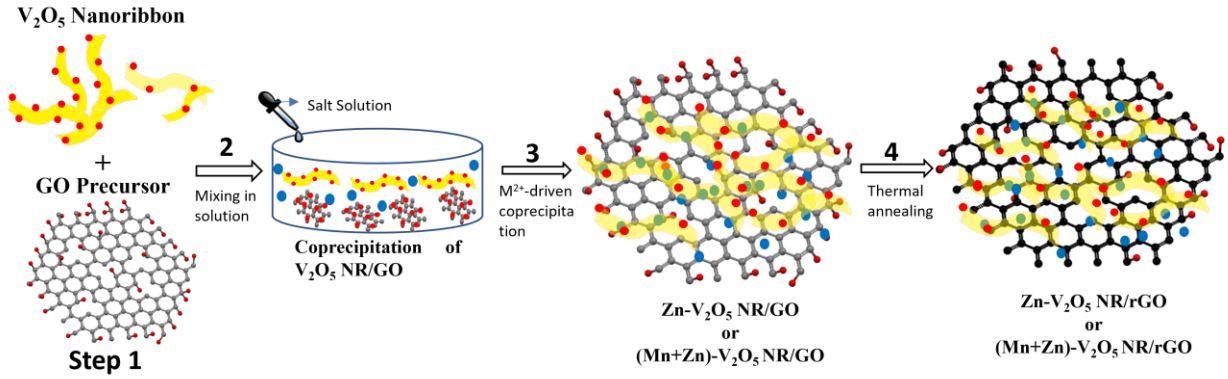

Figure 5.1. A schematic illustration of the M-V_2O_5 NR/rGO hybrids synthesis. Reprinted (adapted) with permission from *ACS Sustainable Chem. Eng.* 2023, 11, 6, 2670–2679. Copyright 2023 American Chemical Society.

5.3.2 Materials Characterization of M-V_2O_5 NR/rGO Hybrids

5.3.2.1 Structural Characterization:

TEM images of bare rGO and V_2O_5 NRs are shown in Figure C.2. Bare rGO has a typical wrinkled morphology spanning several microns in lateral direction. Bulk V_2O_5 has a thin two-dimensional structure with several microns' width. After exfoliation, V_2O_5 NRs were found to be randomly stacked long ribbons with a width of 10 - 30 nm and a length of several microns as shown in Figure 5.2a. After forming M-V_2O_5 NR/rGO hybrids, V_2O_5 NRs were found to get anchored on the planar surface of rGO which had become rigid devoid of wrinkles. The length of V_2O_5 NRs got shortened to 200 - 400 nm as shown in Figures 5.2b and 5.2c. SEM images show the morphologies of microwave exfoliated V_2O_5 NR aggregates and M-V_2O_5 NR/rGO hybrids

(Figure 5.2d). V_2O_5 NRs aggregate into rigid rod-like fibers of 1 - 10 µm wide and several tens of micron length. In contrast, both Zn-V_2O_5 NR/rGO and (Zn+Mn)-V_2O_5 NR/rGO exhibit plate like morphology indicating stacked layers of rGO and V_2O_5 NRs (Figures 5.2e and 5.2f). Their thickness and lateral size ranges between 1 to 5 µm and up to 50 µm, respectively. Between the two hybrids, (Zn+Mn)-V_2O_5 NR/rGO exhibit a more disordered structure with thinner, wrinkled plates probably due to introduction of Mn^{2+} cations.

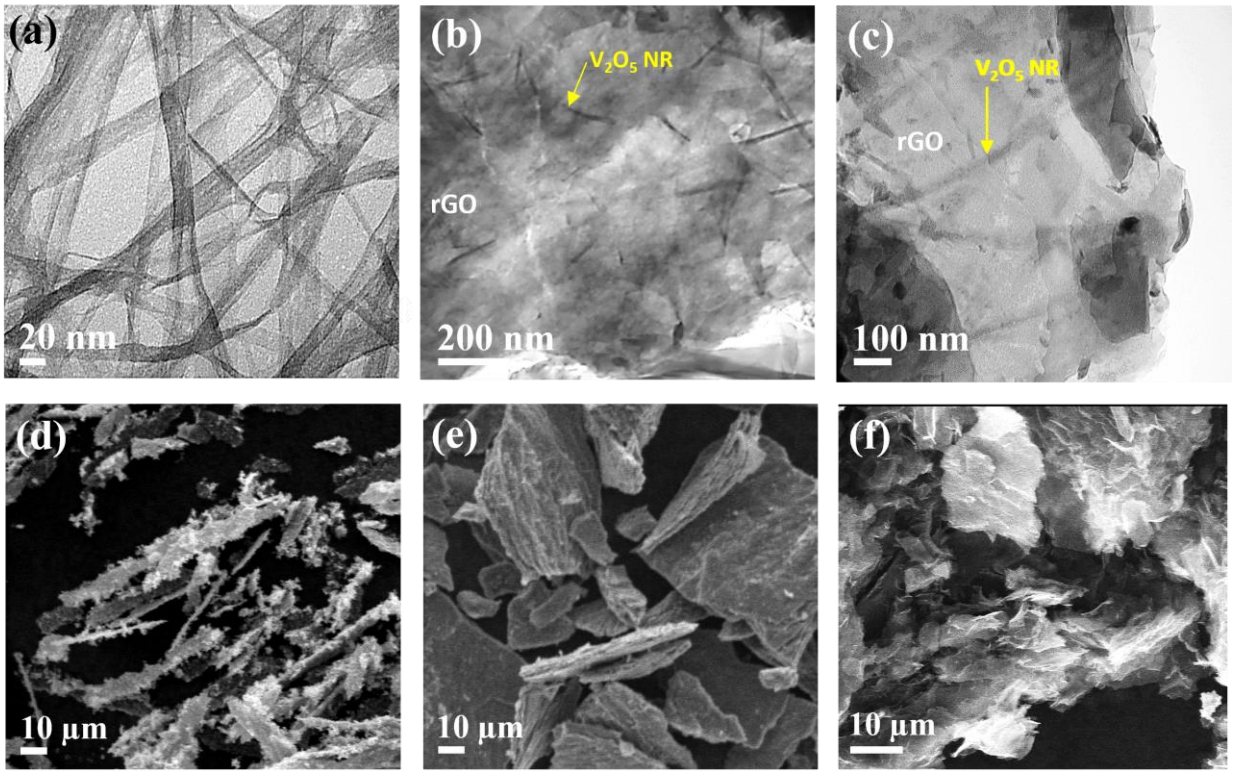

Figure 5.2. TEM images of (a) V_2O_5 nanoribbons, (b) Zn-V_2O_5 NR/rGO and (c) (Zn+Mn)-V_2O_5 NR/rGO. FESEM images of (d) V_2O_5 nanoribbons, (e) Zn-V_2O_5 NR/rGO and (f) (Zn+Mn)-V_2O_5 NR/rGO. Reprinted (adapted) with permission from *ACS Sustainable Chem. Eng.* 2023, 11, 6, 2670–2679. Copyright 2023 American Chemical Society.

5.3.2.2 Chemical Characterization

XRD measurements were done to analyze the phase composition of the M-V_2O_5 NR/rGO and the results are shown in Figure 5.3a. The XRD spectra of V_2O_5 NRs match well with that of

bulk V_2O_5 and the standard JCPDS data (41-1426) of orthorhombic α-V_2O_5 suggesting preservation of chemical structure after exfoliation. The intensity of (001) peak is relatively high than other peaks in V_2O_5 NRs indicating preferential stacking in the (001) direction. SAED pattern shown in Figure 5.3b corroborates well with the XRD results confirming the α-V_2O_5 structure of V_2O_5 NRs. The sampled V_2O_5 NRs was determined to be perpendicular to the electron beam based on the reciprocal lattice parameters. Based on this, the SAED spots were indexed as (hk0) as shown in Figure 5.3c. With the formation of Zn-V_2O_5 NR/rGO and (Zn+Mn)-V_2O_5 NR/rGO hybrids, a drastic change in the XRD spectra was observed. Due to disordering of the V_2O_5 structure with the intercalation of Zn^{2+}, only the (001) and (101) diffraction peaks at 19.80° and 21.05° were present. The Zn^{2+} intercalation expanded the d-spacing to 0.447 nm, as showed by the shift in 2θ value of (001) peak from 20.26° to 19.80°. Expanded interlayer spacing is expected to benefit during cycling by enabling facile Zn^{2+} intercalation and deintercalation. In the case of (Zn+Mn)-V_2O_5 NR/rGO, only a broad peak was observed which could indicate a larger degree of disordering in the structure, consistent with the FESEM observation. In clear contrast, with the co-precipitation with monovalent Na^+ ions, the XRD spectra appears quite similar to that of pristine V_2O_5 NRs indicating minimal disruption to the structure (Figure C.4). The precursor and hybrid materials were further characterized using Raman spectroscopy. The presence of Raman bands at 140.9, 281.6, 403.1, 529.4, 695.3, and 991.3 cm^{-1} corresponding to the -O-V-O-V- stretching, V-O_1 bending, V-O_3 bending, V-O_2 stretching, V-O_3 stretching, and V-O_1 stretching confirms the existence of orthorhombic V_2O_5 in all the samples. From Figure C.5, it can be seen that the Raman spectra of V_2O_5 NR resembles similar to that of bulk V_2O_5. This observation is additional evidence for the absence of disruption in the crystal structure of V_2O_5 NR after microwave-assisted exfoliation. The existence of Raman bands at 1350 and 1598 cm^{-1} that can be attributed to D and

G bands of graphene confirms the presence of rGO in the hybrid nanomaterials. The I_D/I_G ratios are low at 0.83, 0.92 and 0.87 for Zn-V_2O_5 NR/rGO, (Zn+Mn)-V_2O_5 NR/rGO and Na-V_2O_5 NR/rGO respectively. This suggests successful reduction of GO to rGO during thermal annealing. A broad peak at ~ 870 cm^{-1} was observed only in divalent cation mediated hybrids that can be attributed to the presence of multiple oxidation states of vanadium due to stronger interaction of the pre-intercalated cations. The peak is absent in Na-V_2O_5 NR/rGO which could indicate weaker interactions of Na^+ with V_2O_5 NR and rGO.

The surface chemical composition of the hybrids was determined using XPS analysis (Figures C.6 and C.7). In all samples, >82% of vanadium atoms exist as V^{5+} with the remaining exist as V^{4+}. The percentages of V^{4+} in V_2O_5 NRs, Zn-V_2O_5 NR/rGO, and (Zn+Mn)-V_2O_5 NR/rGO are 14.57%, 12.30%, and 17.30%, respectively. For comparison, it is 8.90% in bulk V_2O_5. The V^{4+} atoms were reported to lower polarization and improve ion diffusion during electrochemical cycling. The pre-intercalated Zn^{2+} and Mn^{2+} ions interact electronically with the V^{4+} centers preferably as evidenced by positive shifts in the BEs of V^{4+} $2p_{3/2}$ only compared to pristine V_2O_5 NRs. From the deconvolution of Zn 2p peaks of Zn-V_2O_5 NR/rGO, it was found that 76.4% exist as Zn^{2+} which are bound strongly to V_2O_5. The remaining Zn^{2+} exists as ZnO (12.8%) and acetate salt (10.8%). In (Zn+Mn)-V_2O_5 NR/rGO, 46.0% of Zn exists in +2 oxidation state bound to V_2O_5, while Mn exists in three different oxidation states: +2 (9.21%), +3 (41.50%), +4 (49.29%). Higher oxidation states of Mn could interact strongly with V_2O_5 and rGO due to stronger electrostatic interactions. The shift in C-metal ion to a higher BE compared to that of Zn-V_2O_5 NR/rGO validates the suggested stronger interaction between Mn ions and rGO which might help to stabilize the structure during cycling. Based on the results of XPS analysis, the elemental formula of Zn-V_2O_5 NR/rGO and (Zn+Mn)-V_2O_5 NR/rGO are estimated as $Zn_{0.42}V_2O_{7.54}$ and

$Zn_{0.12}Mn_{0.14}V_2O_{7.16}$, respectively. It is to be noted that the contribution from oxides of intercalated metals and rGO could have led to an excess of oxygen atoms. TGA was conducted in nitrogen atmosphere to determine the bulk composition of the hybrids (Figure C.8 and Table C-1). The wt% of M-V_2O_5 in Zn-V_2O_5 NR/rGO, (Zn+Mn)-V_2O_5 NR/rGO and Na-V_2O_5 NR/rGO are 78.34%, 87.02%, and 94.4% respectively. The rGO contents are 21.66%, 12.98%, and 5.6% respectively. The lower rGO content in Na-V_2O_5 NR/rGO is indicative of the ineffectiveness of monovalent Na^+ ions to coprecipitate V_2O_5 NRs and GO nanosheets effectively.

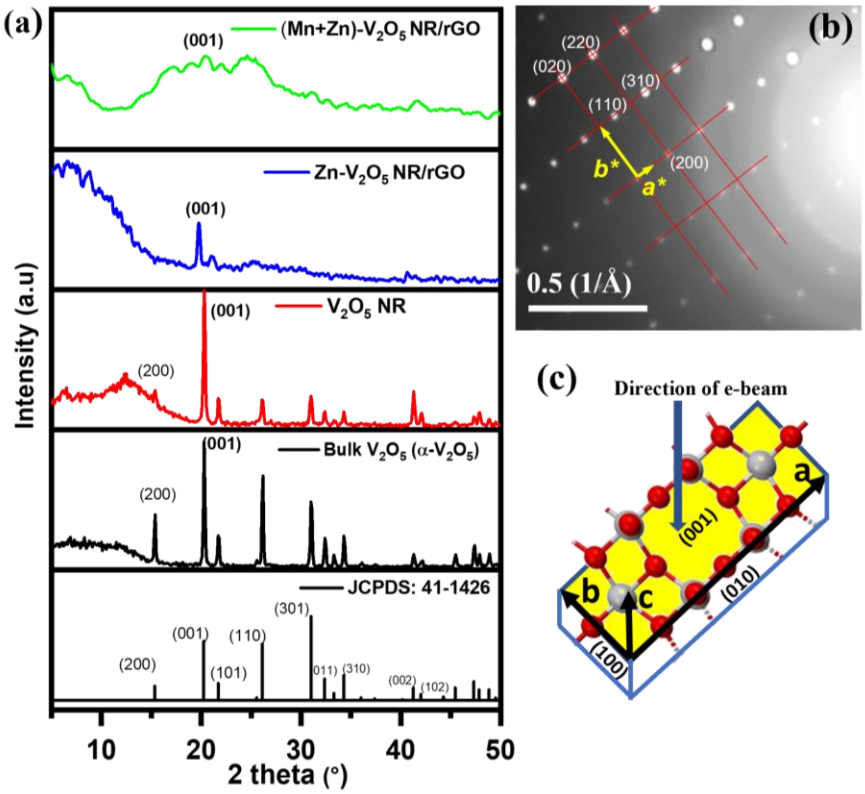

Figure 5.3. (a) Comparison of X-ray diffraction patterns of (Mn+Zn)-V_2O_5 NR/rGO and Zn-V_2O_5 NR/rGO with bulk V_2O_5 and V_2O_5 NR. (b) Selected area diffraction pattern and (c) crystal orientation of V_2O_5 NR. Reprinted (adapted) with permission from *ACS Sustainable Chem. Eng.* 2023, 11, 6, 2670–2679. Copyright 2023 American Chemical Society.

5.3.2.3 Electrochemical Characterization:

The synthesized hybrid materials and control samples were tested using galvanostatic charge/discharge tests to determine their specific capacities at different rates and to evaluate their long-term cycling stability (Figures 5.4a – 5.4e, C.9 – C.12). Zn-V_2O_5 NR/rGO was found to exhibit the highest specific capacity of 395 mAh/g at 0.50 A/g, which is equivalent to ~ 1.34 Zn^{2+} ion per V_2O_5 unit. The high specific capacity can be attributed to the availability of more active sites for Zn^{2+} intercalation due to the expansion of V_2O_5 interlayers caused by pre-intercalated Zn^{2+} during synthesis. With the increase in rates to 1.0, 2.0, 4.0, 6.0 A/g, the specific capacity decreased to 351, 287, 216, and 185 mAh/g, respectively. When cycled at 0.50 A/g again after completion of 50 cycles, the capacity declined by 25.6% to 293 mAh/g. The (Zn+Mn)-V_2O_5 NR/rGO hybrid delivered a relatively lower specific capacity of 291 mAh/g at 0.50 A/g probably due to occupation of some of the sites by Mn ions. However, at higher rates, the (Zn+Mn)-V_2O_5 NR/rGO exhibited specific capacities higher than that of Zn-V_2O_5 NR/rGO. At higher rates of 1.0, 2.0, 4.0 A/g, the specific capacities were 271, 248, and 231 mAh/g, respectively. Also, when switched the cycling rate back to 0.50 A/g, the capacity decayed by only 16%. The better capacity retention and rate performance characteristics of (Zn+Mn)-V_2O_5 NR/rGO can be attributed to the facile Zn^{2+} intercalation/deintercalation kinetics in combination with structural stability offered by the inactive Mn ions. The Na^+ expanded sample exhibited a decent specific capacity of 269 mAh/g at a low rate of 0.5 A/g. At higher rates, the specific capacity decreased by larger magnitudes, eventually to near zero at 6.0 A/g. The low rGO content and minimally disrupted V_2O_5 structure of Na-V_2O_5 NR/rGO could be the factors leading to its poor performance at high rates. As control, the rate performance tests were carried out for V_2O_5 NRs, bulk V_2O_5, rGO and physically mixed V_2O_5 NRs and rGO. Bulk V_2O_5 and bare rGO showed negligible specific capacities (<15 mAh/g)

while V_2O_5 NRs delivered ~ 80 mAh/g at 0.50 A/g. This is significantly higher than that of bulk V_2O_5 but much lower than that of M-V_2O_5/rGO hybrids. Mixing rGO to V_2O_5 NRs physically did not improve the specific capacity and exhibited poor performance at high rates due to insufficient interaction between them.

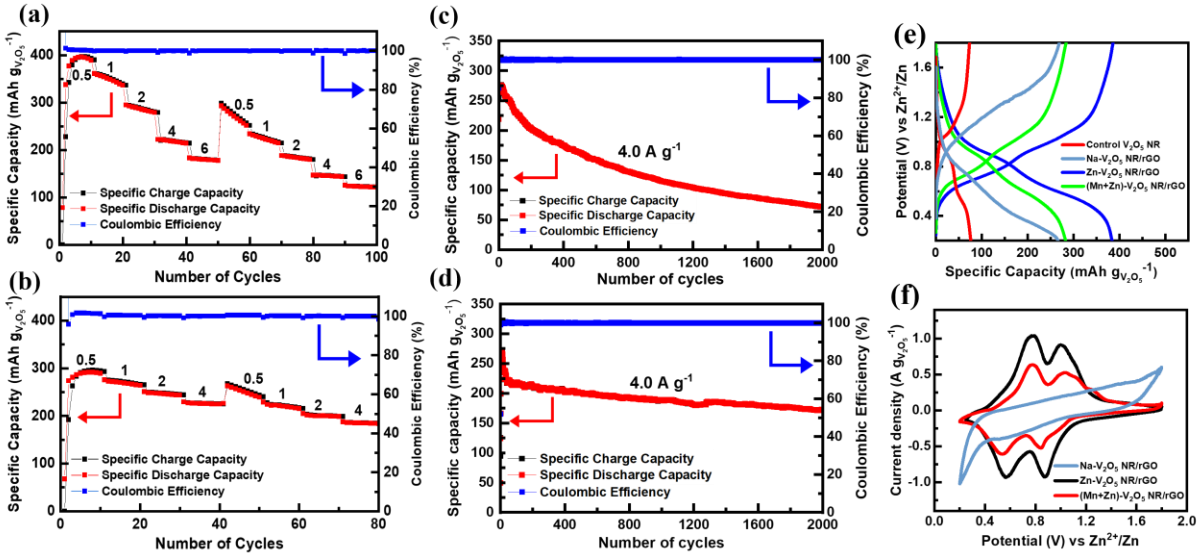

Figure 5.4. Rate performance of (a) Zn-V_2O_5 NR/rGO and (b) (Mn+Zn)-V_2O_5 NR/rGO. Cycle life performance of (c) Zn-V_2O_5 NR/rGO and (d) (Mn+Zn)-V_2O_5 NR/rGO at 4.0 A/g rate. (e) Typical galvanostatic charge/discharge curves and (f) cyclic voltammograms of different cathode materials. Reprinted (adapted) with permission from *ACS Sustainable Chem. Eng.* 2023, 11, 6, 2670–2679. Copyright 2023 American Chemical Society.

The long-term cycling results showcase the structural stability of (Zn+Mn)-V_2O_5 NR/rGO. The hybrid cathode delivered a specific capacity of 172 mAh/g at the end of 2000 cycles at 4.0 A/g. This corresponds to a 77% capacity retention from cycle #50 to cycle #2000. The specific capacity and the long-term cycling stability of (Zn+Mn)-V_2O_5 NR/rGO is comparable to that of other state-of-the-art V_2O_5 based AZIB cathodes (Table C-3). On the other hand, the Zn-V_2O_5 NR/rGO's specific capacity degraded much faster to 72 mAh/g in 2000 cycles at 4.0 A/g. While the monovalent Na^+ co-precipitated Na-V_2O_5/rGO delivered a very low capacity of 34 mAh/g

which decayed further by about 40% at the end of 500 cycles. Analysis of the initial cycles of cycling revealed that (Zn+Mn)-V_2O_5 NR/rGO activates slowly during which the specific capacity increases from 50 mAh/g in the 1st cycle to a maximum of 272 mAh/g in the 10th cycle. Following that, the capacity decreases slightly and get stabilized at 222 mAh/g in the 50th cycle. In the case of Zn-V_2O_5 NR/rGO, the activation occurs relatively faster exhibiting a capacity of 250 mAh/g delivered during the first discharge. It increases slightly to 276 mAh/g in the 15th cycle and then stabilizes at 254 mAh/g in the 50th cycle. The activation process that can be attributed to the reconfiguration of Zn^{2+} ion diffusion pathways is slower for (Zn+Mn)-V_2O_5 NR/rGO due to the stronger interaction between the Mn ions of different oxidation states and the V_2O_5 host. It is to be noted that Na-V_2O_5 NR/rGO exhibits no such activation with the specific capacity beginning to decrease right from the first cycle. This suggests that neither new sites nor new pathways open up for Zn^{2+} ion diffusion.

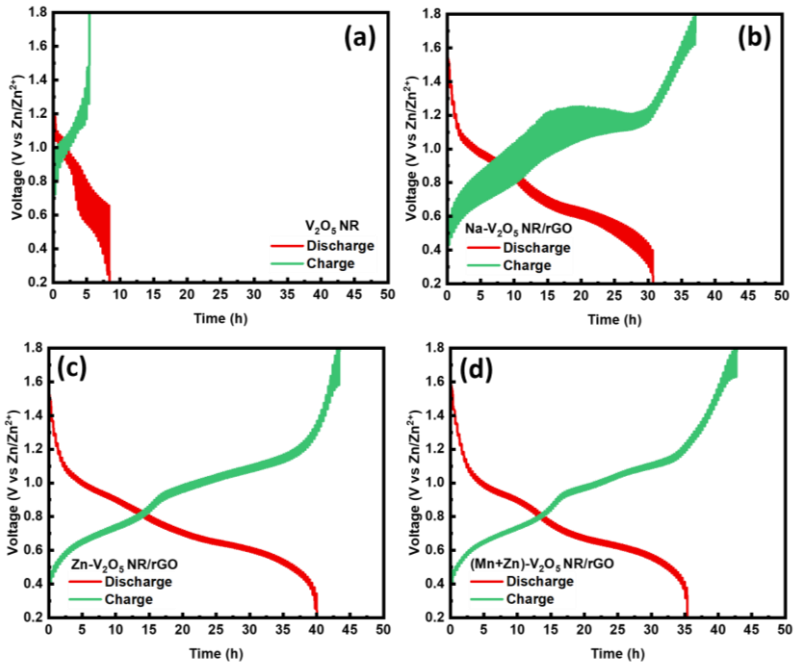

Figure 5.5. GITT discharge and charge voltage profiles for the (a) V_2O_5 NR, (b) Na-V_2O_5 NR/rGO, (c) Zn-V_2O_5 NR/rGO, (d) (Mn+Zn)-V_2O_5 NR/rGO. Reprinted (adapted) with permission from *ACS Sustainable Chem. Eng.* 2023, 11, 6, 2670–2679. Copyright 2023 American Chemical Society.

As shown in Figures 5.4f and C.13, cyclic voltammograms for Zn-V_2O_5 NR/rGO and (Zn+Mn)-V_2O_5 NR/rGO exhibit two pairs of peaks centered around 0.95 and 0.65 V, respectively. Each pair of peaks correspond to two step redox reactions consistent with the plateaus present in galvanostatic charge/discharge voltage curves. The hybrids exhibit activation similar to the activation process observed during galvanostatic cycling. In comparison, a stark contrast in the cyclic voltammogram was observed for Na-V_2O_5 NR/rGO electrode which does not contain any redox peaks suggesting a dominant capacitive behavior which explains the absence of activation during cycling. GITT studies were conducted to understand the kinetics of Zn^{2+} ion intercalation in different cathode materials (Figures 5.5, C.14). From the reduction in amplitude of voltage changes during the application of GITT current pulses, it can be qualitatively determined that the Zn^{2+} ion diffusion kinetics increase with the expansion of V_2O_5 NRs by pre-intercalation of divalent cations. From the GITT calculations (Figure C.15 and Table C-2), the Zn^{2+} diffusion coefficients were found to increase in the following order - V_2O_5 NR < Na-V_2O_5 NR/rGO < (Zn+Mn)-V_2O_5 NR/rGO < Zn-V_2O_5 NR/rGO. These studies help to deduce the following understandings. Zn-V_2O_5 NR/rGO provides the highest specific capacity owing to the participation of bridging Zn ions during charge/discharge which makes most sites available for Zn^{2+} intercalation. However, intercalation and deintercalation of bridging Zn ions destabilizes the structure leading to rapid capacity fading. In the case of (Zn+Mn)-V_2O_5 NR/rGO, the occupation of some of the possible sites by Mn ions of multiple valence states results in the slight decrease in specific capacity and Zn^{2+} diffusion kinetics. The stronger interaction provided by the Mn ions instead act as pillars helping to keep the hybrid structure stable during cycling. With the use of monovalent cations in Na-V_2O_5/rGO, the ineffective hybrid formation and the minimally disrupted V_2O_5 structure lead to their poor performance.

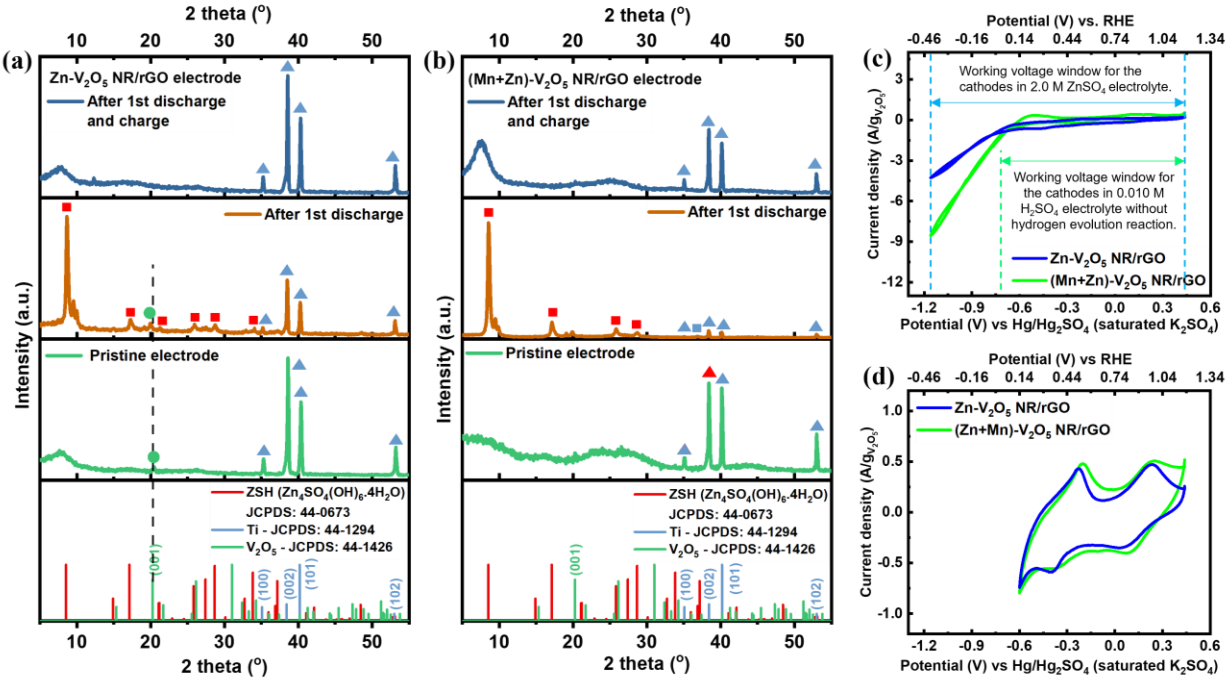

Figure 5.6. Ex-situ XRD spectra of (a) Zn-V_2O_5 NR/rGO and (b) (Zn+Mn)-V_2O_5 NR/rGO electrodes after discharge/charge in the first cycle. Cyclic Voltammograms of (Zn+Mn)-V_2O_5 NR/rGO and Zn-V_2O_5 NR/rGO electrodes in 0.010 M H_2SO_4 solution in potential windows of (c) -1.16 V to +0.44 V, (d) -0.60 V to +0.44 V (vs Hg/Hg_2SO_4 (satd. K_2SO_4)). Reprinted (adapted) with permission from *ACS Sustainable Chem. Eng.* 2023, 11, 6, 2670–2679. Copyright 2023 American Chemical Society.

Ex-situ XRD measurements of for Zn-V_2O_5 NR/rGO and (Zn+Mn)-V_2O_5 NR/rGO after discharge and charge were conducted to understand the involvement of H^+ during intercalation (Figure 5.6a and Figure 5.6b). In the discharged electrodes, formation of $Zn_4SO_4(OH)_6.4H_2O$ was observed. This indicates that possible intercalation of H^+ ions which cause an increase in local pH leading to formation of $Zn_4SO_4(OH)_6.4H_2O$ crystals likely on the exterior surface of V_2O_5 NRs. The absence of XRD peaks corresponding to $Zn_4SO_4(OH)_6.4H_2O$ in charged electrodes show that H^+ intercalation is reversible. Reversible intercalation/deintercalation of H^+ ions help to boost the capacity of V_2O_5 beyond its theoretical capacity of 294 mAh/g. CV studies (Figures 5.6c and 5.6d) show the occurrence of H^+ intercalation in the hybrid cathodes in 0.010 M H_2SO_4 solution at

pH=1.70. However, the evolution of hydrogen does not occur on these cathode materials in the 2.0 M $ZnSO_4$ electrolyte in the voltage window used. Though the capacity contribution due to H^+ ions might be minimal considering its low concentration (~ 10^{-7} M) compared to that of Zn^{2+} (2.0 M), exact quantification needs further studies.

5.4 Conclusion

Synthesis of nanostructured M-V_2O_5 NRs/rGO hybrids was demonstrated utilizing a scalable, facile coprecipitation technique facilitated by divalent cations, compared to hydrothermal synthesis methods. The comparable performance of the synthesized hybrids in comparison to the state-of-the-art V_2O_5 cathodes synthesized by other methods proves the effectiveness of the method. The Zn-V_2O_5 NRs/rGO exhibits the highest specific capacity of ~ 395 mAh/g at 0.50 A/g, but the stability is poor. Though, the pre-intercalation of Mn^{2+} ions along with Zn^{2+} ions decreases the specific capacity to ~ 291 mAh/g at 0.50 A/g, the (Mn+Zn)-V_2O_5 NRs/rGO exhibits superior cycling stability at 4.0 A/g rate with a capacity retention of 77%. This enhanced stability is attributed to the stronger interactions between Mn^{n+} ions and V_2O_5 units. The storage mechanism of the hybrid cathodes is found to be due to the intercalation/deintercalation of Zn^{2+} as well as H^+ ions. This study illustrates a facile technique that has the potential to adjust the hybrid's specific capacity and cycling stability by altering the pre-intercalated metal ions, thereby advancing the development of AZIB cathodes.

Chapter 6 - Ongoing Studies

6.1 Li Electrodeposition on Au Coated VACNFs

As seen in Chapter 3, it is important to induce homogeneous nucleation under a wide range of current densities. A common strategy to improve Li nucleation homogeneity, lithiophilic coatings are typically applied to 3-D hosts which are intrinsically lithiophobic.[243, 244] Lithiophilic materials reduce the interfacial energy lowering the contact angle between lithium and the substrate surface.[161] Common lithiophilic coatings composed of Au, Ag, ZnO, MgO, etc. have been demonstrated to improve the cycle life of planar as well as 3-D LMA hosts.[245-249]

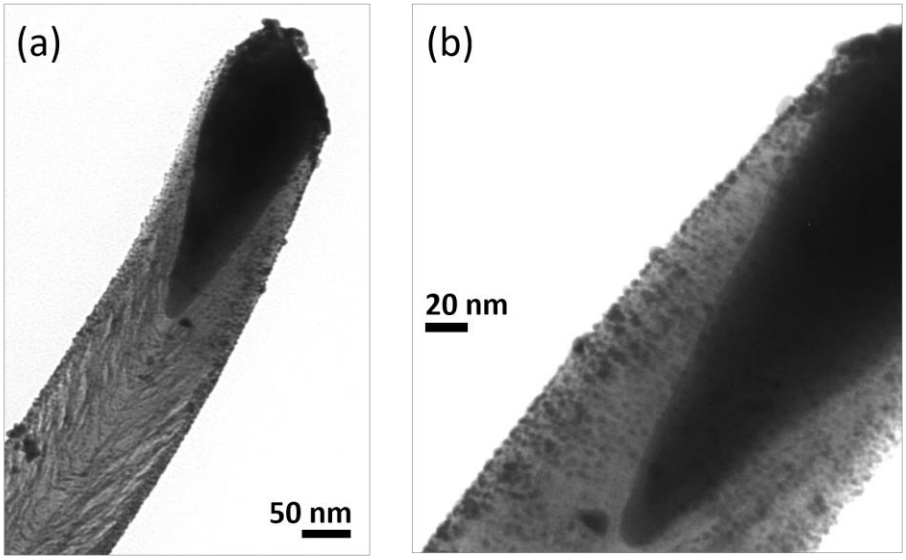

Figure 6.1. TEM images of a VACNF sputter-coated with Au of 10 nm nominal thickness.

In this study, we have chosen to deposit Au nanoparticles on VACNFs using ion-beam sputtering technique and study their effect on the lithium electrodeposition and electrochemical performance. Using Gatan ion-beam coater, a nominal thickness of 10 nm of Au was sputter-coated on VACNF electrodes of 15 mm diameter. The height of the individual VACNFs is about

~ 14 µm. The Au10/VACNFs were first characterized using TEM. Figure 6.1 shows that Au got deposited mostly as spherical nanoparticles of avg. diameter ~ 3.2 nm with some agglomerated particles. The Au nanoparticles were found to get deposited throughout the length of the VACNFs. Then, electrochemical characterization of Au10/VACNF/Cu electrodes were carried out and their results are shown in Figure 6.2. When subjected to CE cycling test at 1.0 mA/cm^2 with a cycling capacity of 2.0 mAh/cm^2, Au10/VACNF/Cu electrode exhibited an improved cycle life reaching 79.0% in 212 cycles, in comparison to that of pristine VACNF/Cu electrode (80.3% in 171 cycles). The average CE during the first 100 cycles is the same at 97.8% for both Au-coated and pristine VACNF electrodes. With the deposition of Au, the Li nucleation overpotential got reduced further to 5.6 mV compared to that of VACNF without any coatings. This shows that deposition of Au nanoparticles clearly improves the lithiophilicity of the electrode. However, incorporating Au did not improve the coulombic efficiency, i.e., the repeated formation of SEI did not get prevented. This was reflected in the symmetric cell cycling performance where Au10/VACNF/Cu electrode lasted for only 155 hours, slightly less than that of VACNF/Cu electrode (161 hours).

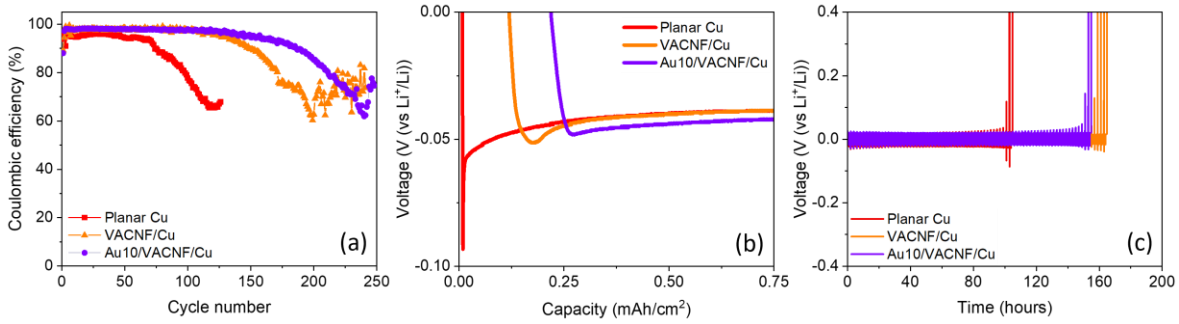

Figure 6.2. (a) CE cycling performance at 1.0 mA/cm^2 with a cycling capacity of 2.0 mAh/cm^2. (b) Li plating voltage curves illustrating the difference in Li nucleation overpotential among various hosts studied. (c) Symmetric cell performance of different electrodes pre-plated with 2.0 mAh/cm^2 cycled at a current density of 1.0 mA/cm^2 with a cycling capacity of 1.0 mAh/cm^2.

The evolution of Li nucleation overpotential over cycles is shown in Figure 6.3. With cycling, an increase in nucleation overpotential along with the decrease in the capacity it takes for the potential to reach the nucleation dip was observed. Figure 3b clearly shows that the Li nucleation overpotential increase over cycles reaching a stable value which is similar to that of pristine VACNF/Cu electrode (~ 25 to 30 mV). This observation could indicate the waning of effectiveness of gold in reducing the nucleation overpotential within the few initial cycles. From this, it can be understood that lithiophilic Au coatings are ineffective for long-term cycling.

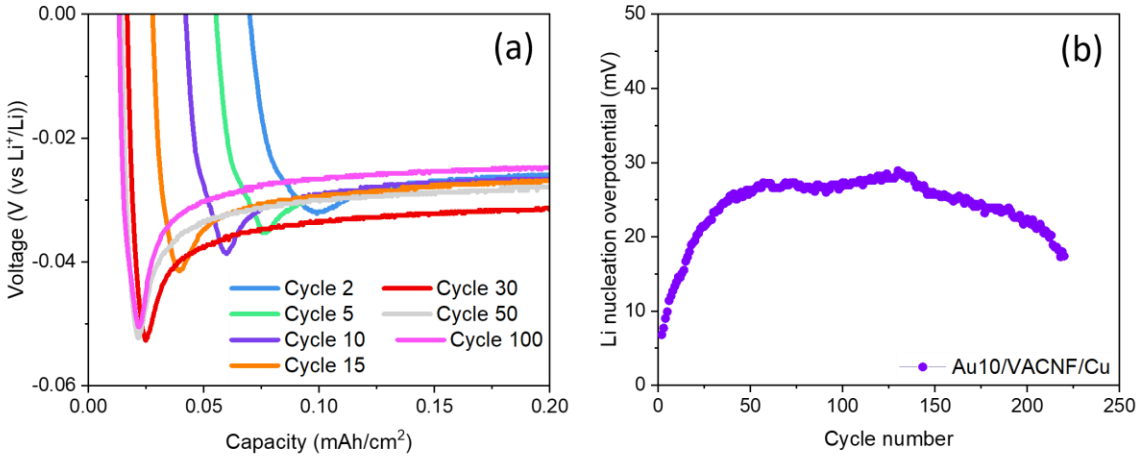

Figure 6.3. Evolution of (a) Li plating voltage curves and (b) Li nucleation overpotential over cycling at 1.0 mA/cm^2.

In-situ Raman studies were conducted using Au10/VACNF/Cu electrodes to understand whether there is any enhancement in SERS effect leading to identification of SEI components such as LiF, Li_2O, etc. other than Li_2C_2. As observed earlier for pristine VACNFs, similar changes to the VACNFs' characteristic D and G bands were observed during Li intercalation/Li plating. However, a drastic difference was observed in the onset of Li_2C_2 band. In VACNF/Cu electrode, the band corresponding to Li_2C_2 started to appear only when the Li plating started to occur at potentials below 0 V vs Li^+/Li. Interestingly, in Au10/VACNF/Cu electrode, the Li_2C_2 band

appeared much earlier during the Li intercalation stage at positive potentials higher than 0 V (Figures 6.4a and 6.4b). If the early appearance of Li_2C_2 band is due to SERS effect from Au nanoparticles, they should appear in the very first cycle when the SEI forms and continue to be present after deintercalation. But the Li_2C_2 band disappears with Li deintercalation as shown in Figure 6.4b. Similar phenomenon was observed during Li plating/stripping as well (Figure 6.4d). It is well known that Au reversibly forms alloys with Li at potentials higher than 0 V.[250] Considering this together with the observed pattern in changes to the Li_2C_2 band can only be attributed to the presence of SERS effect of Li-Au alloys in addition to the SERS effect of nanoscale lithium. Further studies are required to explain the observed phenomenon in detail. It is worth noting that repeated observation of the phenomenon for a number of cycles implies that Au nanoparticles do remain active during cycling.

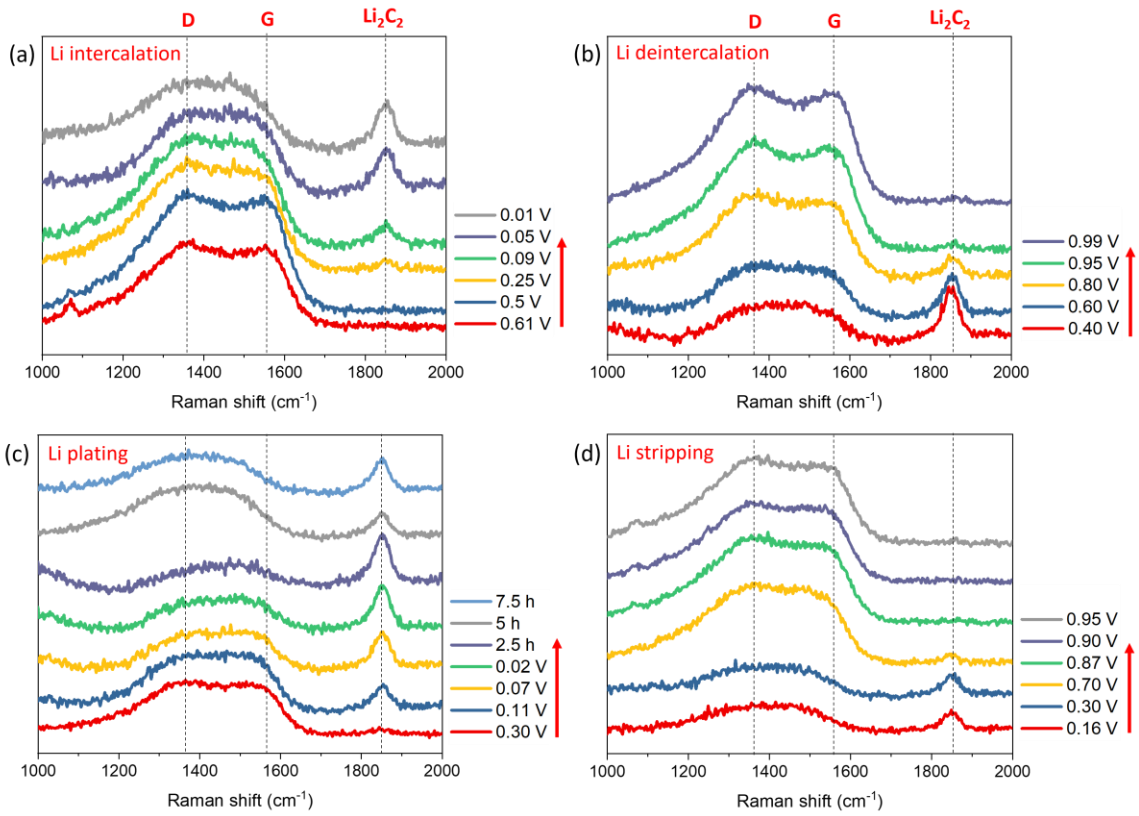

Figure 6.4. In-situ Raman measurements of Au10/VACNF/Cu electrode during (a) Li intercalation, (b) Li deintercalation, (c) Li plating, and (d) Li stripping processes.

One of the expected implications of enhanced lithiophilicity is the improved homogeneity in Li electrodeposition, especially at low current densities. To understand this, morphology of Li electrodeposited at 0.10 mA/cm^2 for a capacity of 0.75 mAh/cm^2 was studied using FESEM. The optical images of Au10/VACNF/Cu electrode after lithium plating and after complete stripping are shown in Figures 6.5a and 6.5b, respectively. The metallic lithium was found to get electrodeposited throughout the entire surface of the electrode. The black colored electrode after the Li stripping step indicates that the electrodeposited lithium was stripped completely. Figures 6.5c – 6.5f show the morphology of electrodeposited lithium on VACNF/Cu electrode, while Figures 6.5g – 6.5j show the morphology on Au10/VACNF/Cu electrode. By comparison, it can be deduced that Au nanoparticles do help to increase the density of nucleation leading to relatively smaller islands (~ 20 – 100 μm). The density of infiltrated Li micro-columns also improved. A small number of spherical Li particles can also be observed. Even though the particle density was improved, sputtering of Au of 10 nm nominal thickness did not improve the homogeneity satisfactorily. The highly porous noodle-like Li which was found to be undesirable for reversible cycling was still present. The effectiveness of lithiophilic coatings that exist during the nucleation stage is quite minimal during Li growth. Similar results can be found in Woo-Bin Jung's work where even with well-separated large Au nanodots of 300 nm diameter and 50 nm thickness induced uniform, preferential nucleation on Au nanodots but did not form homogeneous islands with further plating. Use of thicker lithiophilic coatings, similar to other works, might help towards achieving homogeneous electrodeposition. However, thick coatings would reduce the anode's Li plating capacity and the energy density of the battery. Use of core-shell structures made up of amorphous carbon shell with lithiophilic seeds on the insides of a hollow core could be beneficial to controllably confine Li growth inside the structure.[250, 251]

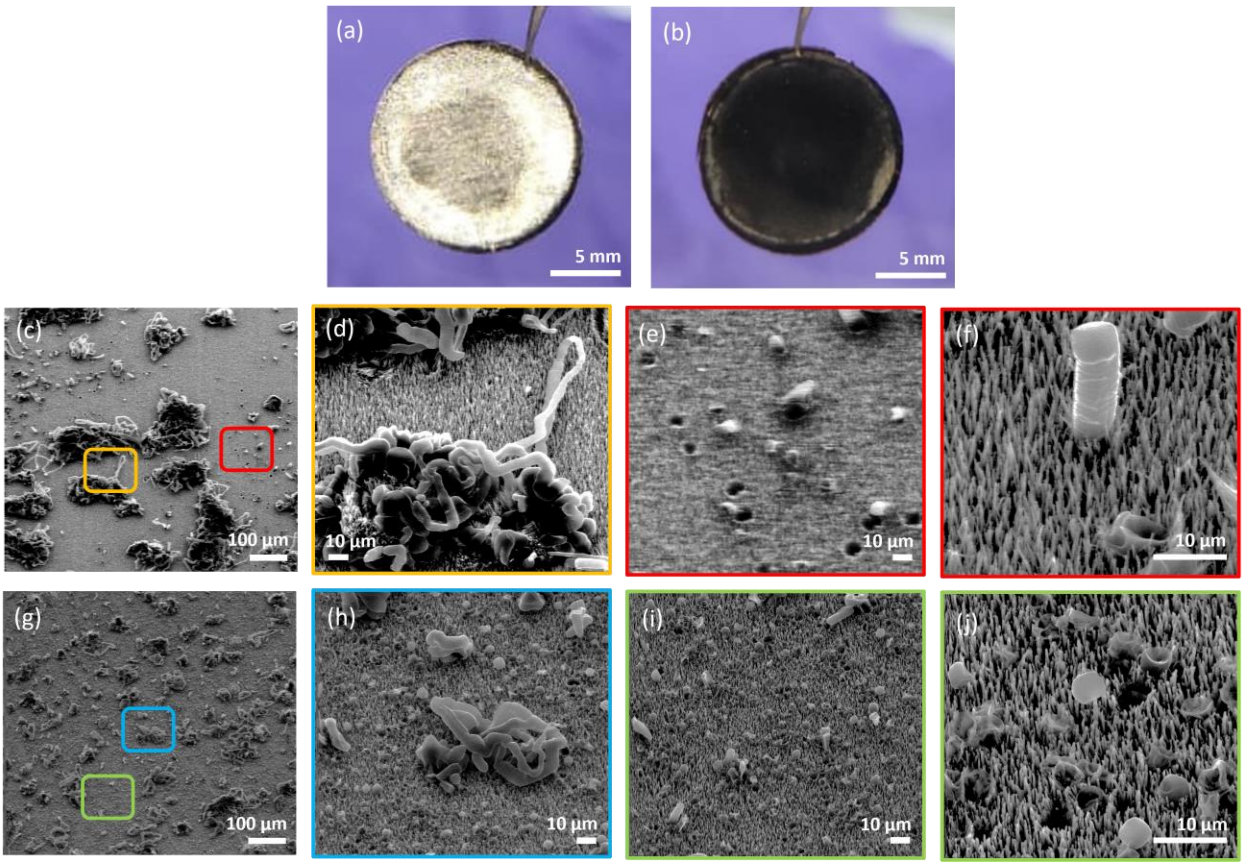

Figure 6.5. Optical images of Au10/VACNF/Cu electrodes (a) after plating 0.75 mAh/cm^2 of Li at 0.10 mA/cm^2 and (b) after complete stripping. 30° perspective FESEM images of (c)-(f) VACNF/Cu and (g)-(j) Au10/VACNF/Cu electrodes after plating 0.75 mAh/cm^2 of Li at 0.10 mA/cm^2.

Similar to previous observations, homogeneous large islands were observed in Au10/VACNF/Cu electrode at regions close to the periphery of the electrode due to higher internal pressure. High magnification images of the VACNFs which were not engulfed by the micron size Li particles after electrodepositing with 0.75 mAh/cm^2 Li at 0.10 mA/cm^2 were shown in Figure 6.6a. The average diameter of the VACNFs were determined to be 235.4 ± 48.7 nm (shown in Figure 6.6c), which is significantly higher than the diameter of pristine VACNFs (~ 154 nm). This indicates the presence of ~ 40 nm thick nanoscale Li and SEI. Highly aligned vertical structure without formation of micro-bundles is another evidence for nanoscale deposition on VACNFs'

surface. Upon complete stripping, the diameter of VACNFs shrunk to 183.4 ± 39.4 nm (Figures 6.6b and 6.6d). The larger dimensions than that of pristine VACNF is due to the presence of co-axial SEI.

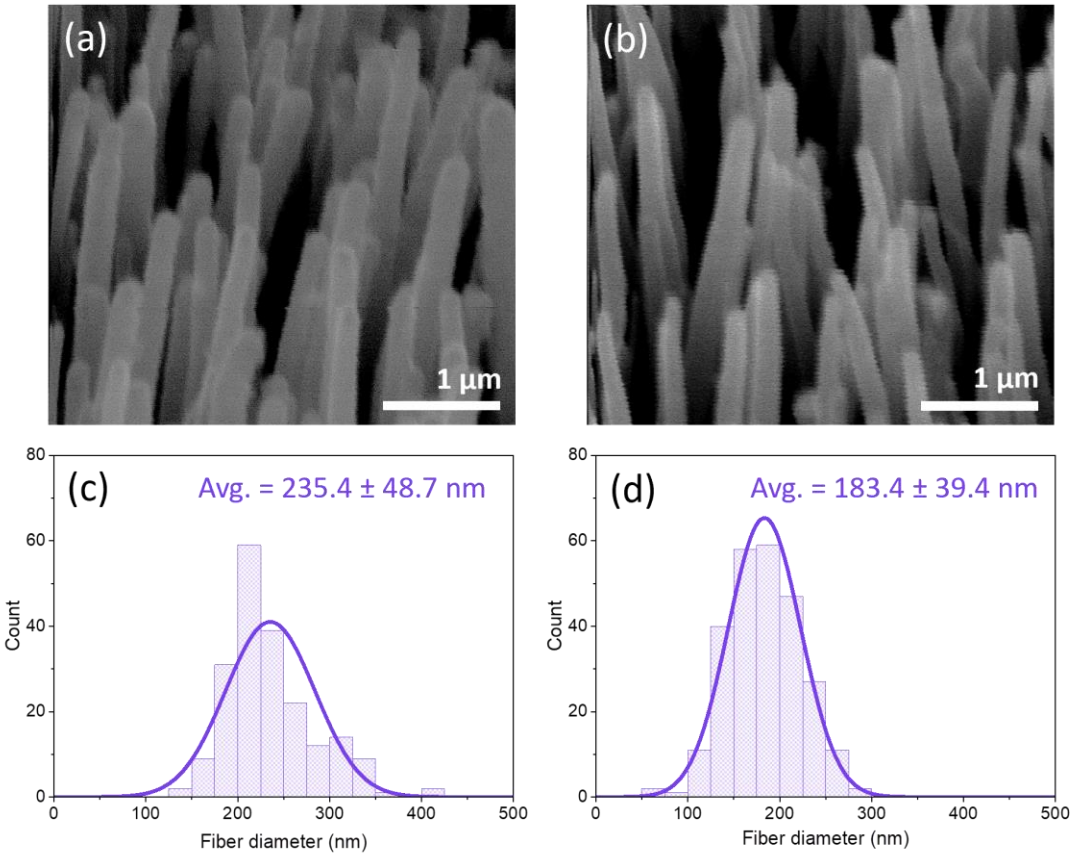

Figure 6.6. FESEM images of Au10/VACNF/Cu (a) after plating at 0.10 mA/cm^2 for a capacity of 0.75 mAh/cm^2 and (b) after complete stripping, taken at a 30° perspective. Corresponding size distribution histograms of VACNF diameter after (c) Li plating and (d) Li stripping.

For further analysis of nanoscale Li, VACNFs that were scraped off after electrodeposition were imaged using cryo-TEM. Figure 6.7 shows the uniform coverage of individual VACNFs by co-axial sheaths of electrodeposited Li. Dark splotches that can be observed inside the nanoscale Li are most likely the sputter-coated Au nanoparticles that got aggregated and transformed.

Considering that these are sampled from an electrode which had experienced a single Li plating step, the transformation of spherical Au nanoparticles to irregularly shaped particles is consistent with the increase in Li nucleation overpotential that begins from the first cycle. Over cycles, it is expected that Au nanoparticles would further aggregate and disconnect from the surface eventually leading to being completely ineffective to function as intended. Similar aggregation and redistribution of alloy-forming Ag nanoparticles were observed by Sun et al.[252] It has been further demonstrated that TiO_2 which only forms Li-intercalation compounds remain as stable nucleation seeds during cycling.

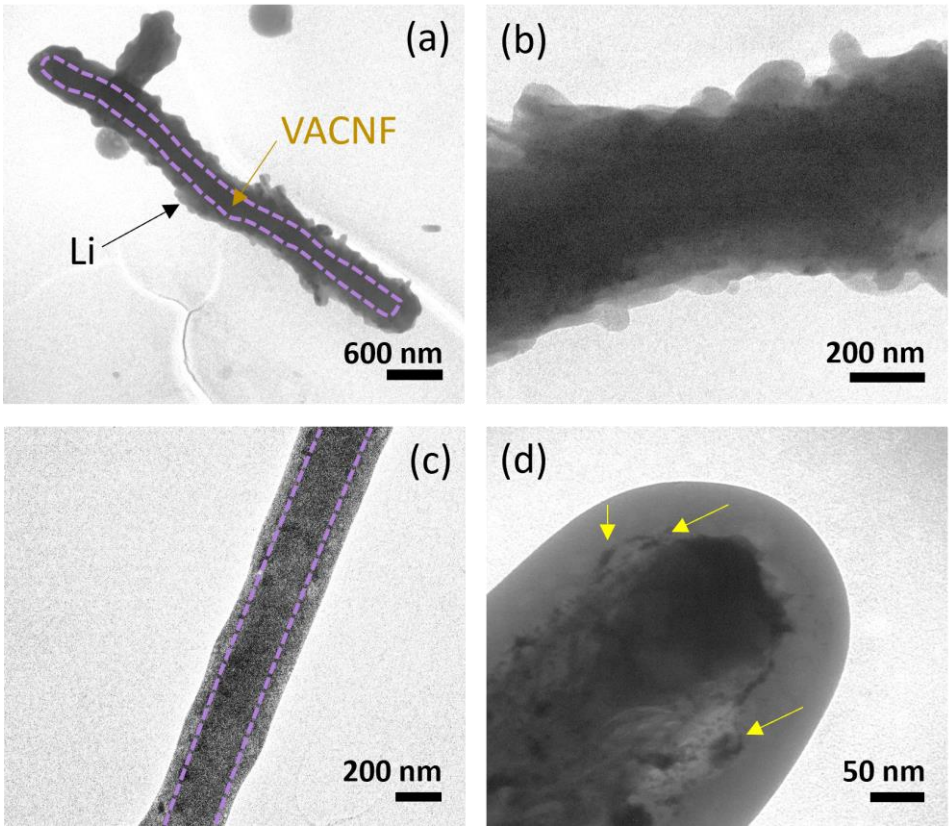

Figure 6.7. Cryo-TEM images of individual fibers removed from Li plated Au10/VACNF/Cu electrode of 0.75 mAh/cm^2 plated at 0.10 mA/cm^2. Yellow-colored arrows highlight the aggregated Au nanoparticles.

Au nanoparticles coating on VACNFs only play a limited role in reducing the Li nucleation overpotential in the initial cycles and in improving the nucleation density at low current densities. They do not enhance the coulombic efficiency and tend to become ineffective over cycling. Hence, based on this study, it can be concluded that lithiophilic thin films that form alloys with Li are not effective coatings for 3-D hosts.

6.2 Low-Tortuous Electrospun Carbon Nanofibers as LMA Hosts

Though VACNFs possess ideal characteristics for a LMA host, their Li storage capacity is limited by the height of the fibers which has an upper limit of 20 – 30 µm. To address that, in this study, we aimed to develop low-tortuous electrospun carbon nanofibers as LMA hosts with high plating capacity. Electrospinning is a versatile technique to produce free-standing nanofibers composed of various materials such as polymers, carbon, etc. It is possible to develop a wide array of microscopic (hollow, porous, solid) and macroscopic (random, ring like, aligned) structures using this technique.[253, 254] The electrospun materials have been demonstrated to be applicable for a range of applications such as batteries, fuel cells, biomaterials, etc.[125, 255-260] Unlike VACNF-based electrodes, electrospun fibers can be fabricated with thicknesses ranging from tens of microns to hundreds of microns. Since they are binder-free in nature, multiple electrospun mats can be stacked to increase the total Li storage capacity easily. The conductive nature of carbon nanofibers (CNFs) makes it viable for its use as current collector/host. However, electrospun carbon mats have disadvantages such as lithiophobic surface and tortuous structure that need to be overcome in order to make them applicable as hosts for LMAs.[261, 262] To achieve the aim to develop aligned electrospun LMA host structures and to subsequently study the effect of tortuosity and nano-confinement effects in hollow structures, the first goal is to develop electrospun mats that

have a well-defined, uniaxially, or biaxially aligned pore structure such that the tortuosity for lithium-ion diffusion is minimal. The electrodes should also possess sufficient mechanical strength and suitable porosity to accommodate lithium.

Polyacrylonitrile (PAN) is a widely used polymer to produce carbon fibers.[263] The use of PAN for electrospinning has been studied extensively.[264, 265] Hence, we chose PAN as the precursor for CNFs. A schematic for producing CNF membrane is shown in Figure 6.8. To do the electrospinning, a suitable high voltage (13 – 18 kV) was applied to the emitter through which a PAN solution consisting of 0.8g of PAN and 8.0 g of dimethylformamide (DMF) was pumped at 1.0 mL/h. The collector is electrically grounded and is separated from the collector by a distance of 17 cm. Under the coulombic force exerted by the external field and due to electrostatic repulsion between the surface charges of the polymer solution, a Taylor cone forms.[266, 267] When the magnitude of electrostatic forces exceeds the surface tension of the polymer solution, a polymer jet is ejected outwards towards the collector. The polymer jet transitions from a stable translation to the characteristic whipping motion. During the transport of the jet from the emitter to the collector, the solvent evaporation occurs in addition to stretching resulting in deposition of solid, thin PAN fibers. An aluminum foil wrapped around a rotating drum collector rotating at 100 rpm was used as the substrate for collecting the PAN fibers. After electrospinning, the electrospun PAN mat was separated as a free-standing membrane and was thermally treated at 280 °C for 2 hours in air to stabilize the fiber structure. During the oxidizing thermal treatment, cyclization of nitrile group occurs and the color changes from white to brown.[268, 269] The stabilized PAN membrane was thermally decomposed in nitrogen atmosphere at 1000 °C for 1 hour to convert them into conductive CNFs. During the thermal treatment, reduction in mass and fiber diameter occurs.[270]

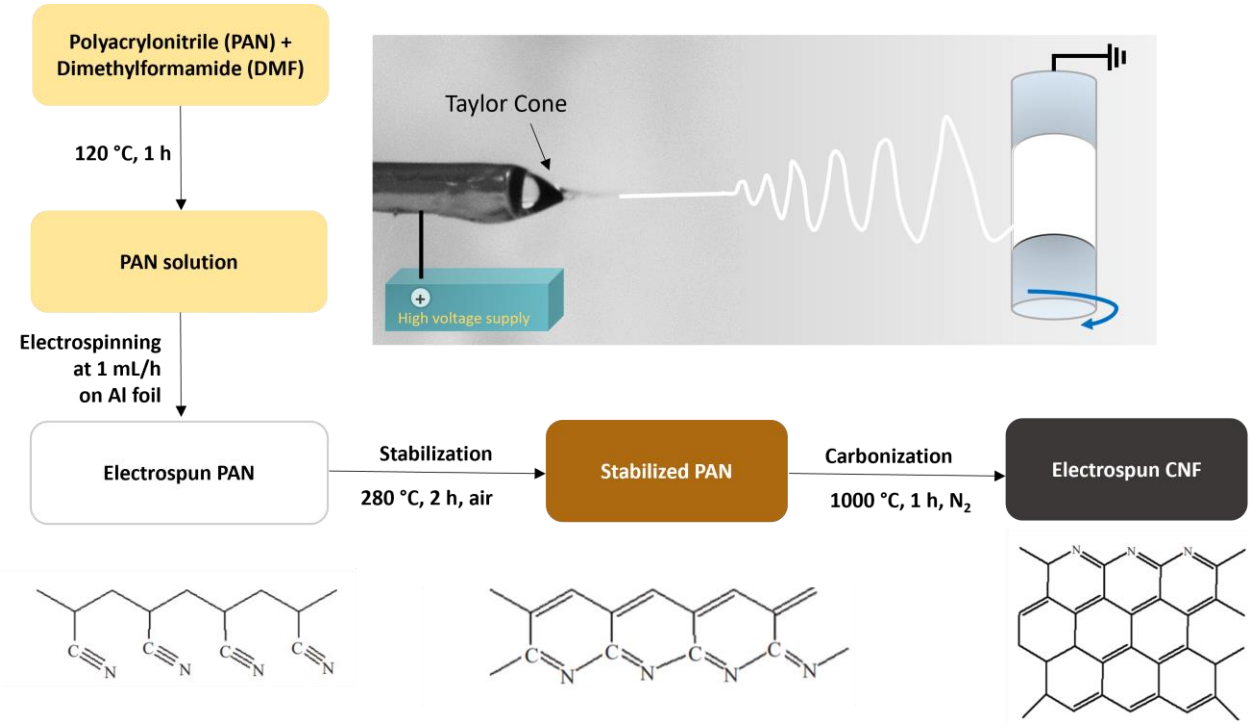

Figure 6.8. A schematic showing the processes involved in the production of electrospun CNF membrane.

The FESEM images of electrospun CNF membranes produced under different operating parameters are shown in Figure 6.9. For an electrospinning duration of 2 hours with an applied high voltage of +17 kV, the obtained CNF membrane was about 7.5 µm thick. The individual nanofibers were randomly stacked, non-porous solid structures having a diameter of 140 nm. With the increase in electrospinning duration to 3 hours, the thickness of the CNF membrane increased to ~ 14 µm. The average fiber diameter was about 127 nm. With a decrease in the applied voltage to 13 kV, the average fiber diameter increased to 285 nm. The given CNF membrane was electrospun for 4 hours to achieve a membrane thickness of 32 µm.

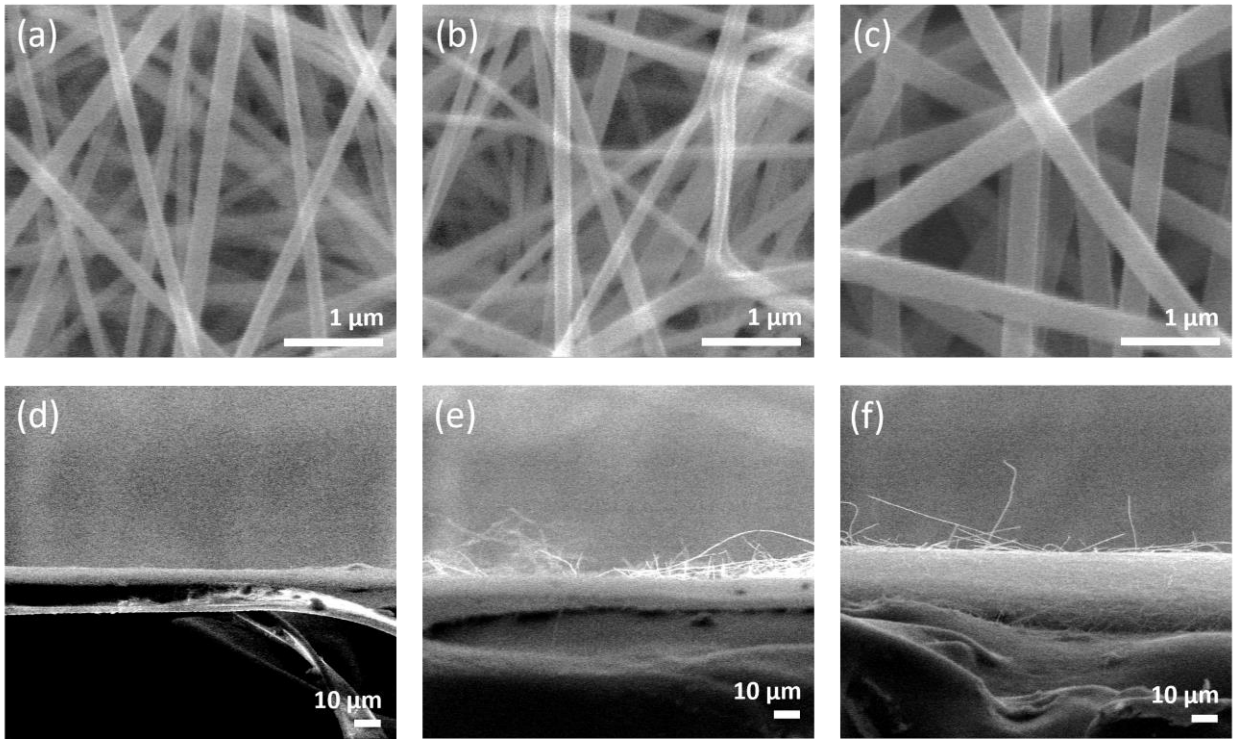

Figure 6.9. FESEM images of electrospun CNF membranes prepared with applied voltages and electrospinning durations of (a), (d) 17 kV and 2 h, (b), (e) 17 kV and 3 h, (c), (f) 13 kV and 4 h.

To produce electrospun CNFs with aligned fibers, two different approaches were attempted. The first one employed electrically grounded aluminum tapes as parallel plate electrodes separated by an insulative quartz plate with its surface raised higher than the electrodes by about 0.3 mm, as shown in Figure 6.10a. When electrospun for 1 min, highly aligned PAN fibers got deposited on the quartz plate across the parallel plates as shown in Figures 6.10b and 6.10c. The electrostatic forces stretch the fibers while the electrostatic repulson between the charged fibers force them to align.[271, 272] With continuous electrospinning for about 60 min, the density of uniaxially aligned PAN fibers increased (Figures 6.10d and 6.10e). However, most of the fibers deposition occurred on the aluminum as randomly stacked fibers rather than as aligned fibers on the quartz plate. After a certain duration, the density of aligned PAN fibers did not

increase further due to the electrostatic repulsion between the incoming fibers and the already deposited ones. There were not enough layers of aligned PAN fibers to be able to separate from the quartz plate. Hence, carbonization of PAN fibers was done together with the quartz plate. Upon carbonization, the density of fibers and size of fibers decreased further (Figures 6.10f and 6.10g). Since thick, free-standing membranes could not be produced, this method cannot be utilized to produce 3-D electrodes for LMA host application.

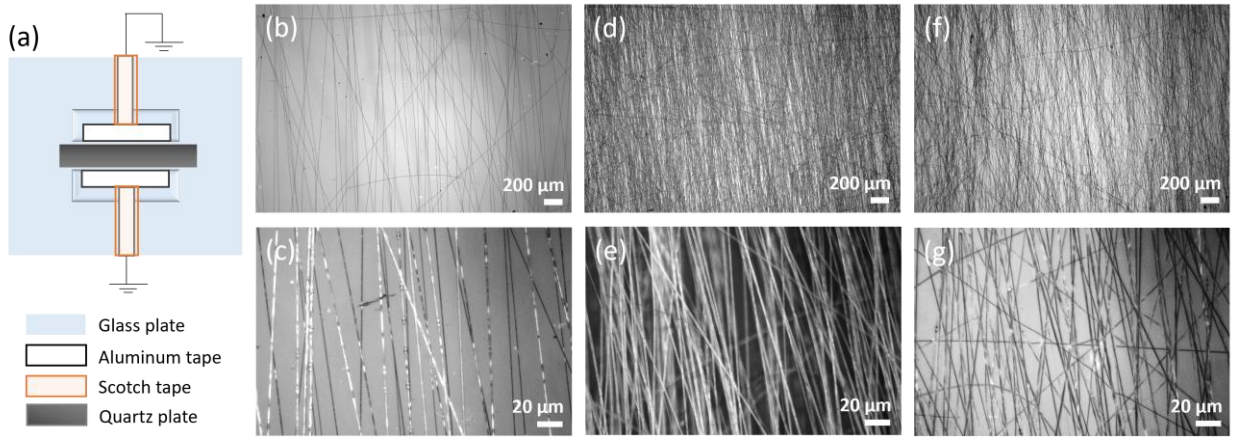

Figure 6.10. (a) A schematic showing parallel-plate electrodes for preparation of uniaxial fibers. Optical images of uniaxially aligned PAN fibers electrospun for (b), (c) 1 min, (d), (e) 60 min. (f), (g) Optical images of uniaxially aligned CNFs by calcination of the aligned PAN fibers.

The second approach utilizes mechanical forces using the drum collector was rotated at high speeds greater than 1000 rpm to align the collected PAN fibers along the direction perpendicular to the axis of rotation.[253] The electrospun fibers were obtained with different collector rotation speeds of 1250, 1500 and 3000 rpm. At rotation speeds of 1250 and 1500 rpm, stable Taylor's cone was obtained with an applied voltage of 12 kV. With the rotation speed increased to 3000 rpm, the polymer jet got split into two at an applied voltage of 11 kV. The optical images of PAN fibers are shown in Figures 6.11a – 6.11c and their angular alignments were analyzed. For the rotation speeds of 1250, 1500, and 3000 rpm, the fraction of fibers aligned within

-20° to +20° with respect to the direction of rotation were 62, 71, and 75% respectively (Figures 6.11d – 6.11f). With the increase in rotation speed, the fraction of aligned fibers increases. Compared to the parallel-plate method, the quality of uniaxial alignment via high-speed rotating collector is inferior. However, thicker free-standing PAN membranes that can processed further can be obtained using the high-speed rotating collector.

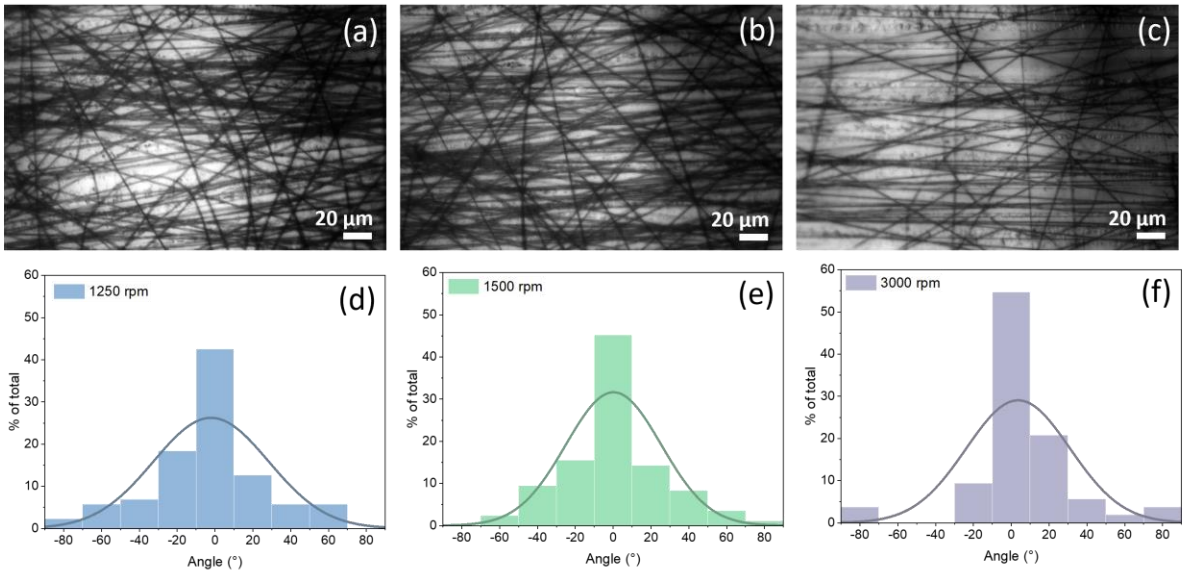

Figure 6.11. Optical images of electrospun PAN fibers deposited on a collector rotating at (a) 1250, (b) 1500, and (c) 3000 rpm. (d) – (f) Corresponding histograms showing the distribution of fiber angles with respect to the axis perpendicular to the axis of rotation.

Uniaxially aligned PAN membranes were electrospun for 4 hours with the collector rotating at a speed of 1500 rpm. The FESEM images of the stabilized and carbonized uniaxially aligned electrospun PAN membranes were shown in Figure 6.12. It is to be noted that upon stabilization and carbonization, the alignment of the fibers was preserved. The diameter of the stabilized PAN and CNFs were 305 nm and 227 nm, respectively. The thickness of the obtained uniaxially aligned CNFs ranged between 21-35 µm.

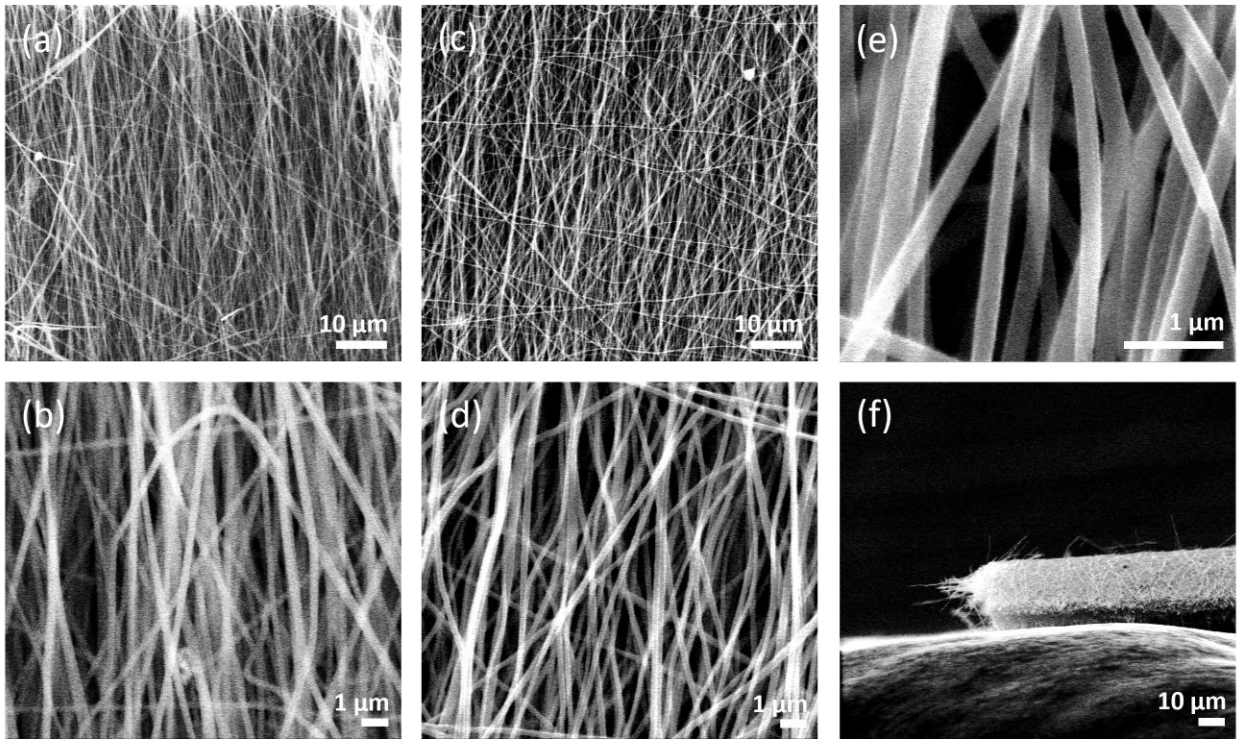

Figure 6.12. FESEM images of aligned (a), (b) stabilized PAN fibers and (c) – (f) CNF fibers deposited on a cylindrical collector rotating at 1500 rpm.

Based on the assumption that the CNFs are amorphous in nature with a density of 2.0 g/cc, the porosity of the electrodes were estimated to be greater than 90 %. Nevertheless, further physical characterization of the electrodes has yet to be carried out. Following that in the future, suitable lithiophilic coatings need to be incorporated before testing their electrochemical performance as a host for LMAs.

Chapter 7 - Conclusion and Future Works

The development of high energy density next-generation batteries is a critical need to assist accelerating the pace of energy transition measures being implemented to combat climate change. The commercialization of these battery technologies is impeded by the numerous challenges at the materials level that limit their performance from reaching practically useful levels. Our objective is to investigate the function of nanostructured electrodes in processes relevant to these advanced batteries, with the goal of gaining new scientific knowledge that could facilitate realizing better materials.

Chapters 2 and 3 are focused on studying the processes associated with LMAs by utilizing VACNFs grown on copper as a model 3-D conductive host. Various characterization tools are employed to elucidate the morphology and composition of e-Li and its associated SEI as well as the lithium intercalation/deintercalation processes. Two different lithium morphologies are present - a dominant micron-scale columnar infiltrative Li and a small amount of nanoscale coaxial Li sheath on VACNFs in the unfilled interstitial area between infiltrative grains. During Li intercalation, an organic-rich loose SEI film forms on the top of VACNF array and an inorganic-rich SEI sheath forms around individual VACNFs. With Li plating, they transform into inorganic dominant SEIs. Upon Li stripping, the SEI on the infiltrative Li remains loosely attached to the VACNF array and irreversibly accumulates during Li plating/stripping cycling. The SEI accumulation causes electrolyte consumption and increased heterogeneity, eventually leading to cell failure.

Microscopic and macroscopic electrochemical chemical characterization are conducted for VACNF/Cu electrode at different Li plating/stripping rates to understand the role of Li

plating/stripping kinetics on the Li morphology and the electrochemical performance in 3-D LMA hosts. Li plating on 3-D VACNF/Cu follows the classical nucleation and growth model. Though Sand's equation predicts a superior performance at lower plating current densities ($\leq$ 0.10 mA/cm^2), the low nucleation overpotential results in formation of sparse porous noodle-like Li. Noodle-like Li exhibits the most inferior performance when the plating and stripping current densities are decoupled. In contrast, a moderate plating density ($\sim$1.0 mA/cm^2) results in more uniform micro-columnar Li infiltrated into the VACNF array which exhibits the best performance. At a high plating current density ($\sim$5.0 mA/cm^2), in addition to the columnar Li, Li micro-spheres start to form at VACNFs' tips which adversely affects the performance. These new scientific insights gained will be beneficial for advancing the development of 3-D conductive host structures for high performance LMAs. Further efforts toward achieving enhanced lithiophilicity and prevention of repeated SEI formation during cycling are required. A holistic approach of use of incorporation of spatially variable artificial SEI and lithiophilic seeds on 3-D host structures will be carried out in the future in addition to extending the studies discussed in Chapter 6.

In Chapter 4, the development of binder-free electrodes based on VACNFs grown on carbon substrates as air cathodes is presented. The utilization of Ni and PtRu enhances the discharge capacity and cycling stability of bare VACNF. VACNF-Ni electrode delivers the highest specific and areal discharge capacities of 14.92 Ah/g and 4.32 mAh/cm^2, respectively at 0.10 mA/cm^2. The incorporation of PtRu enhances the capacity (9.07 Ah/g, 2.62 mAh/cm^2) and delivers a stable performance for 27 cycles with 100% CE. XPS analysis of discharged electrodes reveals the suppression of Li_2CO_3 formation by the coverage of VACNFs' surface with catalyst nanoparticles. Further studies under different DoD and rates will be carried out to understand the limitations in operating conditions and the corresponding modes of failure. Understanding the

limiting factors would help to incorporate suitable solutions to enhance the cycling stability further.

Followed by that, a facile coprecipitation approach for the synthesis of hybrid nanomaterials based on vanadium pentoxide NRs as potential cathodes for AZIBs is introduced in Chapter 5. V_2O_5 NR/rGO hybrids pre-intercalated with divalent cations are successfully synthesized. Zn-V_2O_5 NR/rGO hybrid, prepared using Zn^{2+} ions for coprecipitation, shows a very high reversible specific capacity of ~395 mAh g^{-1} at 0.50 A g^{-1}. However, it exhibits poor stability. With the use of Mn^{2+} together with Zn^{2+} ions for coprecipitation, the stability of the resulting (Mn+Zn)-V_2O_5 NR/rGO hybrid is enhanced significantly with a capacity retention of 77% at the end of 2000 cycles at 4.0 A/g at the expense of a decreased specific capacity of ~291 mAh/g at 0.50 A/g. The Mn^{n+} ions act as stable pillars protecting the structure of V_2O_5 NRs during zinc intercalation/deintercalation. The optimization of amount of pillar ions to maximize both capacity and cycle life and the long-term stability of the hybrids when cycling at low rates are yet to be studied. The effect of different divalent as well as trivalent cations in modifying the properties of M-V_2O_5 NR/rGO hybrids would be an interesting study to explore.

References

1. Calvin, K.; Dasgupta, D.; Krinner, G.; Mukherji, A.; Thorne, P. W.; Trisos, C.; Romero, J.; Aldunce, P.; Barrett, K.; Blanco, G.; Cheung, W. W. L.; Connors, S.; Denton, F.; Diongue-Niang, A.; Dodman, D.; Garschagen, M.; Geden, O.; Hayward, B.; Jones, C.; Jotzo, F.; Krug, T.; Lasco, R.; Lee, Y.-Y.; Masson-Delmotte, V.; Meinshausen, M.; Mintenbeck, K.; Mokssit, A.; Otto, F. E. L.; Pathak, M.; Pirani, A.; Poloczanska, E.; Pörtner, H.-O.; Revi, A.; Roberts, D. C.; Roy, J.; Ruane, A. C.; Skea, J.; Shukla, P. R.; Slade, R.; Slangen, A.; Sokona, Y.; Sörensson, A. A.; Tignor, M.; Van Vuuren, D.; Wei, Y.-M.; Winkler, H.; Zhai, P.; Zommers, Z.; Hourcade, J.-C.; Johnson, F. X.; Pachauri, S.; Simpson, N. P.; Singh, C.; Thomas, A.; Totin, E.; Arias, P.; Bustamante, M.; Elgizouli, I.; Flato, G.; Howden, M.; Méndez-Vallejo, C.; Pereira, J. J.; Pichs-Madruga, R.; Rose, S. K.; Saheb, Y.; Sánchez Rodríguez, R.; Ürge-Vorsatz, D.; Xiao, C.; Yassaa, N.; Alegría, A.; Armour, K.; Bednar-Friedl, B.; Blok, K.; Cissé, G.; Dentener, F.; Eriksen, S.; Fischer, E.; Garner, G.; Guivarch, C.; Haasnoot, M.; Hansen, G.; Hauser, M.; Hawkins, E.; Hermans, T.; Kopp, R.; Leprince-Ringuet, N.; Lewis, J.; Ley, D.; Ludden, C.; Niamir, L.; Nicholls, Z.; Some, S.; Szopa, S.; Trewin, B.; Van Der Wijst, K.-I.; Winter, G.; Witting, M.; Birt, A.; Ha, M.; Romero, J.; Kim, J.; Haites, E. F.; Jung, Y.; Stavins, R.; Birt, A.; Ha, M.; Orendain, D. J. A.; Ignon, L.; Park, S.; Park, Y.; Reisinger, A.; Cammaramo, D.; Fischlin, A.; Fuglestvedt, J. S.; Hansen, G.; Ludden, C.; Masson-Delmotte, V.; Matthews, J. B. R.; Mintenbeck, K.; Pirani, A.; Poloczanska, E.; Leprince-Ringuet, N.; Péan, C. *IPCC, 2023: Climate Change 2023: Synthesis Report. Contribution of Working Groups I, II and III to the Sixth Assessment Report of the Intergovernmental Panel on Climate Change [Core Writing Team, H. Lee and J. Romero (eds.)]. IPCC, Geneva, Switzerland*; Intergovernmental Panel on Climate Change (IPCC): 2023/07/25/, 2023.

2. Ipcc, *Global Warming of 1.5°C: IPCC Special Report on Impacts of Global Warming of 1.5°C above Pre-industrial Levels in Context of Strengthening Response to Climate Change, Sustainable Development, and Efforts to Eradicate Poverty*. 1 ed.; Cambridge University Press: 2022.

3. Betts, R. A.; Jones, C. D.; Knight, J. R.; Keeling, R. F.; Kennedy, J. J., El Niño and a record CO2 rise. *Nature Clim Change* **2016,** *6* (9), 806-810.

4. The Paris Agreement | UNFCCC. https://unfccc.int/process-and-meetings/the-paris-agreement.

5. Ritchie, H.; Roser, M., Sector by sector: where do global greenhouse gas emissions come from? *Our World in Data* **2023**.

6. *Renewables 2023 – Analysis - IEA*.

7. International Energy, A., *Global EV Outlook 2023: Catching up with Climate Ambitions*. OECD: 2023.

8. Boettcher, S. W.; Oener, S. Z.; Lonergan, M. C.; Surendranath, Y.; Ardo, S.; Brozek, C.; Kempler, P. A., Potentially Confusing: Potentials in Electrochemistry. *ACS Energy Lett.* **2021,** *6* (1), 261-266.

9. Goodenough, J. B.; Park, K.-S., The Li-Ion Rechargeable Battery: A Perspective. *J. Am. Chem. Soc.* **2013,** *135* (4), 1167-1176.

10. Al Shaqsi, A. Z.; Sopian, K.; Al-Hinai, A., Review of energy storage services, applications, limitations, and benefits. *Energy Reports* **2020,** *6*, 288-306.

11. Sarma, D. D.; Shukla, A. K., Building Better Batteries: A Travel Back in Time. *ACS Energy Lett.* **2018,** *3* (11), 2841-2845.

12. Scrosati, B., History of lithium batteries. *J Solid State Electrochem* **2011,** *15* (7), 1623-1630.

13. Lopes, P. P.; Stamenkovic, V. R., Past, present, and future of lead–acid batteries. *Science* **2020,** *369* (6506), 923-924.

14. May, G. J.; Davidson, A.; Monahov, B., Lead batteries for utility energy storage: A review. *Journal of Energy Storage* **2018,** *15*, 145-157.

15. Jeyaseelan, C.; Jain, A.; Khurana, P.; Kumar, D.; Thatai, S., Ni-Cd Batteries. In *Rechargeable Batteries*, John Wiley & Sons, Ltd: 2020; pp 177-194.

16. Shin, J.; Choi, J. W., Opportunities and Reality of Aqueous Rechargeable Batteries. *Advanced Energy Materials* **2020,** *10* (28), 2001386.

17. Tsais, P. J.; Chan, L. I., Nickel-based batteries: materials and chemistry. In *Electricity Transmission, Distribution and Storage Systems*, Elsevier: 2013; pp 309-397.

18. Reddy, M. V.; Mauger, A.; Julien, C. M.; Paolella, A.; Zaghib, K., Brief History of Early Lithium-Battery Development. *Materials* **2020,** *13* (8), 1884.

19. Whittingham, M. S., Electrical Energy Storage and Intercalation Chemistry. *Science* **1976,** *192* (4244), 1126-1127.

20. Manthiram, A., A reflection on lithium-ion battery cathode chemistry. *Nature Communications* **2020,** *11* (1), 1550.

21. Yoshino, A., The Birth of the Lithium-Ion Battery. *Angewandte Chemie International Edition* **2012,** *51* (24), 5798-5800.

22. Yoshino, A.; Sanechika, K.; Nakajima, T., Nonaqueous secondary battery. *Japanese patent* **1984,** *2128922*.

23. The Nobel Prize in Chemistry 2019. https://www.nobelprize.org/prizes/chemistry/2019/summary/.

24. Lin, D.; Liu, Y.; Cui, Y., Reviving the lithium metal anode for high-energy batteries. *Nature Nanotech* **2017,** *12* (3), 194-206.

25. Zhang, X.; Yang, Y.; Zhou, Z., Towards practical lithium-metal anodes. *Chemical Society Reviews* **2020,** *49* (10), 3040-3071.

26. Zhang, H.; Yang, Y.; Ren, D.; Wang, L.; He, X., Graphite as anode materials: Fundamental mechanism, recent progress and advances. *Energy Storage Materials* **2021,** *36*, 147-170.

27. Goodenough, J. B.; Kim, Y., Challenges for Rechargeable Li Batteries. *Chemistry of Materials* **2010,** *22* (3), 587-603.

28. Kanamura, K.; Tamura, H.; Shiraishi, S.; Takehara, Z.-i., XPS Analysis of Lithium Surfaces Following Immersion in Various Solvents Containing LiBF4. *J. Electrochem. Soc.* **1995,** *142* (2), 340.

29. Mozhzhukhina, N.; Flores, E.; Lundström, R.; Nyström, V.; Kitz, P. G.; Edström, K.; Berg, E. J., Direct Operando Observation of Double Layer Charging and Early Solid Electrolyte Interphase Formation in Li-Ion Battery Electrolytes. *J. Phys. Chem. Lett.* **2020,** *11* (10), 4119-4123.

30. Peled, E.; Golodnitsky, D.; Ardel, G., Advanced Model for Solid Electrolyte Interphase Electrodes in Liquid and Polymer Electrolytes. *J. Electrochem. Soc.* **1997,** *144* (8), L208.

31. Li, Y.; Li, Y.; Pei, A.; Yan, K.; Sun, Y.; Wu, C.-L.; Joubert, L.-M.; Chin, R.; Koh, A. L.; Yu, Y.; Perrino, J.; Butz, B.; Chu, S.; Cui, Y., Atomic structure of sensitive battery materials and interfaces revealed by cryo–electron microscopy. *Science* **2017,** *358* (6362), 506-510.

32. Han, B.; Li, X.; Bai, S.; Zou, Y.; Lu, B.; Zhang, M.; Ma, X.; Chang, Z.; Meng, Y. S.; Gu, M., Conformal three-dimensional interphase of Li metal anode revealed by low-dose cryoelectron microscopy. *Matter* **2021,** *4* (11), 3741-3752.

33. Wu, J.; Ihsan-Ul-Haq, M.; Chen, Y.; Kim, J.-K., Understanding solid electrolyte interphases: Advanced characterization techniques and theoretical simulations. *Nano Energy* **2021,** *89*, 106489.

34. Wu, H.; Jia, H.; Wang, C.; Zhang, J.-G.; Xu, W., Recent Progress in Understanding Solid Electrolyte Interphase on Lithium Metal Anodes. *Advanced Energy Materials* **2021,** *11* (5), 2003092.

35. Adenusi, H.; Chass, G. A.; Passerini, S.; Tian, K. V.; Chen, G., Lithium Batteries and the Solid Electrolyte Interphase (SEI)—Progress and Outlook. *Advanced Energy Materials* **2023,** *13* (10), 2203307.

36. Chazalviel, J. N., Electrochemical aspects of the generation of ramified metallic electrodeposits. *Phys. Rev. A* **1990,** *42* (12), 7355-7367.

37. Jana, A.; García, R. E., Lithium dendrite growth mechanisms in liquid electrolytes. *Nano Energy* **2017,** *41*, 552-565.

38. Wood, K. N.; Kazyak, E.; Chadwick, A. F.; Chen, K.-H.; Zhang, J.-G.; Thornton, K.; Dasgupta, N. P., Dendrites and Pits: Untangling the Complex Behavior of Lithium Metal Anodes through Operando Video Microscopy. *ACS Cent. Sci.* **2016,** *2* (11), 790-801.

39. Steiger, J.; Kramer, D.; Mönig, R., Mechanisms of dendritic growth investigated by in situ light microscopy during electrodeposition and dissolution of lithium. *Journal of Power Sources* **2014,** *261*, 112-119.

40. Wang, Q.; Jiang, L.; Yu, Y.; Sun, J., Progress of enhancing the safety of lithium ion battery from the electrolyte aspect. *Nano Energy* **2019,** *55*, 93-114.

41. Jiang, F.-N.; Yang, S.-J.; Liu, H.; Cheng, X.-B.; Liu, L.; Xiang, R.; Zhang, Q.; Kaskel, S.; Huang, J.-Q., Mechanism understanding for stripping electrochemistry of Li metal anode. *SusMat* **2021,** *1* (4), 506-536.

42. Fang, C.; Li, J.; Zhang, M.; Zhang, Y.; Yang, F.; Lee, J. Z.; Lee, M.-H.; Alvarado, J.; Schroeder, M. A.; Yang, Y.; Lu, B.; Williams, N.; Ceja, M.; Yang, L.; Cai, M.; Gu, J.; Xu, K.; Wang, X.; Meng, Y. S., Quantifying inactive lithium in lithium metal batteries. *Nature* **2019,** *572* (7770), 511-515.

43. Fang, C.; Wang, X.; Meng, Y. S., Key Issues Hindering a Practical Lithium-Metal Anode. *Trends in Chemistry* **2019,** *1* (2), 152-158.

44. Wu, W.; Luo, W.; Huang, Y., Less is more: a perspective on thinning lithium metal towards high-energy-density rechargeable lithium batteries. *Chemical Society Reviews* **2023,** *52* (8), 2553-2572.

45. Shi, F.; Pei, A.; Vailionis, A.; Xie, J.; Liu, B.; Zhao, J.; Gong, Y.; Cui, Y., Strong texturing of lithium metal in batteries. *Proc. Natl. Acad. Sci. U.S.A.* **2017,** *114* (46), 12138-12143.

46. Efaw, C. M.; Wu, Q.; Gao, N.; Zhang, Y.; Zhu, H.; Gering, K.; Hurley, M. F.; Xiong, H.; Hu, E.; Cao, X.; Xu, W.; Zhang, J.-G.; Dufek, E. J.; Xiao, J.; Yang, X.-Q.; Liu, J.; Qi, Y.; Li, B., Localized high-concentration electrolytes get more localized through micelle-like structures. *Nature Materials* **2023,** *22* (12), 1531-1539.

47. Lin, S.; Hua, H.; Li, Z.; Zhao, J., Functional Localized High-Concentration Ether-Based Electrolyte for Stabilizing High-Voltage Lithium-Metal Battery. *ACS Appl. Mater. Interfaces* **2020,** *12* (30), 33710-33718.

48. Qian, J.; Henderson, W. A.; Xu, W.; Bhattacharya, P.; Engelhard, M.; Borodin, O.; Zhang, J.-G., High rate and stable cycling of lithium metal anode. *Nature Communications* **2015,** *6* (1), 6362.

49. Li, Y.; Huang, W.; Li, Y.; Pei, A.; Boyle, D. T.; Cui, Y., Correlating Structure and Function of Battery Interphases at Atomic Resolution Using Cryoelectron Microscopy. *Joule* **2018,** *2* (10), 2167-2177.

50. Adams, B. D.; Carino, E. V.; Connell, J. G.; Han, K. S.; Cao, R.; Chen, J.; Zheng, J.; Li, Q.; Mueller, K. T.; Henderson, W. A.; Zhang, J.-G., Long term stability of Li-S batteries using high concentration lithium nitrate electrolytes. *Nano Energy* **2017,** *40*, 607-617.

51. Sayavong, P.; Zhang, W.; Oyakhire, S. T.; Boyle, D. T.; Chen, Y.; Kim, S. C.; Vilá, R. A.; Holmes, S. E.; Kim, M. S.; Bent, S. F.; Bao, Z.; Cui, Y., Dissolution of the Solid Electrolyte Interphase and Its Effects on Lithium Metal Anode Cyclability. *J. Am. Chem. Soc.* **2023,** *145* (22), 12342-12350.

52. Boyle, D. T.; Huang, W.; Wang, H.; Li, Y.; Chen, H.; Yu, Z.; Zhang, W.; Bao, Z.; Cui, Y., Corrosion of lithium metal anodes during calendar ageing and its microscopic origins. *Nat Energy* **2021,** *6* (5), 487-494.

53. Fan, L.; Zhuang, H. L.; Gao, L.; Lu, Y.; Archer, L. A., Regulating Li deposition at artificial solid electrolyte interphases. *Journal of Materials Chemistry A* **2017,** *5* (7), 3483-3492.

54. Gao, S.; Sun, F.; Liu, N.; Yang, H.; Cao, P.-F., Ionic conductive polymers as artificial solid electrolyte interphase films in Li metal batteries – A review. *Materials Today* **2020,** *40*, 140-159.

55. Xu, R.; Cheng, X.-B.; Yan, C.; Zhang, X.-Q.; Xiao, Y.; Zhao, C.-Z.; Huang, J.-Q.; Zhang, Q., Artificial Interphases for Highly Stable Lithium Metal Anode. *Matter* **2019,** *1* (2), 317-344.

56. Zhang, S.; Deng, W.; Zhou, X.; He, B.; Liang, J.; Zhao, F.; Guo, Q.; Liu, Z., Controlled lithium plating in three-dimensional hosts through nucleation overpotential regulation toward high-areal-capacity lithium metal anode. *Materials Today Energy* **2021,** *21*, 100770.

57. Zhang, R.; Li, N.-W.; Cheng, X.-B.; Yin, Y.-X.; Zhang, Q.; Guo, Y.-G., Advanced Micro/Nanostructures for Lithium Metal Anodes. *Advanced Science* **2017,** *4* (3), 1600445.

58. Park, S.; Jin, H.-J.; Yun, Y. S., Advances in the Design of 3D-Structured Electrode Materials for Lithium-Metal Anodes. *Advanced Materials* **2020,** *32* (51), 2002193.

59. Xia, S.; Wu, X.; Zhang, Z.; Cui, Y.; Liu, W., Practical Challenges and Future Perspectives of All-Solid-State Lithium-Metal Batteries. *Chem* **2019,** *5* (4), 753-785.

60. Abraham, K. M.; Jiang, Z., A Polymer Electrolyte-Based Rechargeable Lithium/Oxygen Battery. *J. Electrochem. Soc.* **1996,** *143* (1), 1.

61. Jung, J.-W.; Cho, S.-H.; Nam, J. S.; Kim, I.-D., Current and future cathode materials for non-aqueous Li-air (O2) battery technology – A focused review. *Energy Storage Materials* **2020,** *24*, 512-528.

62. Tan, P.; Jiang, H. R.; Zhu, X. B.; An, L.; Jung, C. Y.; Wu, M. C.; Shi, L.; Shyy, W.; Zhao, T. S., Advances and challenges in lithium-air batteries. *Applied Energy* **2017,** *204*, 780-806.

63. Aurbach, D.; McCloskey, B. D.; Nazar, L. F.; Bruce, P. G., Advances in understanding mechanisms underpinning lithium–air batteries. *Nat Energy* **2016,** *1* (9), 1-11.

64. Grande, L.; Paillard, E.; Hassoun, J.; Park, J.-B.; Lee, Y.-J.; Sun, Y.-K.; Passerini, S.; Scrosati, B., The Lithium/Air Battery: Still an Emerging System or a Practical Reality? *Advanced Materials* **2015,** *27* (5), 784-800.

65. Girishkumar, G.; McCloskey, B.; Luntz, A. C.; Swanson, S.; Wilcke, W., Lithium−Air Battery: Promise and Challenges. *J. Phys. Chem. Lett.* **2010,** *1* (14), 2193-2203.

66. Wong, R. A.; Dutta, A.; Yang, C.; Yamanaka, K.; Ohta, T.; Nakao, A.; Waki, K.; Byon, H. R., Structurally Tuning Li2O2 by Controlling the Surface Properties of Carbon Electrodes: Implications for Li–O2 Batteries. *Chemistry of Materials* **2016,** *28* (21), 8006-8015.

67. Johnson, L.; Li, C.; Liu, Z.; Chen, Y.; Freunberger, S. A.; Ashok, P. C.; Praveen, B. B.; Dholakia, K.; Tarascon, J.-M.; Bruce, P. G., The role of LiO2 solubility in O2 reduction in aprotic solvents and its consequences for Li–O2 batteries. *Nature Chemistry* **2014,** *6* (12), 1091-1099.

68. Aetukuri, N. B.; McCloskey, B. D.; García, J. M.; Krupp, L. E.; Viswanathan, V.; Luntz, A. C., Solvating additives drive solution-mediated electrochemistry and enhance toroid growth in non-aqueous Li–O2 batteries. *Nature Chemistry* **2015,** *7* (1), 50-56.

69. Liu, L.; Liu, Y.; Wang, C.; Peng, X.; Fang, W.; Hou, Y.; Wang, J.; Ye, J.; Wu, Y., Li2O2 Formation Electrochemistry and Its Influence on Oxygen Reduction/Evolution Reaction Kinetics in Aprotic Li–O2 Batteries. *Small Methods* **2022,** *6* (1), 2101280.

70. Wen, Z.; Shen, C.; Lu, Y., Air Electrode for the Lithium–Air Batteries: Materials and Structure Designs. *ChemPlusChem* **2015,** *80* (2), 270-287.

71. Inaba, M.; Jensen, A. W.; Sievers, G. W.; Escudero-Escribano, M.; Zana, A.; Arenz, M., Benchmarking high surface area electrocatalysts in a gas diffusion electrode: measurement of oxygen reduction activities under realistic conditions. *Energy Environ. Sci.* **2018,** *11* (4), 988-994.

72. Zhang, S. S.; Foster, D.; Read, J., Discharge characteristic of a non-aqueous electrolyte Li/O2 battery. *Journal of Power Sources* **2010,** *195* (4), 1235-1240.

73. Viswanathan, V.; Thygesen, K. S.; Hummelshøj, J. S.; Nørskov, J. K.; Girishkumar, G.; McCloskey, B. D.; Luntz, A. C., Electrical conductivity in Li2O2 and its role in determining capacity limitations in non-aqueous Li-O2 batteries. *The Journal of Chemical Physics* **2011,** *135* (21), 214704.

74. Bevara, V.; Andrei, P., Changing the Cathode Microstructure to Improve the Capacity of Li-Air Batteries: Theoretical Predictions. *J. Electrochem. Soc.* **2014,** *161* (14), A2068.

75. Shao, Y.; Park, S.; Xiao, J.; Zhang, J.-G.; Wang, Y.; Liu, J., Electrocatalysts for Nonaqueous Lithium–Air Batteries: Status, Challenges, and Perspective. *ACS Catal.* **2012,** *2* (5), 844-857.

76. Zhao, Z.; Huang, J.; Peng, Z., Achilles' Heel of Lithium–Air Batteries: Lithium Carbonate. *Angewandte Chemie International Edition* **2018,** *57* (15), 3874-3886.

77. Lim, H.-K.; Lim, H.-D.; Park, K.-Y.; Seo, D.-H.; Gwon, H.; Hong, J.; Goddard, W. A., III; Kim, H.; Kang, K., Toward a Lithium–"Air" Battery: The Effect of CO2 on the Chemistry of a Lithium–Oxygen Cell. *J. Am. Chem. Soc.* **2013,** *135* (26), 9733-9742.

78. McCloskey, B. D.; Valery, A.; Luntz, A. C.; Gowda, S. R.; Wallraff, G. M.; Garcia, J. M.; Mori, T.; Krupp, L. E., Combining Accurate O2 and Li2O2 Assays to Separate Discharge and Charge Stability Limitations in Nonaqueous Li–O2 Batteries. *J. Phys. Chem. Lett.* **2013,** *4* (17), 2989-2993.

79. McCloskey, B. D.; Speidel, A.; Scheffler, R.; Miller, D. C.; Viswanathan, V.; Hummelshøj, J. S.; Nørskov, J. K.; Luntz, A. C., Twin Problems of Interfacial Carbonate Formation in Nonaqueous Li–O2 Batteries. *J. Phys. Chem. Lett.* **2012,** *3* (8), 997-1001.

80. Meini, S.; Piana, M.; Beyer, H.; Schwämmlein, J.; Gasteiger, H. A., Effect of Carbon Surface Area on First Discharge Capacity of Li-O2 Cathodes and Cycle-Life Behavior in Ether-Based Electrolytes. *J. Electrochem. Soc.* **2012,** *159* (12), A2135.

81. Chervin, C. N.; Wattendorf, M. J.; Long, J. W.; Kucko, N. W.; Rolison, D. R., Carbon Nanofoam-Based Cathodes for Li–O2 Batteries: Correlation of Pore–Solid Architecture and Electrochemical Performance. *J. Electrochem. Soc.* **2013,** *160* (9), A1510.

82. Ding, N.; Chien, S. W.; Hor, T. S. A.; Lum, R.; Zong, Y.; Liu, Z., Influence of carbon pore size on the discharge capacity of Li–O ₂ batteries. *J. Mater. Chem. A* **2014,** *2* (31), 12433-12441.

83. Ottakam Thotiyl, M. M.; Freunberger, S. A.; Peng, Z.; Bruce, P. G., The Carbon Electrode in Nonaqueous Li–O2 Cells. *J. Am. Chem. Soc.* **2013,** *135* (1), 494-500.

84. Im, H. J.; Park, Y. J., Interfacial reactions in lithia-based cathodes depending on the binder in the electrode and salt in the electrolyte. *Sci Rep* **2022,** *12* (1), 527.

85. Heine, J.; Rodehorst, U.; Badillo, J. P.; Winter, M.; Bieker, P., Chemical Stability Investigations of Polyisobutylene as New Binder for Application in Lithium Air-Batteries. *Electrochimica Acta* **2015,** *155*, 110-115.

86. Service, R. F., Zinc aims to beat lithium batteries at storing energy. *Science* **2021,** *372* (6545), 890-891.

87. Fang, G.; Zhou, J.; Pan, A.; Liang, S., Recent Advances in Aqueous Zinc-Ion Batteries. *ACS Energy Lett.* **2018,** *3* (10), 2480-2501.

88. Li, Y.; Wang, Z.; Cai, Y.; Pam, M. E.; Yang, Y.; Zhang, D.; Wang, Y.; Huang, S., Designing Advanced Aqueous Zinc-Ion Batteries: Principles, Strategies, and Perspectives. *ENERGY & ENVIRONMENTAL MATERIALS* **2022,** *5* (3), 823-851.

89. Tang, B.; Shan, L.; Liang, S.; Zhou, J., Issues and opportunities facing aqueous zinc-ion batteries. *Energy Environ. Sci.* **2019,** *12* (11), 3288-3304.

90. Li, C.; Xie, X.; Liang, S.; Zhou, J., Issues and Future Perspective on Zinc Metal Anode for Rechargeable Aqueous Zinc-ion Batteries. *ENERGY & ENVIRONMENTAL MATERIALS* **2020,** *3* (2), 146-159.

91. Kundu, D.; Adams, B. D.; Duffort, V.; Vajargah, S. H.; Nazar, L. F., A high-capacity and long-life aqueous rechargeable zinc battery using a metal oxide intercalation cathode. *Nat Energy* **2016,** *1* (10), 16119.

92. Li, G.; Sun, L.; Zhang, S.; Zhang, C.; Jin, H.; Davey, K.; Liang, G.; Liu, S.; Mao, J.; Guo, Z., Developing Cathode Materials for Aqueous Zinc Ion Batteries: Challenges and Practical Prospects. *Advanced Functional Materials* **2024,** *34* (5), 2301291.

93. Liu, A.; Wu, F.; Zhang, Y.; Zhou, J.; Zhou, Y.; Xie, M., Insight on Cathodes Chemistry for Aqueous Zinc-Ion Batteries: From Reaction Mechanisms, Structural Engineering, and Modification Strategies. *Small* **2022,** *18* (28), 2201011.

94. Wang, H.; Tan, R.; Yang, Z.; Feng, Y.; Duan, X.; Ma, J., Stabilization Perspective on Metal Anodes for Aqueous Batteries. *Advanced Energy Materials* **2021,** *11* (2), 2000962.

95. Cao, Z.; Zhuang, P.; Zhang, X.; Ye, M.; Shen, J.; Ajayan, P. M., Strategies for Dendrite-Free Anode in Aqueous Rechargeable Zinc Ion Batteries. *Advanced Energy Materials* **2020,** *10* (30), 2001599.

96. Wang, X.; Zhang, Z.; Xi, B.; Chen, W.; Jia, Y.; Feng, J.; Xiong, S., Advances and Perspectives of Cathode Storage Chemistry in Aqueous Zinc-Ion Batteries. *ACS Nano* **2021,** *15* (6), 9244-9272.

97. Yan, J.; Ang, E. H.; Yang, Y.; Zhang, Y.; Ye, M.; Du, W.; Li, C. C., High-Voltage Zinc-Ion Batteries: Design Strategies and Challenges. *Advanced Functional Materials* **2021,** *31* (22), 2010213.

98. Dai, Y.; Zhang, C.; Li, J.; Gao, X.; Hu, P.; Ye, C.; He, H.; Zhu, J.; Zhang, W.; Chen, R.; Zong, W.; Guo, F.; Parkin, I. P.; Brett, D. J. L.; Shearing, P. R.; Mai, L.; He, G., Inhibition of Vanadium Cathodes Dissolution in Aqueous Zn-Ion Batteries. *Advanced Materials n/a* (n/a), 2310645.

99. Zhang, L.; Hu, J.; Zhang, B.; Liu, J.; Wan, H.; Miao, L.; Jiang, J., Suppressing cathode dissolution via guest engineering for durable aqueous zinc-ion batteries. *Journal of Materials Chemistry A* **2021,** *9* (12), 7631-7639.

100. Yang, G.; Li, Q.; Ma, K.; Hong, C.; Wang, C., The degradation mechanism of vanadium oxide-based aqueous zinc-ion batteries. *Journal of Materials Chemistry A* **2020,** *8* (16), 8084-8095.

101. Liu, N.; Li, B.; He, Z.; Dai, L.; Wang, H.; Wang, L., Recent advances and perspectives on vanadium- and manganese-based cathode materials for aqueous zinc ion batteries. *Journal of Energy Chemistry* **2021,** *59*, 134-159.

102. Lewis, C.-E. M.; Fernando, J. F. S.; Siriwardena, D. P.; Firestein, K. L.; Zhang, C.; von Treifeldt, J. E.; Golberg, D. V., Vanadium-Containing Layered Materials as High-Performance Cathodes for Aqueous Zinc-Ion Batteries. *Advanced Materials Technologies* **2022,** *7* (4), 2100505.

103. Wang, J.; Zhao, X.; Kang, J.; Wang, X.; Yu, H.; Du, C.-F.; Yan, Q., Li + , Na + co-stabilized vanadium oxide nanobelts with a bilayer structure for boosted zinc-ion storage performance. *Journal of Materials Chemistry A* **2022**.

104. Zhang, G.; Wu, T.; Zhou, H.; Jin, H.; Liu, K.; Luo, Y.; Jiang, H.; Huang, K.; Huang, L.; Zhou, J., Rich Alkali Ions Preintercalated Vanadium Oxides for Durable and Fast Zinc-Ion Storage. *ACS Energy Lett.* **2021,** *6* (6), 2111-2120.

105. Yang, Y.; Tang, Y.; Liang, S.; Wu, Z.; Fang, G.; Cao, X.; Wang, C.; Lin, T.; Pan, A.; Zhou, J., Transition metal ion-preintercalated V2O5 as high-performance aqueous zinc-ion battery cathode with broad temperature adaptability. *Nano Energy* **2019,** *61*, 617-625.

106. Zhang, W.; Zuo, C.; Tang, C.; Tang, W.; Lan, B.; Fu, X.; Dong, S.; Luo, P., The Current Developments and Perspectives of V2O5 as Cathode for Rechargeable Aqueous Zinc-Ion Batteries. *Energy Technology* **2021,** *9* (2), 2000789.

107. Wang, B.; Dai, S.; Zhu, Z.; Hu, L.; Su, Z.; Jin, Y.; Xiong, L.; Gao, J.; Wan, J.; Li, Z.; Huang, L., A two-dimensional conductive polymer/V2O5 composite with rapid zinc-ion storage kinetics for high-power aqueous zinc-ion batteries. *Nanoscale* **2022,** *14* (33), 12013-12021.

108. Yong, B.; Ma, D.; Wang, Y.; Mi, H.; He, C.; Zhang, P., Understanding the Design Principles of Advanced Aqueous Zinc-Ion Battery Cathodes: From Transport Kinetics to Structural Engineering, and Future Perspectives. *Advanced Energy Materials* **2020,** *10* (45), 2002354.

109. Ling, W.; Wang, P.; Chen, Z.; Wang, H.; Wang, J.; Ji, Z.; Fei, J.; Ma, Z.; He, N.; Huang, Y., Nanostructure Design Strategies for Aqueous Zinc-Ion Batteries. *ChemElectroChem* **2020,** *7* (14), 2957-2978.

110. Meyyappan, M.; Delzeit, L.; Cassell, A.; Hash, D., Carbon nanotube growth by PECVD: a review. *Plasma Sources Sci. Technol.* **2003,** *12* (2), 205.

111. Xu, M.; Futaba, D. N.; Yumura, M.; Hata, K., Alignment Control of Carbon Nanotube Forest from Random to Nearly Perfectly Aligned by Utilizing the Crowding Effect. *ACS Nano* **2012,** *6* (7), 5837-5844.

112. Banks, C. E.; Davies, T. J.; Wildgoose, G. G.; Compton, R. G., Electrocatalysis at graphite and carbon nanotube modified electrodes: edge-plane sites and tube ends are the reactive sites. *Chem. Commun.* **2005,** (7), 829.

113. Swisher, L. Z.; Syed, L. U.; Prior, A. M.; Madiyar, F. R.; Carlson, K. R.; Nguyen, T. A.; Hua, D. H.; Li, J., Electrochemical Protease Biosensor Based on Enhanced AC Voltammetry Using Carbon Nanofiber Nanoelectrode Arrays. *J. Phys. Chem. C* **2013,** *117* (8), 4268-4277.

114. Cui, H.; Yang, X.; Simpson, M. L.; Lowndes, D. H.; Varela, M., Initial growth of vertically aligned carbon nanofibers. *Applied Physics Letters* **2004,** *84* (20), 4077-4079.

115. Ren, Z. F.; Huang, Z. P.; Wang, D. Z.; Wen, J. G.; Xu, J. W.; Wang, J. H.; Calvet, L. E.; Chen, J.; Klemic, J. F.; Reed, M. A., Growth of a single freestanding multiwall carbon nanotube on each nanonickel dot. *Applied Physics Letters* **1999,** *75* (8), 1086-1088.

116. Chen, Y.; Lin Wang, Z.; Song Yin, J.; Johnson, D. J.; Prince, R. H., Well-aligned graphitic nanofibers synthesized by plasma-assisted chemical vapor deposition. *Chemical Physics Letters* **1997,** *272* (3), 178-182.

117. Ren, Z. F.; Huang, Z. P.; Xu, J. W.; Wang, J. H.; Bush, P.; Siegal, M. P.; Provencio, P. N., Synthesis of Large Arrays of Well-Aligned Carbon Nanotubes on Glass. *Science* **1998,** *282* (5391), 1105-1107.

118. Huang, Z. P.; Wang, D. Z.; Wen, J. G.; Sennett, M.; Gibson, H.; Ren, Z. F., Effect of nickel, iron and cobalt on growth of aligned carbon nanotubes. *Appl Phys A* **2002,** *74* (3), 387-391.

119. Cassell, A. M.; Ye, Q.; Cruden, B. A.; Li, J.; Sarrazin, P. C.; Ng, H. T.; Han, J.; Meyyappan, M., Combinatorial chips for optimizing the growth and integration of carbon nanofibre based devices. *Nanotechnology* **2003,** *15* (1), 9.

120. Melechko, A. V.; Merkulov, V. I.; McKnight, T. E.; Guillorn, M. A.; Klein, K. L.; Lowndes, D. H.; Simpson, M. L., Vertically aligned carbon nanofibers and related structures: Controlled synthesis and directed assembly. *Journal of Applied Physics* **2005,** *97* (4), 041301.

121. Meyyappan, M., A review of plasma enhanced chemical vapour deposition of carbon nanotubes. *J. Phys. D: Appl. Phys.* **2009,** *42* (21), 213001.

122. Melechko, A. V.; Merkulov, V. I.; Lowndes, D. H.; Guillorn, M. A.; Simpson, M. L., Transition between `base' and `tip' carbon nanofiber growth modes. *Chemical Physics Letters* **2002,** *356* (5-6), 527-533.

123. Merkulov, V. I.; Melechko, A. V.; Guillorn, M. A.; Lowndes, D. H.; Simpson, M. L., Alignment mechanism of carbon nanofibers produced by plasma-enhanced chemical-vapor deposition. *Applied Physics Letters* **2001,** *79* (18), 2970-2972.

124. Li, J.; Ng, H. T.; Cassell, A.; Fan, W.; Chen, H.; Ye, Q.; Koehne, J.; Han, J.; Meyyappan, M., Carbon Nanotube Nanoelectrode Array for Ultrasensitive DNA Detection. *Nano Lett.* **2003,** *3* (5), 597-602.

125. Brown, E.; Park, S.-H.; Elangovan, A.; Yuan, Y.; Kim, J.; Sun, X. S.; Zhang, X.; Wang, G.; Li, J., Facilitating high-capacity V2O5 cathodes with stable two and three Li+ insertion using a hybrid membrane structure consisting of amorphous V2O5 shells coaxially deposited on electrospun carbon nanofibers. *Electrochimica Acta* **2018,** *269*, 144-154.

126. Elangovan, A.; Xu, J.; Brown, E.; Liu, B.; Li, J., Fundamental Electrochemical Insights of Vertically Aligned Carbon Nanofiber Architecture as a Catalyst Support for ORR. *J. Electrochem. Soc.* **2020,** *167* (6), 066523.

127. A. Klankowski, S.; A. Rojeski, R.; A. Cruden, B.; Liu, J.; Wu, J.; Li, J., A high-performance lithium-ion battery anode based on the core–shell heterostructure of silicon-coated vertically aligned carbon nanofibers. *Journal of Materials Chemistry A* **2013,** *1* (4), 1055-1064.

128. Chen, Y.; Elangovan, A.; Zeng, D.; Zhang, Y.; Ke, H.; Li, J.; Sun, Y.; Cheng, H., Vertically Aligned Carbon Nanofibers on Cu Foil as a 3D Current Collector for Reversible Li Plating/Stripping toward High-Performance Li–S Batteries. *Advanced Functional Materials* **2020,** *30* (4), 1906444.

129. Li, Y.; Yang, X.-Y.; Feng, Y.; Yuan, Z.-Y.; Su, B.-L., One-Dimensional Metal Oxide Nanotubes, Nanowires, Nanoribbons, and Nanorods: Synthesis, Characterizations, Properties and Applications. *Critical Reviews in Solid State and Materials Sciences* **2012,** *37* (1), 1-74.

130. Wei, Q.; Liu, J.; Feng, W.; Sheng, J.; Tian, X.; He, L.; An, Q.; Mai, L., Hydrated vanadium pentoxide with superior sodium storage capacity. *Journal of Materials Chemistry A* **2015,** *3* (15), 8070-8075.

131. Chen, Y.; Muthukumar, K.; Leban, L.; Li, J., Microwave-assisted high-yield exfoliation of vanadium pentoxide nanoribbons for supercapacitor applications. *Electrochimica Acta* **2020,** *330*, 135200.

132. Park, S. K.; Dose, W. M.; Boruah, B. D.; De Volder, M., In Situ and Operando Analyses of Reaction Mechanisms in Vanadium Oxides for Li-, Na-, Zn-, and Mg-Ions Batteries. *Advanced Materials Technologies* **2022,** *7* (1), 2100799.

133. Hu, P.; Hu, P.; Vu, T. D.; Li, M.; Wang, S.; Ke, Y.; Zeng, X.; Mai, L.; Long, Y., Vanadium Oxide: Phase Diagrams, Structures, Synthesis, and Applications. *Chem. Rev.* **2023,** *123* (8), 4353-4415.

134. Zhang, M.; Liang, R.; Or, T.; Deng, Y.-P.; Yu, A.; Chen, Z., Recent Progress on High-Performance Cathode Materials for Zinc-Ion Batteries. *Small Structures* **2021,** *2* (2), 2000064.

135. Chen, X.; Zhang, H.; Liu, J.-H.; Gao, Y.; Cao, X.; Zhan, C.; Wang, Y.; Wang, S.; Chou, S.-L.; Dou, S.-X.; Cao, D., Vanadium-based cathodes for aqueous zinc-ion batteries: Mechanism, design strategies and challenges. *Energy Storage Materials* **2022,** *50*, 21-46.

136. Chan, C. K.; Peng, H.; Twesten, R. D.; Jarausch, K.; Zhang, X. F.; Cui, Y., Fast, Completely Reversible Li Insertion in Vanadium Pentoxide Nanoribbons. *Nano Lett.* **2007,** *7* (2), 490-495.

137. Zhang, C.; Park, S.-H.; O'Brien, S. E.; Seral-Ascaso, A.; Liang, M.; Hanlon, D.; Krishnan, D.; Crossley, A.; McEvoy, N.; Coleman, J. N.; Nicolosi, V., Liquid exfoliation of interlayer spacing-tunable 2D vanadium oxide nanosheets: High capacity and rate handling Li-ion battery cathodes. *Nano Energy* **2017,** *39*, 151-161.

138. Rui, X.; Lu, Z.; Yu, H.; Yang, D.; Hng, H. H.; Lim, T. M.; Yan, Q., Ultrathin V ₂ O ₅ nanosheet cathodes: realizing ultrafast reversible lithium storage. *Nanoscale* **2013,** *5* (2), 556-560.

139. Lipton, J.; Weng, G.-M.; Röhr, J. A.; Wang, H.; Taylor, A. D., Layer-by-Layer Assembly of Two-Dimensional Materials: Meticulous Control on the Nanoscale. *Matter* **2020,** *2* (5), 1148-1165.

140. Heubner, C.; Maletti, S.; Lohrberg, O.; Lein, T.; Liebmann, T.; Nickol, A.; Schneider, M.; Michaelis, A., Electrochemical Characterization of Battery Materials in 2-Electrode Half-Cell Configuration: A Balancing Act Between Simplicity and Pitfalls. *Batteries & Supercaps* **2021,** *4* (8), 1310-1322.

141. Burrows, B.; Jasinski, R., The Li/Li+ Reference Electrode in Propylene Carbonate. *J. Electrochem. Soc.* **1968,** *115* (4), 365.

142. Dugas, R.; Forero-Saboya, J. D.; Ponrouch, A., Methods and Protocols for Reliable Electrochemical Testing in Post-Li Batteries (Na, K, Mg, and Ca). *Chemistry of Materials* **2019,** *31* (21), 8613-8628.

143. Nölle, R.; Beltrop, K.; Holtstiege, F.; Kasnatscheew, J.; Placke, T.; Winter, M., A reality check and tutorial on electrochemical characterization of battery cell materials: How to choose the appropriate cell setup. *Materials Today* **2020,** *32*, 131-146.

144. Adams, B. D.; Zheng, J.; Ren, X.; Xu, W.; Zhang, J.-G., Accurate Determination of Coulombic Efficiency for Lithium Metal Anodes and Lithium Metal Batteries. *Advanced Energy Materials* **2018,** *8* (7), 1702097.

145. Mohammadi, A.; Djafer, S.; Sayegh, S.; Naylor, A. J.; Bechelany, M.; Younesi, R.; Monconduit, L.; Stievano, L., Assessing Coulombic Efficiency in Lithium Metal Anodes. *Chemistry of Materials* **2023,** *35* (6), 2381-2393.

146. Bruce, P. G.; Freunberger, S. A.; Hardwick, L. J.; Tarascon, J.-M., Li–O 2 and Li–S batteries with high energy storage. *Nature Materials* **2012,** *11* (1), 19-29.

147. Xu, W.; Wang, J.; Ding, F.; Chen, X.; Nasybulin, E.; Zhang, Y.; Zhang, J.-G., Lithium metal anodes for rechargeable batteries. *Energy Environ. Sci.* **2014,** *7* (2), 513-537.

148. Zheng, J.; Tang, T.; Zhao, Q.; Liu, X.; Deng, Y.; Archer, L. A., Physical Orphaning versus Chemical Instability: Is Dendritic Electrodeposition of Li Fatal? *ACS Energy Lett.* **2019,** *4* (6), 1349-1355.

149. Ghazi, Z. A.; Sun, Z.; Sun, C.; Qi, F.; An, B.; Li, F.; Cheng, H.-M., Key Aspects of Lithium Metal Anodes for Lithium Metal Batteries. *Small* **2019,** *15* (32), 1900687.

150. Aryanfar, A.; J. Brooks, D.; J. Colussi, A.; R. Hoffmann, M., Quantifying the dependence of dead lithium losses on the cycling period in lithium metal batteries. *Physical Chemistry Chemical Physics* **2014,** *16* (45), 24965-24970.

151. Jungjohann, K. L.; Gannon, R. N.; Goriparti, S.; Randolph, S. J.; Merrill, L. C.; Johnson, D. C.; Zavadil, K. R.; Harris, S. J.; Harrison, K. L., Cryogenic Laser Ablation Reveals Short-Circuit Mechanism in Lithium Metal Batteries. *ACS Energy Lett.* **2021,** *6* (6), 2138-2144.

152. Yang, C.-P.; Yin, Y.-X.; Zhang, S.-F.; Li, N.-W.; Guo, Y.-G., Accommodating lithium into 3D current collectors with a submicron skeleton towards long-life lithium metal anodes. *Nature Communications* **2015,** *6*.

153. Ding, F.; Xu, W.; Graff, G. L.; Zhang, J.; Sushko, M. L.; Chen, X.; Shao, Y.; Engelhard, M. H.; Nie, Z.; Xiao, J.; Liu, X.; Sushko, P. V.; Liu, J.; Zhang, J.-G., Dendrite-Free Lithium Deposition via Self-Healing Electrostatic Shield Mechanism. *J. Am. Chem. Soc.* **2013,** *135* (11), 4450-4456.

154. Heine, J.; Hilbig, P.; Qi, X.; Niehoff, P.; Winter, M.; Bieker, P., Fluoroethylene Carbonate as Electrolyte Additive in Tetraethylene Glycol Dimethyl Ether Based Electrolytes for Application in Lithium Ion and Lithium Metal Batteries. *J. Electrochem. Soc.* **2015,** *162* (6), A1094.

155. Kazyak, E.; Wood, K. N.; Dasgupta, N. P., Improved Cycle Life and Stability of Lithium Metal Anodes through Ultrathin Atomic Layer Deposition Surface Treatments. *Chemistry of Materials* **2015,** *27* (18), 6457-6462.

156. Wang, C.; Yang, Y.; Liu, X.; Zhong, H.; Xu, H.; Xu, Z.; Shao, H.; Ding, F., Suppression of Lithium Dendrite Formation by Using LAGP-PEO (LiTFSI) Composite Solid Electrolyte and Lithium Metal Anode Modified by PEO (LiTFSI) in All-Solid-State Lithium Batteries. *ACS Appl. Mater. Interfaces* **2017,** *9* (15), 13694-13702.

157. Chen, X.-R.; Yan, C.; Ding, J.-F.; Peng, H.-J.; Zhang, Q., New insights into "dead lithium" during stripping in lithium metal batteries. *Journal of Energy Chemistry* **2021,** *62*, 289-294.

158. Cheng, Y.; Chen, J.; Chen, Y.; Ke, X.; Li, J.; Yang, Y.; Shi, Z., Lithium Host:Advanced architecture components for lithium metal anode. *Energy Storage Materials* **2021,** *38*, 276-298.

159. Yan, X.; Lin, L.; Chen, Q.; Xie, Q.; Qu, B.; Wang, L.; Peng, D.-L., Multifunctional roles of carbon-based hosts for Li-metal anodes: A review. *Carbon Energy* **2021,** *3* (2), 303-329.

160. Chen, X.; Chen, X.-R.; Hou, T.-Z.; Li, B.-Q.; Cheng, X.-B.; Zhang, R.; Zhang, Q., Lithiophilicity chemistry of heteroatom-doped carbon to guide uniform lithium nucleation in lithium metal anodes. *Science Advances* **2019,** *5* (2), eaau7728.

161. Wang, J.; Wang, H.; Xie, J.; Yang, A.; Pei, A.; Wu, C.-L.; Shi, F.; Liu, Y.; Lin, D.; Gong, Y.; Cui, Y., Fundamental study on the wetting property of liquid lithium. *Energy Storage Materials* **2018,** *14*, 345-350.

162. Zhao, X.; Xia, S.; Zhang, X.; Pang, Y.; Xu, F.; Yang, J.; Sun, L.; Zheng, S., Highly Lithiophilic Copper-Reinforced Scaffold Enables Stable Li Metal Anode. *ACS Appl. Mater. Interfaces* **2021,** *13* (17), 20240-20250.

163. Fang, Y.; Zhang, S. L.; Wu, Z.-P.; Luan, D.; Lou, X. W., A highly stable lithium metal anode enabled by Ag nanoparticle–embedded nitrogen-doped carbon macroporous fibers. *Science Advances* **2021,** *7* (21), eabg3626.

164. Li, D.; Xie, C.; Gao, Y.; Hu, H.; Wang, L.; Zheng, Z., Inverted Anode Structure for Long-Life Lithium Metal Batteries. *Advanced Energy Materials* **2022,** *12* (18), 2200584.

165. Shi, Y.; Li, B.; Zhang, Y.; Cui, Y.; Cao, Z.; Du, Z.; Gu, J.; Shen, K.; Yang, S., Tortuosity Modulation toward High-Energy and High-Power Lithium Metal Batteries. *Advanced Energy Materials* **2021,** *11* (12), 2003663.

166. Deng, W.; Zhu, W.; Zhou, X.; Peng, X.; Liu, Z., Highly Reversible Li Plating Confined in Three-Dimensional Interconnected Microchannels toward High-Rate and Stable Metallic Lithium Anodes. *ACS Appl. Mater. Interfaces* **2018,** *10* (24), 20387-20395.

167. Zhang, Y.; Luo, W.; Wang, C.; Li, Y.; Chen, C.; Song, J.; Dai, J.; Hitz, E. M.; Xu, S.; Yang, C.; Wang, Y.; Hu, L., High-capacity, low-tortuosity, and channel-guided lithium metal anode. *Proc. Natl. Acad. Sci. U.S.A.* **2017,** *114* (14), 3584-3589.

168. Lin, D.; Liu, Y.; Liang, Z.; Lee, H.-W.; Sun, J.; Wang, H.; Yan, K.; Xie, J.; Cui, Y., Layered reduced graphene oxide with nanoscale interlayer gaps as a stable host for lithium metal anodes. *Nature Nanotech* **2016,** *11* (7), 626-632.

169. Li, H.; Chao, D.; Chen, B.; Chen, X.; Chuah, C.; Tang, Y.; Jiao, Y.; Jaroniec, M.; Qiao, S.-Z., Revealing Principles for Design of Lean-Electrolyte Lithium Metal Anode via In Situ Spectroscopy. *J. Am. Chem. Soc.* **2020,** *142* (4), 2012-2022.

170. Zhang, R.; Chen, X.-R.; Chen, X.; Cheng, X.-B.; Zhang, X.-Q.; Yan, C.; Zhang, Q., Lithiophilic Sites in Doped Graphene Guide Uniform Lithium Nucleation for Dendrite-Free Lithium Metal Anodes. *Angewandte Chemie International Edition* **2017,** *56* (27), 7764-7768.

171. Zhan, Y.-X.; Shi, P.; Zhang, X.-Q.; Ding, F.; Huang, J.-Q.; Jin, Z.; Xiang, R.; Liu, X.; Zhang, Q., The Insights of Lithium Metal Plating/Stripping in Porous Hosts: Progress and Perspectives. *Energy Technology* **2021,** *9* (2), 2000700.

172. Klankowski, S. A.; Pandey, G. P.; Cruden, B. A.; Liu, J.; Wu, J.; Rojeski, R. A.; Li, J., Anomalous capacity increase at high-rates in lithium-ion battery anodes based on silicon-coated vertically aligned carbon nanofibers. *Journal of Power Sources* **2015,** *276*, 73-79.

173. Zhang, Z.; Wang, J.; Yan, X.; Zhang, S.; Yang, W.; Zhuang, Z.; Han, W.-Q., In-situ growth of hierarchical N-doped CNTs/Ni Foam scaffold for dendrite-free lithium metal anode. *Energy Storage Materials* **2020,** *29*, 332-340.

174. Shen, X.; Zhang, X.-Q.; Ding, F.; Huang, J.-Q.; Xu, R.; Chen, X.; Yan, C.; Su, F.-Y.; Chen, C.-M.; Liu, X.; Zhang, Q., Advanced Electrode Materials in Lithium Batteries: Retrospect and Prospect. *Energy Mater Adv* **2021,** *2021*, 2021/1205324.

175. An, Y.; Tian, Y.; Li, Y.; Wei, C.; Tao, Y.; Liu, Y.; Xi, B.; Xiong, S.; Feng, J.; Qian, Y., Heteroatom-doped 3D porous carbon architectures for highly stable aqueous zinc metal batteries and non-aqueous lithium metal batteries. *Chemical Engineering Journal* **2020,** *400*, 125843.

176. Chen, H.; Pei, A.; Wan, J.; Lin, D.; Vilá, R.; Wang, H.; Mackanic, D.; Steinrück, H.-G.; Huang, W.; Li, Y.; Yang, A.; Xie, J.; Wu, Y.; Wang, H.; Cui, Y., Tortuosity Effects in Lithium-Metal Host Anodes. *Joule* **2020,** *4* (4), 938-952.

177. Liu, F.; Xu, R.; Wu, Y.; Boyle, D. T.; Yang, A.; Xu, J.; Zhu, Y.; Ye, Y.; Yu, Z.; Zhang, Z.; Xiao, X.; Huang, W.; Wang, H.; Chen, H.; Cui, Y., Dynamic spatial progression of isolated lithium during battery operations. *Nature* **2021,** *600* (7890), 659-663.

178. Chen, K.-H.; N. Wood, K.; Kazyak, E.; S. LePage, W.; L. Davis, A.; J. Sanchez, A.; P. Dasgupta, N., Dead lithium: mass transport effects on voltage, capacity, and failure of lithium metal anodes. *Journal of Materials Chemistry A* **2017,** *5* (23), 11671-11681.

179. Ma, Q.; Zhang, X.; Wang, A.; Xia, Y.; Liu, X.; Luo, J., Stabilizing Solid Electrolyte Interphases on Both Anode and Cathode for High Areal Capacity, High-Voltage Lithium Metal Batteries with High Li Utilization and Lean Electrolyte. *Advanced Functional Materials* **2020,** *30* (32), 2002824.

180. Yang, Y.; Yin, Y.; Davies, D. M.; Zhang, M.; Mayer, M., Liquefied Gas Electrolytes for Wide-Temperature Lithium Metal Batteries. *Environmental Science*.

181. Pei, A.; Zheng, G.; Shi, F.; Li, Y.; Cui, Y., Nanoscale Nucleation and Growth of Electrodeposited Lithium Metal. *Nano Lett.* **2017,** *17* (2), 1132-1139.

182. Park, S. H.; Lee, Y. J., Morphological control of electrodeposited lithium metal via seeded growth: stepwise spherical to fibrous lithium growth. *Journal of Materials Chemistry A* **2021,** *9* (3), 1803-1811.

183. Fonseca Rodrigues, M.-T.; Maroni, V. A.; Gosztola, D. J.; Yao, K. P. C.; Kalaga, K.; Shkrob, I. A.; Abraham, D. P., Lithium Acetylide: A Spectroscopic Marker for Lithium Deposition During Fast Charging of Li-Ion Cells. *ACS Appl. Energy Mater.* **2019,** *2* (1), 873-881.

184. Migge, S.; Sandmann, G.; Rahner, D.; Dietz, H.; Plieth, W., Studying lithium intercalation into graphite particles via in situ Raman spectroscopy and confocal microscopy. *J Solid State Electrochem* **2005,** *9* (3), 132-137.

185. Bao, W.; Wan, J.; Han, X.; Cai, X.; Zhu, H.; Kim, D.; Ma, D.; Xu, Y.; Munday, J. N.; Drew, H. D.; Fuhrer, M. S.; Hu, L., Approaching the limits of transparency and conductivity in graphitic materials through lithium intercalation. *Nature Communications* **2014,** *5* (1), 4224.

186. Shi, P.; Li, T.; Zhang, R.; Shen, X.; Cheng, X.-B.; Xu, R.; Huang, J.-Q.; Chen, X.-R.; Liu, H.; Zhang, Q., Lithiophilic LiC6 Layers on Carbon Hosts Enabling Stable Li Metal Anode in Working Batteries. *Advanced Materials* **2019,** *31* (8), 1807131.

187. Lodico, J. J.; Woodall, M.; Chan, H. L.; Hubbard, W. A.; Regan, B. C., In Situ Optical Microscopy of the Electrochemical Intercalation of Lithium into Single Crystal Graphite. *Microscopy and Microanalysis* **2017,** *23* (S1), 1982-1983.

188. von Holtum, B.; Kubot, M.; Peschel, C.; Rodehorst, U.; Winter, M.; Nowak, S.; Wiemers-Meyer, S., Accessing the Primary Solid–Electrolyte Interphase on Lithium Metal: A Method for Low-Concentration Compound Analysis. *ChemSusChem n/a* (n/a), e202201912.

189. Liu, Q.; Cresce, A.; Schroeder, M.; Xu, K.; Mu, D.; Wu, B.; Shi, L.; Wu, F., Insight on lithium metal anode interphasial chemistry: Reduction mechanism of cyclic ether solvent and SEI film formation. *Energy Storage Materials* **2019,** *17*, 366-373.

190. Jaumann, T.; Balach, J.; Klose, M.; Oswald, S.; Eckert, J.; Giebeler, L., Role of 1,3-Dioxolane and LiNO3 Addition on the Long Term Stability of Nanostructured Silicon/Carbon Anodes for Rechargeable Lithium Batteries. *J. Electrochem. Soc.* **2016,** *163* (3), A557.

191. Wang, Y.; Lin, C.-F.; Rao, J.; Gaskell, K.; Rubloff, G.; Lee, S. B., Electrochemically Controlled Solid Electrolyte Interphase Layers Enable Superior Li–S Batteries. *ACS Appl. Mater. Interfaces* **2018,** *10* (29), 24554-24563.

192. Li, W.; Yao, H.; Yan, K.; Zheng, G.; Liang, Z.; Chiang, Y.-M.; Cui, Y., The synergetic effect of lithium polysulfide and lithium nitrate to prevent lithium dendrite growth. *Nature Communications* **2015,** *6* (1), 7436.

193. Nguyen-Vu, T. D. B.; Chen, H.; Cassell, A. M.; Andrews, R. J.; Meyyappan, M.; Li, J., Vertically Aligned Carbon Nanofiber Architecture as a Multifunctional 3-D Neural Electrical Interface. *IEEE Transactions on Biomedical Engineering* **2007,** *54* (6), 1121-1128.

194. de Asis, E. D.; Nguyen-Vu, T. D. B.; Arumugam, P. U.; Chen, H.; Cassell, A. M.; Andrews, R. J.; Yang, C. Y.; Li, J., High efficient electrical stimulation of hippocampal slices with vertically aligned carbon nanofiber microbrush array. *Biomed Microdevices* **2009,** *11* (4), 801-808.

195. Nguyen-Vu, T. D. B.; Chen, H.; Cassell, A. M.; Andrews, R.; Meyyappan, M.; Li, J., Vertically Aligned Carbon Nanofiber Arrays: An Advance toward Electrical–Neural Interfaces. *Small* **2006,** *2* (1), 89-94.

196. Wang, X.; Pawar, G.; Li, Y.; Ren, X.; Zhang, M.; Lu, B.; Banerjee, A.; Liu, P.; Dufek, E. J.; Zhang, J.-G.; Xiao, J.; Liu, J.; Meng, Y. S.; Liaw, B., Glassy Li metal anode for high-performance rechargeable Li batteries. *Nature Materials* **2020**, 1-7.

197. Zhan, Y.-X.; Shi, P.; Ma, X.-X.; Jin, C.-B.; Zhang, Q.-K.; Yang, S.-J.; Li, B.-Q.; Zhang, X.-Q.; Huang, J.-Q., Failure Mechanism of Lithiophilic Sites in Composite Lithium Metal Anode under Practical Conditions. *Advanced Energy Materials* **2022,** *12* (2), 2103291.

198. Kittner, N.; Lill, F.; Kammen, D. M., Energy storage deployment and innovation for the clean energy transition. *Nat Energy* **2017,** *2* (9), 1-6.

199. Kim, S.; Park, G.; Lee, S. J.; Seo, S.; Ryu, K.; Kim, C. H.; Choi, J. W., Lithium-Metal Batteries: From Fundamental Research to Industrialization. *Advanced Materials* **2023,** *35* (43), 2206625.

200. Liu, J.; Bao, Z.; Cui, Y.; Dufek, E. J.; Goodenough, J. B.; Khalifah, P.; Li, Q.; Liaw, B. Y.; Liu, P.; Manthiram, A.; Meng, Y. S.; Subramanian, V. R.; Toney, M. F.; Viswanathan, V. V.; Whittingham, M. S.; Xiao, J.; Xu, W.; Yang, J.; Yang, X.-Q.; Zhang, J.-G., Pathways for practical high-energy long-cycling lithium metal batteries. *Nat Energy* **2019,** *4* (3), 180-186.

201. Nanda, S.; Gupta, A.; Manthiram, A., Anode-Free Full Cells: A Pathway to High-Energy Density Lithium-Metal Batteries. *Advanced Energy Materials* **2021,** *11* (2), 2000804.

202. Shao, A.; Tang, X.; Zhang, M.; Bai, M.; Ma, Y., Challenges, Strategies, and Prospects of the Anode-Free Lithium Metal Batteries. *Advanced Energy and Sustainability Research* **2022,** *3* (4), 2100197.

203. Wu, B.; Chen, C.; Raijmakers, L. H. J.; Liu, J.; Danilov, D. L.; Eichel, R.-A.; Notten, P. H. L., Li-growth and SEI engineering for anode-free Li-metal rechargeable batteries: A review of current advances. *Energy Storage Materials* **2023,** *57*, 508-539.

204. Weber, R.; Genovese, M.; Louli, A. J.; Hames, S.; Martin, C.; Hill, I. G.; Dahn, J. R., Long cycle life and dendrite-free lithium morphology in anode-free lithium pouch cells enabled by a dual-salt liquid electrolyte. *Nat Energy* **2019,** *4* (8), 683-689.

205. Fang, C.; Lu, B.; Pawar, G.; Zhang, M.; Cheng, D.; Chen, S.; Ceja, M.; Doux, J.-M.; Musrock, H.; Cai, M.; Liaw, B.; Meng, Y. S., Pressure-tailored lithium deposition and dissolution in lithium metal batteries. *Nat Energy* **2021,** *6* (10), 987-994.

206. Zhao, Q.; Deng, Y.; Utomo, N. W.; Zheng, J.; Biswal, P.; Yin, J.; Archer, L. A., On the crystallography and reversibility of lithium electrodeposits at ultrahigh capacity. *Nat Commun* **2021,** *12* (1), 6034.

207. Wang, X.; Pawar, G.; Li, Y.; Ren, X.; Zhang, M.; Lu, B.; Banerjee, A.; Liu, P.; Dufek, E. J.; Zhang, J.-G.; Xiao, J.; Liu, J.; Meng, Y. S.; Liaw, B., Glassy Li metal anode for high-performance rechargeable Li batteries. *Nat. Mater.* **2020,** *19* (12), 1339-1345.

208. Zheng, G.; Lee, S. W.; Liang, Z.; Lee, H.-W.; Yan, K.; Yao, H.; Wang, H.; Li, W.; Chu, S.; Cui, Y., Interconnected hollow carbon nanospheres for stable lithium metal anodes. *Nature Nanotech* **2014,** *9* (8), 618-623.

209. Yan, K.; Wang, J.; Zhao, S.; Zhou, D.; Sun, B.; Cui, Y.; Wang, G., Temperature-Dependent Nucleation and Growth of Dendrite-Free Lithium Metal Anodes. *Angewandte Chemie* **2019,** *131* (33), 11486-11490.

210. Pei, A.; Zheng, G.; Shi, F.; Li, Y.; Cui, Y., Nanoscale Nucleation and Growth of Electrodeposited Lithium Metal. *Nano Lett* **2017,** *17* (2), 1132-1139.

211. Sano, H.; Sakaebe, H.; Senoh, H.; Matsumoto, H., Effect of Current Density on Morphology of Lithium Electrodeposited in Ionic Liquid-Based Electrolytes. *J. Electrochem. Soc.* **2014,** *161* (9), A1236.

212. Jung, H.; Lee, B.; Lengyel, M.; Axelbaum, R.; Yoo, J.; Kim, Y. S.; Jun, Y. S., Nanoscale detection of nucleation and growth of Li electrodeposition at various current densities. *J. Mater. Chem. A* **2018,** *6* (11), 4629-4635.

213. Dong, K.; Xu, Y.; Tan, J.; Osenberg, M.; Sun, F.; Kochovski, Z.; Pham, D. T.; Mei, S.; Hilger, A.; Ryan, E.; Lu, Y.; Banhart, J.; Manke, I., Unravelling the Mechanism of Lithium Nucleation and Growth and the Interaction with the Solid Electrolyte Interface. *ACS Energy Lett.* **2021,** *6* (5), 1719-1728.

214. Biswal, P.; Stalin, S.; Kludze, A.; Choudhury, S.; Archer, L. A., Nucleation and Early Stage Growth of Li Electrodeposits. *Nano Lett.* **2019,** *19* (11), 8191-8200.

215. Xu, X.; Jiao, X.; Kapitanova, O. O.; Wang, J.; Volkov, V. S.; Liu, Y.; Xiong, S., Diffusion Limited Current Density: A Watershed in Electrodeposition of Lithium Metal Anode. *Advanced Energy Materials* **2022,** *12* (19), 2200244.

216. Boyle, D. T.; Li, Y.; Pei, A.; Vilá, R. A.; Zhang, Z.; Sayavong, P.; Kim, M. S.; Huang, W.; Wang, H.; Liu, Y.; Xu, R.; Sinclair, R.; Qin, J.; Bao, Z.; Cui, Y., Resolving Current-Dependent Regimes of Electroplating Mechanisms for Fast Charging Lithium Metal Anodes. *Nano Lett.* **2022,** *22* (20), 8224-8232.

217. Aurbach, D.; Zinigrad, E.; Cohen, Y.; Teller, H., A short review of failure mechanisms of lithium metal and lithiated graphite anodes in liquid electrolyte solutions. *Solid State Ionics* **2002,** *148* (3), 405-416.

218. Lang, J.; Qi, L.; Luo, Y.; Wu, H., High performance lithium metal anode: Progress and prospects. *Energy Storage Materials* **2017,** *7*, 115-129.

219. Yang, C.-P.; Yin, Y.-X.; Zhang, S.-F.; Li, N.-W.; Guo, Y.-G., Accommodating lithium into 3D current collectors with a submicron skeleton towards long-life lithium metal anodes. *Nat Commun* **2015,** *6* (1), 8058.

220. Fan, X.; Li, Y.; Luo, C.; Luo, S.; Huang, B.; Liu, S.; Sun, W., Vertically aligned MnO2 nanosheets on carbon fiber cloth as lithiophilic host enables dendrite-free lithium metal anode. *Electrochimica Acta* **2023,** *464*, 142896.

221. Wang, Y.; Sang, H.-Q.; Zhang, W.; Qi, Y.; He, R.-X.; Chen, B.; Sun, W.; Zhao, X.-Z.; Fu, D.; Liu, Y., Electrophoretic Deposited Black Phosphorus on 3D Porous Current Collectors to Regulate Li Nucleation for Dendrite-Free Lithium Metal Anodes. *ACS Appl. Mater. Interfaces* **2020,** *12* (46), 51563-51572.

222. Huang, Z.; Zhou, G.; Lv, W.; Deng, Y.; Zhang, Y.; Zhang, C.; Kang, F.; Yang, Q.-H., Seeding lithium seeds towards uniform lithium deposition for stable lithium metal anodes. *Nano Energy* **2019,** *61*, 47-53.

223. Li, J.; Pandey, G. P., Advanced Physical Chemistry of Carbon Nanotubes. *Annual Review of Physical Chemistry* **2015,** *66* (1), 331-356.

224. Rajendran, S.; Sekar, A.; Li, J., Mechanistic understanding of Li metal anode processes in a model 3D conductive host based on vertically aligned carbon nanofibers. *Carbon* **2023,** *212*, 118174.

225. He, Y.; Ren, X.; Xu, Y.; Engelhard, M. H.; Li, X.; Xiao, J.; Liu, J.; Zhang, J.-G.; Xu, W.; Wang, C., Origin of lithium whisker formation and growth under stress. *Nature Nanotech* **2019,** *14* (11), 1042-1047.

226. Kazyak, E.; Wang, M. J.; Lee, K.; Yadavalli, S.; Sanchez, A. J.; Thouless, M. D.; Sakamoto, J.; Dasgupta, N. P., Understanding the electro-chemo-mechanics of Li plating in anode-free solid-state batteries with operando 3D microscopy. *Matter* **2022,** *5* (11), 3912-3934.

227. Shen, X.; Zhang, R.; Shi, P.; Chen, X.; Zhang, Q., How Does External Pressure Shape Li Dendrites in Li Metal Batteries? *Advanced Energy Materials* **2021,** *11* (10), 2003416.

228. Liu, J.; Essner, J.; Li, J., Hybrid Supercapacitor Based on Coaxially Coated Manganese Oxide on Vertically Aligned Carbon Nanofiber Arrays. *Chemistry of Materials* **2010,** *22* (17), 5022-5030.

229. Zaidi, S. S. H.; Rajendran, S.; Sekar, A.; Elangovan, A.; Li, J.; Li, X., Binder-free Li-O₂battery cathodes using Ni- and PtRu-coated vertically aligned carbon nanofibers as electrocatalysts for enhanced stability. *Nano Research Energy* **2023,** *2* (2), e9120055.

230. Brissot, C.; Rosso, M.; Chazalviel, J. N.; Lascaud, S., Dendritic growth mechanisms in lithium/polymer cells. *Journal of Power Sources* **1999,** *81-82*, 925-929.

231. Hou, Z.; Gao, Y.; Zhou, R.; Zhang, B., Unraveling the Rate-Dependent Stability of Metal Anodes and Its Implication in Designing Cycling Protocol. *Advanced Functional Materials* **2022,** *32* (7), 2107584.

232. Feng, G.; Shi, Y.; Jia, H.; Risal, S.; Yang, X.; Ruchhoeft, P.; Shih, W.-C.; Fan, Z.; Xu, W.; Shan, X., Progressive and instantaneous nature of lithium nucleation discovered by dynamic and operando imaging. *Science Advances* **2023,** *9* (21), eadg6813.

233. Wang, S.; Qu, J.; Wu, F.; Yan, K.; Zhang, C., Cycling Performance and Kinetic Mechanism Analysis of a Li Metal Anode in Series-Concentrated Ether Electrolytes. *ACS Appl. Mater. Interfaces* **2020,** *12* (7), 8366-8375.

234. Xie, J.-D.; Liu, W.-J.; Li, C.; Patra, J.; Gandomi, Y. A.; Dong, Q.-F.; Chang, J.-K., Superior coulombic efficiency of lithium anodes for rechargeable batteries utilizing high-concentration ether electrolytes. *Electrochimica Acta* **2019,** *319*, 625-633.

235. Liu, X.; Xu, P.; Zhang, J.; Hu, X.; Hou, Q.; Lin, X.; Zheng, M.; Dong, Q., A Highly Reversible Lithium Metal Anode by Constructing Lithiophilic Bi-Nanosheets. *Small* **2021,** *17* (45), 2102016.

236. Deng, W.; Yin, X.; Bao, W.; Zhou, X.; Hu, Z.; He, B.; Qiu, B.; Meng, Y. S.; Liu, Z., Quantification of reversible and irreversible lithium in practical lithium-metal batteries. *Nat Energy* **2022,** *7* (11), 1031-1041.

237. Yu, Z.; Rudnicki, P. E.; Zhang, Z.; Huang, Z.; Celik, H.; Oyakhire, S. T.; Chen, Y.; Kong, X.; Kim, S. C.; Xiao, X.; Wang, H.; Zheng, Y.; Kamat, G. A.; Kim, M. S.; Bent, S. F.; Qin, J.; Cui, Y.; Bao, Z., Rational solvent molecule tuning for high-performance lithium metal battery electrolytes. *Nat Energy* **2022,** *7* (1), 94-106.

238. Ren, X. D.; Zou, L. F.; Cao, X.; Engelhard, M. H.; Liu, W.; Burton, S. D.; Lee, H.; Niu, C. J.; Matthews, B. E.; Zhu, Z. H.; Wang, C. M.; Arey, B. W.; Xiao, J.; Liu, J.; Zhang, J. G.; Xu, W., Enabling High-Voltage Lithium-Metal Batteries under Practical Conditions. *Joule* **2019,** *3* (7), 1662-1676.

239. Jeon, J.; Yoon, G. H.; Vegge, T.; Chang, J. H., Phase-Field Investigation of Lithium Electrodeposition at Different Applied Overpotentials and Operating Temperatures. *ACS Appl. Mater. Interfaces* **2022,** *14* (13), 15275-15286.

240. Sun, X.; Zhang, X.; Ma, Q.; Guan, X.; Wang, W.; Luo, J., Revisiting the Electroplating Process for Lithium-Metal Anodes for Lithium-Metal Batteries. *Angewandte Chemie International Edition* **2020,** *59* (17), 6665-6674.

241. Chen, J.; Qiao, X.; Fu, W.; Han, X.; Wu, Q.; Wang, Y.; Zhang, Y.; Shi, L.; Zhao, J.; Ma, Y., Lithiophilic hyperbranched Cu nanostructure for stable Li metal anodes. *SmartMat* **2023,** *4* (3), e1174.

242. Xu, X.; Liu, Y.; Hwang, J.-Y.; Kapitanova, O. O.; Song, Z.; Sun, Y.-K.; Matic, A.; Xiong, S., Role of Li-Ion Depletion on Electrode Surface: Underlying Mechanism for Electrodeposition Behavior of Lithium Metal Anode. *Advanced Energy Materials* **2020,** *10* (44), 2002390.

243. Li, Y.; Li, Y.; Zhang, L.; Tao, H.; Li, Q.; Zhang, J.; Yang, X., Lithiophilicity: The key to efficient lithium metal anodes for lithium batteries. *Journal of Energy Chemistry* **2023,** *77*, 123-136.

244. Chen, X.-R.; Chen, X.; Yan, C.; Zhang, X.-Q.; Zhang, Q.; Huang, J.-Q., Role of Lithiophilic Metal Sites in Lithium Metal Anodes. *Energy Fuels* **2021,** *35* (15), 12746-12752.

245. Luo, Z.; Qiu, X.; Liu, C.; Li, S.; Wang, C.; Zou, G.; Hou, H.; Ji, X., Interfacial challenges towards stable Li metal anode. *Nano Energy* **2021,** *79*, 105507.

246. Yang, C.; Yao, Y.; He, S.; Xie, H.; Hitz, E.; Hu, L., Ultrafine Silver Nanoparticles for Seeded Lithium Deposition toward Stable Lithium Metal Anode. *Advanced Materials* **2017,** *29* (38), 1702714.

247. Pu, J.; Li, J.; Shen, Z.; Zhong, C.; Liu, J.; Ma, H.; Zhu, J.; Zhang, H.; Braun, P. V., Interlayer Lithium Plating in Au Nanoparticles Pillared Reduced Graphene Oxide for Lithium Metal Anodes. *Advanced Functional Materials* **2018,** *28* (41), 1804133.

248. Ke, X.; Liang, Y.; Ou, L.; Liu, H.; Chen, Y.; Wu, W.; Cheng, Y.; Guo, Z.; Lai, Y.; Liu, P.; Shi, Z., Surface engineering of commercial Ni foams for stable Li metal anodes. *Energy Storage Materials* **2019,** *23*, 547-555.

249. Chi, S.-S.; Wang, Q.; Han, B.; Luo, C.; Jiang, Y.; Wang, J.; Wang, C.; Yu, Y.; Deng, Y., Lithiophilic Zn Sites in Porous CuZn Alloy Induced Uniform Li Nucleation and Dendrite-free Li Metal Deposition. *Nano Lett.* **2020,** *20* (4), 2724-2732.

250. Lan, X.; Ye, W.; Zheng, H.; Cheng, Y.; Zhang, Q.; Peng, D.-L.; Wang, M.-S., Encapsulating lithium and sodium inside amorphous carbon nanotubes through gold-seeded growth. *Nano Energy* **2019,** *66*, 104178.

251. Yan, K.; Lu, Z.; Lee, H.-W.; Xiong, F.; Hsu, P.-C.; Li, Y.; Zhao, J.; Chu, S.; Cui, Y., Selective deposition and stable encapsulation of lithium through heterogeneous seeded growth. *Nat Energy* **2016,** *1* (3), 16010.

252. Sun, J.; Cheng, Y.; Zhang, H.; Yan, X.; Sun, Z.; Ye, W.; Li, W.; Zhang, M.; Gao, H.; Han, J.; Peng, D.-L.; Yang, Y.; Wang, M.-S., Enhanced Cyclability of Lithium Metal Anodes Enabled by Anti-aggregation of Lithiophilic Seeds. *Nano Lett.* **2022,** *22* (14), 5874-5882.

253. Teo, W. E.; Ramakrishna, S., A review on electrospinning design and nanofibre assemblies. *Nanotechnology* **2006,** *17* (14), R89.

254. Xue, J.; Xie, J.; Liu, W.; Xia, Y., Electrospun Nanofibers: New Concepts, Materials, and Applications. *Acc. Chem. Res.* **2017,** *50* (8), 1976-1987.

255. Banitaba, S. N.; Ehrmann, A., Application of Electrospun Nanofibers for Fabrication of Versatile and Highly Efficient Electrochemical Devices: A Review. *Polymers* **2021,** *13* (11), 1741.

256. Park, S.-H.; Jung, H.-R.; Lee, W.-J., Hollow activated carbon nanofibers prepared by electrospinning as counter electrodes for dye-sensitized solar cells. *Electrochimica Acta* **2013,** *102*, 423-428.

257. Formo, E.; S. Yavuz, M.; P. Lee, E.; Lane, L.; Xia, Y., Functionalization of electrospun ceramic nanofibre membranes with noble-metal nanostructures for catalytic applications. *Journal of Materials Chemistry* **2009,** *19* (23), 3878-3882.

258. Formo, E.; Lee, E.; Campbell, D.; Xia, Y., Functionalization of Electrospun TiO2 Nanofibers with Pt Nanoparticles and Nanowires for Catalytic Applications. *Nano Lett.* **2008,** *8* (2), 668-672.

259. Xue, J.; Pisignano, D.; Xia, Y., Maneuvering the Migration and Differentiation of Stem Cells with Electrospun Nanofibers. *Advanced Science* **2020,** *7* (15), 2000735.

260. Peng, S.; Jin, G.; Li, L.; Li, K.; Srinivasan, M.; Ramakrishna, S.; Chen, J., Multi-functional electrospun nanofibres for advances in tissue regeneration, energy conversion & storage, and water treatment. *Chemical Society Reviews* **2016,** *45* (5), 1225-1241.

261. Kim, B. G.; Kang, D. W.; Park, G.; Park, S. H.; Lee, S.-M.; Choi, J. W., Electrospun Li-confinable hollow carbon fibers for highly stable Li-metal batteries. *Chemical Engineering Journal* **2021,** *422*, 130017.

262. Li, T.; Gu, S.; Chen, L.; Zhang, L.; Qin, X.; Huang, Z.; He, Y.-B.; Lv, W.; Kang, F., Bidirectional Lithiophilic Gradients Modification of Ultralight 3D Carbon Nanofiber Host for Stable Lithium Metal Anode. *Small* **2022,** *18* (33), 2203273.

263. Newcomb, B. A., Processing, structure, and properties of carbon fibers. *Composites Part A: Applied Science and Manufacturing* **2016,** *91*, 262-282.

264. Liu, C.-K.; Lai, K.; Liu, W.; Yao, M.; Sun, R.-J., Preparation of carbon nanofibres through electrospinning and thermal treatment. *Polymer International* **2009,** *58* (12), 1341-1349.

265. Li, S.-H. P. J., Electrospun Carbon Nanofibers for Energy Conversion and Storage. In *Nanocarbon Electronics*, Jenny Stanford Publishing: 2020.

266. Li, D.; Xia, Y., Electrospinning of Nanofibers: Reinventing the Wheel? *Advanced Materials* **2004,** *16* (14), 1151-1170.

267. Greiner, A.; Wendorff, J. H., Electrospinning: A Fascinating Method for the Preparation of Ultrathin Fibers. *Angewandte Chemie International Edition* **2007,** *46* (30), 5670-5703.

268. Goodhew, P. J.; Clarke, A. J.; Bailey, J. E., A review of the fabrication and properties of carbon fibres. *Materials Science and Engineering* **1975,** *17* (1), 3-30.

269. Damodaran, S.; Desai, P.; Abhiraman, A. S., Chemical and Physical Aspects of the Formation of Carbon Fibres from PAN-based Precursors. *The Journal of The Textile Institute* **1990,** *81* (4), 384-420.

270. Schierholz, R.; Kröger, D.; Weinrich, H.; Gehring, M.; Tempel, H.; Kungl, H.; Mayer, J.; Eichel, R.-A., The carbonization of polyacrylonitrile-derived electrospun carbon nanofibers studied by in situ transmission electron microscopy. *RSC Advances* **2019,** *9* (11), 6267-6277.

271. Li, D.; Wang, Y.; Xia, Y., Electrospinning of Polymeric and Ceramic Nanofibers as Uniaxially Aligned Arrays. *Nano Lett.* **2003,** *3* (8), 1167-1171.

272. Li, D.; Wang, Y.; Xia, Y., Electrospinning Nanofibers as Uniaxially Aligned Arrays and Layer-by-Layer Stacked Films. *Advanced Materials* **2004,** *16* (4), 361-366.

273. Huang, S.; Yang, H.; Hu, J.; Liu, Y.; Wang, K.; Peng, H.; Zhang, H.; Fan, L.-Z., Early Lithium Plating Behavior in Confined Nanospace of 3D Lithiophilic Carbon Matrix for Stable Solid-State Lithium Metal Batteries. *Small* **2019,** *15* (43), 1904216.

274. Liu, S.; Wang, A.; Li, Q.; Wu, J.; Chiou, K.; Huang, J.; Luo, J., Crumpled Graphene Balls Stabilized Dendrite-free Lithium Metal Anodes. *Joule* **2018,** *2* (1), 184-193.

275. Shi, L.; Hu, Z.; Hong, Y., PVDF-supported graphene foam as a robust current collector for lithium metal anodes. *RSC Advances* **2020,** *10* (35), 20915-20920.

276. Wu, Q.; Qin, M.; Yan, H.; Zhong, W.; Zhang, W.; Liu, M.; Cheng, S.; Xie, J., Facile Replacement Reaction Enables Nano-Ag-Decorated Three-Dimensional Cu Foam as High-Rate Lithium Metal Anode. *ACS Appl. Mater. Interfaces* **2022,** *14* (37), 42030-42037.

277. Lyu, Z.; Lim, G. J. H.; Guo, R.; Pan, Z.; Zhang, X.; Zhang, H.; He, Z.; Adams, S.; Chen, W.; Ding, J.; Wang, J., 3D-printed electrodes for lithium metal batteries with high areal capacity and high-rate capability. *Energy Storage Materials* **2020,** *24*, 336-342.

278. Chen, L.; Chen, G.; Wen, Z.; Wu, D.; Qin, Z.; Zhang, N.; Liu, X.; Ma, R., Electroplating CuO nanoneedle arrays on Ni foam as superior 3D scaffold for dendrite-free and stable Li metal anode. *Applied Surface Science* **2022,** *599*, 153955.

279. Chen, L.; Chen, H.; Wang, Z.; Gong, X.; Chen, X.; Wang, M.; Jiao, S., Self-supporting lithiophilic N-doped carbon rod array for dendrite-free lithium metal anode. *Chemical Engineering Journal* **2019,** *363*, 270-277.

280. Zhan, Y.-X.; Shi, P.; Zhang, R.; Zhang, X.-Q.; Shen, X.; Jin, C.-B.; Li, B.-Q.; Huang, J.-Q., Deciphering the Effect of Electrical Conductivity of Hosts on Lithium Deposition in Composite Lithium Metal Anodes. *Advanced Energy Materials* **2021,** *11* (37), 2101654.

281. Fang, Y.; Zeng, Y.; Jin, Q.; Lu, X. F.; Luan, D.; Zhang, X.; Lou, X. W., Nitrogen-Doped Amorphous Zn–Carbon Multichannel Fibers for Stable Lithium Metal Anodes. *Angewandte Chemie International Edition* **2021,** *60* (15), 8515-8520.

282. Xu, Z.; Xu, L.; Xu, Z.; Deng, Z.; Wang, X., N, O-Codoped Carbon Nanosheet Array Enabling Stable Lithium Metal Anode. *Advanced Functional Materials* **2021,** *31* (40), 2102354.

283. Noh, H.-J.; Lee, M.-H.; Kim, B. G.; Park, J.-H.; Lee, S.-M.; Choi, J.-H., 3D Carbon-Based Porous Anode with a Pore-Size Gradient for High-Performance Lithium Metal Batteries. *ACS Appl. Mater. Interfaces* **2021,** *13* (46), 55227-55234.

284. Muthukumar, K.; Rajendran, S.; Sekar, A.; Chen, Y.; Li, J., Synthesis of V2O5 Nanoribbon–Reduced Graphene Oxide Hybrids as Stable Aqueous Zinc-Ion Battery Cathodes via Divalent Transition Metal Cation-Mediated Coprecipitation. *ACS Sustainable Chemistry & Engineering* **2023,** *11* (6), 2670-2679.

285. Xu, J.; Zhang, Y.; Liu, C.; Cheng, H.; Cai, X.; Jia, D.; Lin, H., Al3+ Introduction Hydrated Vanadium Oxide Induced High Performance for Aqueous Zinc-Ion Batteries. *Small* **2022,** *18* (47), 2204180.

286. He, P.; Zhang, G.; Liao, X.; Yan, M.; Xu, X.; An, Q.; Liu, J.; Mai, L., Sodium Ion Stabilized Vanadium Oxide Nanowire Cathode for High-Performance Zinc-Ion Batteries. *Advanced Energy Materials* **2018,** *8* (10), 1702463.

287. Liu, C.; Tian, M.; Wang, M.; Zheng, J.; Wang, S.; Yan, M.; Wang, Z.; Yin, Z.; Yang, J.; Cao, G., Catalyzing zinc-ion intercalation in hydrated vanadates for aqueous zinc-ion batteries. *J. Mater. Chem. A* **2020,** *8* (16), 7713-7723.

288. Luo, P.; Zhang, W.; Wang, S.; Liu, G.; Xiao, Y.; Zuo, C.; Tang, W.; Fu, X.; Dong, S., Electroactivation-induced hydrated zinc vanadate as cathode for high-performance aqueous zinc-ion batteries. *Journal of Alloys and Compounds* **2021,** *884*, 161147.

289. Kundu, D.; Adams, B. D.; Duffort, V.; Vajargah, S. H.; Nazar, L. F., A high-capacity and long-life aqueous rechargeable zinc battery using a metal oxide intercalation cathode. *Nature Energy* **2016,** *1* (10), 1-8.

290. Sun, J.; Zhang, Y.; Liu, Y.; Jiang, H.; Dong, X.; Hu, T.; Meng, C., Synthesis and electrochemical properties of V2O5nH2O compound with reduced graphene oxide/polyvinyl alcohol film as the free-standing cathode for coin-typed aqueous Zn-ion batteries. *Colloids and Surfaces A: Physicochemical and Engineering Aspects* **2021,** *613*, 126087.

291. Feng, Z.; Zhang, Y.; Sun, J.; Liu, Y.; Jiang, H.; Cui, M.; Hu, T.; Meng, C., Dual ions enable vanadium oxide hydration with superior Zn2+ storage for aqueous zinc-ion batteries. *Chemical Engineering Journal* **2022,** *433*, 133795.

292. Xu, G.; Liu, X.; Huang, S.; Li, L.; Wei, X.; Cao, J.; Yang, L.; Chu, P. K., Freestanding, Hierarchical, and Porous Bilayered NaxV2O5·nH2O/rGO/CNT Composites as High-Performance Cathode Materials for Nonaqueous K-Ion Batteries and Aqueous Zinc-Ion Batteries. *ACS Appl. Mater. Interfaces* **2020,** *12* (1), 706-716.

293. Qin, H.; Chen, L.; Wang, L.; Chen, X.; Yang, Z., V2O5 hollow spheres as high rate and long life cathode for aqueous rechargeable zinc ion batteries. *Electrochimica Acta* **2019,** *306*, 307-316.

294. Ming, F.; Liang, H.; Lei, Y.; Kandambeth, S.; Eddaoudi, M.; Alshareef, H. N., Layered MgxV2O5·nH2O as Cathode Material for High-Performance Aqueous Zinc Ion Batteries. *ACS Energy Lett.* **2018,** *3* (10), 2602-2609.

295. Hao, Y.; Zhang, S.; Tao, P.; Shen, T.; Huang, Z.; Yan, J.; Chen, Y., Pillaring Effect of K Ion Anchoring for Stable V2O5-Based Zinc-Ion Battery Cathodes. *ChemNanoMat* **2020,** *6* (5), 797-805.

296. Chen, X.; Wang, L.; Li, H.; Cheng, F.; Chen, J., Porous V2O5 nanofibers as cathode materials for rechargeable aqueous zinc-ion batteries. *Journal of Energy Chemistry* **2019,** *38*, 20-25.

297. Tong, Y.; Li, X.; Su, S.; Li, J.; Fang, J.; Liang, B.; Hou, J.; Luo, M., Hydrated lithium ions intercalated V2O5 with dual-ion synergistic insertion mechanism for high-performance aqueous zinc-ion batteries. *Journal of Colloid and Interface Science* **2022,** *606*, 645-653.

298. Fan, L.; Li, Z.; Kang, W., Spontaneous Growth of Alkali Metal Ion-Preintercalated Vanadium Pentoxide for High-Performance Aqueous Zinc-Ion Batteries. *ACS Sustainable Chemistry & Engineering* **2021,** *9* (14), 5095-5104.

Appendix A - Supplementary Information for Chapter 2

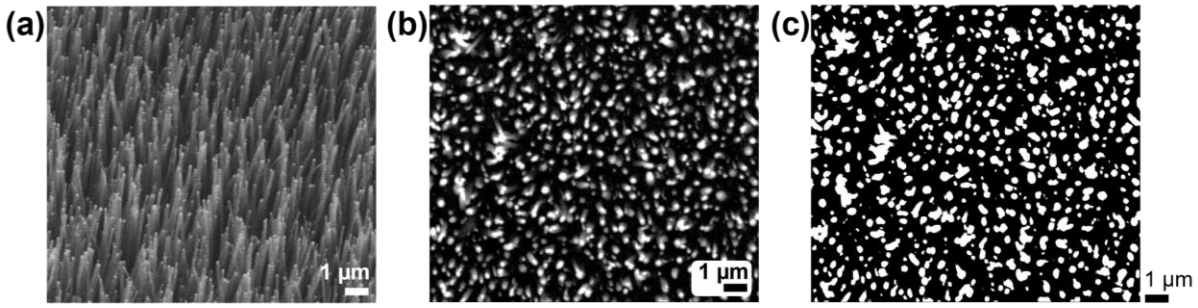

Figure A.1. FESEM images of pristine VACNF/Cu at (a) a 30° perspective and (b) a 0° top view. (c) Color threshold adjusted image of Fig. A1b processed using ImageJ software to calculate the porosity. The fraction of bright pixels which correspond to area covered by tips of VACNFs is 21.4 %. The remaining area of 78.6 % is the estimated porosity of the electrode.

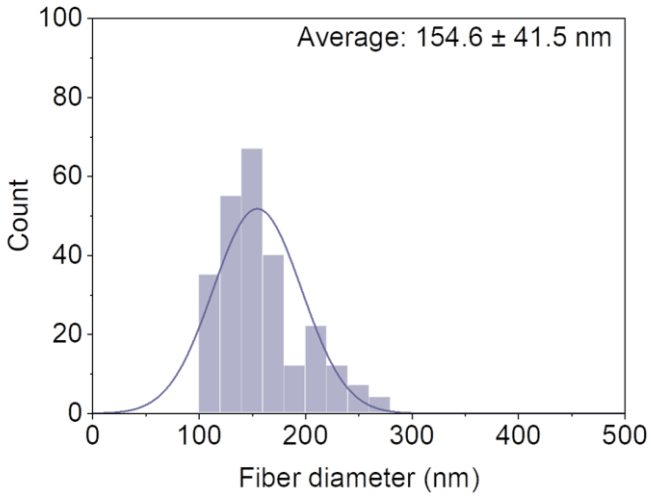

Figure A.2. Histogram of diameter of pristine VACNFs.

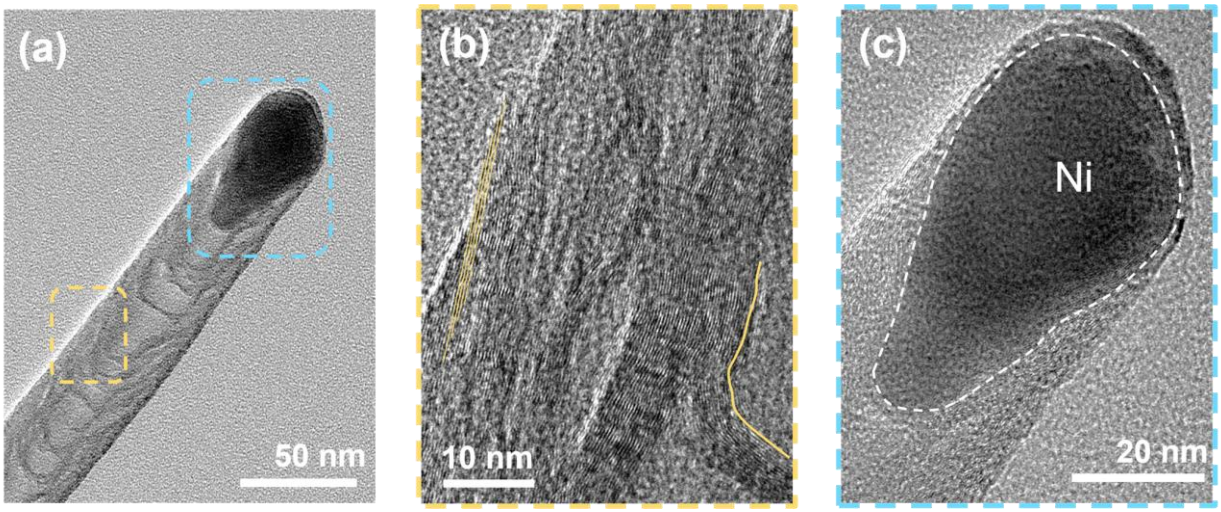

Figure A.3. TEM images of (a) pristine VACNF and its (b) and (c) high-magnification images of areas highlighted using orange and blue rectangles, respectively.

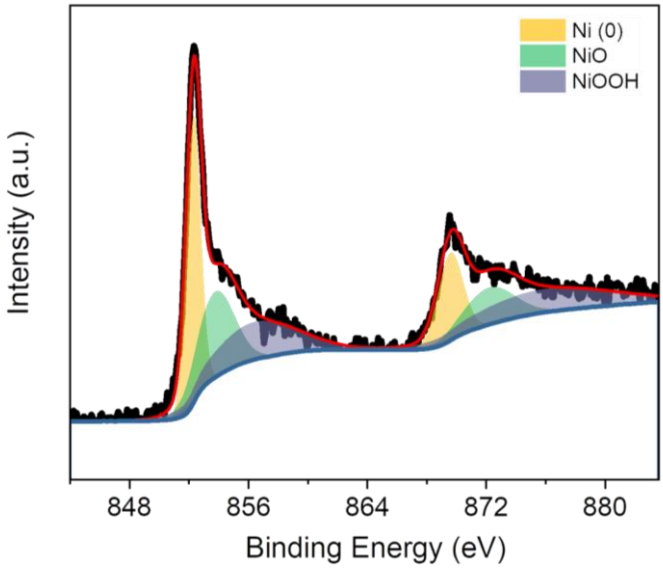

Figure A.4. High resolution Ni 2p XPS spectra of pristine VACNF.

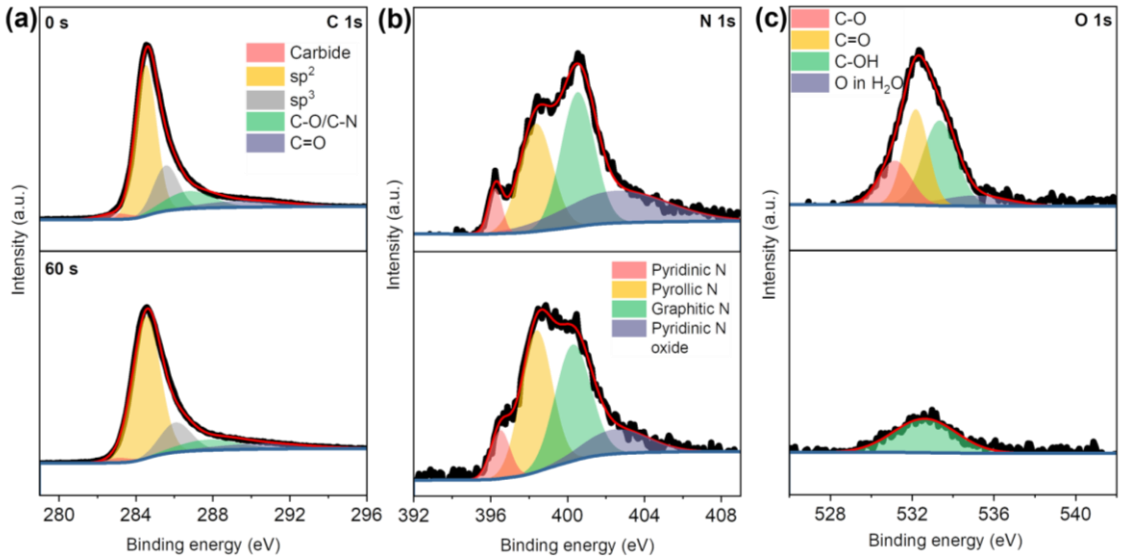

Figure A.5. XPS depth profiling of a pristine VACNF/Cu electrode before and after 60 s of Ar^+ ion etching. High-resolution spectra of (a) C 1s, (c) N 1s, (d) O 2p. Ar^+ ion etching rate is 0.08 nm/s calibrated using Ta_2O_3.

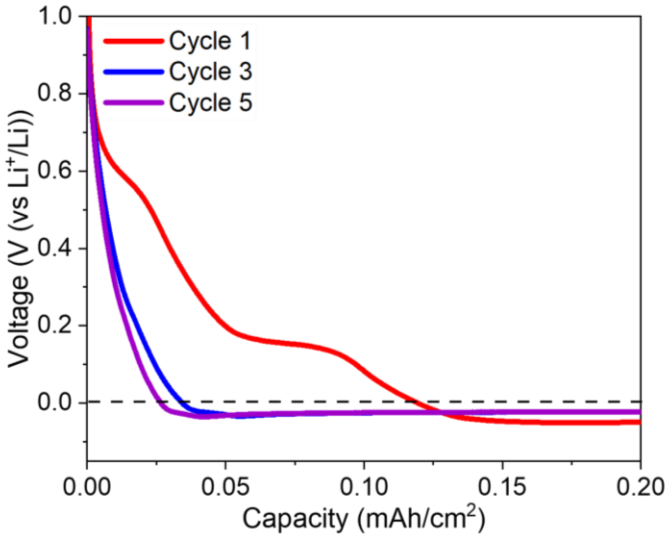

Figure A zoomed in view of galvanostatic charge voltage curves during the initial Li plating cycles at 1.0 mA/cm^2.

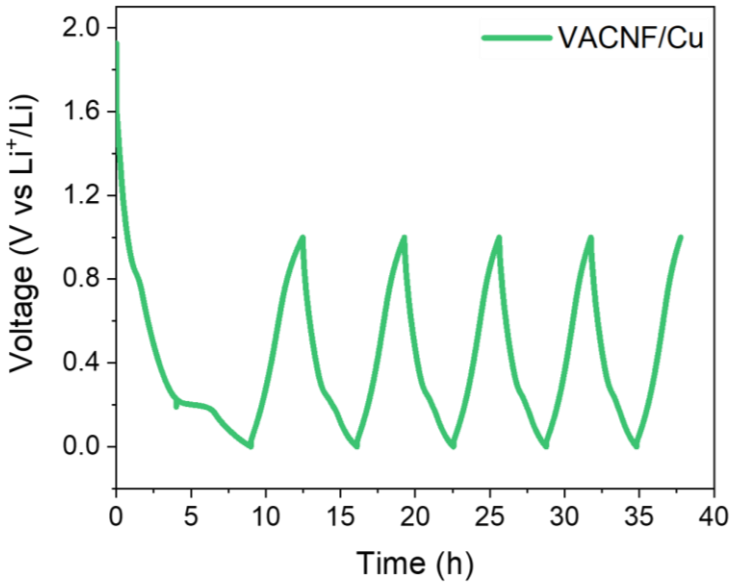

Figure A.7. Voltage curves of VACNF/Cu electrode cycled at 0.028 mA/cm^2 between 0 – 1 V (Li$^+$/Li).

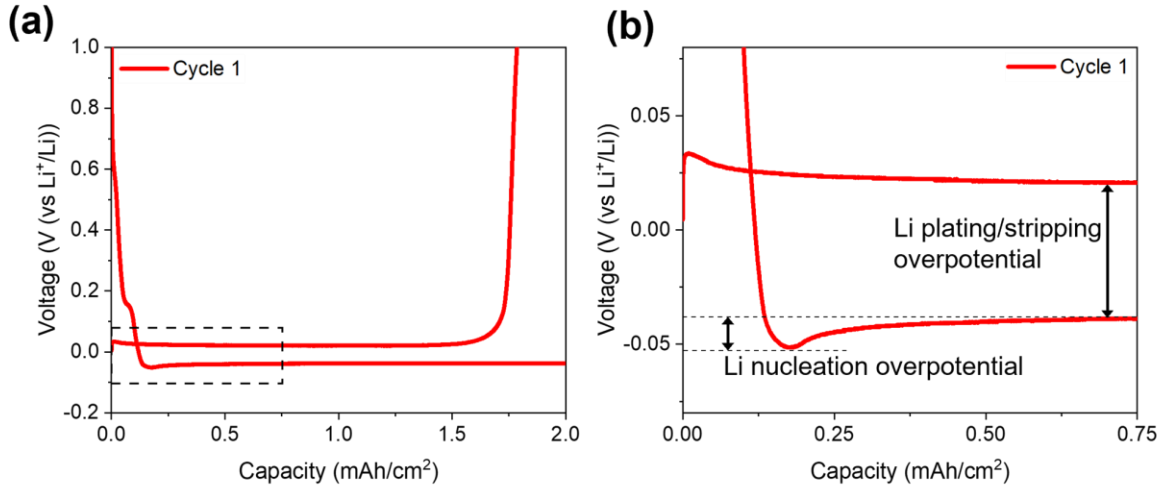

Figure A.8. (a) Li plating/stripping voltage curves of VACNF/Cu electrode in the first cycle at 1.0 mA/cm^2. (b) An enlarged view of the region highlighted in panel (a) to illustrate how the Li nucleation overpotential and Li plating/stripping overpotential were determined.

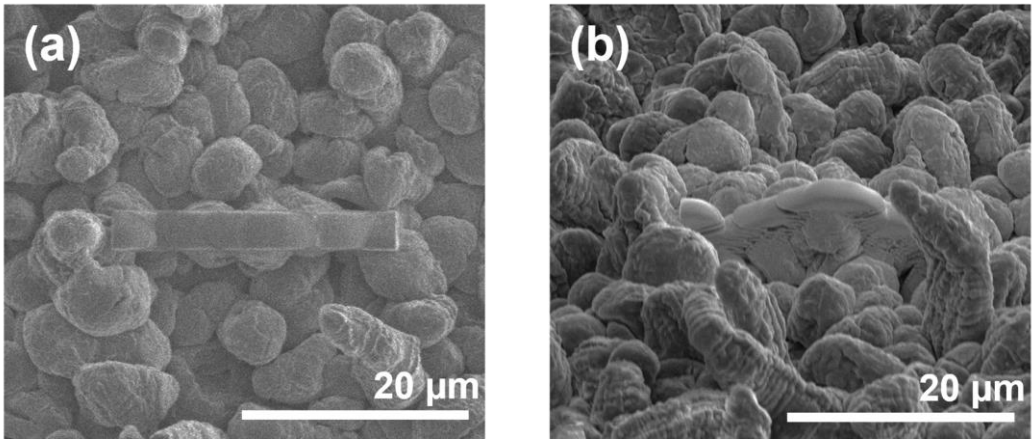

Figure A.9. (a) Ga^+ ion beam image of 2 µm Pt deposited VACNF/Cu electrode plated with 2.0 mAh/cm^2 capacity of Li plated at 1.0 mA/cm^2 before milling and (b) the corresponding electron beam image at an angle of 52°.

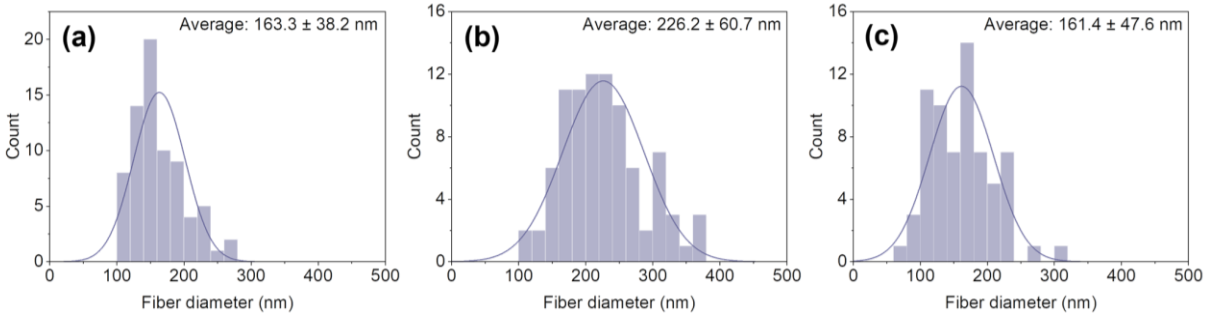

Figure A.10. Histograms of total thickness of VACNF (a) after plating with 0.75 mAh/cm^2 Li, (b) after plating with 2.0 mAh/cm^2 Li, and (c) after Li stripping. For all samples, the current density applied was 1.0 mA/cm^2.

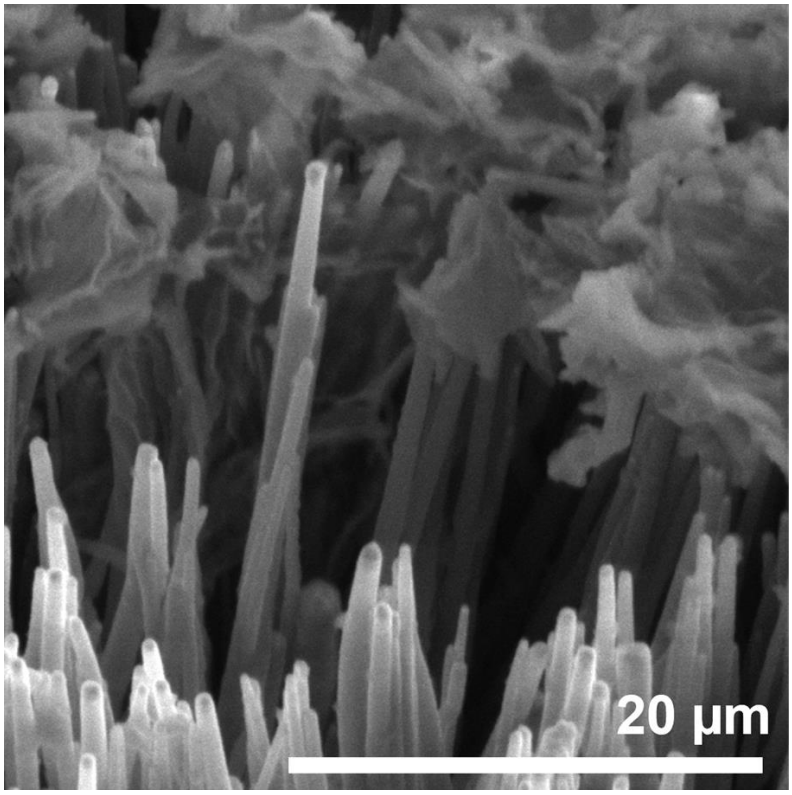

Figure A.11. FESEM perspective images of VACNF/Cu electrodes after completely stripping the plated 2.0 mAh/cm^2 Li at a rate of 1.0 mA/cm^2.

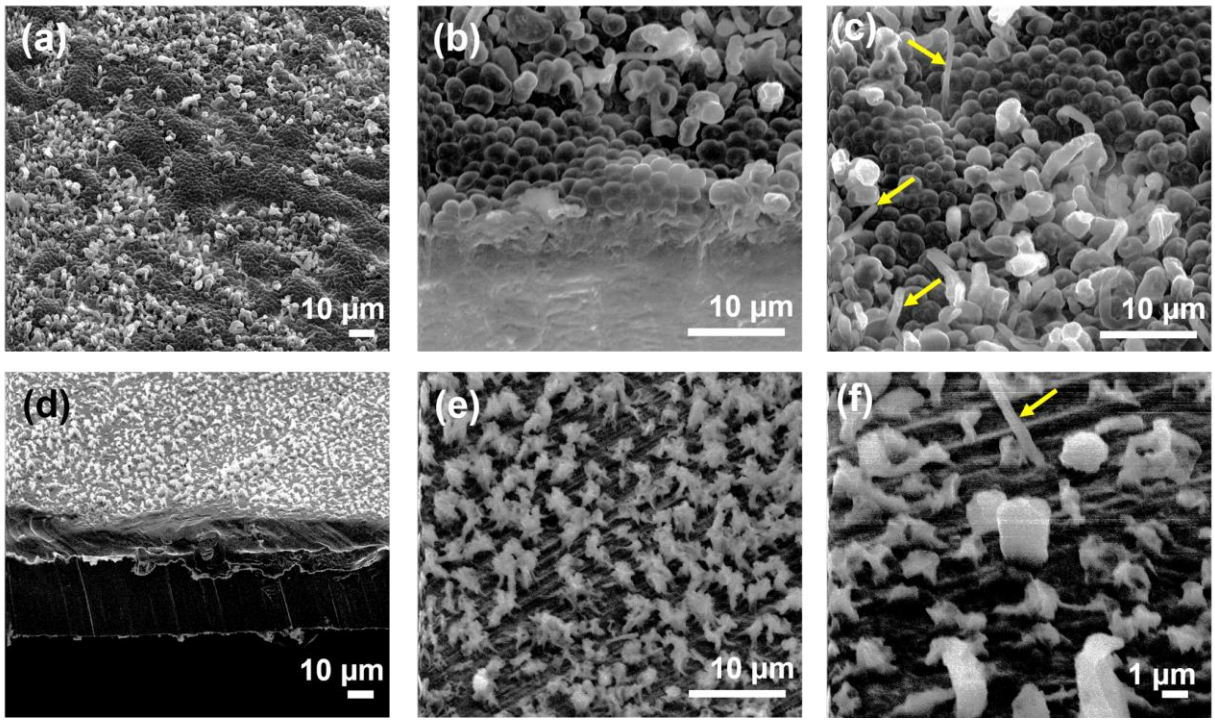

Figure A.12. FESEM images of a planar Cu electrode (a), (b), and (c) after plating with 0.75 mAh/cm^2 Li at 1.0 mA/cm^2; and (d), (e) and (f) after complete Li stripping. Dendritic structures are highlighted using yellow arrows in (c) and (f). Images in (b) and (d) were taken from the cut edge to reveal the cross-sectional information.

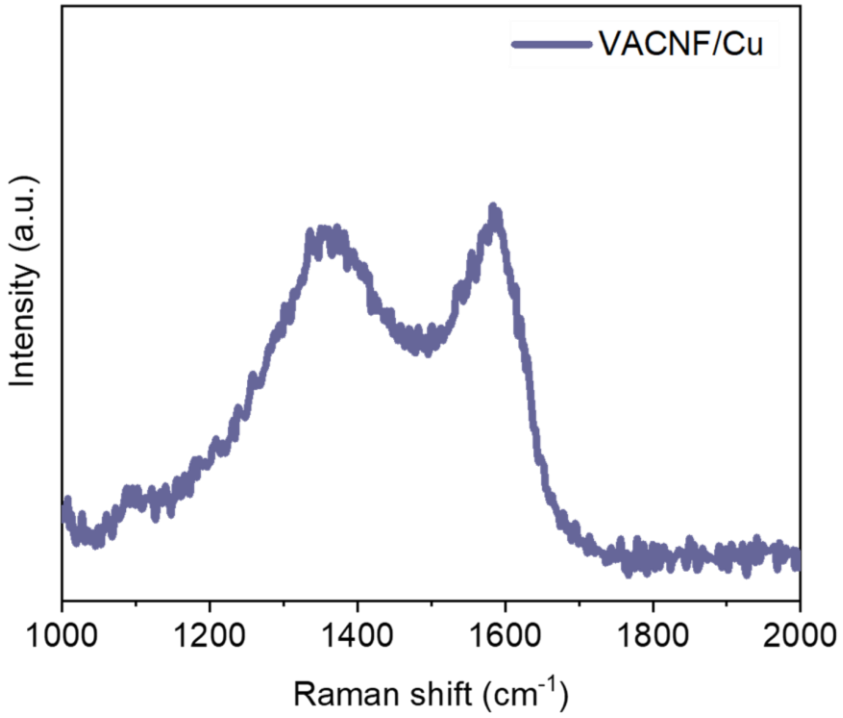

Figure A.13. Raman spectrum of pristine VACNF/Cu.

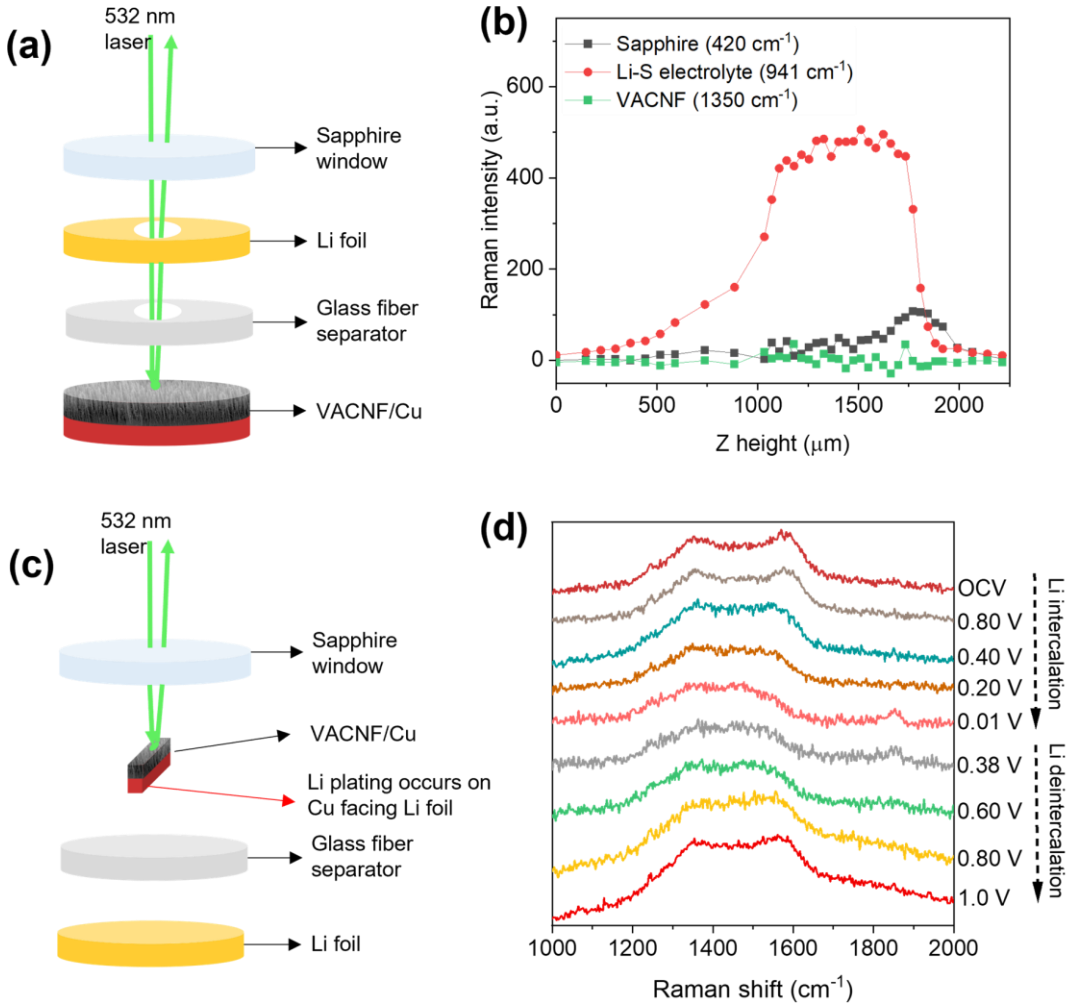

Figure A.14. (a) Coin cell like configuration and (b) the depth profiling of intensities of different bands associated with the sapphire window, electrolyte and VACNFs measured using the same configuration. The background signal from the electrolyte masked the signals from VACNF making it unsuitable for in-situ Raman experiments. (c) The inverted configuration and (d) the corresponding Raman spectra obtained during a lithium intercalation and deintercalation cycle. This configuration showed changes in VACNFs' Raman signals with Li intercalation/deintercalation but when Li plating was done, lithium got electrodeposited on surface of copper substrate facing the Li foil, which is undesirable.

Description of setup for in-situ Raman spectroscopy measurements:

The in-situ Raman spectroscopy experiments were performed using a commercially available optical cell from El-cell. We first attempted to do the measurements with the configuration like a coin cell as shown in Fig. S14a. However, the background scattering from the electrolyte masked the Raman scattering signals from VACNFs (Fig. S14b). With the employment of the second configuration (Fig. S14c) with a strip of inverted VACNF/Cu electrode directly under the sapphire window, Raman signals from VACNF could be collected as shown in Fig. S14d. From the in-situ Raman data, the occurrence of lithium intercalation and deintercalation on VACNFs could be deduced from the changes in its D and G bands. However, with this configuration, the electric field predominantly exists between the copper surface at the backside of the VACNF/Cu electrode causing substantial lithium plating and stripping on the copper surface rather than on VACNF. Hence, a side-by-side configuration (Fig. 3a) was found to be the optimal set up with minimal background signal from electrolyte while proper electrochemical control can be applied. It is to be noted that a potential gradient exists across the electrode surface in this configuration. To minimize this effect, a low current of 10 μA was used to allow sufficient time for the Li^+ ion diffusion. Normal charge-discharge curves could be obtained, and the measurements were made at designated potentials in Fig. 3b without disrupting the processes.

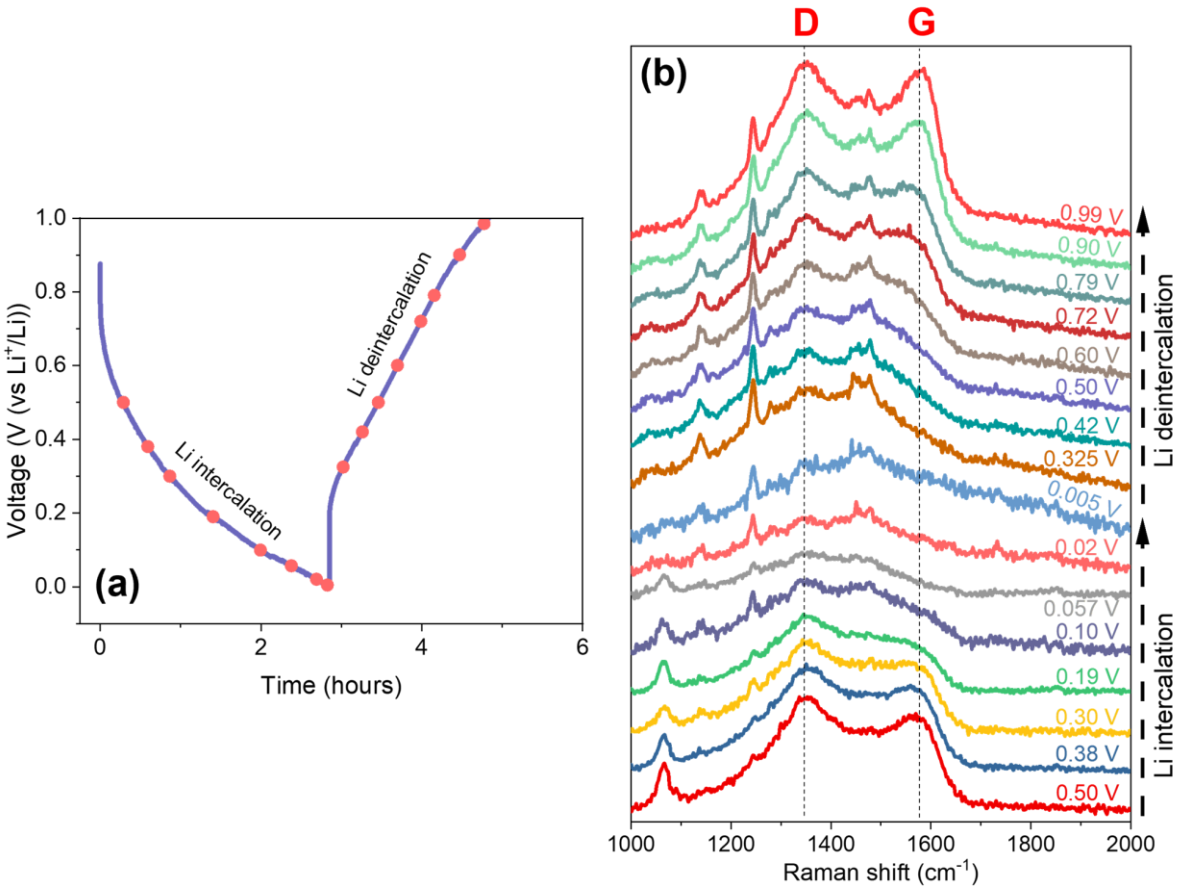

Figure A.15. (a) Voltage curves of Li intercalation/deintercalation at 10 µA for VACNF/Cu electrode during in-situ Raman measurements. The voltages at which Raman spectra were collected are highlighted. (b) Corresponding In-situ Raman spectra of VACNF/Cu electrode during Li intercalation/deintercalation at 10 µA.

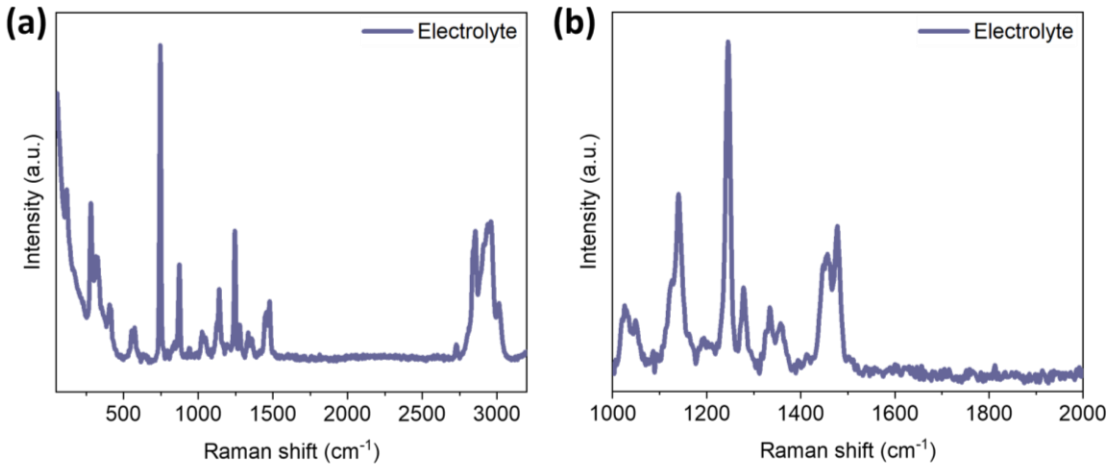

Figure A.16. (a) Raman spectrum of the electrolyte – 1.0 M LiTFSI in DOL/DME (1:1 v/v) with 1 wt% $LiNO_3$ and (b) its enlarged view with the Raman shift ranging between 1000 cm^{-1} and 2000 cm^{-1}.

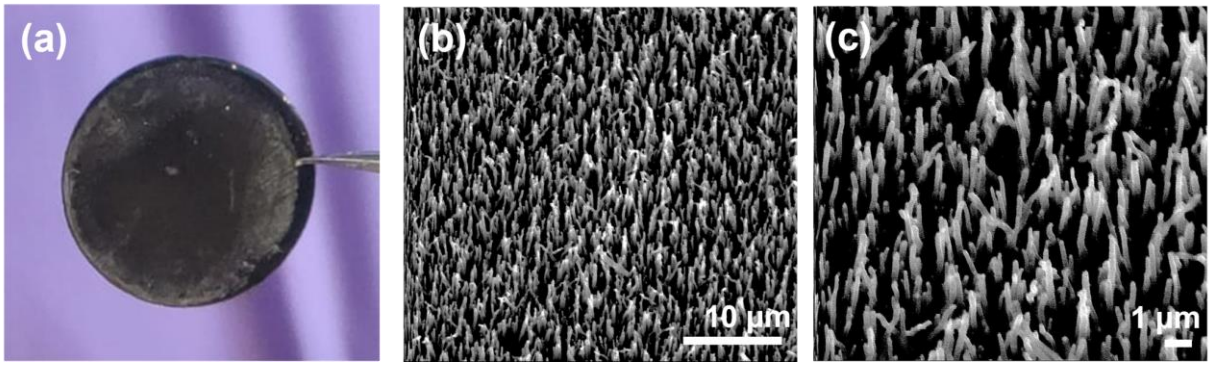

Figure A.17. (a) Optical image and their corresponding (b) and (c) FESEM images of Li intercalated VACNF/Cu.

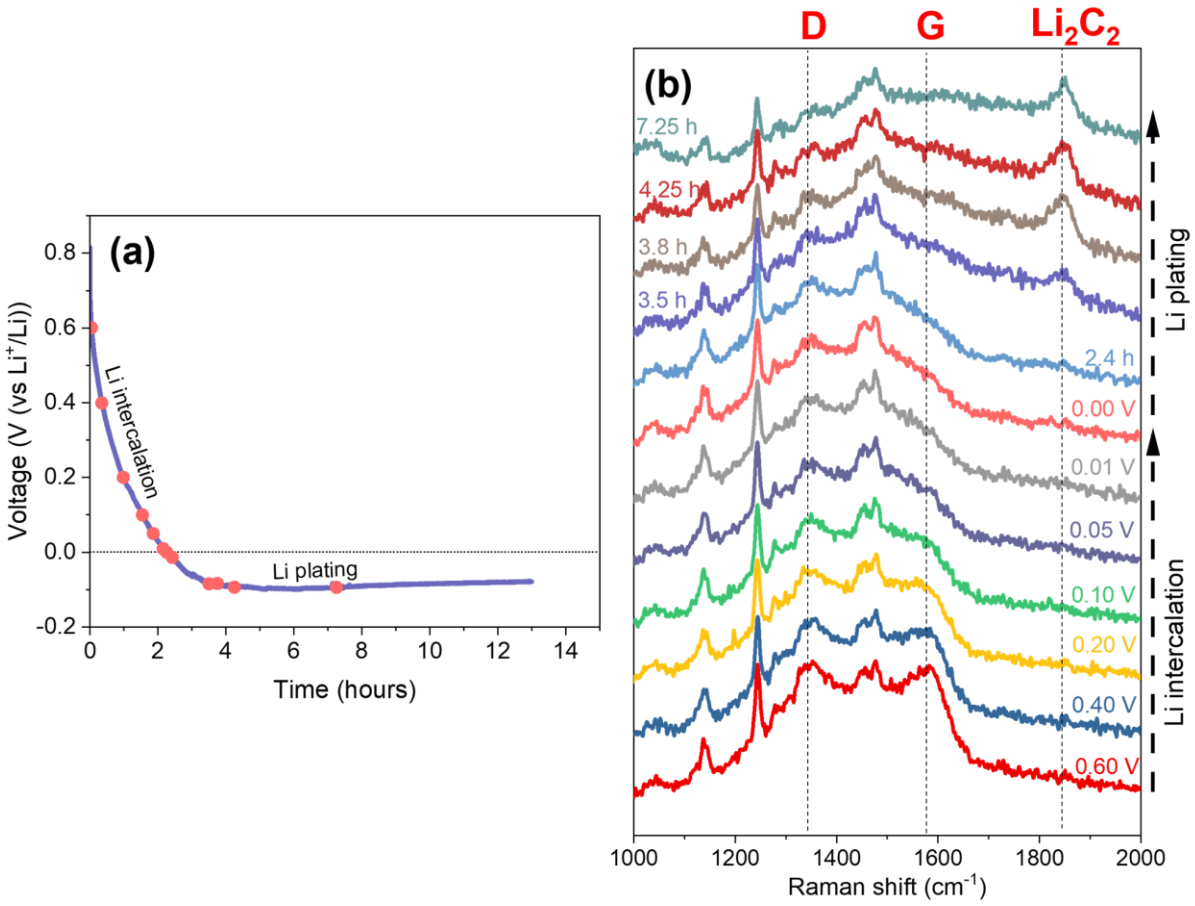

Figure A.18. (a) Voltage curves of Li plating at 10 µA for VACNF/Cu electrode during in-situ Raman measurements. The voltages or Li plating time at which Raman spectra were collected are highlighted. (b) Corresponding In-situ Raman spectra of VACNF/Cu electrode during Li plating.

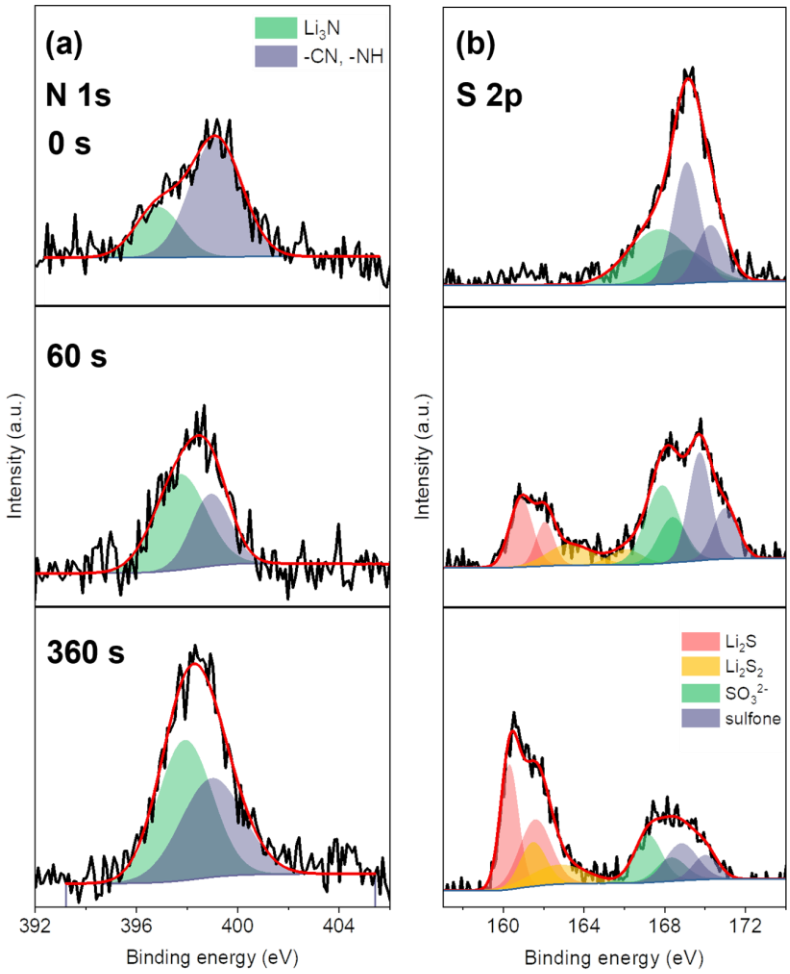

Figure A.19. XPS depth profiling of lithium intercalated VACNF/Cu electrode. High-resolution spectra of (a) N 1s, (b) S 2p. Ar^+ ion etching rate is 0.08 nm/s calibrated using Ta_2O_3.

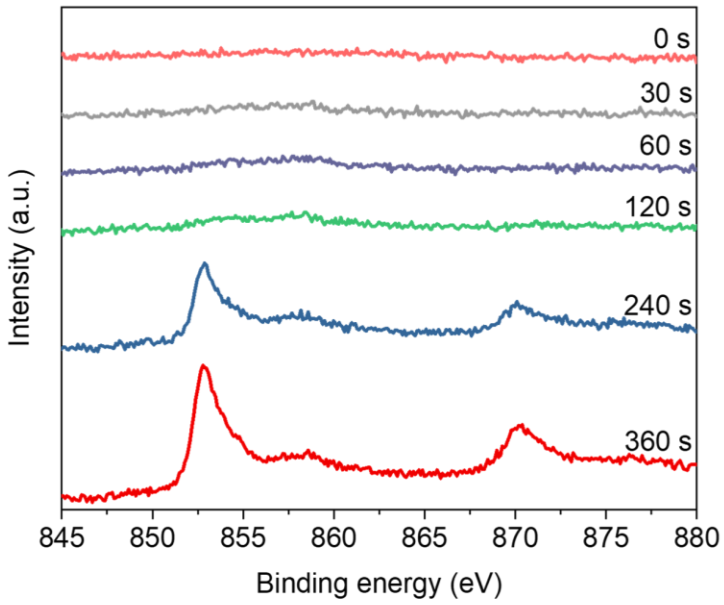

Figure A.20. XPS depth profiling of lithium intercalated VACNF/Cu electrode. High-resolution spectra of Ni 2p. Ar^+ ion etching rate is 0.08 nm/s calibrated using Ta_2O_3.

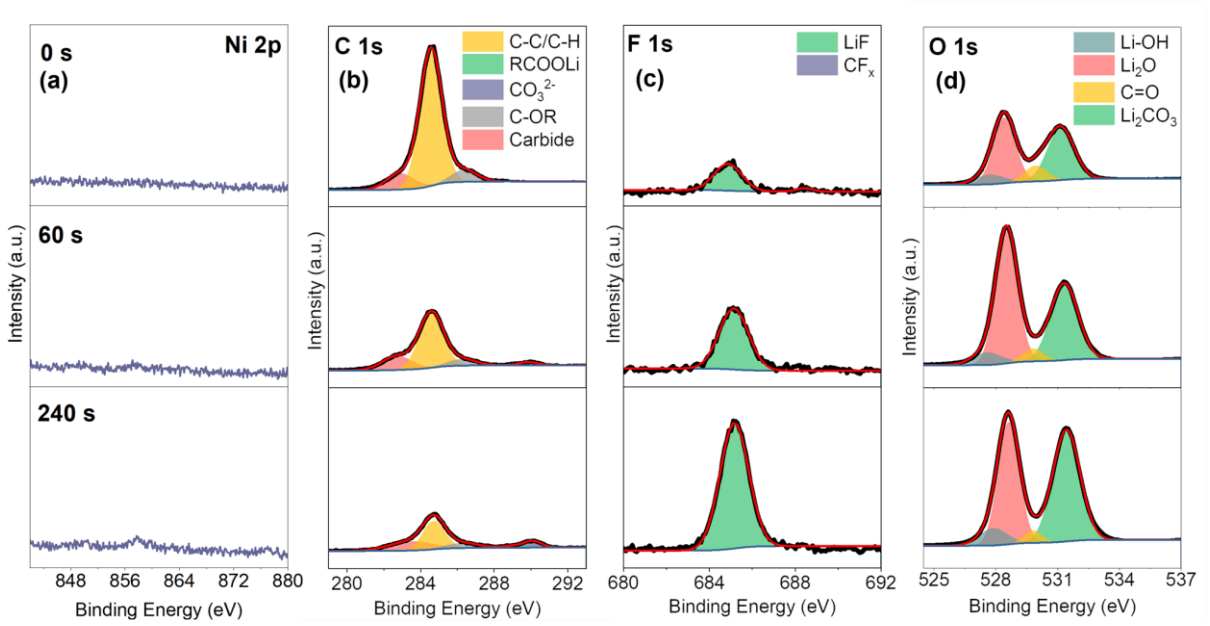

Figure A.21. XPS depth profiling of VACNF/Cu electrode plated with 2.0 mAh/cm^2 Li at 1.0 mA/cm^2. High resolution spectra of (a) Ni 2p, (b) C 1s, (c) F 1s, (d) O 2p. Ar^+ ion etching rate is 0.08 nm/s calibrated using Ta_2O_3.

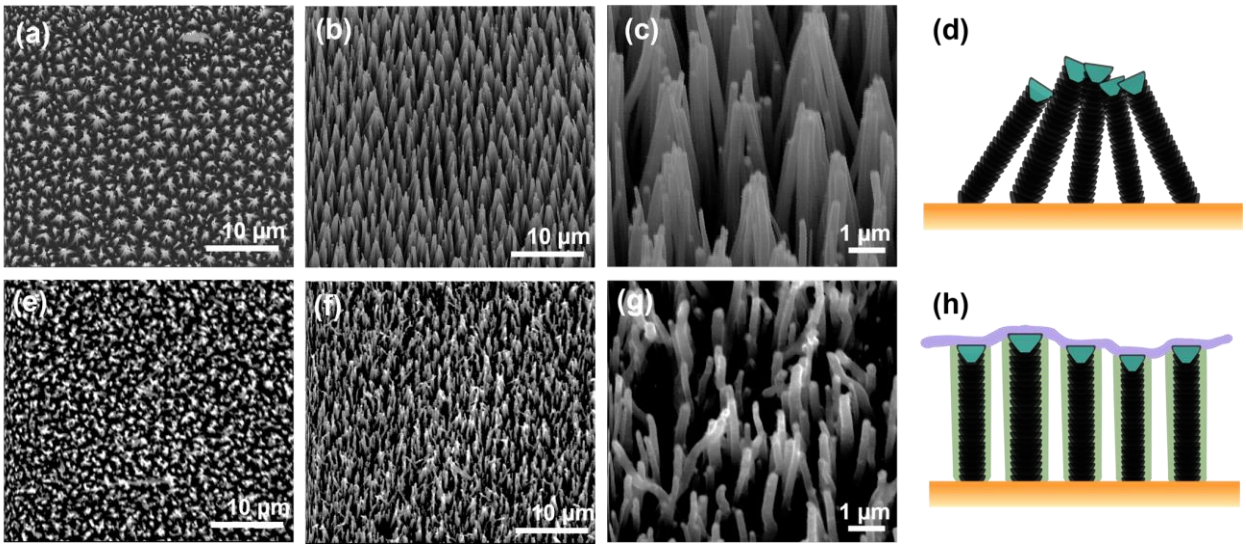

Figure A.22. (a) Top-view and (b), (c) 30° perspective view of FESEM images of pristine VACNF/Cu after being washed with DME and then dried. (d) A schematic to show the collapse of VACNFs due to the elastocapillary effects induced by drying of solvents. (d) Top-view and (e), (f) 30° perspective view of FESEM images of VACNF/Cu after Li intercalation. (h) A schematic to illustrate the preserved vertical alignment of VACNFs owing to the presence of SEIs.

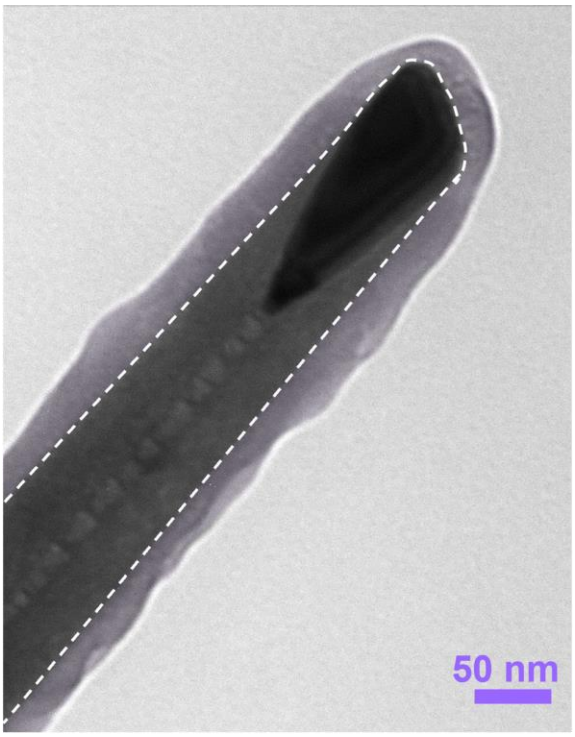

Figure A.23. Cryo-TEM image of a VACNF after plating 0.75 mAh/cm^2 of Li at 1.0 mA/cm^2.

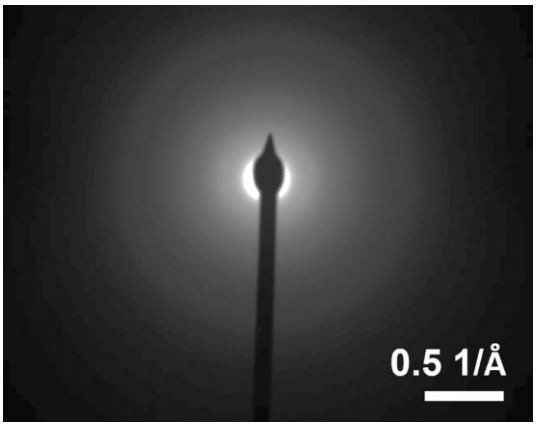

Figure A.24. SAED image of electrodeposited Li on individual VACNF fibers corresponding to Figure 2.3c.

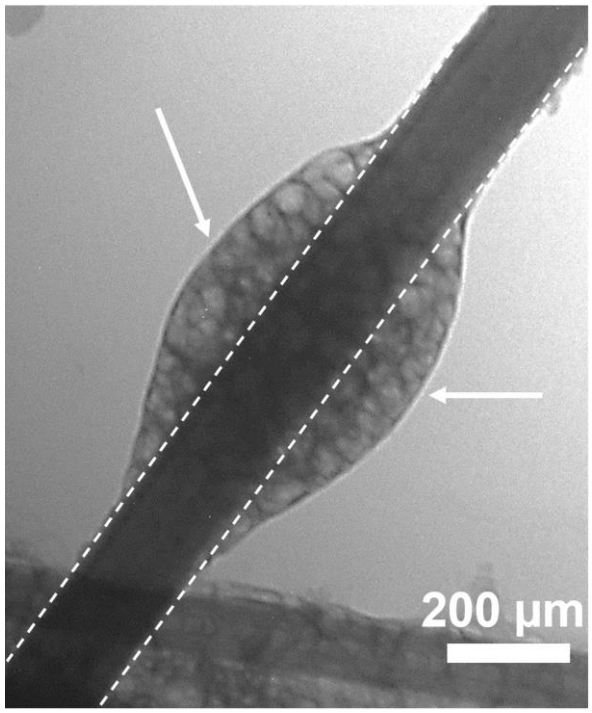

Figure A.25. Cryo-TEM image of a VACNF after complete stripping at 1.0 mA/cm^2. The electron beam damage of co-axial SEI on the VACNF can be observed.

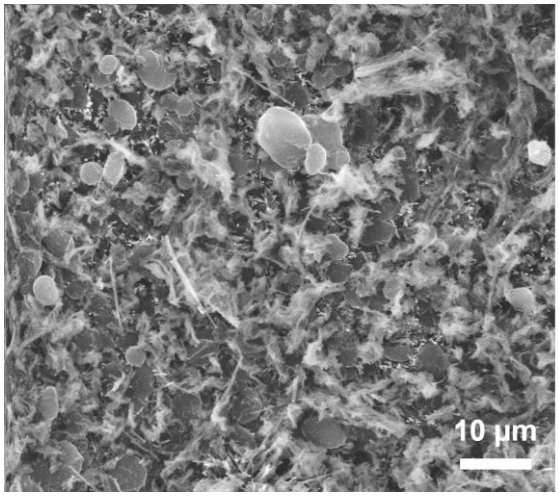

Figure A.26. Top view FESEM image of VACNF/Cu@Li electrode plated with 0.75 mAh/cm^2 of Li at 1 mA/cm^2 after 7 cycles.

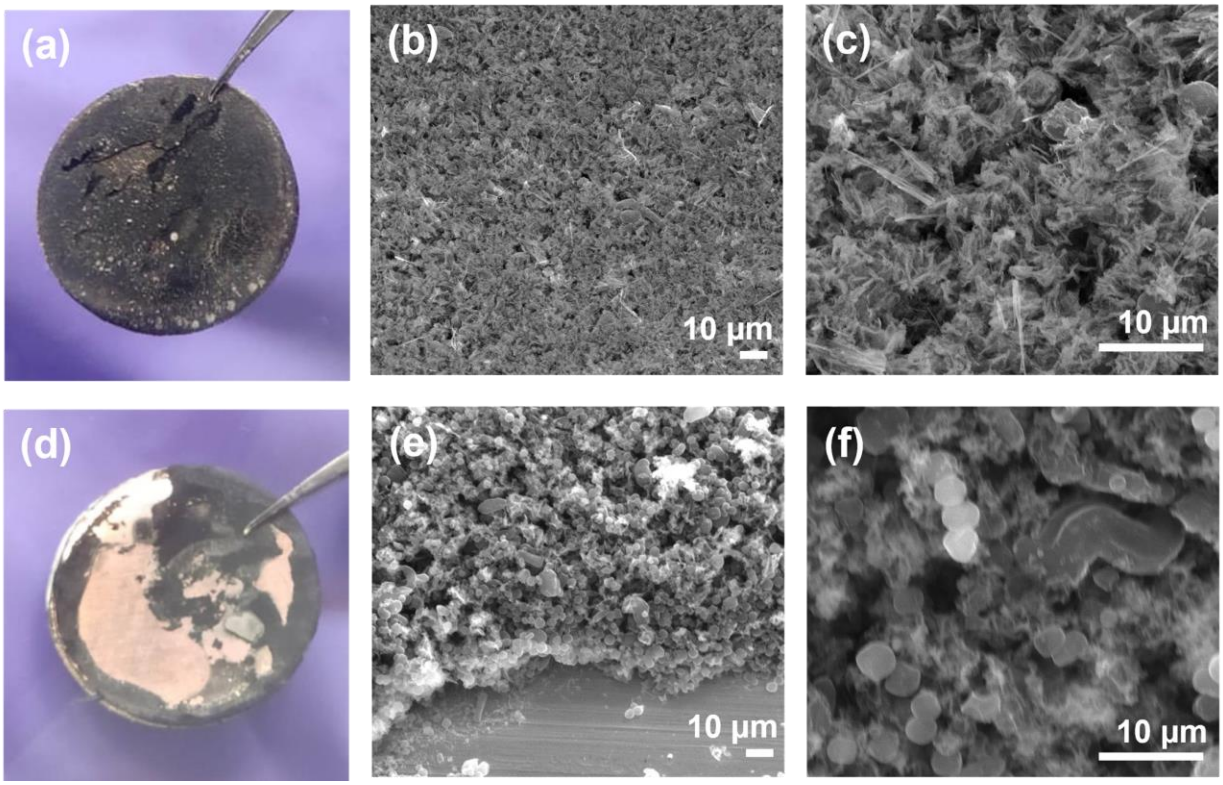

Figure A.27. (a) Optical image and (b), (c) the corresponding 30° perspective view FESEM images of a VACNF/Cu electrode in the stripped condition after 50 Li plating/stripping cycles. (d) Optical image and its (e), (f) the corresponding 30° perspective view FESEM images of a planar Cu electrode in the stripped condition after 50 Li plating/stripping cycles.

Table A-1: A summary of 3D hosts for lithium metal anodes.

Sl. No.	Material	Thickness	Porosity	Pore size	Tortuosity	Electrolyte	Coulombic efficiency	Ref.
1	VACNF/Cu	15 µm	80 %	100 – 300 nm	Low	1.0 M LiTFSI in 1:1 (v/v) DOL:DME with 1 wt% $LiNO_3$	98% for 130 cycles at 1 mA/cm^2, 1 mAh/cm^2	224
2	3D Cu foil with submicron skeleton	24 µm	62.5 %	1.0 µm	Low	1.0 M LiTFSI in 1:1 (v/v) DOL:DME with 1 wt% $LiNO_3$, 0.005 M Li_2S_6	98.5% for 50 cycles at 0.5 mA/cm^2, 1 mAh/cm^2	152
3	Vertical graphene on 3D Cu mesh	50 µm (Cu), 500 nm (Graphene)	NA	75 µm (Cu), 100 to 500 nm (Graphene)	Low (Cu), High (Graphene)	1.0 M $LiPF_6$ in EC/DEC	98% for 250 cycles at 2 mA/cm^2 for 1 mAh/cm^2	273
4	Vertically aligned graphene aerogel	125 µm	99.8 %	~ 10 µm	Low	1.0 M LiTFSI in 1:1 (v/v) DOL:DME with 1 wt% $LiNO_3$	99.1% for 300 cycles at 1 mA/cm^2, 1 mAh/cm^2	176
5	Nanocopper reinforced electrospun CNF	60.7 µm	NA	Upto several µm	High	1.0 M LiTFSI in 1:1 (v/v) DOL:DME with 0.2 M $LiNO_3$	94.3% at 300^{th} cycle at 1 mA/cm^2, 1 mAh/cm^2	162
6	Crumpled graphene balls coated on Cu	8 µm, 40 µm, 120 µm	75.30%	0.1 - 0.5 µm	High	1.0 M LiTFSI in 1:1 (v/v) DOL:DME with 1 wt% $LiNO_3$	97.5% for 750 cycles 0.5 mA/cm^2, 0.5 mAh/cm^2	274
7	CuO deposited carbon cloth	250 µm	NA	10 - 100 µm	High	1.0 M LiTFSI in 1:1 (v/v) DOL:DME with 2 wt% $LiNO_3$	NA	164
8	PVDF coated CVD grown graphene foam	1000 µm	NA	> 100 µm	High	1 M $LiPF_6$ in 1:1 (v/v) EC and DEC	99% for 100 cycles at 0.5 mA/cm^2, 1.0 mAh/cm^2	275
9	Ag nanoparticle decorated Cu foam	100 µm	NA	> 100 µm	High	1.0 M LiTFSI in 1:1 (v/v) DOL:DME with 2 wt% $LiNO_3$	99% for 300 cycles at 1 mA/cm^2, 1 mAh/cm^2	276
10	3D printed N doped carbon framework	NA	NA	200 µm	Low	1.0 M LiTFSI in 1:1 (v/v) DOL:DME with 1 wt% $LiNO_3$	97.9% for 100 cycles at 1 mA/cm^2, 10 mAh/cm^2	277

11	CuO nanoneedles on Ni foam	380 µm	NA	> 100 µm	High	1.0 M LiTFSI in 1:1 (v/v) DOL:DME with 1 wt% $LiNO_3$	96% for 150 cycles 1 mA/cm^2, 1 mAh/cm^2	278
12	N doped CNTs on Ni foam	400 µm	NA	> 100 µm	High	1.0 M LiTFSI in 1:1 (v/v) DOL:DME with 1 wt% $LiNO_3$	98.2% for 200 cycles, 1 mA/cm^2, 1 mAh/cm^2	173
13	N-doped carbon rod array on Cu foil	15 µm	NA	1-3 µm	Low	1.0 M LiTFSI in 1:1 (v/v) DOL:DME with 2 wt% $LiNO_3$	98% for 120 cycles, 1 mA/cm^2, 1 mAh/cm^2	279
14	Ag nanoparticle embedded N doped carbon macroporous fibers	53 µm	NA	Upto 5 µm	High	1.0 M LiTFSI in 1:1 (v/v) DOL:DME with 2 wt% $LiNO_3$	98% for 800 cycles, 1 mA/cm^2, 1 mAh/cm^2	163
15	Copper mesh	NA	NA	50 µm	Low	1.0 M $LiPF_6$ in 1:4 (v/v) FEC/DMC	93.8% at 139 cycles, 1 mA/cm^2, 1 mAh/cm^2	280
16	Carbon paper	NA	NA	10 - 100 µm	High	1.0 M $LiPF_6$ in 1:4 (v/v) FEC/DMC	98% at 124 cycles, 1 mA/cm^2, 1 mAh/cm^2	280
17	N-doped amorphous Zn–carbon multichannel fibers decorated with carbon cages	NA	NA	Upto 10 µm	High	1.0 M LiTFSI in 1:1 (v/v) DOL:DME with 2 wt% $LiNO_3$	98% for 800 cycles, 1 mA/cm^2, 1 mAh/cm^2	281
18	N, O co-doped carbon nanosheet arrays on Cu	300 – 400 nm	NA	100 - 200 nm	Not applicable	1.0 M LiTFSI in 1:1 (v/v) DOL:DME with 1 wt% $LiNO_3$	98% for 310 cycles, 0.5 mA/cm^2, 1 mAh/cm^2	282
19	3D pore size gradient carbon host	60 µm	60 - 65 %	15 - 50 µm	High	1 M $LiPF_6$ in 1:1 (v/v) EC:PEC with 10 wt% FEC	98.8% for 250 cycles	283

Appendix B - Supplementary Information for Chapter 3

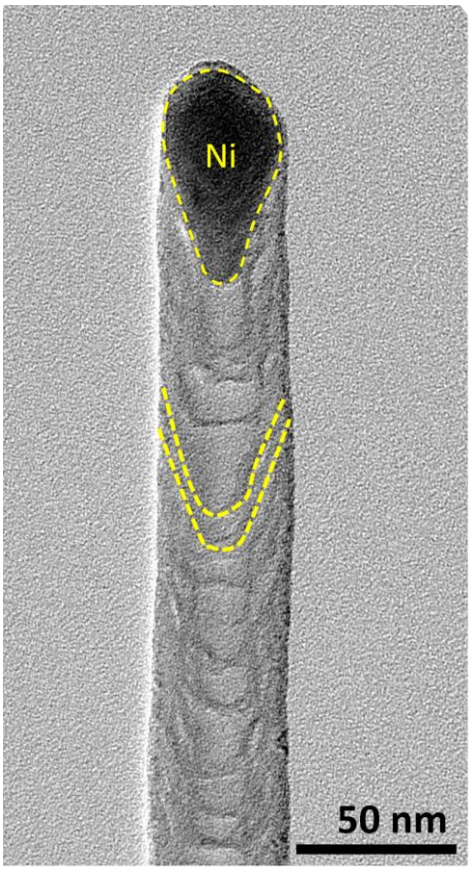

Figure B.1. TEM image of pristine VACNF.

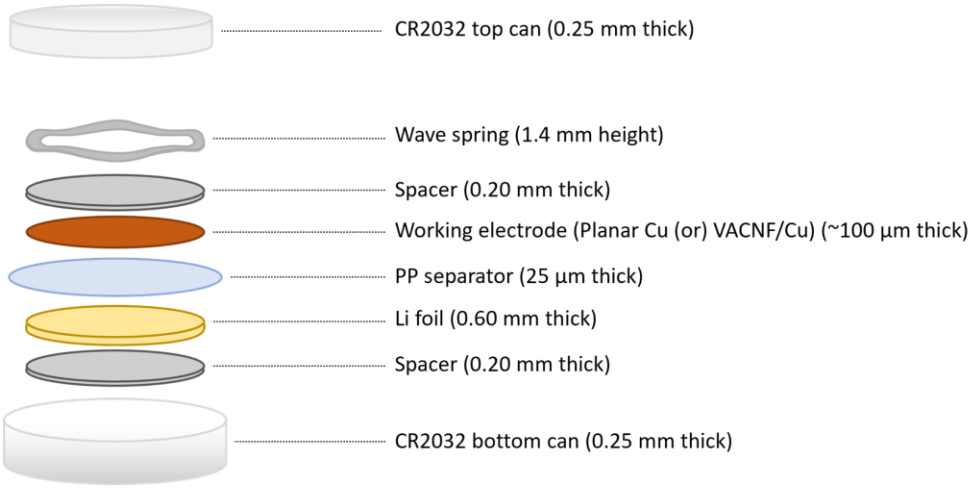

Figure B.2. Schematic of the typical coin-cell assembly configuration used for the experiments.

Compression % calculation:

Since, the wave spring is the only compressible element, the compression percentage is calculated as the ratio of the change in height of wave spring from the uncompressed state to the compressed state, relative to its height in the uncompressed state.

$$Compression\ \% = \frac{h_{uncompressed} - h_{compressed}}{h_{uncompressed}}$$

Where,

$h_{uncompressed}$ = height of the wave spring under uncompressed condition,

$h_{compressed}$ = height of the wave spring under compressed condition.

For the configuration as in Fig. S2, the compression is only a few percent. To achieve 16% compression, an additional spacer of 0.20 mm thickness was used. While for 38% compression, the same quantity of elements as in Fig. S2 were used, but within a CR2025 cell casing.

Table B-1: Compression % for different coin-cell configurations.

Sl. No.	Total thickness of all components without compression (mm)	$h_{uncompressed}$ (mm)	Sealed coin cell height (mm)	$h_{compressed}$ (mm)	Compression %
1	3.025	1.4	3.0	1.375	1.8% (Typical)
2	3.225	1.4	3.0	1.175	16%
3	3.025	1.4	2.5	0.875	38%

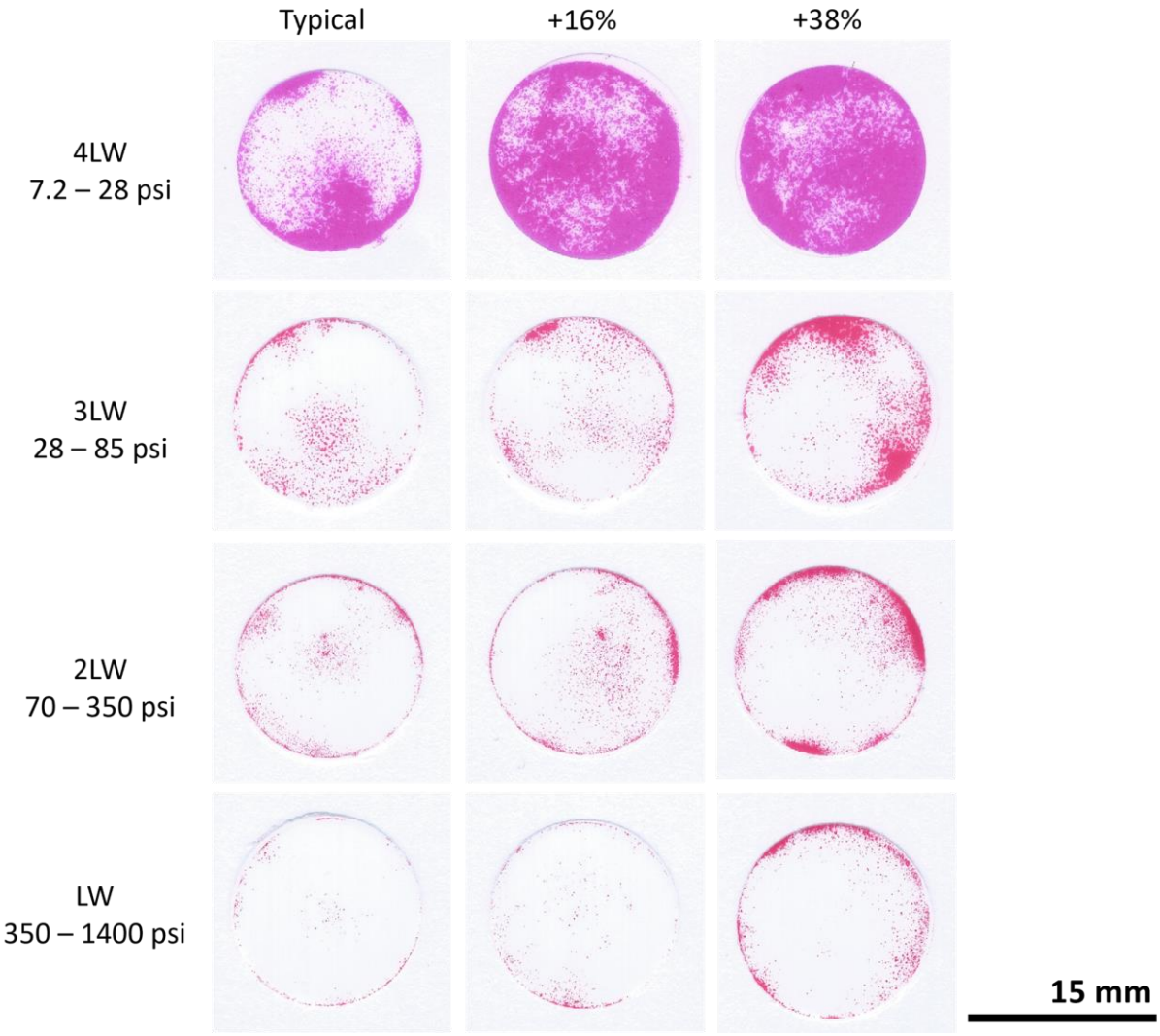

Figure B.3. Developed Prescale films of different working pressure ranges illustrating the pressure distribution inside coin cells under different levels of compression.

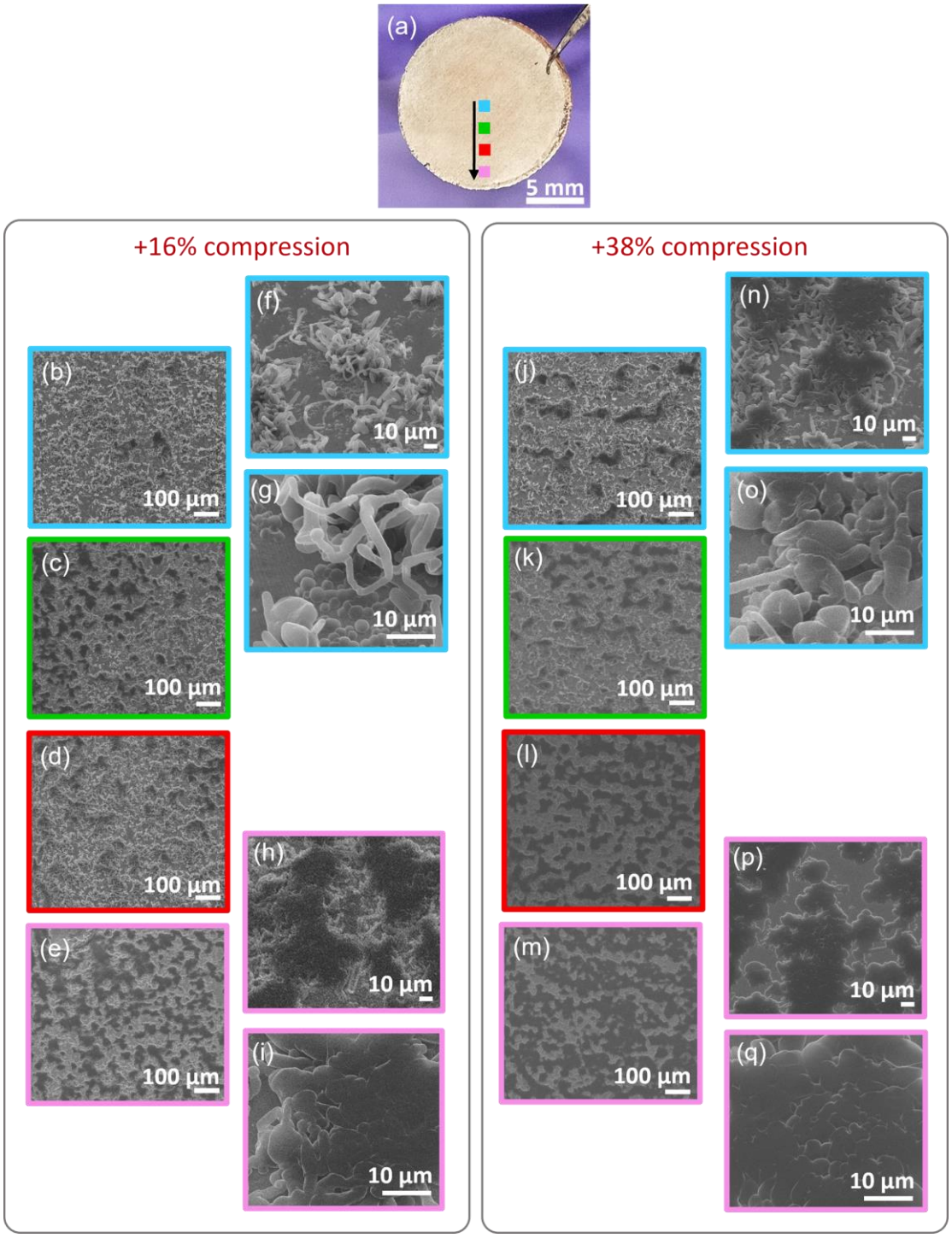

Figure B.4. (a) A representative optical image of Cu plated with 0.75 mAh/cm^2 Li at 0.10 mA/cm^2 and its corresponding (b) – (q) FESEM images imaged at highlighted locations. Lithium was plated with compression percentages of (b) – (i) 16% and (j) – (q) 38%. Figs. S4j – S4m are top view images while others were imaged from a 30º perspective.

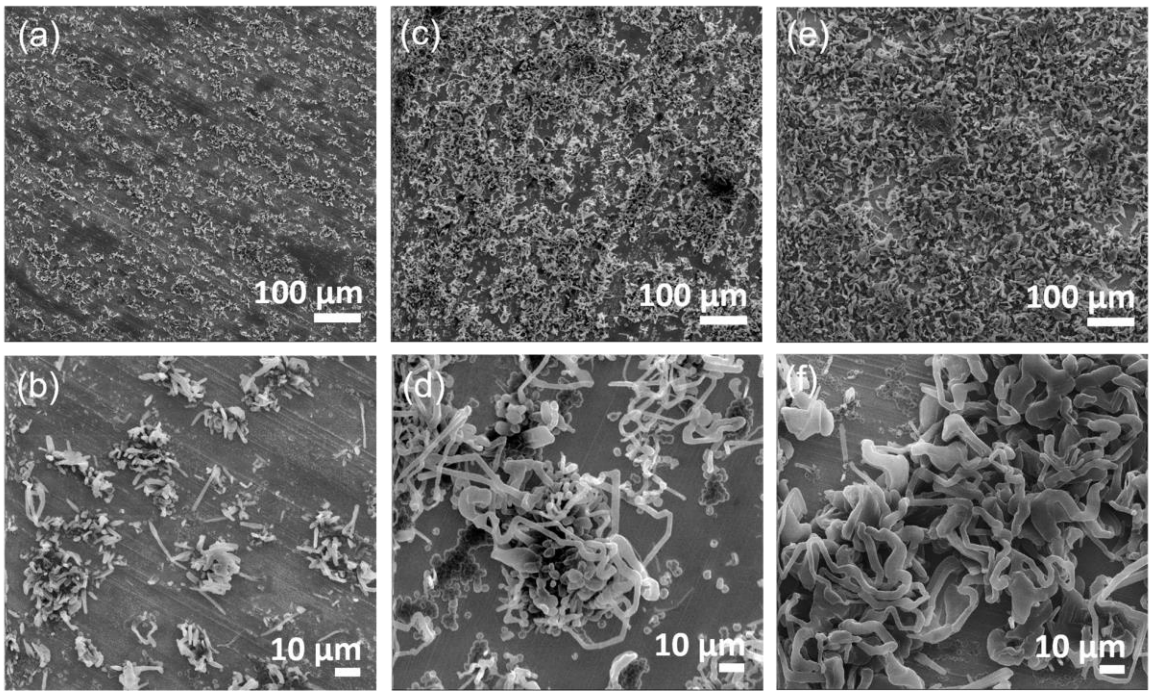

Figure B.5. Top-view FESEM images of planar Cu after electrodepositing Li of (a) & (b) 0.20 mAh/cm^2, (c) & (d) 0.75 mAh/cm^2, and (e) & (f) 2.0 mAh/cm^2 capacities at a low current density of 0.10 mA/cm^2.

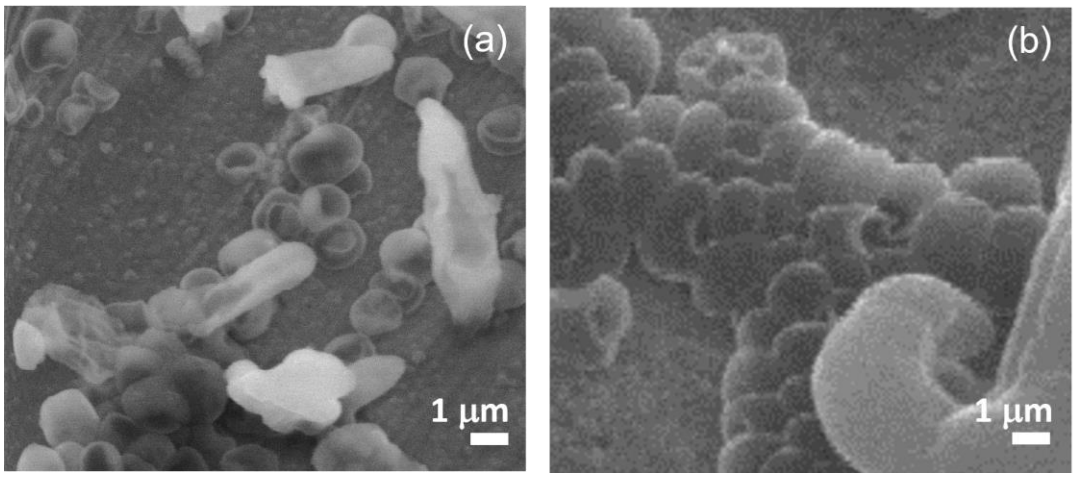

Figure .6. FESEM images of electrodeposited Li on planar Cu at 0.1 mA/cm^2 for a capacity of (a) 0.20 mAh/cm^2 and (b) 2.0 mAh/cm^2.

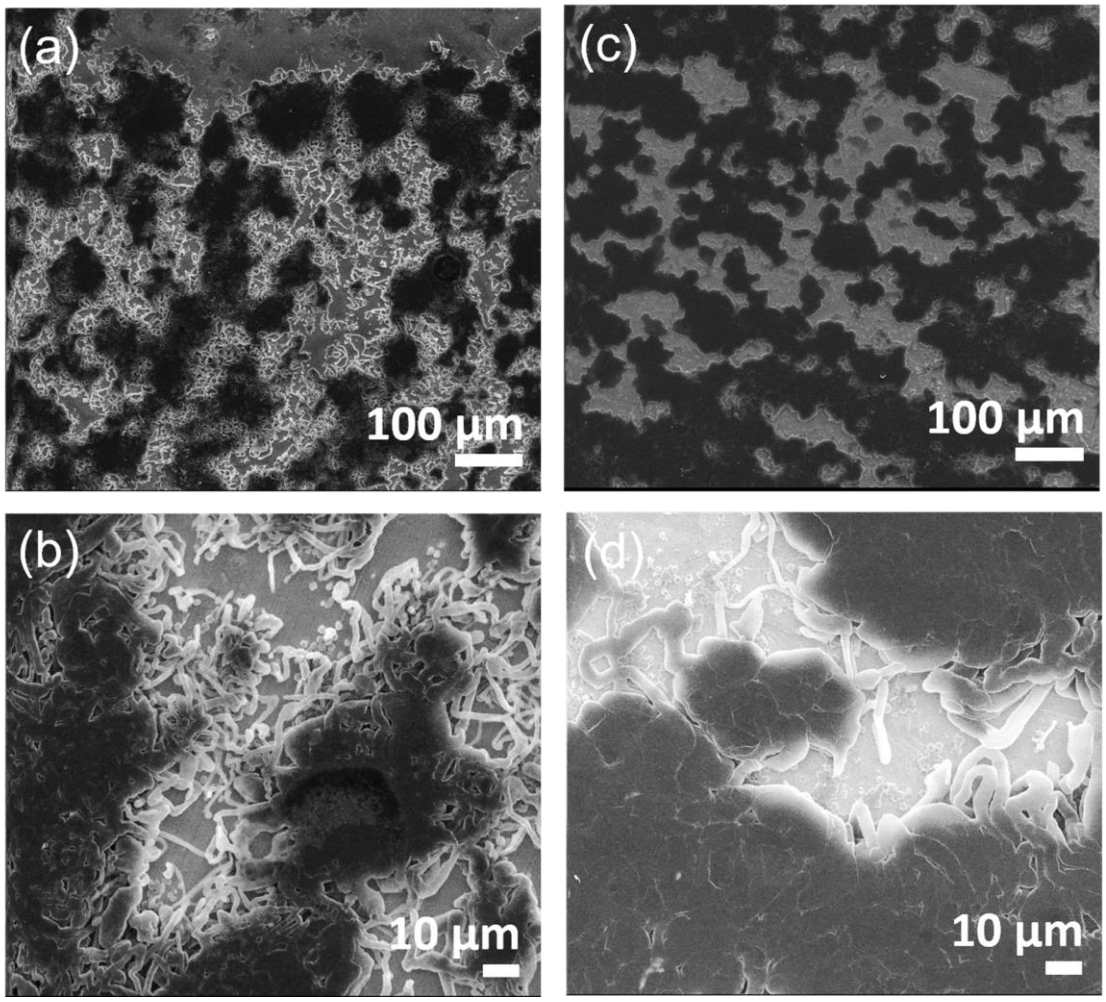

Figure B.7. Top-view FESEM images of Cu plated with (a) & (b) 0.75 mAh/cm^2 and (c) & (d) 2.0 mAh/cm^2 capacity of Li at 0.10 mA/cm^2 imaged at periphery of the electrode.

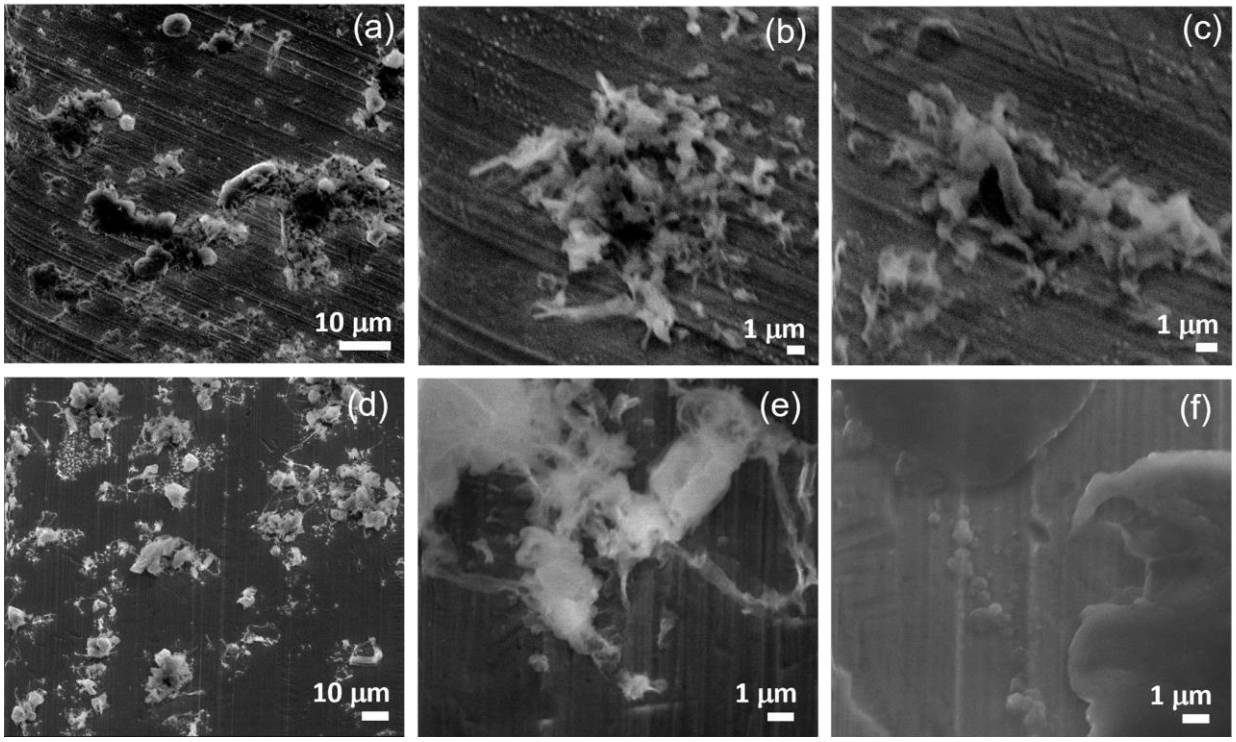

Figure B.8. 30º perspective FESEM images of 0.75 mAh/cm^2 of Li plated on the planar Cu electrode at 0.10 mA/cm^2 and then stripped completely at (a) – (c) 0.10 mA/cm^2 and (d) – (e) 1.0 mA/cm^2 respectively.

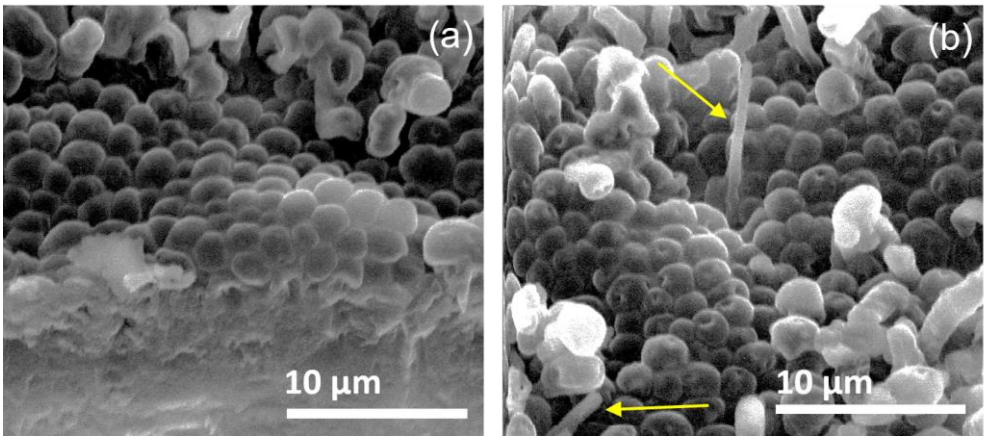

Figure B.9. 30º perspective FESEM images of planar Cu plated with 0.75 mAh/cm^2 at 1.0 mA/cm^2. Yellow arrows indicate dendrite-like Li growth.

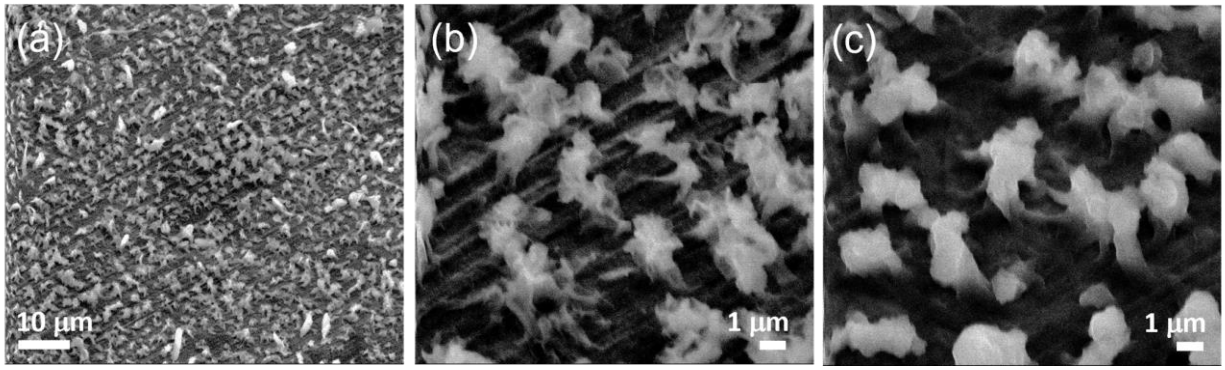

Figure B.10. 30º perspective FESEM images of electrodeposited Li of 0.75 mAh/cm^2 capacity on planar Cu at 1.0 mA/cm^2 and then stripped completely at 1.0 mA/cm^2.

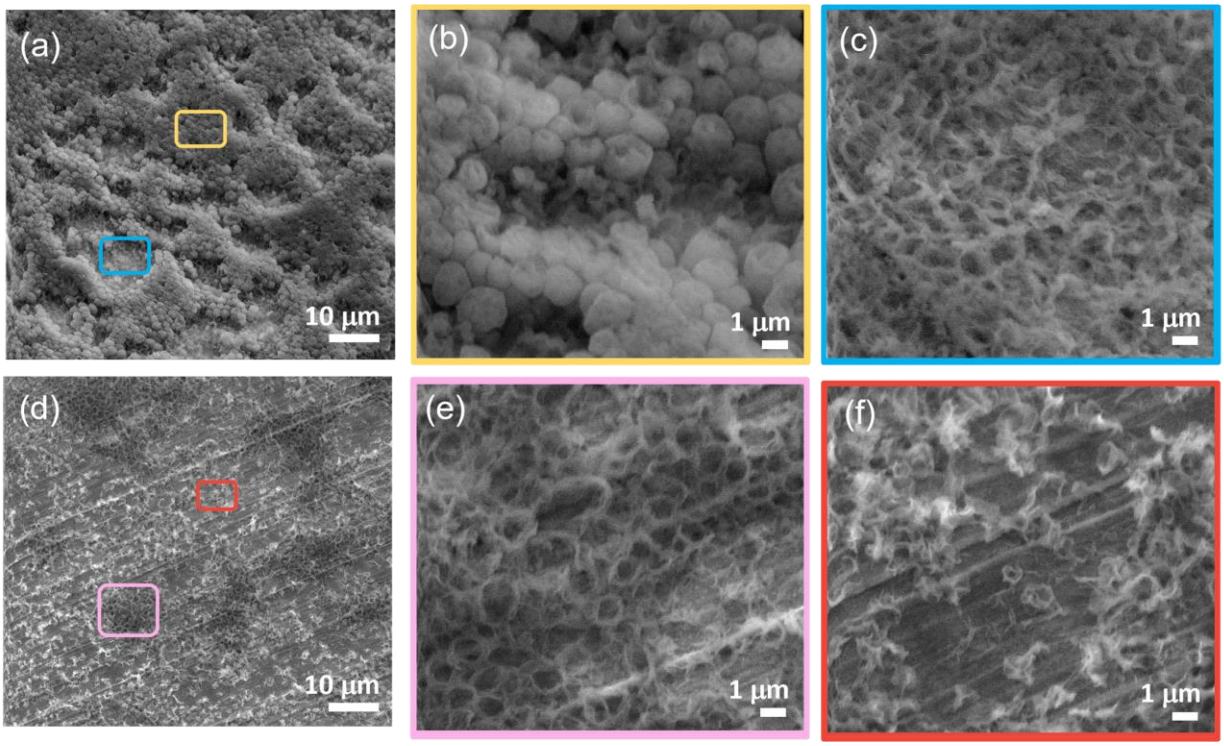

Figure B.11. FESEM images of 0.75 mAh/cm^2 of Li plated on Cu at 5.0 mA/cm^2 and then stripped completely at (a) – (c) 5.0 mA/cm^2 and (d) – (f) 1.0 mA/cm^2 at a 30^o perspective. Higher magnification images of regions highlighted using colored rectangles are bordered to match the respective colors of the rectangles.

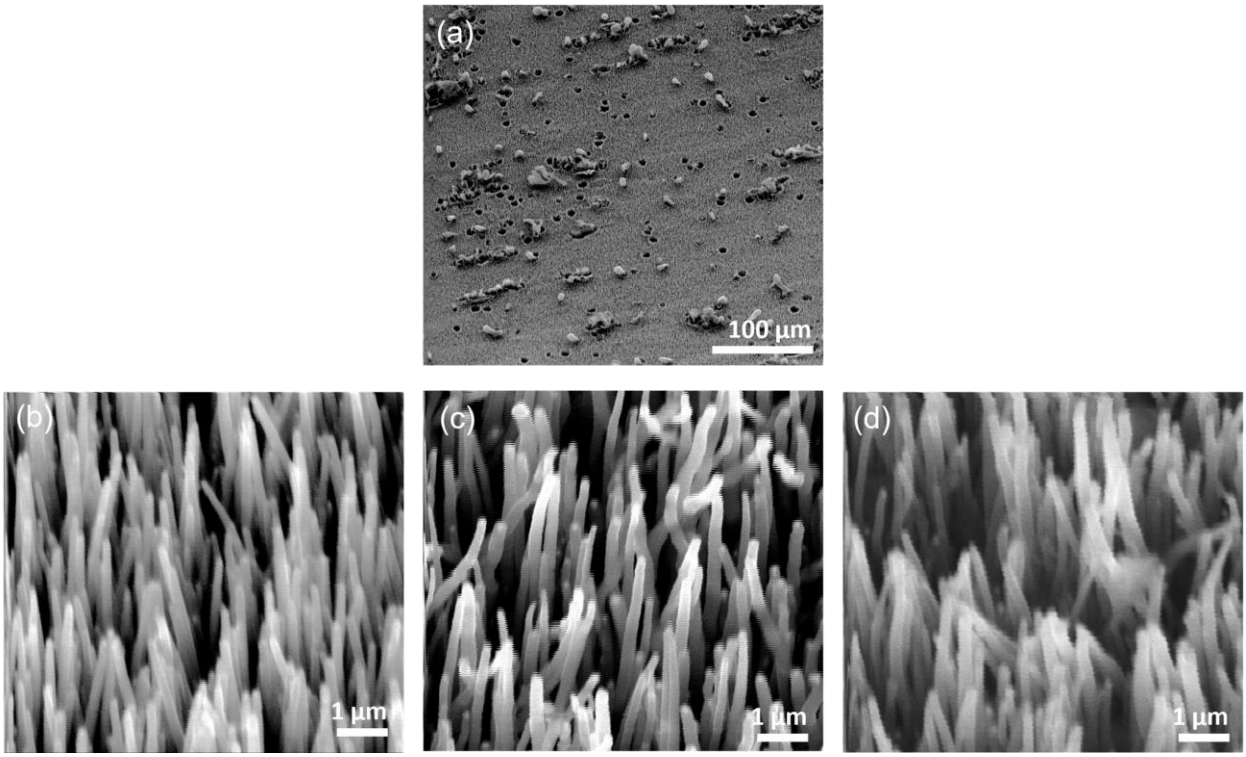

Figure B.12. FESEM images of VACNF/Cu plated with 0.20 mAh/cm^2 Li at (a) & (b) 0.10 mA/cm^2, (c) 1.0 mA/cm^2, (d) 5.0 mA/cm^2 at a 30^o perspective.

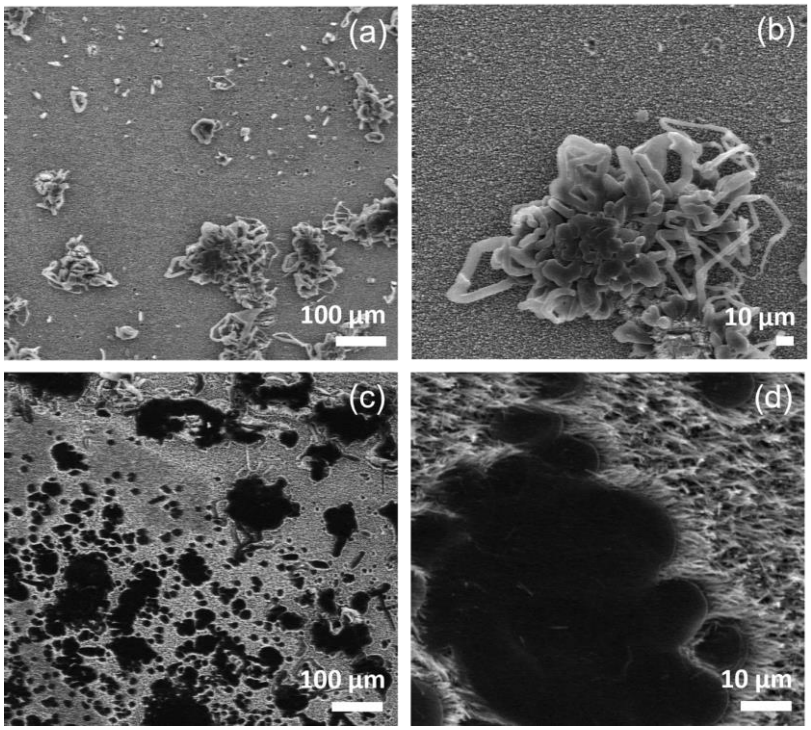

Figure B.13. Top-view FESEM images of VACNF/Cu plated with 0.75 mAh/cm^2 Li at 0.10 mA/cm^2 imaged at (a) & (b) center and (c) & (d) periphery of the electrode.

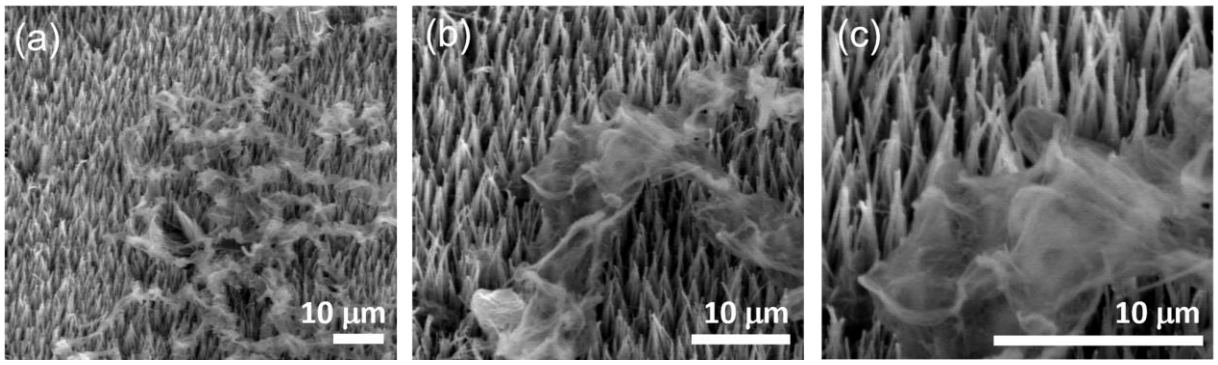

Figure B.14. 30º perspective FESEM images of electrodeposited Li on VACNF/Cu at current densities of 0.10 mA/cm^2 for a capacity of 0.75 mAh/cm^2 and then stripped completely at respective current densities.

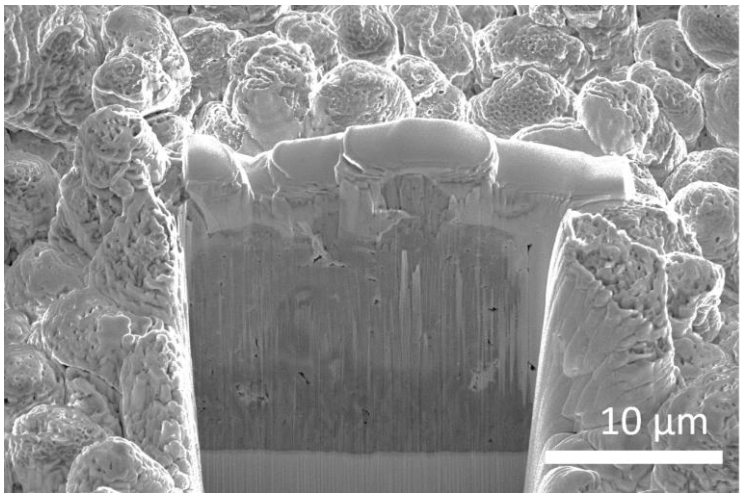

Figure .15. FIB-FESEM image of VACNF/Cu plated with 2.0 mAh/cm^2 Li at 1.0 mA/cm^2 at a 45^o perspective.

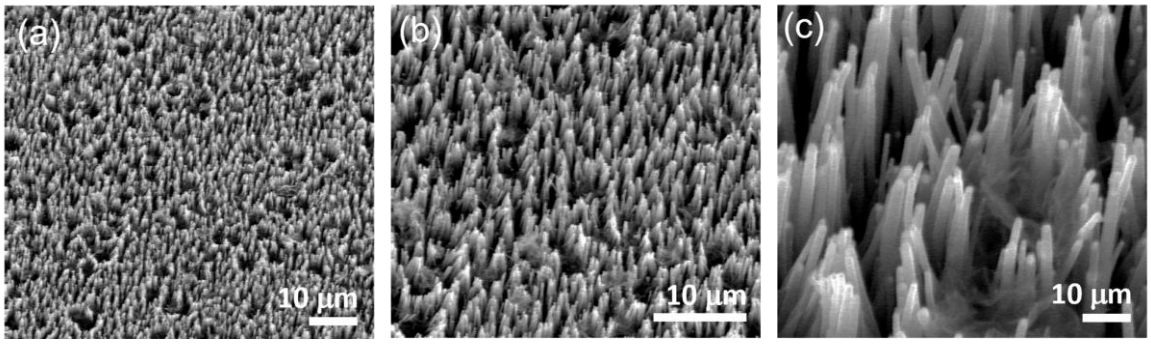

Figure B.16. 30º perspective FESEM images of electrodeposited Li on VACNF/Cu at current densities of 1.0 mA/cm^2 for a capacity of 0.75 mAh/cm^2 and then stripped completely at respective current densities.

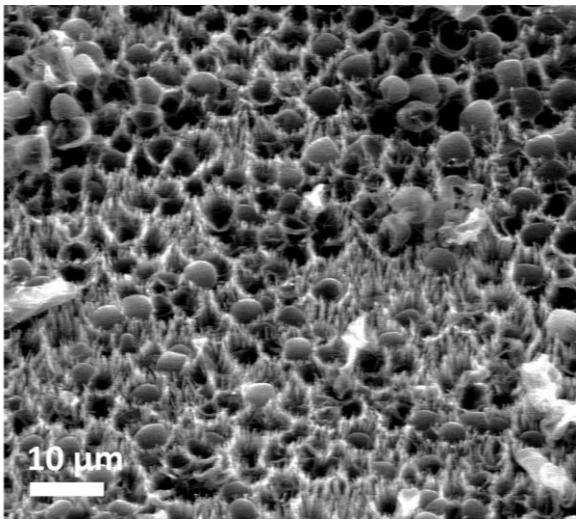

Figure B.17. A 30º perspective FESEM image of VACNF/Cu plated with 0.75 mAh/cm^2 Li at 0.5 mA/cm^2.

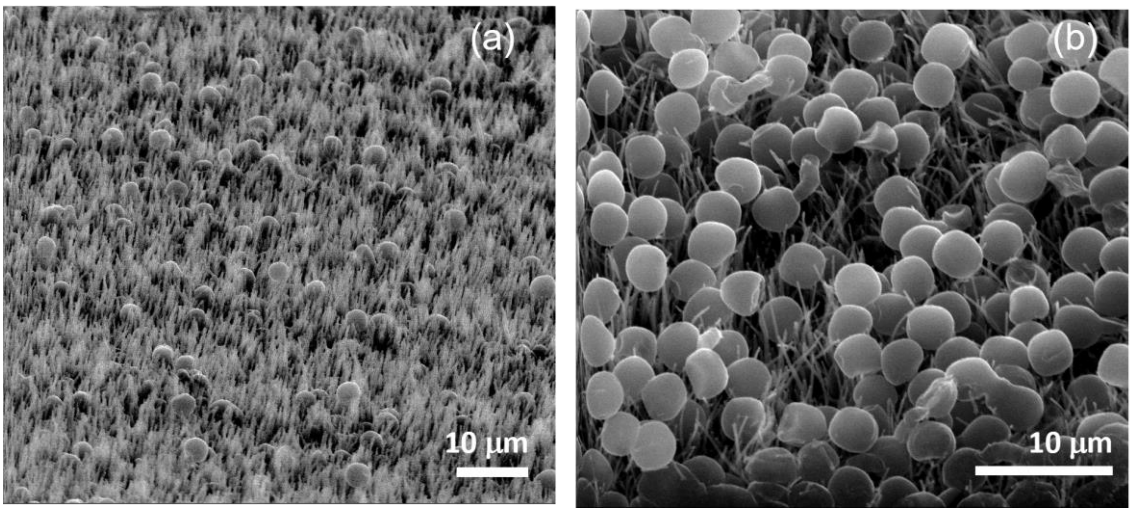

Figure B.18. 30º perspective FESEM images of electrodeposited Li on VACNF/Cu at a current density of 5.0 mA/cm^2 for a capacity of 0.75 mAh/cm^2.

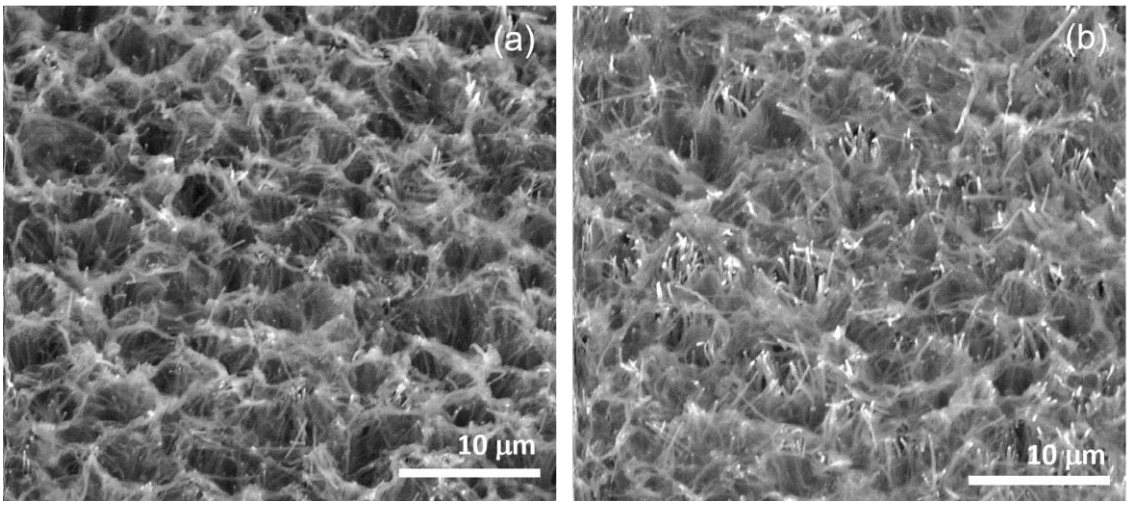

Figure B.19. 30º perspective FESEM images of electrodeposited Li on VACNF/Cu at a current density of 5.0 mA/cm^2 for a capacity of 2.0 mAh/cm^2 and then stripped completely at (a) 1.0 mA/cm^2 and (b) 5.0 mA/cm^2.

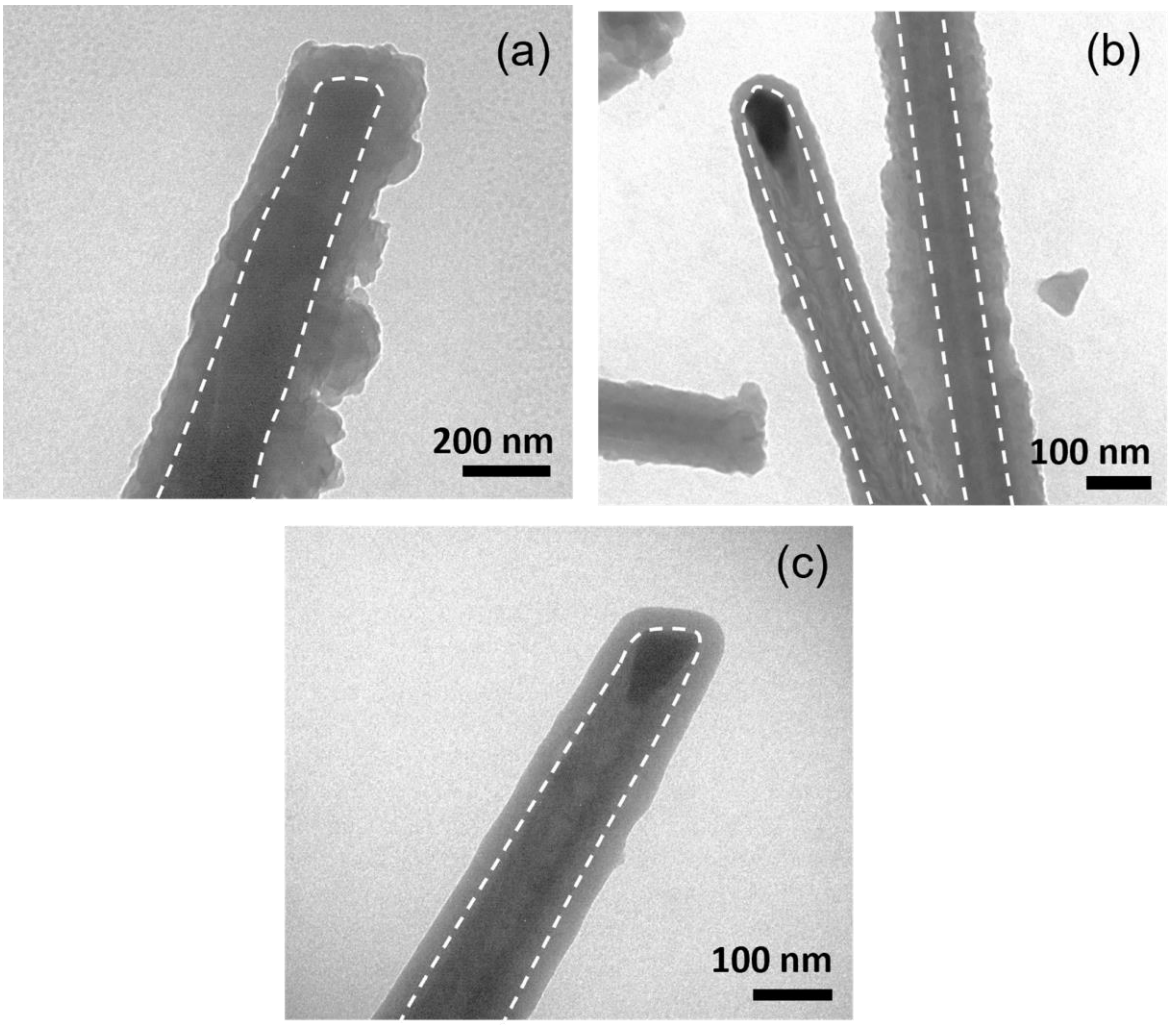

Figure B.20. Cryo-TEM images of Li deposited VACNF with 0.75 mAh/cm^2 Li at (a) 0.10 mA/cm^2, (b) 1.0 mA/cm^2, (c) 5.0 mA/cm^2 current densities.

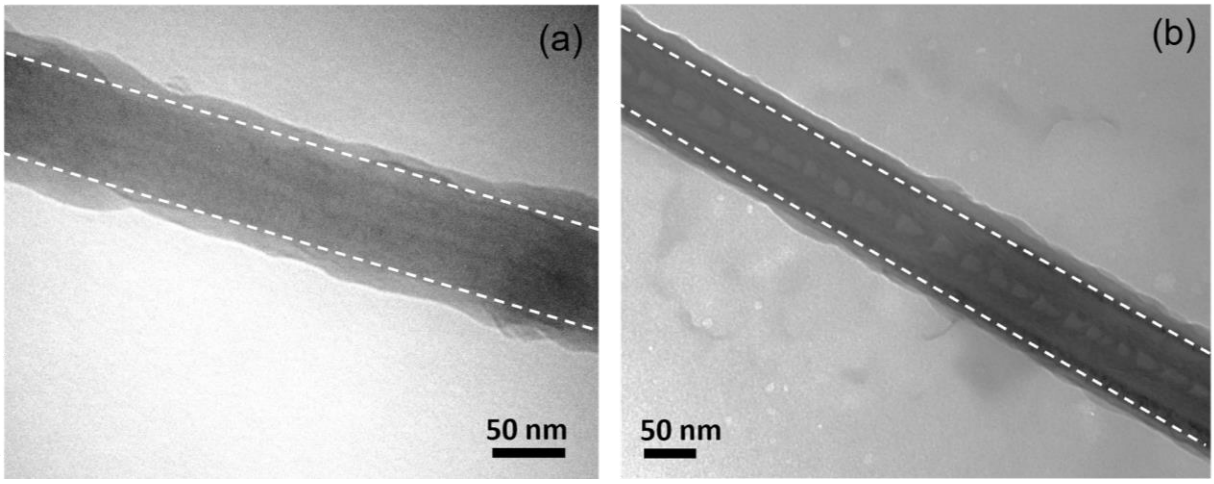

Figure B.21. Cryo-TEM images of VACNFs deposited with 0.75 mAh/cm^2 Li at (a) 0.10 mA/cm^2, (b) 1.0 mA/cm^2 and then completely stripped.

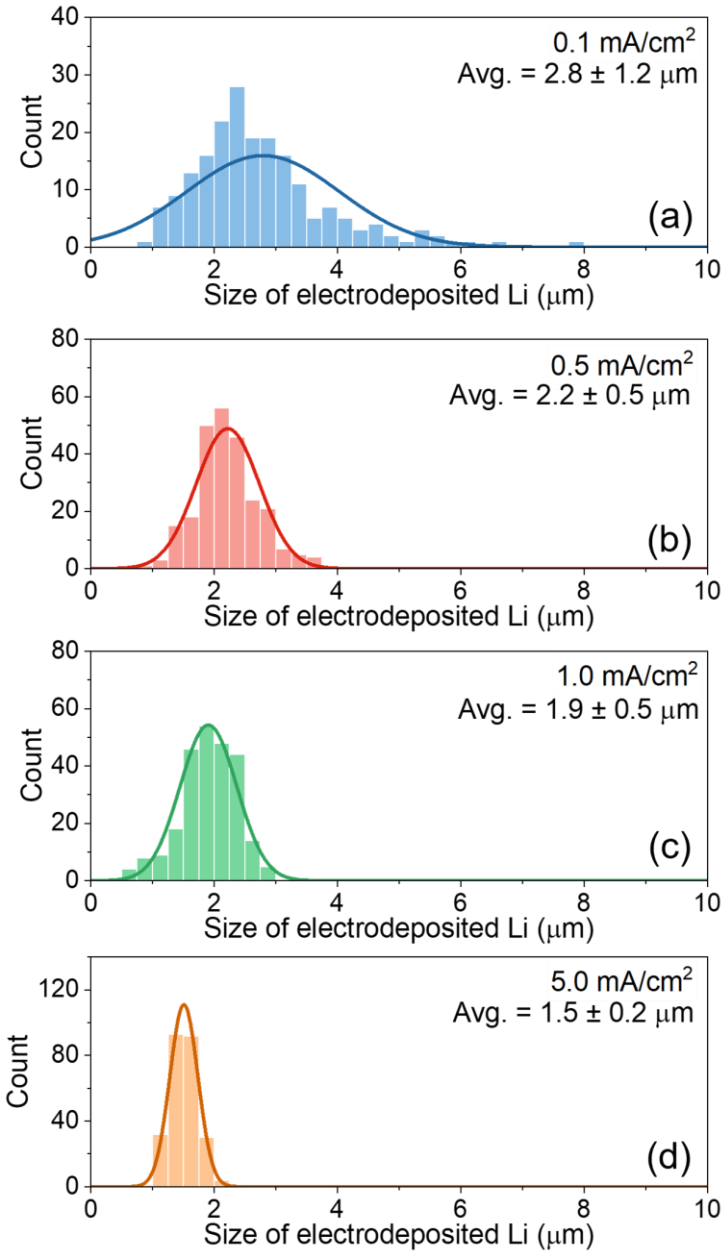

Figure B.22. Histogram for size of electrodeposited Li for a capacity of 0.75 mAh/cm^2 on planar Cu at current densities of (a) 0.10 mA/cm^2, (b) 0.50 mA/cm^2, (c) 1.0 mA/cm^2, and (d) 5.0 mA/cm^2.

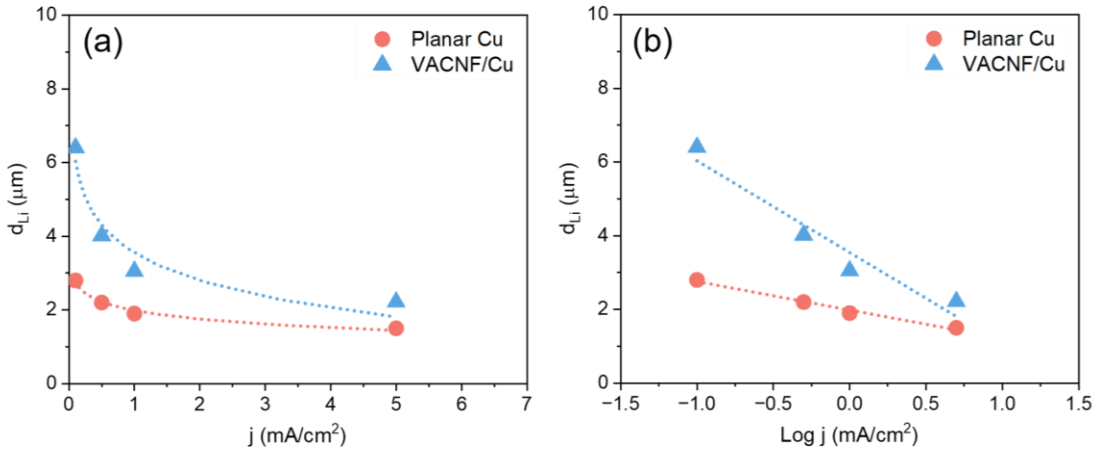

Figure B.23. Effect of the current density (*j*) on the size of Li grains (d_{Li}) on planar Cu and VACNF/Cu electrodes: (a) d_{Li} vs. *j* and (b) d_{Li} vs. *logj*.

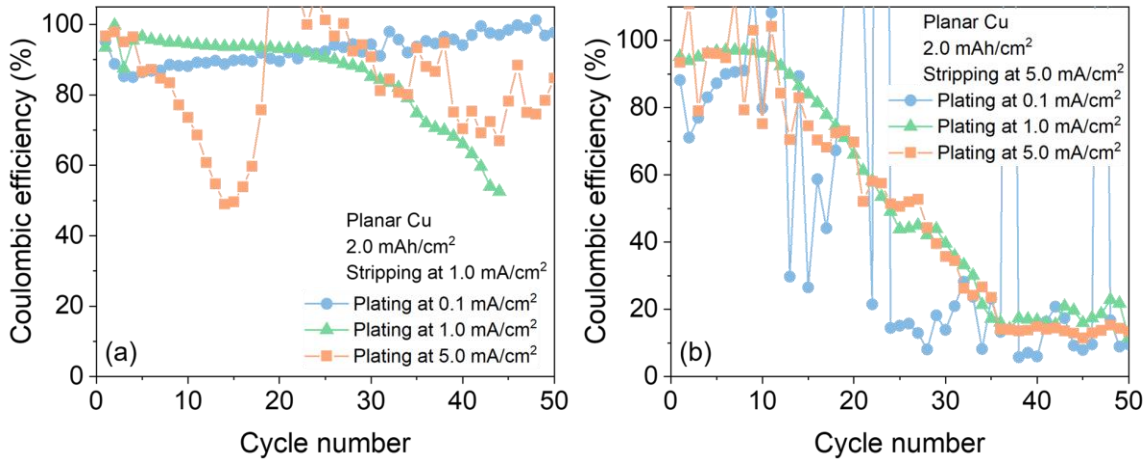

Figure B.24. Coulombic efficiency cycling performance of planar Cu at different plating current densities with the stripping current density at (a) 1.0 mA/cm^2 and (b) 5.0 mA/cm^2.

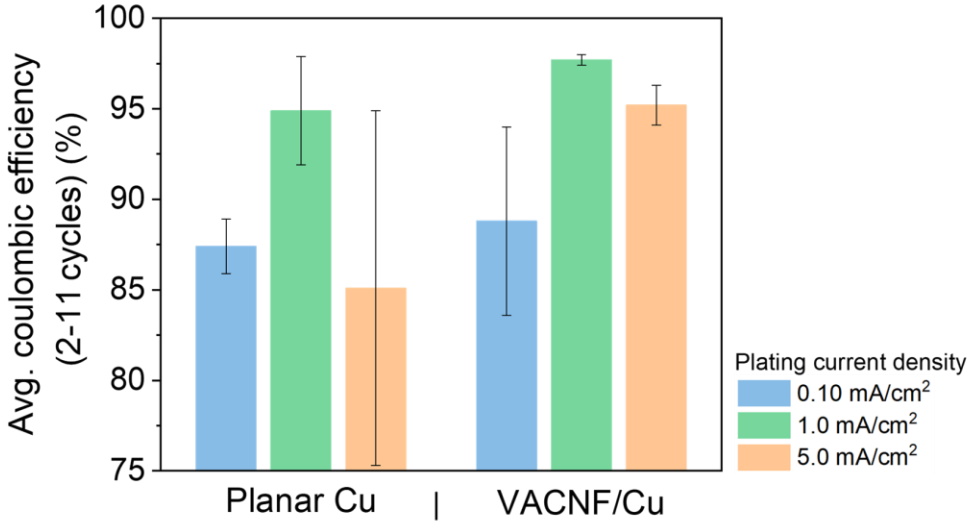

Figure B.25. Average coulombic efficiency for cycles 2-11 with different plating current densities and with the same stripping current density of 1.0 mA/cm^2 for planar Cu and VACNF/Cu electrodes.

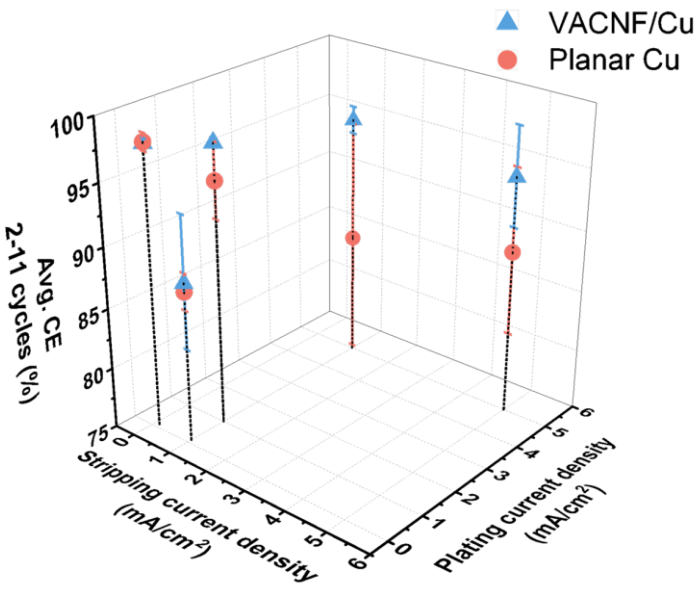

Figure B.26. Average coulombic efficiency for planar Cu and VACNF/Cu electrodes under different plating and stripping current densities.

Appendix C - Supplementary Information for Chapter 5

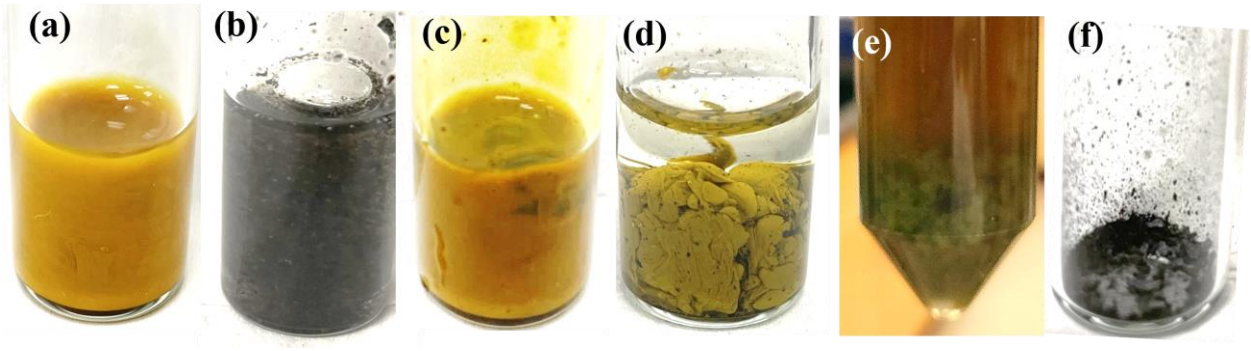

Figure C.1. Optical images of homogeneous aqueous suspensions of (a) V_2O_5 NRs, (b) GO, (c) V_2O_5 NRs and GO mixed together, (d) divalent cation mediated and (e) monovalent cation mediated co-precipitation products, and (f) thermally annealed M- V_2O_5 NRs/rGO hybrid.

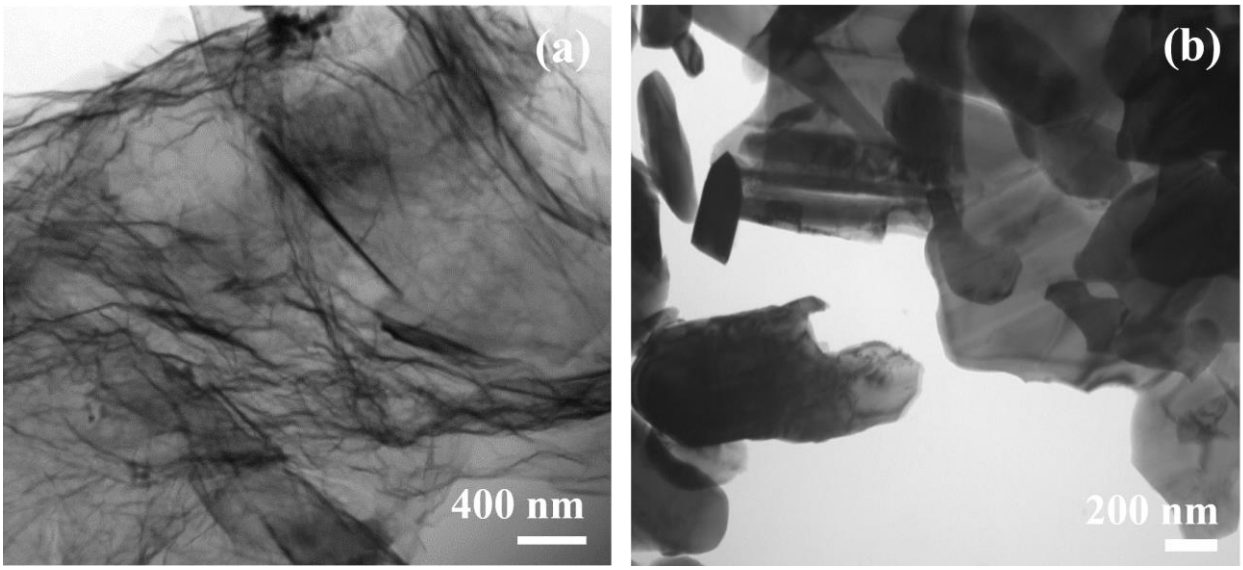

Figure C.2. TEM images of (a) GO and (b) bulk V_2O_5 powder.

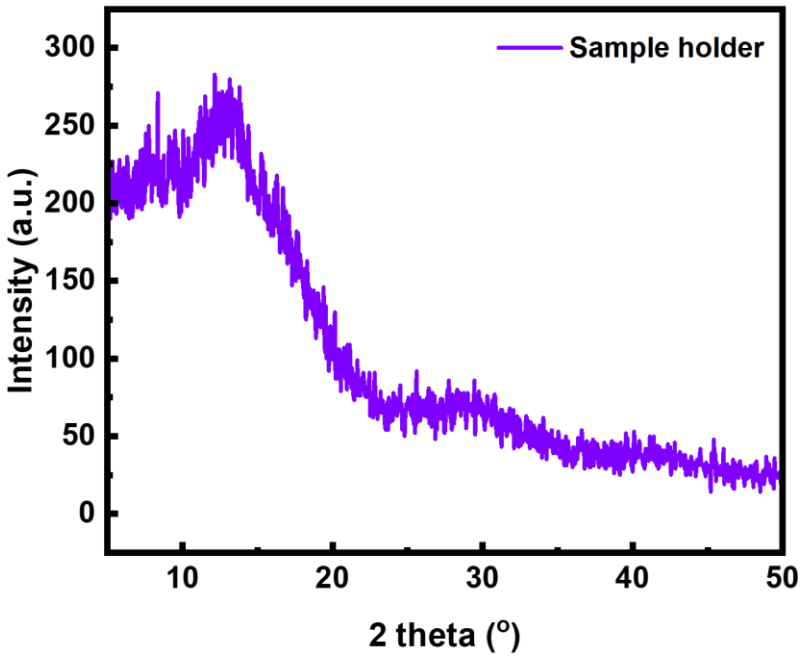

Figure C.3. XRD spectrum of the sample holder.

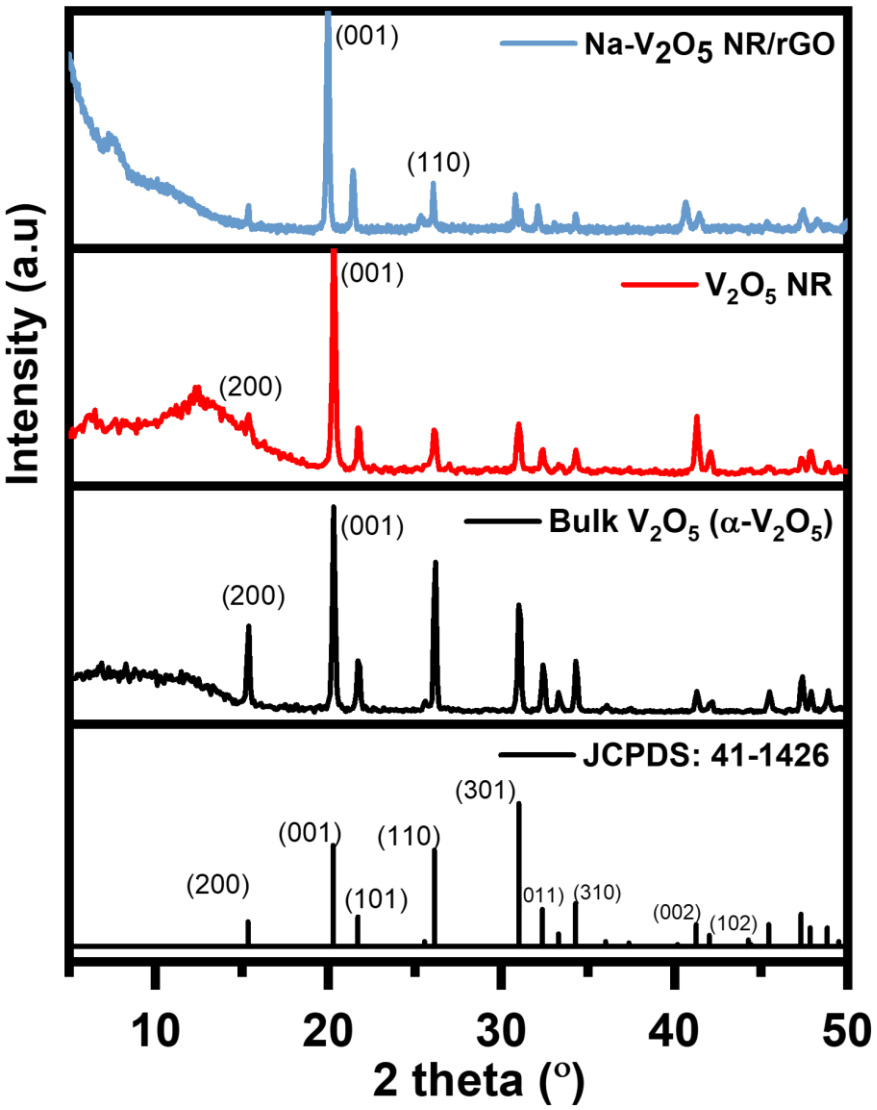

Figure C.4. XRD spectra of Na-V_2O_5 NRs/rGO compared with those of V_2O_5 NRs and bulk V_2O_5.

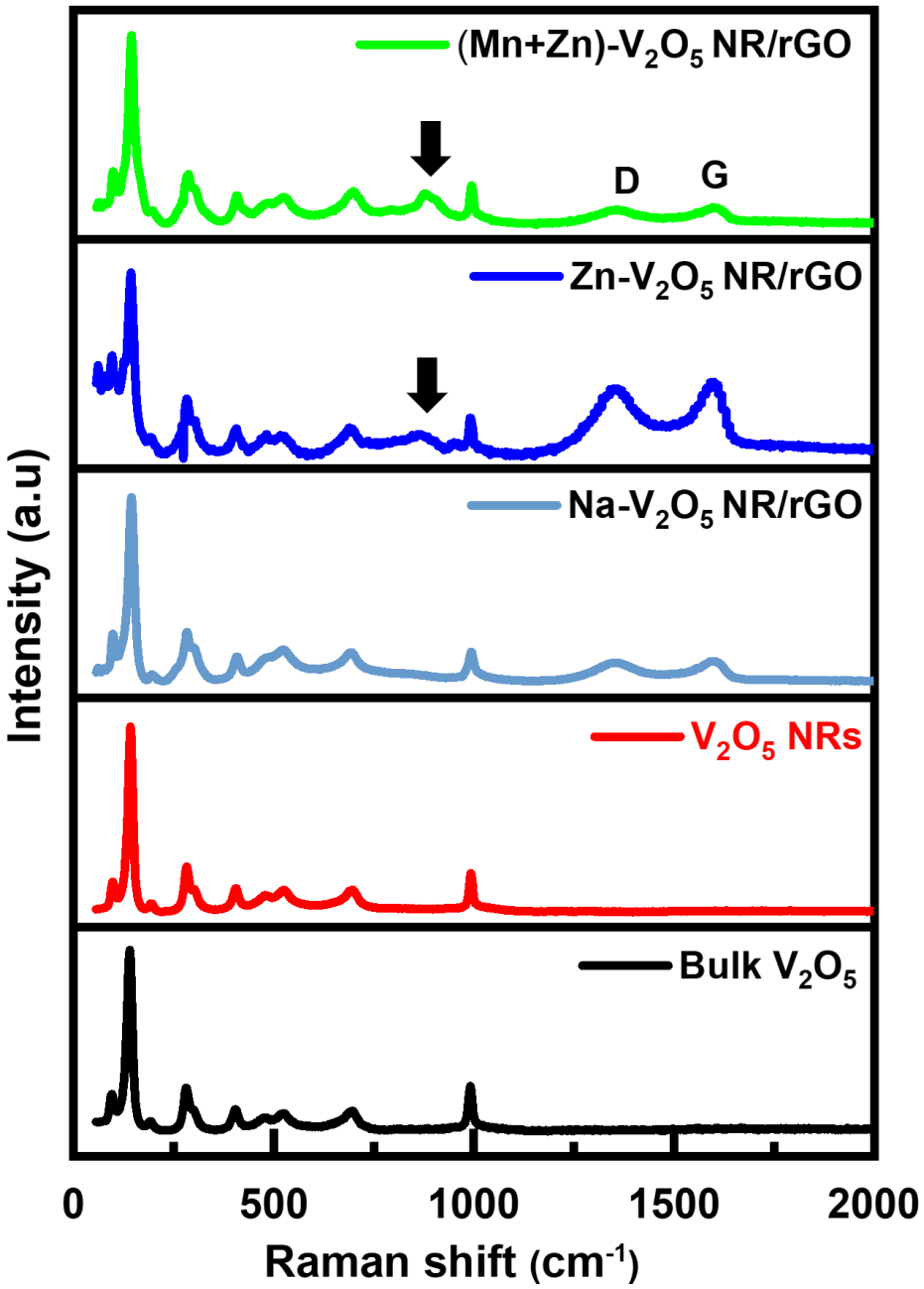

Figure C.5. Raman spectra of various V_2O_5-based materials tested for ZIB cathodes.

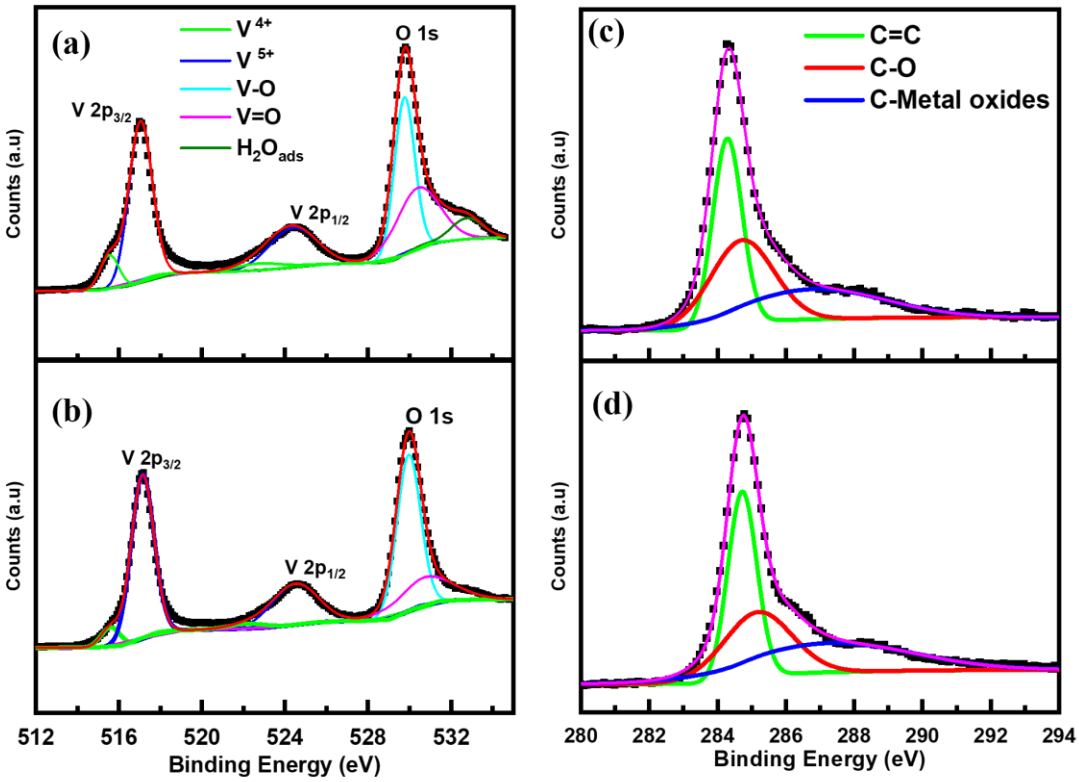

Figure C.6. High-resolution XPS spectra of V2p and O1s peaks of (a) V_2O_5 NRs and (b) bulk V_2O_5 powder. High-resolution C1s XPS peak of (c) Zn-V_2O_5 NR/rGO and (d) (Mn+Zn)-V_2O_5 NR/rGO.

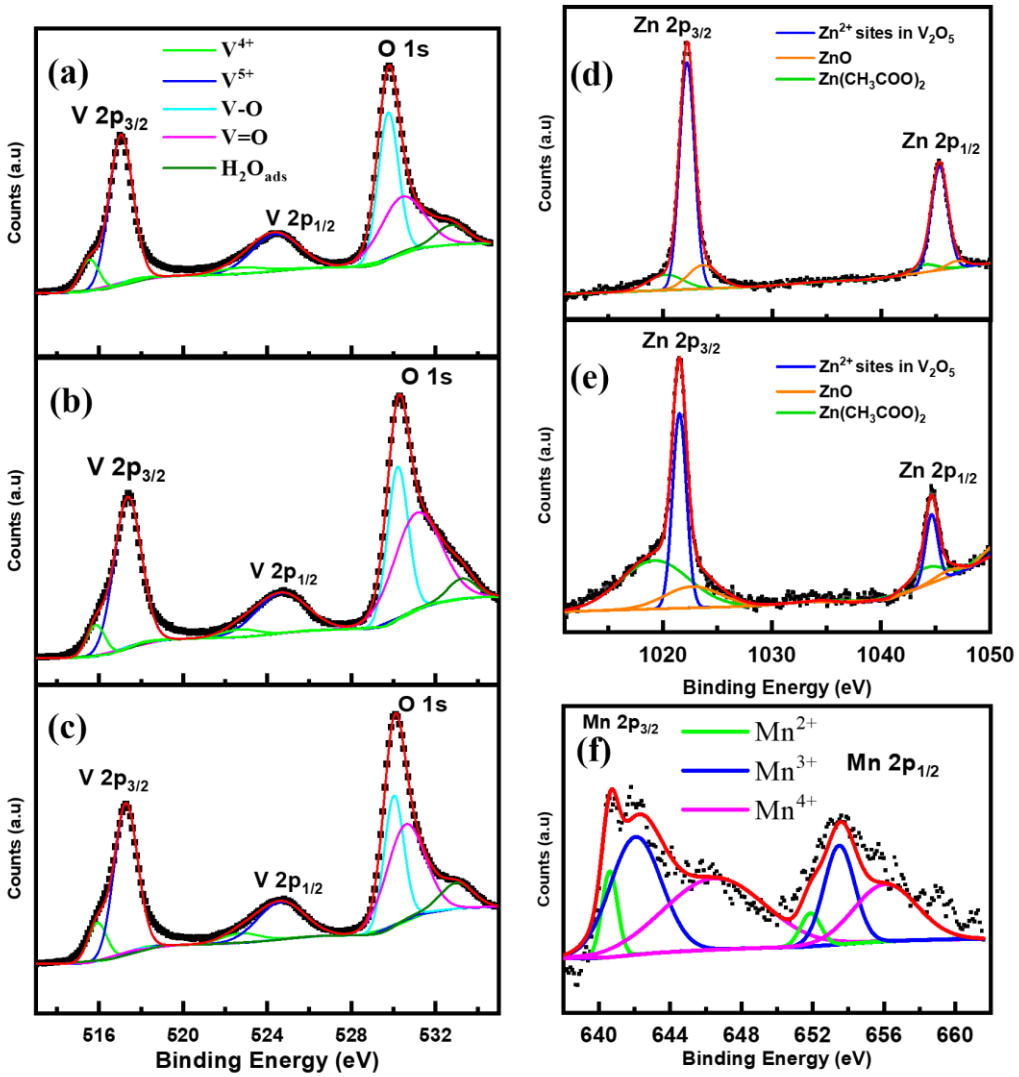

Figure C.7. High-resolution XPS spectra of V2p and O1s peaks of (a) V_2O_5 NR, (b) Zn-V_2O_5 NR/rGO and (c) (Mn+Zn)-V_2O_5 NR/rGO. The Zn2p spectra of (d) Zn-V_2O_5 NR/rGO and (e) (Mn+Zn)-V_2O_5 NR/rGO. (f) The Mn2p spectra of (Mn+Zn)-V_2O_5 NR/rGO.

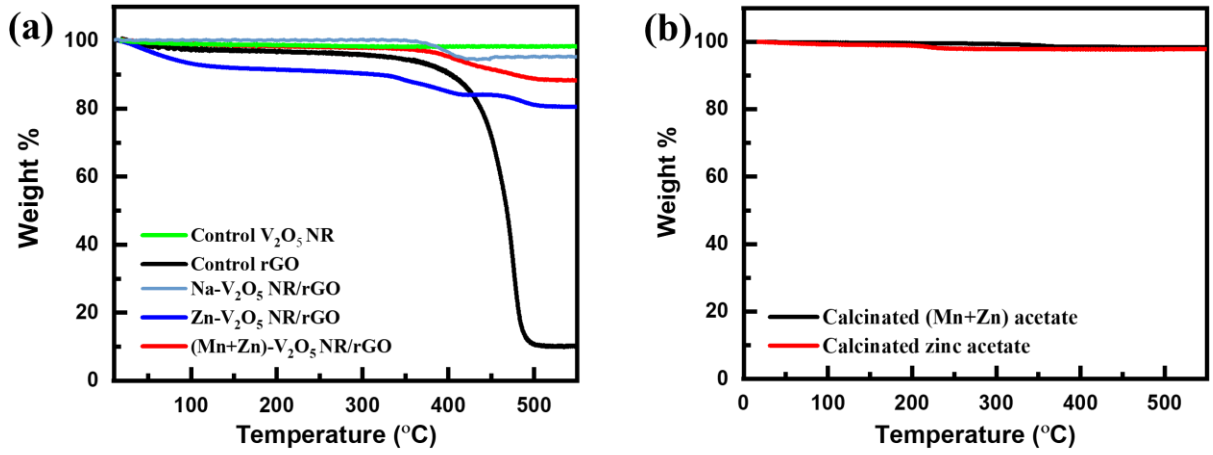

Figure C.8. TGA curves of various hybrid materials and their precursors.

Table C-1: Composition of different ZIB cathodes determined using TGA.

Samples (annealed at 300 °C)	Wt% of samples at 550 °C	Wt% of M-V_2O_5	Wt% of rGO
Zn-V_2O_5 NR/rGO	80.54	78.34	21.66
(Mn+Zn)-V_2O_5 NR/rGO	88.34	87.02	12.98
Na-V_2O_5 NR/rGO	95.34	94.4	5.6
Control rGO	10.16	-	-
Control V_2O_5 NR	100	-	-

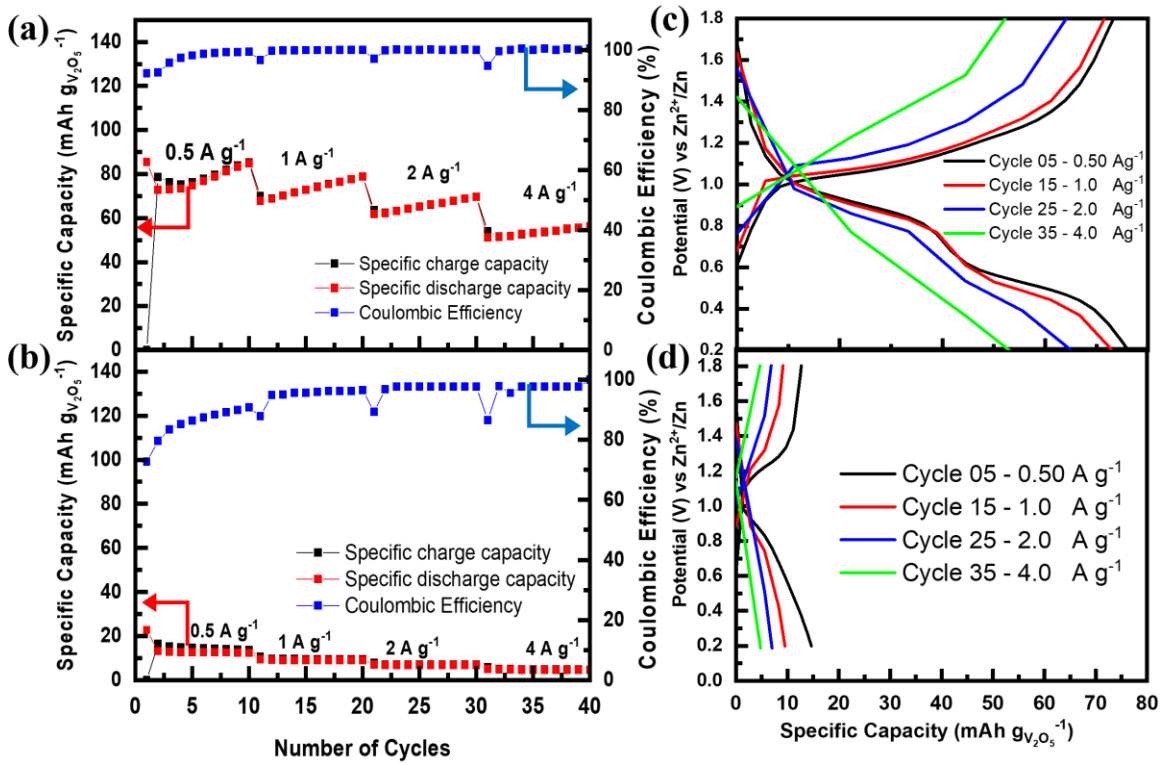

Figure C.9. Rate performance and corresponding galvanostatic charge/discharge voltage curves of (a), (c) V_2O_5 NRs and (b), (d) bulk V_2O_5 powder.

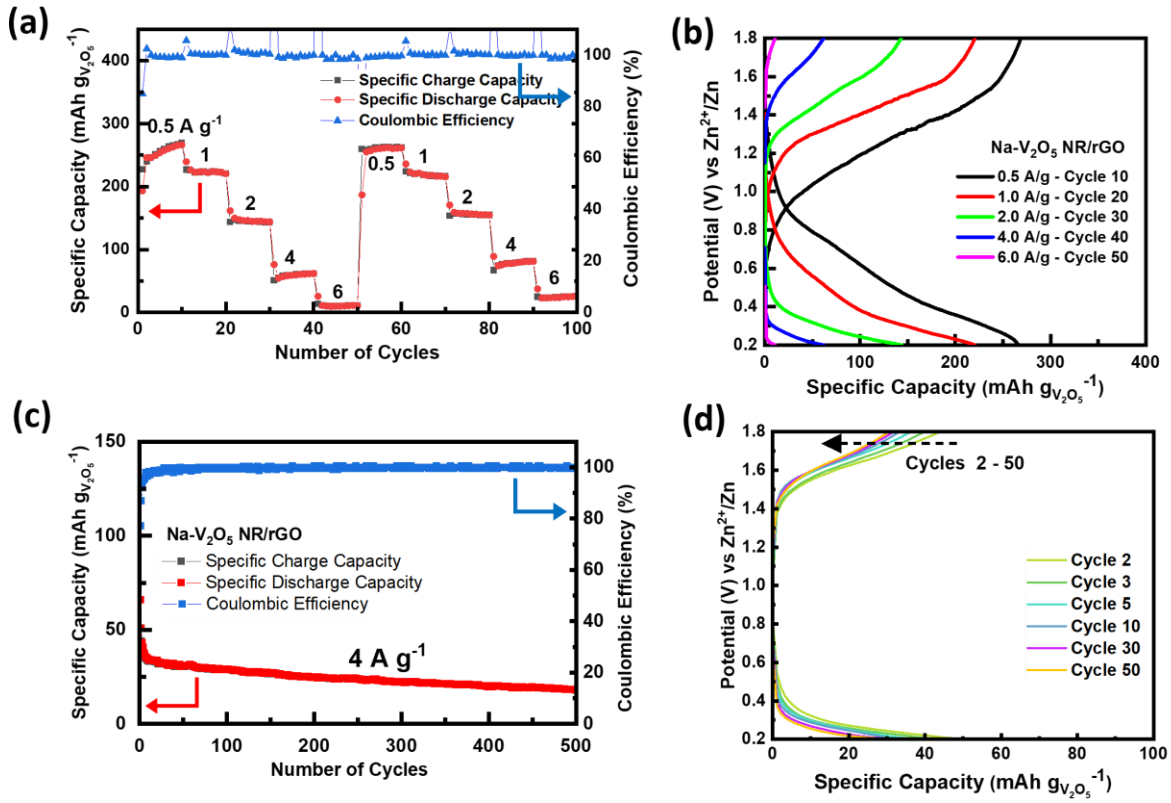

Figure C.10. Electrochemical performance of Na-V_2O_5 NR/rGO cathode: (a) rate performance at different current densities and its corresponding (b) charge/discharge voltage curves, evolution of (c) specific capacity and (d) charge/discharge voltage curves during the long-cycle test at 4.0 A/g.

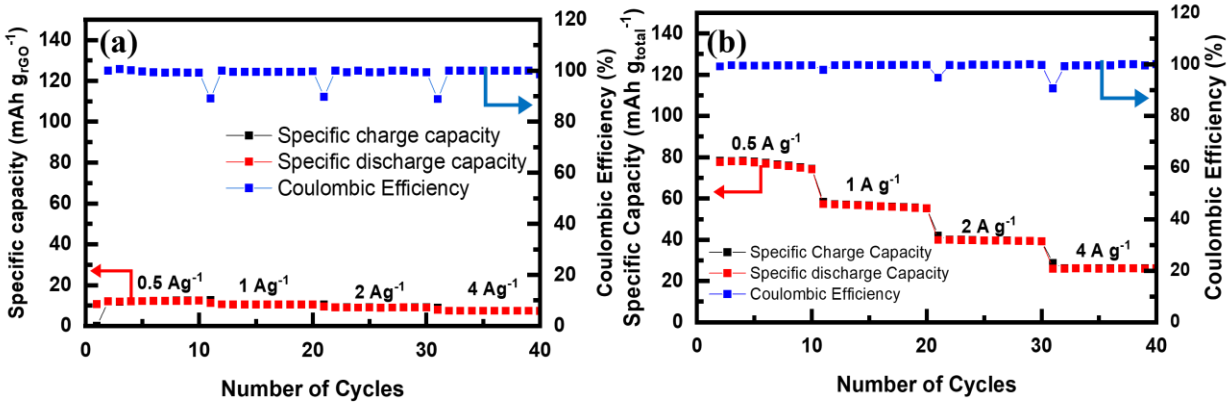

Figure C.11. Rate performance for (a) control rGO and (b) physically mixed V_2O_5 NRs and rGO powders without mediation of any cations.

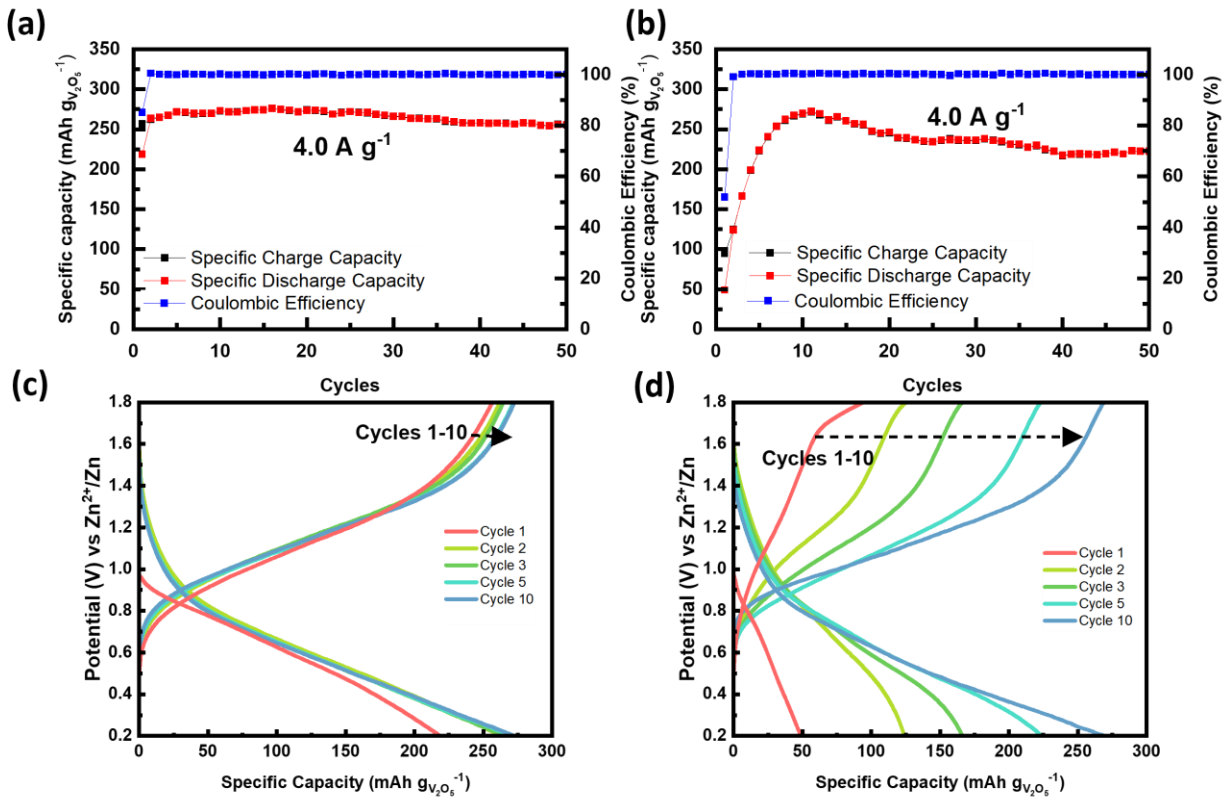

Figure C.12. First 50 cycles of long-cycle tests of the aqueous ZIBs at a fixed current density of 4.0 A g^{-1} of (a) Zn-V_2O_5 NR/rGO and (b) (Mn+Zn)-V_2O_5 NR/rGO cathodes. And corresponding galvanostatic charge-discharge profiles of (c) Zn-V_2O_5 NR/rGO cathode and (d) (Mn+Zn)-V_2O_5 NR/rGO.

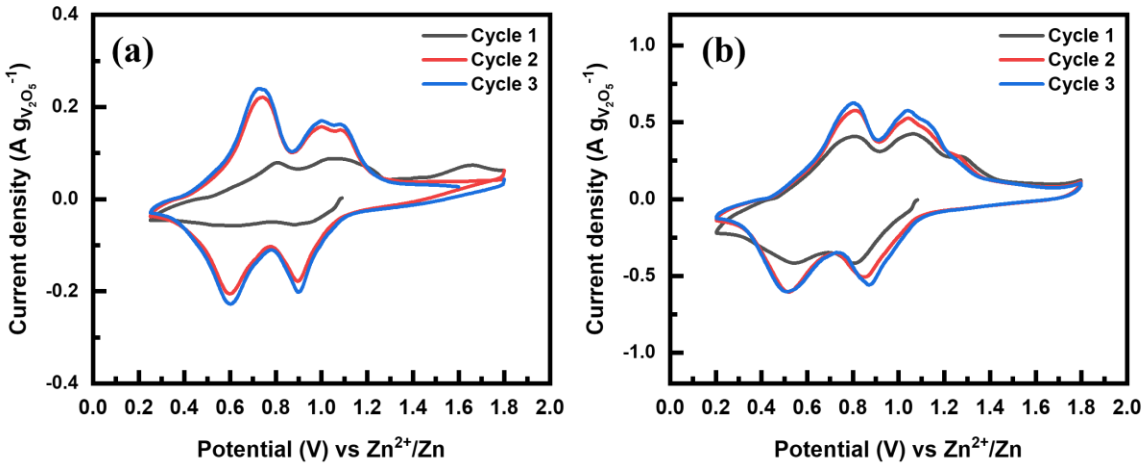

Figure C.13. The cyclic voltammograms of initial cycles of (a) Zn-V_2O_5 NR/rGO at 0.10 mV/s scan rate and (b) (Mn+Zn)-V_2O_5 NR/rGO at 0.50 mV/s scan rate in the potential window of 0.20-1.80 V vs. Zn^{2+}/Zn.

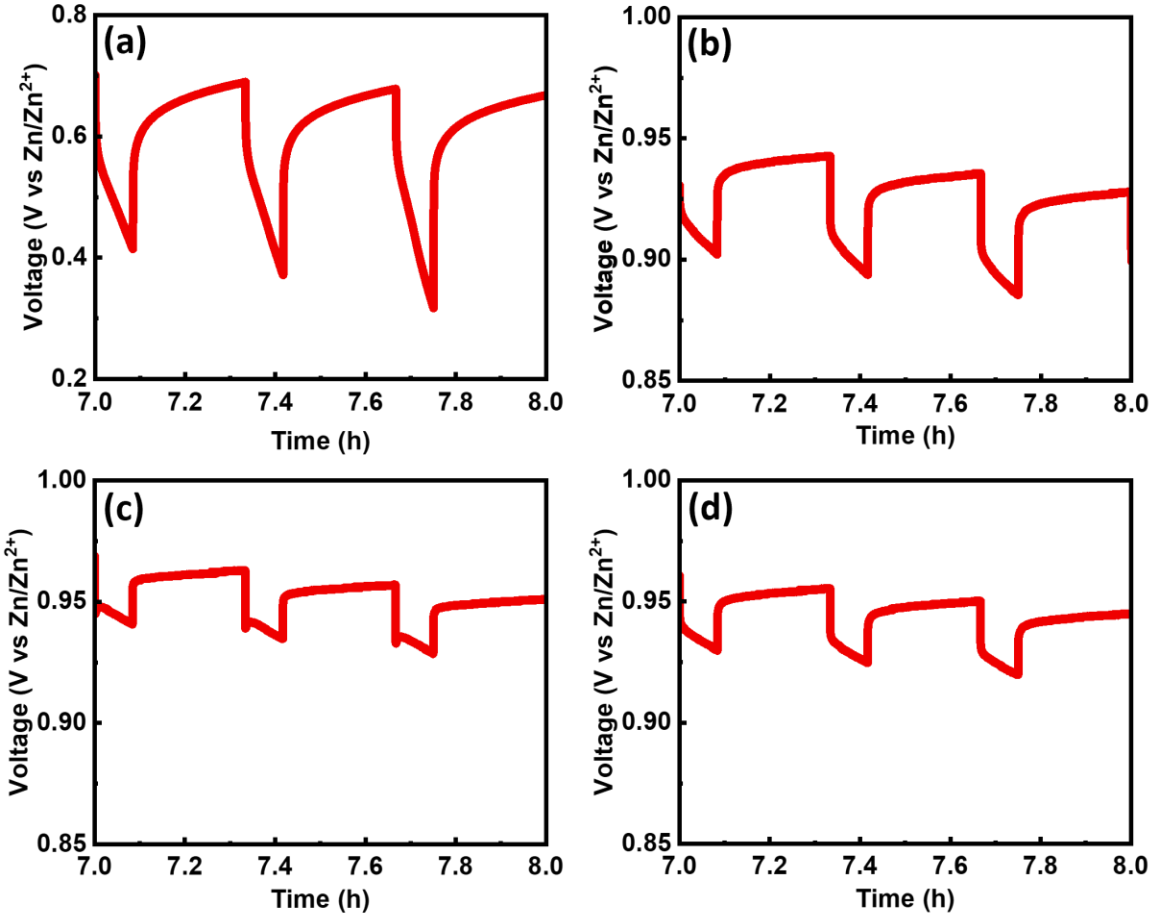

Figure C.14. GITT discharge voltage profiles of (a) V_2O_5 NR, (b) Na-V_2O_5 NR/rGO, (c) Zn-V_2O_5 NR/rGO, (d) (Mn+Zn)-V_2O_5 NR/rGO during 7.0 - 8.0 hour.

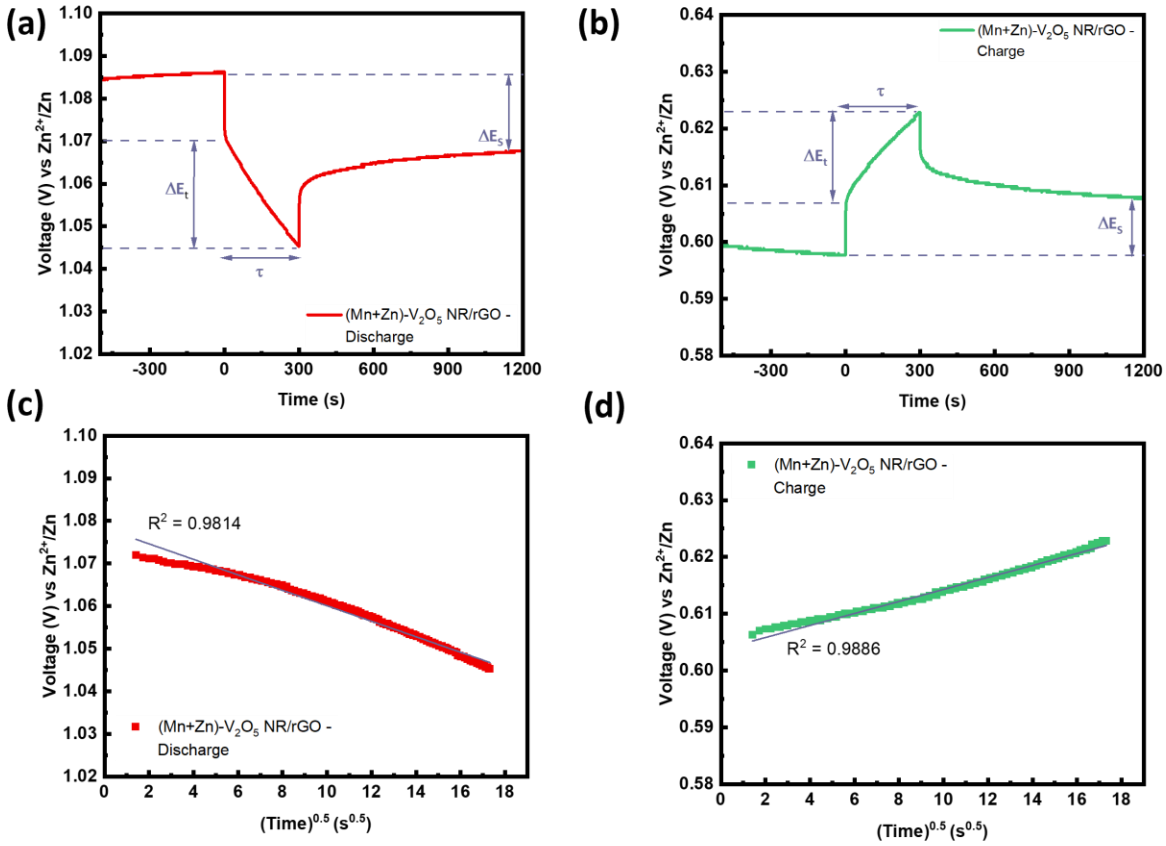

Figure C.15. A representative single GITT voltage profile for the (a) discharge and (b) charge pulses to illustrate the voltage response during the current pulse and the relaxation during rest and the corresponding Voltage vs (time)$^{0.5}$ plots which fits linearly for the (c) discharge and (d) charge pulses.

Table C-2: Zn^{2+} diffusion coefficient for different ZIB cathodes synthesized.

Cathode Materials	Zn^{2+} Diffusion coefficient D_{Zn2+} (cm^2/s)
V_2O_5 NR	3.4×10^{-13}
Na-V_2O_5 NR/rGO	2.2×10^{-11}
Zn-V_2O_5 NR/rGO	9.7×10^{-11}
(Mn+Zn)-V_2O_5 NR/rGO	3.1×10^{-11}

Table C-3: Comparison of the synthesis method and electrochemical performance of vanadium oxide-based materials as the cathode for zinc ion batteries.

Sl. No.	Materials	Synthesis	Electrolyte & voltage window vs. Zn^{2+}/Zn	Rate Performance	Capacity Retention	Ref.
1	Zn-V_2O_5 NR/rGO	Microwave synthesis for 1 h followed by co-precipitation and annealing at 300 °C for 2 h.	2.0 M $ZnSO_4$ 0.20 - 1.80 V	0.50 A/g - 395 mAh/g, 1.0 A/g - 351 mAh/g, 4.0 A/g – 214 mAh/g.	28% from 50th to 2000th cycle 4.0 A/g (254 to 72 mAh/g)	284
	(Zn+Mn)-V_2O_5 NR/rGO			0.50 A/g - 291 mAh/g, 1.0 A/g - 271 mAh/g, 4.0 A/g – 225 mAh/g.	77% from 50th to 2000th cycle 4.0 A/g (222 to 172 mAh/g)	
	Na-V_2O_5 NR/rGO			0.50 A/g - 266 mAh/g 1.0 A/g - 221 mAh/g. 4.0 A/g – 56-63 mAh/g	40% from 10th to 500th cycle 4.0 A/g (34 to 13.7 mAh/g)	
2	$AlV_5O_{12}.6H_2O$/rGO	Hydrothermal at 180 °C for 24 h.	3.0 M $Zn(CF_3SO_3)_2$ 0.20 - 1.60 V	0.20 A/g - 480.7 mAh/g 0.50 A/g - 462.1 mAh/g 5.0 A/g - 325.4 mAh/g	65% after 1000 cycles at 10.0 A/g (228 mAh/g).	285
3	$Na_{0.33}V_2O_5$ nanowire	Hydrothermal at 200 °C for 48 h.	3.0 M $Zn(CF_3SO_3)_2$ 0.20 - 1.60 V	0.50 A/g - 173.4 mAh/g, 1.0 A/g - 137.5 mAh/g.	93% after 1000 cycles at 1.0 A/g (from cycle 2) (218.4 mAh/g). ~300 mAh/g - 1st cycle.	286
4	$CuV_2O_5.1.6H_2O$	Hydrothermal at 120 °C for 6 h.	3.0 M $Zn(CF_3SO_3)_2$ 0.20 - 1.60 V	0.50 A/g - 379 mAh/g.	93% after 1000 cycles at 4.0 A/g (~260 mAh/g).	287
	MgV_20_5. $1.6H_2O$			0.50 A/g - 349 mAh/g.	78% after 1000 cycles at 4.0 A/g (195 mAh/g).	
5	$Zn_{0.34}V_2O_5 \cdot 0.37H_2O$	Hydrothermal at 200 °C for 3 h and annealing at 350 °C for 2 h.	2.0 M $Zn(CF_3SO_3)_2$ 0.20 - 1.60 V	0.50 A/g - 323.6 mAh/g, 4.0 A/g - 180 mAh/g.	85.2% after 1000 cycles at 8.0 A/g (113.3 mAh/g).	288
6	$Zn_{0.25}V_2O_5.nH_2O$ nanobelts	Microwave synthesis for 100 min at 180 °C.	1.0 M ZnSO4 0.50 – 1.40 V	0.3 A/g – 279.5 mAh/g 4.5 A/g – 223 mAh/g	82% after 1000 cycles at 4.5 A/g (183 mAh/g)	289
7	$V_2O_5.nH_2O$/rGO-PVA	Hydrothermal at 180 °C for 12 h.	3.0 M $Zn(CF_3SO_3)_2$ 0.10 - 1.80 V	0.50 A/g - 208 mAh/g, 1.0 A/g - 47 mAh/g.	78.3 % after 300 cycles at 0.5 A/g (152 mAh/g).	290
8	$K_{0.62}Mg_{0.06}V_2O_5.nH_2O$	Hydrothermal at 120 °C for 6 h.	3.0 M $Zn(CF_3SO_3)_2$ 0.20 - 1.50 V	0.50 A/g – 335 mAh/g.	72% after 2000 cycles at 4.0 A/g (222 mAh/g).	291
	$K_xV_2O_5.nH_2O$			0.50 A/g – 200 mAh/g.	88% after 2000 cycles at 4.0 A/g (190 mAh/g).	
	$MgV_2O_5.nH_2O$			0.50 A/g – 200 mAh/g.	50 % after 2000 cycles at 4.0 A/g (126 mAh/g).	

9	$Na_xV_2O_5{\cdot}nH_2O$/rGO/CNT	Hydrothermal at 180 °C for 24 h.	3.0 M $Zn(CF_3SO_3)_2$ 0.20 - 1.60 V	1.0 A/g - 450.5 mAh/g.	83.1% after 1800 cycles at 10.0 A/g (301.9 mAh/g).	292
10	V_2O_5 hollow spheres	Hydrothermal at 180 °C for 20 h and annealing at 350 °C for 2 h.	3.0 M $ZnSO_4$ 0.20 - 1.60 V	0.50 A/g - 170 mAh/g.	49% after 265 cycles at 0.50 A/g.	293
11	$Mg_{0.34}V_2O_5{\cdot}\ nH_2O$ nanobelts	Hydrothermal at 220 °C for 48 h.	3.0 M $Zn(CF_3SO_3)_2$ 0.10 - 1.80 V	0.50 A/g - 291 mAh/g.	97% after 2000 cycles at 5.0 A/g (88 mAh/g).	294
12	CuV_2O_5-300	Hydrothermal at 200 °C for 48 h and annealing at 300 °C for 2 h.	2.0 M $ZnSO_4$ 0.30 - 1.40 V	1.0 A/g - 359 mAh/g.	66% after 5 cycles (204 mAh/g) and then 88% after 10000 cycles at 10.0 A/g (179.5 mAh/g).	105
	ZnV_2O_5-300			1.0 A/g - 260 mAh/g.	88% after 500 cycles at 10.0 A/g (225 mAh/g).	
13	$K_{0.5}V_2O_5$	Hydrothermal at 200 °C for 48 h and annealing at 250 °C for 2 h.	3.0 M $ZnSO_4$ 0.40 - 1.40 V.	1.0 A/g - 272.2 mAh/g.	62% after 200 cycles at 2.0 A/g (167.1 mAh/g). 75% after 3000 cycles at 5.0 A/g (140.3 mAh/g).	295
14	Porous V_2O_5 nanofibers	Electrospinning and annealing at 400 °C for 1 h.	3 M $Zn(CF_3SO_3)_2$ 0.50 - 1.50 V	0.60 A/g - 204 mAh/g.	81% after 500 cycles at 0.60 A/g (166 mAh/g).	296
15	$Li_{0.45}V_2O_5.0.89H_2O$	Hydrothermal at 180 °C for 30 h.	2.0 M $ZnSO_4$ 0.30 - 1.55 V	0.50 A/g - 298 mAh/g.	86% after 1000 cycles at 10.0 A/g (126 mAh/g).	297
16	LiV_2O_5 - 200	Ageing in salt solution for 96 h and annealing for 2 h.	2.0 M $Zn(CF_3SO_3)_2$ 0.20 to 1.60 V	0.50 A/g - 332 mAh/g.	91.92 % after 1000 cycles at 10.0 A/g (158 mAh/g).	298
	NaV_2O_5 - 300			0.50 A/g - 351 mAh/g.	89.47% after 1000 cycles at 10.0 A/g (172 mAh/g).	
	KV_2O_5 - 300			0.50 A/g - 341 mAh/g.	83.56 % after 1000 cycles at 10.0 A/g (158 mAh/g).	

Appendix D - Publications, Presentations and Awards

Publications:

1. **Rajendran, S.**; Sekar, A.; Li, J. Deciphering the Effect of Nucleation/Growth Kinetics on the Morphology of Li Plating/Stripping on Vertically Aligned Carbon Nanofibers – a Low-Tortuosity 3-D Nanostructured Carbon Host. ***Chemical Engineering Journal*** **2024**, 484, 149515. DOI: 10.1016/j.cej.2024.149515.

2. Sekar, A.; Muthukumar, K.; **Rajendran, S.**; Li, J. Synthesis of Defect-Engineered Molybdenum Sulfides on Reduced Graphene Oxide for Enhanced Hydrogen Evolution Reaction Kinetics. ***International Journal of Hydrogen Energy*** 51, **2024**, Pages 1387-1396. DOI: 10.1016/j.ijhydene.2023.11.107.

3. Mayyahi, A. A.; Sekar, A.; **Rajendran, S.**; Sigdel, S.; Lu, L.; Wang, J.; Wang, G.; Li, J.; Amama, P. B. Hierarchical TiO_2-g-C_3N_4 Photocatalyst with Purification Effect for NO_x Oxidation under Cyan Light. ***Journal of Photochemistry and Photobiology A: Chemistry*** **2023**, 444, 114965. DOI: 10.1016/j.jphotochem.2023.114965.

4. **Rajendran, S.**; Sekar, A.; Li, J. Mechanistic Understanding of Li Metal Anode Processes in a Model 3D Conductive Host Based on Vertically Aligned Carbon Nanofibers. ***Carbon*** **2023**, 212, 118174. DOI: 10.1016/j.carbon.2023.118174.

5. Zaidi, S. S. H.; **Rajendran, S.**; Sekar, A.; Elangovan, A.; Li, J.; Li, X. Binder-Free Li-O_2 Battery Cathodes Using Ni- and PtRu-Coated Vertically Aligned Carbon Nanofibers as Electrocatalysts for Enhanced Stability. ***Nano Research Energy*** **2023**, 2 (2), e9120055. DOI: 26599/NRE.2023.9120055.

6. Muthukumar, K.; **Rajendran, S.**; Sekar, A.; Chen, Y.; Li, J. Synthesis of V_2O_5 Nanoribbon-Reduced Graphene Oxide Hybrids as Stable Aqueous Zinc-Ion Battery Cathodes via Divalent Transition Metal Cation-Mediated Coprecipitation. ***ACS Sustainable Chem. Eng.*** **2023**, 11 (6), 2670–2679. DOI: 10.1021/acssuschemeng.2c07629.

7. Sekar, A.; Metzger, N.; **Rajendran, S.**; Elangovan, A.; Cao, Y.; Peng, F.; Li, X.; Li, J. PtRu Catalysts on Nitrogen-Doped Carbon Nanotubes with Conformal Hydrogenated TiO_2 Shells for Methanol Oxidation. ***ACS Appl. Nano Mater.*** **2022**, 5 (3), 3275–3288. DOI: 10.1021/acsanm.1c03742.

8. Elangovan, A.; Xu, J.; Sekar, A.; **Rajendran, S.**; Liu, B.; Li, J. Platinum Deposited Nitrogen-Doped Vertically Aligned Carbon Nanofibers as Methanol Tolerant Catalyst for Oxygen Reduction Reaction with Improved Durability. ***Applied Nano*** **2021**, 2 (4), 303–318. DOI: 10.3390/applnano2040022.

9. Song, Yang; Wright, J.; Anderson, M.; **Rajendran, S**.; Ren, Z.; Hua, D.; Koehne, J. E.; Meyyappan, M.; Li, J., Quantitative Detection of Cathepsin B Activity in Neutral pH Buffers Using Gold Microelectrode Arrays: Toward Direct Multiplex Analyses of Extracellular Proteases in Human Serum. ***ACS Sensors*** **2021**, 6, 3621-3631. DOI: 10.1021/acssensors.1c01175.

Presentations:

1. **Rajendran, S.**; and Li, J., Mechanistic Understanding of Lithium Plating/Stripping Processes in a 3D Conductive Host Based on Vertically Aligned Carbon Nanofibers for Li Metal Anodes. **242nd Electrochemical Society Meeting**, Atlanta, GA, USA, 2022 - Oral Presentation.

2. **Rajendran, S.**; and Li, J., Kinetic Control on the Morphology of Electrodeposited Lithium on a Low Tortuous, Three-Dimensional Nanostructured Carbon Host for Lithium Metal Anodes. **ACS Fall 2023**, San Francisco, CA - Oral and Poster Presentations.

Awards:

1. Ohno Award, Department of Chemistry, Kansas State University (2024).
2. NOTICXE Graduate Student Fellowship, Department of Chemistry, Kansas State University (2024).
3. Meloan Award for Outstanding Research in Analytical Chemistry, Department of Chemistry, Kansas State University (2023).
4. Travel Award, Phi Lambda Upsilon, Department of Chemistry, Kansas State University (2022, 2023).
5. Travel Award, Graduate Student Council, Kansas State University (2022, 2023).
6. Travel Award, College of Arts and Sciences, Kansas State University (2022, 2023).
7. Graduate Classroom Award, Phi Lambda Upsilon, Department of Chemistry, Kansas State University (2021).
8. Lindquist Tacha Cancer Research Award, Johnson Cancer Research Institute, Kansas State University (2021).